QUANTUM COMMUNICATION CHANNELS BETWEEN EARTH AND SPACE AND SPACE TO EARTH

DOTTORANDO: ANDREA TOMAELLO

SUPERVISORE: CH.MO PROF. GIAMPIERO NALETTO

CO-SUPERVISORE: CH.MO PROF. PAOLO VILLORESI

Scuola di Dottorato in:
Scienze Tecnologie e Misure Spaziali

Indirizzo: Astronautica e Scienze da satellite

XXIV CICLO

Introduction

About a decade ago, several groups endeavoured the porting of quantum communication outside the cradle of the lab, in the adverse outdoor conditions: [34], [62]. Current fiber and free-space links cannot implement a real global-scale quantum communication system. Fiber links have the advantage that the photon transfer is scarcely affected by external conditions, like background light, weather or environmental obstructions. On the other hand the extension of fiber links beyond a few hundred kilometers is problematic, due to attenuation and polarization-preservation issues. Terrestrial free-space links show some advantages: the atmosphere provides low absorption and is essentially non-birefringent, allowing almost unperturbed propagation of polarization states. On the other hand, the optical mode is not confined in a wave guide, so it is sensitive to the external environment: objects interposed in the line of sight, beam distortion induced by atmospheric turbulence and weather conditions. A solution to this problem comes from the space and satellite technology. Space-based links can potentially lead to global-scale quantum networking since they can connect any two points on the Earth surface with reduced losses as compared with terrestrial channels. This is mainly due to the fact that most of the propagation path is in empty space, with no absorption and turbulence only for a small fraction of it (corresponding to less than $10km$. However, many technical problems must be overcome in order to realize a working quantum communication link between Earth and space. The experimental demonstration of the feasibility of single photon exchange between Space and a ground receiver has been also demonstrated in our group recently [94]. In this thesis some technical and engineering issues, related to free space quantum communication will be addressed.

The work presented is the result of a set of research activities done at the CNR-IFN Luxor laboratory over these three years. The main goal that we would reach is the feasibility demonstration of quantum communication in free-space, without excluding any possible scenario encounterable on a global quantum network. The research done, may help to lead to a global quantum network all over the world, that involves satellites and Earth stations. On a global network we may identify three major link families:

- Satellite to Earth and Earth to satellite link - *called in the thesis Vertical link*
- Point to point horizontal link - *called in the thesis Horizontal link*
- Satellite to satellite link - *called in the thesis Intersatellite link*

The thesis is arranged as follows: a first chapter introduce the atmospheric model and the most common quantities used in this field to describe the effects of turbulence. Follows an analysis and simulation chapter (Ch.2) on space to Earth and Earth to space quantum links. The treatment proceed with the experimental results of the Canary campaign (Ch.3) on horizontal quantum link. Chapters 4 and 5 are related on the polarimetry topic: starting from formalisms and definitions, are presented the simulations that have lead to the requirements for polarimeter design. In the

second-last (Ch.6) is described the polarimeter in all its subsystems, calibration and first test results.
Chapter 7, the last one, regards on intersatellite quantum link: the treatment is purely focused on model definition and feasibility analysis.
The work is mainly focused on vertical Earth-space and space-Earth quantum link, and on long distance horizontal quantum link.

For each of the possible links encounterable in a global quantum network, the thesis address an open issues:

- Satellite to Earth and Earth to satellite link: link modelization and simulation to verify the feasibility and define the transmitter and receiver requirements. In chapter 2 are reported the simulation results that I did using the model defined by my research group and me.
  Another open issue in quantum free space communication, based on polarized photons, is the preservation and compensation of the polarization state over the link. In fact, the non-ideality due to the channel, affects, degrades and even destroys the polarization state of the photons and the information enclosed in them. The ability to analyse and compensate for the channel distortion is de facto a crucial problem to pave the way for further implementation of quantum communication on space scale.
  I addressed the problem of polarization analysis on a space quantum channel. Since the information in our quantum communication system is codified on the photons polarization state, is crucial to proof experimentally that the polarization, and hence the information, is preserved along the channel. If it is not so then the space-Earth and Earth-space links would not make sense. The existing Laser Ranging Facilities, are example of space optical links that can be exploited for this experimental research. The advantage is that we don't need a transmitter or receiver in space, but we only have to analyse the polarization state of the ranging feedback signal. At this purpose I and my research group designed a polarimeter to be integrated with the Matera Laser Ranging station (MLRO): we stared with a theoretical and simulation analysis (Ch.5) and proceeded designing the polarimeter in all its part (Ch.6). I worked on the link simulation and on the polarimeter design, realization and integration at Matera. We designed the optical, mechanical and electronic layout of the instrument: as first we assembled the instrument in our laboratory in Padova and after we brought and installed it at Matera. The instrument is still there and will be used for data acquisition for long time.

- Point to point horizontal link: in parallel to the previous work, we addressed the issue of atmospheric turbulence compensation for long distance quantum channels, that can be summarized in a transmitter-receiver pointing problem. The work, reported in Ch.3, done at the Canary Island leaded us to improve our knowledge on horizontal laser beam propagation and setup requirement definition. In overall we spent two month at the Canary Island over two years to test what we designed in Padova. We established an optical link of $144km$ between Canary islands in order to improve the knowledge on horizontal laser propagation over atmosphere and to define the setup requirements and the most suitable condition to get an effective quantum link. The outcomes of this activities was the design and realization of a telescope optimized for long distance quantum communication in free space. We get some data on the effects of atmosphere that, maybe, should help to better understand the horizontal propagation and to define an horizontal propagation model (still in-existent in literature).
  I was a member of the team that designed and did the experiment at the Canary Island. The work we did and the telescope we realized my be used in the future for quantum free space experiments, like: teleportation, cryptography, etc.

- Satellite to satellite link (Ch.7): this chapter complete the scenario of a global quantum communication network analysing the feasibility of intersatellite quantum link. I worked on link modelling and simulation to verify the feasibility of this communication scheme. The results obtained may be used to justify future experiments and space missions.

Sommario

Il lavoro presentato in questa tesi, riguardante la comunicazione quantistica su scala globale, e' il risultato di una serie di attivita' di ricerca svolte presso il laboratorio CNR-IFN Luxor nel corso di questi tre anni. L'obiettivo principale che si vuole raggiungere e' la dimostrazione della fattibilita' della comunicazione quantistica in spazio libero, senza escludere dalla definizione "spazio libero" ogni possibile scenario che si puo' incontrare su una rete globale. Proseguendo in questa direzione in un futuro si potrebbe arrivare ad una rete quantistica mondiale, che coinvolge satelliti e stazioni terrestri. Allo scopo di aiutare il lettore a classificare le attivita' di ricerca presentate, possiamo identificare tre principali "famiglie" di link:

- Link satellite - Terra e Terra - satellite - *chiamato nella tesi Vertical link*
- Link orizzontale punto punto - *chiamato nella tesi Horizontal link*
- Link satellite - satellite - *chiamato nella tesi Intersatellite link*

Attraverso la modellizzazione e la simulazione numerica e/o campagne di test sperimentali abbiamo cercato di affrontare problematiche inerenti a tutte e tre le tipologie.
I temi di maggior rilievo, tuttavia, sono quelli relativi alle campagne sperimentali, rispettivamente:

- Propagazione di fasci laser in spazio libero su link orizzontale: e' stato realizzato un link ottico di $144 km$ tra le isole Canarie, al fine di approfondire la conoscenza sulla propagazione della radiazione laser su link orizzontali in atmosfera. I risultati ottenuti hanno consentito di definire le specifiche e la configurazione piu' adatta per rendere stabile ed affidabile il link quantistico. Questo lavoro viene presentato nel capitolo 3.
- Mantenimento della polarizzazione su un canale quantistico spaziale: abbiamo progettato, realizzato e installato un polarimetro presso il centro MLRO[1] allo scopo di ricostruire lo stato di polarizzazione dei fotoni in un canale quantistico spaziale. La nostra informazione quantistica, infatti, e' codificata nello stato di polarizzazione dei fotoni. Per aprire la strada a sviluppi futuri e all'effettiva implementazione di questa tecnologia (es. trasmettitore e ricevitore quantistici installati a bordo di satelliti) dobbiamo prima dimostrare che il canale preserva lo stato di polarizzazione e che e' possibile ricostruirne il valore iniziale. Le gia' esistenti strutture impiegate per il laser ranging sono un esempio di link ottico tra la Terra e lo spazio che puo' essere sfruttato per l'analisi e la ricostruzione della polarizzazione, opportunamente integrando nel sistema un polarimetro. Questo lavoro viene presentato nel capitolo 6.

La tesi e' strutturata come segue: un primo capitolo introduce il modello atmosferico e le grandezze comunemente utilizzate in questo campo per descrivere gli effetti della turbolenza atmosferica. Segue un capitolo di analisi e simulazione (cap.2) sui link quantistici spazio - Terra e Terra

---

[1] Matera Laser Ranging Observatory

- spazio. Nel capitolo 3 sono riportati i risultati sperimentali sul link ottico orizzontale, ottenuti nelle campagne di test svoltesi presso le isole Canarie.
I capitoli 4 e 5 sono riguardanti il tema della polarimetria: dopo un'introduzione sui formalismi e le definizioni, sono presentate le simulazioni che hanno fornito le specifiche per la progettazione del polarimetro. Nel penultimo capitolo (cap.6) e' descritto il polarimetro in tutti i suoi sottosistemi: passando dalla progettazione, alla taratura per finire con i risultati dei primi test.
L'ultimo capitolo 7 riguarda i collegamenti intersatellitari quantistici: la trattazione e' esclusivamente focalizzata sulla definizione del modello e sull'analisi di fattibilita'.

Un riassunto del contenuto dei principali capitoli e' riportato di seguito:

- Capitolo 2 - Link verticale - (Capitolo di analisi e simulazione numerica): Come accennato precedentemente, su una rete spaziale quantistica globale abbiamo a che fare con link satellite - Terra e Terra - satellite. Per studiare la fattibilita' della comunicazione quantistica su queste lunghe distanze dobbiamo analizzare la propagazione di un raggio laser in un mezzo turbolento.
  Come introdotto nel capitolo [1], la turbolenza atmosferica da origine al wandering - "ballamento" - e allo spreading - "allargamento" - del fascio, rispettivamente in base alle dimensioni dei vortici, piccoli o grandi rispetto alle dimensioni del fascio. Questi diversi effetti sono apprezzabili considerando il tempo di esposizione: su scale brevi il fascio appare allargato, ma ancor di piu', vaga rispetto alla posizione ideale del centroide. Su scale di tempo lunghe gli effetti del wandering sono integrati nel tempo, dando luogo ad un consistente allargamento del fascio. Il fascio conserva il suo profilo gaussiano, ma ha dimensioni nettamente maggiori.
  Un fascio che attraversa l'atmosfera all'inizio del suo percorso subira' una degradazione per cui arrivera' al ricevitore lontano dalla posizione ideale. Allo stesso modo, un fascio che incontra l'atmosfera alla fine del suo percorso sara' degradato in modo molto meno marcato. I risultati ottenuti dimostrano che l'effetto del wandering sul fascio e' fortemente diverso per l'uplink e il downlink, fino a circa due ordini di grandezza: da poche decine di migliaia di metri di raggio su distanze molto lunghe (come i satelliti GEO) in uplink, a un raggio dell'ordine di poche centinaia di metri in downlink.
  Dalle simulazioni dello spostamento del fascio dalla sua posizione ideale, β, e' chiaramente evidente che tale effetto e' trascurabile per il downlink, in cui la degradazione principale e' l'allargamento causato dai vortici della turbolenza, quindi legato a effetti su scala temporale breve. Invece per l'uplink lo spostamento del fascio appare crescere monotonamente con la distanza, a causa dell'atmosfera all'inizio del percorso. Per il downlink una porzione maggiore di cielo, rispetto al uplink, cade nel "cono a buon SNR[2]", questo permette uno slot temporale piu' lungo per la comunicazione quantistica. L' SNR e' circa $0.7dB$ allo zenith per i satelliti Galileo, la situazione e' piu' promettente per i satelliti GPS in cui l' SNR e' di circa $2.2dB$. In entrambi i casi i valori ottenuti di fatto dimostrano l'infattibilita' della comunicazione quantistica con la configurazione simulata, ma danno buoni auspici per ulteriori miglioramenti tecnologici.
  Nelle condizioni attuali, la fattibilita' della QKD[3] e' relegata a distanze nel range delle orbite LEO, in cui un buon SNR puo' essere ottenuto senza imporre vincoli troppo stringenti per il campo di vista del telescopio e senza spingere la progettazione al limite tecnologico. Piccoli miglioramenti sul IFOV[4] possono spostare il limite di fattibilita' verso orbite piu' alte, consentendo la comunicazione quantistica anche con satelliti GPS e Galileo.

---

[2] Rapporto Segnale Rumore

[3] Quantum Key Distribution

[4] Campo di Vista Istantaneo

- Capitolo 3 - Link ottico orizzontale in spazio libero su lunga distanza - (Risultati sperimentali delle campagne di test alle Canarie): Nella prospettiva di estendere la Comunicazione Quantistica (QC) in spazio libero su lunghe distanze, l'analisi dei fenomeni che coinvolgono la propagazione in atmosfera di un fascio ottico visibile o nel vicino infrarosso e' di fondamentale importanza per determinare il terminale ottica piu' adatto. La ricerca sui link Terra-Terra e' utile anche nel campo della QC spaziale, oltre che per la ricerca sulle comunicazioni satellitari classiche [58] .
  Piu' in dettaglio, la propagazione ottica in atmosfera, nel caso di distanze oltre i $100km$ e' influenzata da diverse trasformazioni dei parametri del fascio, con un conseguente aumento delle perdite nel link. Per di piu', le comunicazioni ottiche su lunga distanza a singolo fotone che implementano i protocolli quantistici, dall'altro lato, si differenziano dai protocolli classici per il fatto che il segnale da trasmettere non puo' essere intensificato, essendo un treno di impulsi con una media di circa un fotoni per impulso.
  La comprensione degli effetti indotti dalla propagazione, al trasmettitore e al ricevitore, nonche' nella statistica temporale dei fotoni e' cruciale per valutare la qualita' della comunicazione e la fattibilita' del collegamento. Su link molto lunghi, il fading e le perdite sono indotte dal disaccoppiamento del fascio con il ricevitore a causa dello spostamento dello stesso: come e' stato analizzato per il canale spaziale [86].
  In questa prospettiva, di link a singolo fotone in spazio libero a lunga distanza, abbiamo fatto una serie di campagne sperimentali per studiare la propagazione di fasci singoli o doppi su diverse scale di lunghezza scala: da alcune decine ad alcune centinaia di chilometri.
  Negli esperimenti si e' proceduto con l'osservazione globale del fascio combinata alla misura dell'irradianza locale dal lato del ricevitore: misura eseguita classicamente e poi proiettata al caso di link a singolo fotone. Inoltre, con l'obiettivo di stabilizzare la posizione del centroide al ricevitore, si e' studiata la propagazione di due fasci che formano mutuamente un piccolo angolo, nei casi di angolo isoplanatico per i modi spaziali di basso ed alto ordine.
  I modelli sperimentali sono stati implementati nelle Alpi, come pure tra Tenerife e La Palma presso le isole Canarie. Si sono effettuate acquisizioni dello spot completo al ricevitore ed analisi sulla scintillazione, confrontando i risultati con i modelli teorici includendovi i dati meteorologici degli Osservatori alle Canarie.
  Il design della configurazione ottica per la comunicazione quantistica su lunga distanza e' di fondamentale importanza: abbiamo affrontato il problema sviluppando un telescopio ottimizzato per i nostri esperimenti.
  La letteratura sulla propagazione orizzontale e' piuttosto scarsa soprattutto a causa di decenni in cui l'interesse si e' concentrato sulla propagazione verticale per scopi astronomici.
  Come primo passo avevamo bisogno di capire gli effetti della turbolenza atmosferica nella propagazione del fascio come: wandering, spreading e scintillazione. Questo ci ha portato a identificare i migliori parametri di progettazione per trasmettitore e ricevitore e alla scelta del protocollo di comunicazione.
  Con i dati che abbiamo acquisito vogliamo definire un modello o un insieme di criteri da considerare nella progettazione di un link ottico quantistico per prevedere quali saranno le perdite sul link reale, ed eventualmente sfruttare la variazione temporale delle perdite per la selezione degli slot con il piu' alto rapporto segnale-rumore [77].
  Lo studio della propagazione di un fascio singolo o una coppia di fasci su link di oltre $100km$ ha dimostrato che il fronte d'onda e' sottoposto a frazionamento in piu' spot. Il suo diametro, su lunga esposizione, puo' essere confinato ad una fattore 3 a 5 il limite di diffrazione. Questi risultati sono stati ottenuti utilizzando un telescopio aplanatico rifrattivo con apertura adeguatamente grande. L'uso di tale schema porta ad una significativa riduzione delle perdite nei link di comunicazione quantistica in condizioni estreme. Questa configurazione e' stata usata in entrambi i link: OGS (Tenerife)-JKT (La Palma) e viceversa.

La riduzione delle perdite e' un aspetto fondamentale per migliorare l'efficacia e l'affidabilita' della comunicazione. Nelle comunicazioni quantistiche a singolo fotone le perdite di comunicazione richiedono di allungare il tempo di comunicazione: infatti, a differenza dei canali classici in cui le perdite possono essere compensata aumentando la potenza del trasmettitore, nella comunicazione quantistica possiamo solamente iterare la trasmissione dei singoli fotoni fino a quando sara' stata raggiunta una quantita' sufficiente di dati. Le correlazioni nella propagazione di fasci nella stessa direzione e nella propagazione di fasci opposti (segnale beacon dal ricevitore) hanno dimostrato la possibilita' di controllare il puntamento del canale quantistico con l'uso di un fascio ausiliario co-propagante o con l'uso di un fascio intenso proveniente dal ricevitore. L'impiego alternato o combinato di entrambe le tipologie e' la soluzione vincente per ottenere un link quantistico stabile ed affidabile. Il sistema presentato e testato si propone di essere una soluzione affidabile per stabilire un canale quantistico in spazio libero. Le tecniche descritte consentono la trasmissione di un laser intenso (cosiddetto "ausiliario") per sondare la turbolenza e per compensarla contemporaneamente allo scambio di singoli fotoni.

- Capitolo 5 - Comunicazioni quantistiche nello spazio - (Capitolo di analisi e simulazione numerica): Circa un decennio fa, diversi gruppi hanno tentato di portare la comunicazione quantistica in generale e la distribuzione quantistica di chiavi (QKD), come primo esempio, al di fuori dell'ambiente "protetto" del laboratorio, per applicarle nelle avverse condizioni esterne: [34], [62]. L'estensione naturale dei canali di Comunicazione Quantistica (QC) in spazio libero e' lo spazio, a causa delle restrizioni imposte dalla curvatura terrestre cosi' come dalla turbolenza atmosferica.
  La dimostrazione sperimentale della fattibilita' dello scambio di singoli fotoni tra lo spazio e un ricevitore a terra e' stata dimostrato recentemente dal nostro gruppo [94]. La capacita' di controllare lo stato di polarizzazione lungo un canale spaziale e' importante per aprire la strada ad ulteriori sviluppi nelle QC spaziali.
  Abbiamo stimato il link budget per il sito di Matera al fine di progettare un polarimetro: eseguita la simulazione per il satellite Goce abbiamo ottenuto i valori di SNR con visibilita' minima e massima. I risultati della simulazione possono essere opportunamente esteso per gli altri satelliti.

- Capitolo 6 - Esperimento SPOLAR-M - (Capitolo di progettazione e sviluppo): Le simulazioni hanno mostrato il link budget richiesto per un link terra-spazio e spazio-terra a singolo fotone, giustificando l'uso di siti per il Laser Ranging per fare i test sperimentali. In questo capitolo dopo una breve introduzione sulla polarimetria di Stokes, sara' presentato il polarimetro utilizzato presso il centro MLRO, progettato e sviluppato presso il Laboratorio di Luxor. Il sistema utilizzato nell'esperimento SPOLAR-M e' un polarimetro a quattro canali che utilizza beam splitter non polarizzanti. Il polarimetro utilizza due beam splitter non polarizzanti, un lamina ritardatrice a quarto d'onda, un beam splitter polarizzante e due polarizzatori lineari. Le misure di intensita' sono fatte da quattro rivelatori. Il vettore di Stokes in input e' determinato dalle quattro misure dei rivelatori e dall'utilizzo di una matrice di Mueller ricavata durante la procedura di calibrazione. Il capitolo tratta la progettazione di tale strumento, da integrare al il sistema di laser ranging di Matera. Il progetto sara' orientato in modo da ridurre al minimo le modifiche alla configurazione esistente e per assicurare il normale funzionamento della stazione.

- Capitolo 7 - Link intersatellitari - (Capitolo di analisi e simulazione numerica): Questo capitolo completa lo scenario di una rete globale di comunicazione quantistica analizzando la fattibilita' di link intersatellitari quantistici.
  Nella sezione 7.1 verra' modellizzata la propagazione di fasci laser tra satelliti al fine di ottenere

informazioni sul link budget (attenuazione, rumore, SNR) e quindi studiarne la fattibilita'. Come nel capitolo [2] sul link verticale, i risultati delle simulazioni mostrano che una reale implementazione di un protocollo di QKD nello spazio, basata sull'uso stati coerenti, richiede una attenta progettazione del trasmettitore: campo di vista, puntamento e tracking del telescopio, efficienza dei rivelatori a singolo fotone ecc. Le dimensioni dello spot al ricevitore risultano essere di alcune decine di metri per lunghezze d'onda corte. L'attenuazione aumenta rapidamente dalle condizioni relativamente buone con link corti passando via via a distante superiori. Il livello di attenuazione e' dentro il range ottenuto per il downlink e l'uplink nel caso di terminale sulla Terra [30] . Se si utilizza la parte dell'orbita corrispondente al massimo avvicinamento, la QKD risulta essere fattibile. In generale, il livello delle perdite associate a satelliti con terminali dotati di ottica fino a $500mm$ di diametro rende difficilmente praticabile il link simultaneo-doppio per la distribuzione di coppie entangled: il rumore di fondo limita l'SNR a livelli molto bassi. La fattibilita' dipende anche dalla capacita' di predizione orbitale e dalla precisione di puntamento su intervalli prolungati. In conclusione, abbiamo visto che sotto alcune condizioni l'estensione delle comunicazioni e delle tecnologie quantistiche appare praticabile anche nello scenario estremo delle reti ottiche quantistiche satellitari.

Abstract

The work presented in this thesis, on the topics of global quantum network, is the result of a set of research activities done at the CNR-IFN Luxor laboratory over these three years. The main goal that we would reach is the feasibility demonstration of quantum communication in free-space, without excluding from the definition "free space" any possible scenario. This is the way that in the future may lead to a global quantum network all over the world, that involves satellites and earth station. We may identify three major link families, that should help the reader to classify the research activities presented:

- Satellite to Earth and Earth to satellite link - *called in the thesis Vertical link*
- Point to point horizontal link - *called in the thesis Horizontal link*
- Satellite to satellite link - *called in the thesis Intersatellite link*

In a certain way we tried to deal with all of them trough analysis and simulation or experimental campaigns.
The core topics of this works however are those related to the experimental campaigns, respectively:

- Laser beam propagation in a free-space horizontal link: we established an optical link of $144km$ between Canary islands in order to improve the knowledge on horizontal laser propagation over atmosphere and to define the setup requirements and the most suitable condition to get an effective quantum link. This work is presented in Chapter 3.
- Polarization maintenance over a space quantum link: we designed, realized and installed a polarimeter to reconstruct the polarization state of photons in a space optical link in the MLRO[5]. Our quantum information, in fact, is codified in the polarization state of photons. To pave the way for future developments and implementations (i.e. quantum transmitter and receiver hosted in satellites) we must as first prove the maintenance or the retreadability of the polarization state. The yet existing laser ranging facilities are examples of optical links between Earth and space that can be exploited for polarization analysis and reconstruction providing them with a polarimeter. This work is presented in Chapter 6.

The thesis is arranged as follows: a first chapter introduce the atmospheric model and the most common quantities used in this field to describe the effects of turbulence. Follows an analysis and simulation chapter (Ch.2) on space to Earth and Earth to space quantum links. The treatment proceed with the experimental results of the Canary campaign (Ch.3) on horizontal quantum link. Chapters 4 and 5 are related on the polarimetry topic: starting from formalisms and definitions, are presented the simulations that have lead to the requirements for polarimeter design. In the second-last (Ch.6) is described the polarimeter in all its subsystems, calibration and first test results.

---

[5] Matera Laser Ranging Observatory

Chapter 7, the last one, regards on intersatellite quantum link: the treatment is purely focused on model definition and feasibility analysis.

A detailed abstract of the main chapters is reported below:

- Chapter 2 - Vertical Link - (Analysis and numerical simulation chapter): As mentioned in the introduction: on a global space quantum network we have to deal with satellite to earth and earth to satellite links. To investigate the feasibility of quantum communication over these long distance in a space scale we have to understand the behaviour of a laser beam propagating into a turbulent media.
  As introduced in chapter [1], the atmospheric turbulence is a source of beam wandering and beam spreading respectively due to small or large eddies if compared with the beam size. These different effects are appreciable considering the exposure time: for short time, the beam appears spread but more over, wandering from the ideal centroid positions; instead for long time scale the wandering effects integrated over time, gives rise to a dominant beam broadening. The beam preserves its Gaussian profile, but more larger in size.
  A beam affected at the start of its path by the degradation induced by atmosphere will arrive at the receiver plane far away from the unperturbed expected position. On the same way, a beam affected at the end of its path will be barely modified. The results obtained show that the effect of beam wandering is strongly different for the uplink and downlink, up to about two orders of magnitude. A few ten thousand meters of beam radius are reached in a very long distance (like GEO satellite) in the uplink, while a beam radius on the order of few hundred meters is calculated in the case of downlink.
  From simulation of the beam displacement β, appears that it is clearly negligible for downlink in which the main input affecting the beam is the broadening due to turbulence eddies, therefore related to short term beam effects. Instead for the uplink the beam displacement appears monotonically increasing with the distance, due to the atmosphere at the beginning of the path. For a downlink a greater portion of sky compared to uplink falls in the "good SNR[6] cone", allowing a longer time-slot for quantum communication. The SNR is closed to $0.7dB$ at zenith for Galileo satellites; the situation is most promising for GPS satellites in which the SNR is around $2.2dB$. In both cases the values, de facto prove the unfeasibility of quantum communication with the simulated setup, but gives good wishes related to further technological improvements.
  The actual feasibility of QKD[7] is related to link distances in the range of LEO orbits, a good SNR can be achieved without stretching the telescope field-of-view to the technological limit. Small improvements on IFOV[8] can shift the link distance feasibility limit toward higher orbits, allowing quantum communication even with GPS and Galileo satellites.

- Chapter 3 - Free-space long distance horizontal optical link - (Canary experimental results): In the perspective of the extension of Quantum Communication (QC) in free-space to long distances, the analysis of the phenomena that occur to a visible or near-infrared beam in the propagation in atmosphere and their understanding is of crucial importance for devising the most convenient optical terminal. The investigation on the ground-ground case is used also to envisage the space QC, along with a vast area of research in satellite Classical Communications [58].
  More in details, optical propagation in atmosphere in the case of links length of over $100km$ is

---

[6] Signal to Noise ratio

[7] Quantum Key Distribution

[8] Instantaneous Field of View

affected by several transformations of the beam parameters, resulting in an increase of the link losses. Moreover, the long range optical communication at the single photon limit exploiting the quantum protocols, on the other side, differs from the classical protocols in that the signal to be transmitted cannot be intensified, being a train of very weak pulses with an average about one photon per pulse.

The understanding of the effects induced by the propagation in both the irradiance at the receiver as well as in the temporal statistics is crucial to assess the quality of the communication and eventually the feasibility of the link. Moreover, for the very long links, fading and losses are induced by the decoupling of the beam with the receiver due to large wandering of the beam spot, as it was also investigated for the space channel [86].

In this perspective of free-space long range single-photon quantum link, we planned a set of experimental campaigns to study the propagation of a single or twin optical beams in scale length of several tens to a few hundreds kilometres.

We address in this work the study of the phenomena induced in very long propagation by using of laser beams to investigate links whose length is of several tens to a few hundreds kilometers. In the experiments, the observation of the whole beam combined to the measure of the local irradiance at the receiver side are performed and then projected to the case of single photons links. In addition, with the aim to stabilize the centroid position at the receiver, the propagation of two beams forming a small mutual angle is studied in the framework of the isoplanatic angle spread for low and high orders of the beam spatial modes.

The experimental models were realized in Alpine links as well as between the Tenerife and La Palma link in the Canary archipelagos. The whole beam at the receiver was acquired and the scintillation analysis carried out and compared to models including the meteorological data from the Canary Observatories.

The design of the optical setup for long range quantum communications is crucial, and we addressed this issue by developing an optimized telescope for the experiments.

The literature on horizontal propagation is quite poor mainly because for decades of years the interest was focused on vertical propagation -for astronomical purposes-.

As first we needed to understand the effects of atmospheric turbulence in beam propagation: like wandering, spreading and scintillation. This led us, as last step, to identify the best design parameters for transmitters and receiver and for communication protocol.

With the gained data we want to define a model or a set of criteria to be considered in designing an optical quantum link and to predict the link losses for a realistic receiver and, possibly to envisage the exploitation of the time-varying losses for the selection of the portion with the highest signal-to-noise ratio [77].

The observation of the propagation of a single or a pair of beams along very long paths of over $100km$ have shown that the beam is subjected to splitting into multiple spots but that its long-term diameter may be confined to a spot that is only a factor 3 to 5 the diffraction limit. This results have been obtained by using a suitable large aperture aplanatic refractive transmitter. In this way a significant reduction of the link losses for quantum communication channels in this extreme conditions are possible by the implementation of such scheme. This setup was used in both the OGS (Tenerife)-to-JKT (La Palma) propagation and the reverse. The losses reduction is a fundamental aspect to improve the communication effectiveness and reliability. In single photon quantum communications link losses require to stretch the communication time: in fact, unlike the classical channel in which high losses can be compensated increasing the transmitter power, in quantum communication we can only iterate the single photons transmission until a sufficient amount of data is reached. The correlations of the two spots in the twin beam propagation and in opposite propagation (beacon signal from receiver) have demonstrated the possibility of the centroid control of the quantum channel by the use of an auxiliary co-propagating beam or by the use of an intense beam from the receiver. Alternative or combined use of both systems is the winning solution for an effective and stable quantum link. The system presented and tested aims to be a reliable solution to establish a free space quantum channel. The techniques described allow the transmission of an intense laser (the so called "auxiliary") for turbulence probing and compensation while simultaneously being exchange single photons.

- Chapter 5 - Space Quantum Communications - (Analysis and numerical simulation chapter): About a decade ago, several groups endeavoured the porting of quantum communication in general and Quantum Key Distribution (QKD) as first example outside the cradle of the lab, in the adverse outdoor conditions: [34], [62]. The natural extent of free space Quantum Communication (QC) is space, due to the restrictions imposed on the Earth surface by the Earth curvature as well as atmospheric turbulence.
  The experimental demonstration of the feasibility of single photon exchange between Space and a ground receiver has been also demonstrated in our group recently [94]. The demonstration of the control of the polarization state along the Space channel is important to pave the way to further steps in space QC.
  We estimated the link budget at the Matera site to design a polarimeter: performed the simulation for Goce we obtained the values for SNR at the minimum and maximum satellite visibility. The simulation results can be properly extended for the other satellites.

- Chapter 6 - SPOLAR-M experiment - (Design and development chapter): The simulation showed the link budget required for earth-space and space-earth single photons channel, and justify the use of Laser Ranging sites to experimentally test the link. In this chapter after a brief introduction on Stokes Polarimetry will be presented the polarimeter used at the MLRO, designed and developed at the Luxor Laboratory. The system used in the SPOLAR-M experiment is a Four-Channel Polarimeter using Non Polarizing Beam Splitter. This polarimeter use two non polarizing beam splitter, a quarter-wave retarder, a polarizing beam splitter and two linear polarizers. Readings are made at four detectors. The input Stokes vector is determined from the four detector measurements and from use of a transfer Mueller matrix found during the calibration procedure. The chapter discuss the design of the instrument to be integrated with the Matera laser ranging facility. The design will be oriented in order to reduce the changes to the existing setup and to ensure the normal operation of the station.

- Chapter 7 - Intersatellite link - (Analysis and numerical simulation chapter): This chapter complete the scenario of a global quantum communication network analysing the feasibility of intersatellite quantum link.
  In section 7.1 will me modelled the propagation of laser beam in a satellite to satellite link in order to get information on the link budget (attenuation, noise, SNR) and hence on its feasibility. As in chapter [2] for vertical link, the simulation results show that a real implementation of a QKD protocol in space, based on coherent states, requires a careful design of the transmitter: field-of-view, telescope pointing and tracking, efficient single photon detectors etc. The spot size at the target is of the order of a few tens of meter for short-wavelength transmission systems. The corresponding attenuation is rapidly increasing from the relatively good conditions of closest approach of the satellites. The level of attenuation ranges between the cases of downlink and uplink in the case with a terminal on the Earth[30]. Anyway, using the part of the orbit in which the satellites are sufficiently close, the QKD appears feasible. In general, the level of losses that are associated with terminals equipped with optics up to $500mm$ in diameter makes hardly feasible the double simultaneous link for the distribution of an entangled pair. The background noise is here limiting the SNR to very low levels. The feasibility is also dependent on the capacity of orbital prediction and pointing accuracy over extended intervals. In conclusion, we have seen that in some conditions the extension of quan-

tum communications and technologies appears feasible in the extreme scenario of the satellite optical quantum networks.

Contents

List of Figures

List of Tables

Chapter 1

Optical Link

In this chapter will be introduced the propagation model of a Gaussian laser beam over turbulent atmosphere. The model presented is at the base of the next chapters in which the laser beam propagation will be analysed in real specific scenarios (links): vertical - space to earth and earth to space, space - intrasatellite and terrestrial - horizontal.
More details can be found in: [73], [58], [89] and [90].

1.1 Gaussian Beam

The treatment will be focused on Gaussian beams: the most frequent experimental condition. The optical intensity of a Gaussian beam $I(\rho) = |U(\rho)|^2$, where $U(\rho)$ is the electric field, is a function of the axial and radial position, z and $\rho = \sqrt{x^2 + y^2}$:

$$I(\rho, z) = I_0 \left[\frac{W_0}{W(z)}\right]^2 \cdot e^{\left[-\frac{2\rho^2}{W^2(z)}\right]} \tag{1.1}$$

At any value of the propagation axis z the intensity is a Gaussian function of the radial distance ρ. The Gaussian function has its peak on the z axis, at $\rho = 0$, and decreases monotonically as ρ increases. The beam width $W(z)$ of the Gaussian distribution increases with the axial distance z. On the beam propagation axis ($\rho = 0$) the intensity in (1.1) reduces to:

$$I(0, z) = \frac{I_0}{1 + (z/z_0)^2} \tag{1.2}$$

1.1.1 Beam Width

At any transverse plane, the beam intensity assumes its peak value on the beam axis, and decreases by a factor $1/e^2$ at the radial distance $\rho = W(z)$. The quantity $W(z)$ is called beam radius. The relation of the beam width on z is given by:

$$W(z) = W_0 \sqrt{1 + \left(\frac{z}{z_0}\right)^2} \tag{1.3}$$

The beam waist W_0, known as the *waist radius*, is the minimum value assumed by $W(z)$, at the plane $z = 0$. The waist diameter $2W_0$ is also called the spot size. The beam width increases monotonically with z, and assumes the value $\sqrt{2}W_0$ at $z = \pm z_0$

1.1.2 Beam Divergence

The first term of (1.3) may be neglected for $z >> Z_0$, which results in the linear relation:

$$W(z) \approx \frac{W_0}{z_0} z = \Theta_0 z \tag{1.4}$$

where Θ_0 is the half-angle at which the cone of the beam diverges.

1.1.3 Depth of Focus

Since the beam achieves its best focus at the plane $z = 0$, it has its minimum width at $z = 0$, it . We define the *depth-of-focus* or *confocal parameter* as the axial distance within which the beam width is no greater than a factor of $\sqrt{2}$ time its minimum value, (at this distance the area is within a factor of 2 of the minimum).

1.2 Atmospheric model

The atmospheric turbulence is a crucial issues that has to be taken into account to study an optical link.
In fact, little variations in the temperature of the air ($< 1°C$) are sources of local variations in the wind velocity, that give rise to eddies. The temperature gradient, also, affects the local density of the atmosphere, and hence its refraction index. These variations, always on the order of 10^{-6} can be accumulated, giving rise to considerable inhomogeneities on the refraction index of the atmosphere.
A beam, propagating in a turbulent atmosphere can be affected by:

- Beam Wandering
- Scintillation
- Beam Spreading

The effects of variations in the refractive index can be idealized as a set of small lenses: they focus and redirect the beam and through interferometric phenomena cause intensity fluctuations.
It can be assumed that each one of this lenses has the dimension of the eddy that generated it.
Although this model introduces discontinuities that in the atmosphere are not really present, the thin lenses approximation is often used.
The propagation over atmosphere is not yet formally described, mainly in small scale phenomena and for horizontal propagation.
A variety of models that describes the mean effect: like total beam wandering, beam spreading, and scintillation, are present in literature but mainly are related to vertical propagation for its interest in astronomy. Due to its complexity, the atmospheric turbulence theory is bases on statistical analysis.

1.2.1 Structural constant of the refraction index

The turbulence intensity, is represented via the structural constant of the refraction index C_n^2. It varies with the seasons, days, and hours and is related to the geographic position and altitude.
An accurate theoretical model, for every condition doesn't exist.
From experimental observations, Hufnagel suggested the following relation:

$$C_n^2 = \{[(2.2 \cdot 10^{-53})h^{10}(W/27)^2]e^{-h/1000} + 10^{-16}e^{-h/1500}\}e^{[r(h,t)]} \; [m^{-2/3}] \tag{1.5}$$

where h is the height in meters at the sea level, W is the wind correlation factor and *r(h,t)* is a zero mean Gaussian random variable; $v(h)$ is the wind velocity at the height h.
The wind correlation factor is expressed by:

$$W = \left[(1/15km) \int_{5km}^{20km} v^2(h)dh \right]^{1/2} \tag{1.6}$$

For the wind velocity can be used the Bufton's model [89], [90]:

$$v(z) = 5 + 30e^{-[(z-9400)/4800]^2} \tag{1.7}$$

where z and v are expressed respectively in [m] and [m/s].
Below is reported a wind velocity profile, as a function of the altitude:

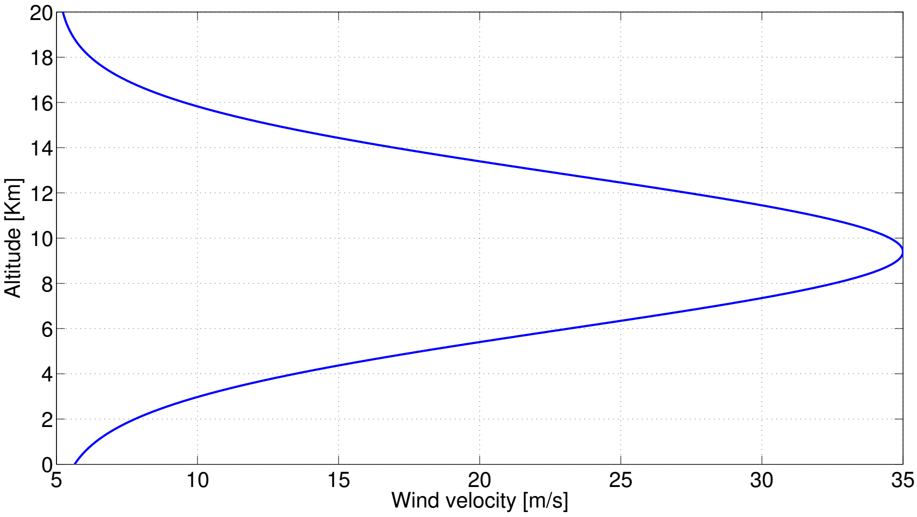

Figure 1.1: Wind velocity profile

An useful quantity, that represents the maximum collecting diameter of an heterodyne receiver, before that the distortions induced by the atmosphere limit the receiver performances, is the zeroth-order turbulence momentum that provides a measure of the spatial coherence length, also called Fried coherent length:

$$r_0 = \{0.423k^2 sec(\xi)\mu_0\}^{-3/5} \ [m] \tag{1.8}$$

where ξ is the zenith angle, μ_0 is the zeroth-order of the turbulence moment, defined as:

$$\mu_n := \int C_n^2(h)h^n(h)dh \tag{1.9}$$

At the same time, the atmospheric time constant is derived from the 5/3 velocity moment:

$$\tau_0 = \{2.91k^2 sec(\xi)v_{5/3}\}^{-3/5} \ [sec] \tag{1.10}$$

where

$$v_n := \int C_n^2(h) v^n(h) dh \tag{1.11}$$

For night-time operation viewing at good astronomical sites we can use the following formulation, based on the Hufnagel-Valley profile ([89], [91], [90]):

$$C_n^2(h) = 8.16 \cdot 10^{-54} h^{10} e^{-h/1000} + 3.02 \cdot 10^{-17} e^{-h/1500} + 1.90 \cdot 10^{-15} e^{-h/100} \tag{1.12}$$

An alternative model is [30]:

$$C_n^2(h) = 0.00594 (v/27)^2 (h \cdot 10^{-5})^{10} e^{-h/1000} + 2.7 \cdot 10^{-16} e^{-h/1500} + 1.7 \cdot 10^{-14} e^{-h/100} \tag{1.13}$$

The two models are compared in the picture below:

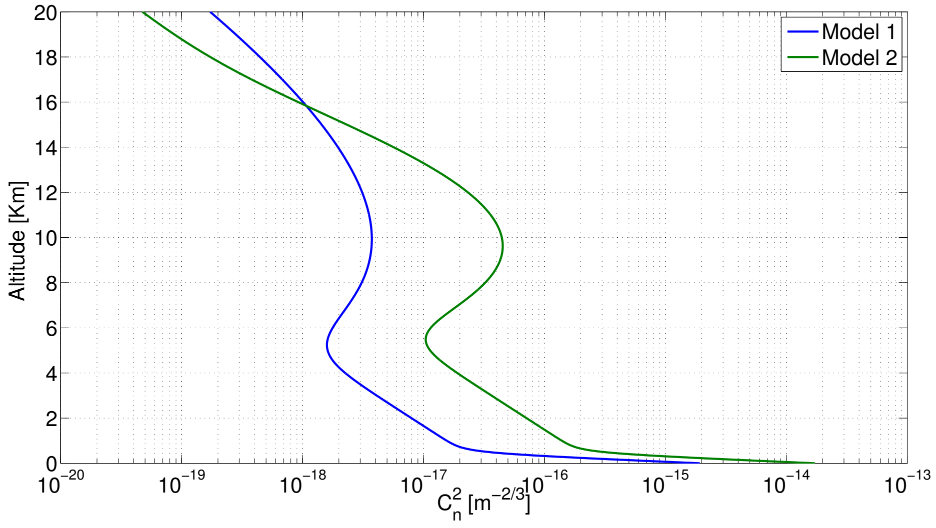

Figure 1.2: C_n^2 profile for models 1 and 2

1.3 Turbulence effects

The atmospheric turbulence is source of spread on the range of high spatial frequency, wander for low spatial frequency and intensity variations.

Eddies smaller than the beam size, cause beam spreading, whereas eddies larger than the beam size cause wander. Intensity fluctuations are due to eddies on the order of $\sqrt{\lambda L}$ where λ is the wavelength and L is the propagation distance.

1.3.1 Scintillation

The intensity variations are usually expressed as the log amplitude fluctuations. The scintillation effects are relevant for receiver with small entrance aperture; otherwise, for large aperture are mediated on the whole receiving area.

In terms of irradiance, for large aperture, the effects will be less significant.
The scintillation is expressed as a variation of the irradiance:

$$\sigma_I^2 = A[e^{4\sigma_\chi^2} - 1]\ [W/cm^2] \tag{1.14}$$

where A is the aperture average factor, that for weak turbulences and small value of l_0 (the smallest eddies size) can be estimated by:

$$A = \left[1 + 1.07\left(\frac{kD^2}{4L}\right)^{7/6}\right]^{-1} \tag{1.15}$$

For a plane wave σ_χ^2 is defined as $0.307k^{7/6}L^{11/6}C_n^2$, and for a spherical wave as $0.124k^{7/6}L^{11/6}C_n^2$, L is the link distance and D is the aperture diameter.

1.3.2 Beam wander

A beam propagating over a turbulent atmosphere, is affected by deviation from its ideal position (wander). Considering the velocity of this effects, we can divide them into two classes:

- Jitter: for fast dynamic wander
- Drift: for slow dynamic wander

According to the coherence length, we can estimate the tilt variance as:

$$\alpha^2 = 0.364\left(\frac{D}{r_0}\right)^{5/3}\left(\frac{\lambda}{D}\right)^2 \tag{1.16}$$

We can describe the *tilt* with two different formulations:

- G-tilt through the mean gradient of the wave front (it represents what is seen by a quadrant detector)
- Z-tilt through the normal to the plane that minimize the wave front distortion (it represents the tilt terms on the Zernike's expansion)

For an adaptive optics compensation analysis is possible to use only the characteristic frequency of the tilt: usually called *Tilt Greenwood frequency.* For the differents formulations we have:

$$f_{TG} = 0.331D^{-1/6}\lambda^{-1}sec^{1/2}\beta\left[\int_0^L C_n^2(z)v_w^2 dz\right]^2 \tag{1.17}$$

$$f_{TZ} = 0.368D^{-1/6}\lambda^{-1}sec^{1/2}\beta\left[\int_0^L C_n^2(z)v_w^2 dz\right]^2 \tag{1.18}$$

where β is the zenith angle.
An Adaptive Optics system at least should have a bandwidth four times greater that the Greenwood frequency.

Chapter 2

Vertical Link

As mentioned in the introduction: on a global space quantum network we have to deal with satellite to earth and earth to satellite links. To investigate the feasibility of quantum communication over these long distance in a space scale we have to understand the behaviour of a laser beam propagating into a turbulent media.
As introduced in chapter [1], the atmospheric turbulence is a source of beam wandering and beam spreading respectively due to small or large eddies if compared with the beam size. These different effects are appreciable considering the exposure time: for short time, the beam appears spread but more over, wandering from the ideal centroid positions; instead for long time scale the wandering effects integrated over time, gives rise to a dominant beam broadening. The beam preserves its Gaussian profile, but more larger in size.
The results obtained from this analysis has been published in [83].

2.1 Beam size distortions due to atmospheric turbulence

To investigate the feasibility of quantum communication, as first, we have to determine the distortions introduced by the atmosphere in order to get information on the power and number of photons at the receiver. In this section will be analysed the effects, on beams size, of the beam propagation over atmospheric turbulence. A Gaussian beam of waist w_0 and intensity I_0, has an average long-term (long-exposure) spatial distribution of intensity, given by [23], [30], [84]:

$$\langle I(r,L)\rangle = I_0 e^{-2r^2/w_{LT}^2} \tag{2.1}$$

where L is the link distance, r is the radial distance from the center of the beam, w_{LT} is the long-term beam radius defined as:

$$w_{LT}^2 = w_{ST}^2 + 2\left\langle \beta^2 \right\rangle \tag{2.2}$$

here β is the instantaneous beam displacement from the unperturbed position, while w_{ST} is the short-term beam width. The long-term beam width, for a collimated beam, is:

$$w_{LT}^2 = w_0^2\left(1+\frac{L^2}{Z_0^2}\right) + 2\left(\frac{4L}{kr_0}\right)^2 \tag{2.3}$$

where Z_0 is the Rayleigh parameter of the beam, and r_0 is the Fried parameter (for the uplink), given by [89]:

$$r_0 = \left[0.423sec(\theta_{zn})k^2 \int_{h_0}^{L} C_n^2(z)\left(\frac{L-z}{L}\right)^{5/3} dz\right]^{-3/5} \tag{2.4}$$

where h_0 is the altitude of the Earth station and θ_{zn} is the zenith angle.
For a circular or a near circular orbit we can estimate the effective link distance, considering the geometry formed by an orbiting satellite and an Earth station as:

$$L = \frac{-2R_T cos\theta_{zn} + \sqrt{(2R_E cos\theta_{zn})^2 + 4((R_{SAT+R_E})^2 - R_E)^2}}{2} \tag{2.5}$$

where R_E and R_{SAT} are respectively the mean Earth radius and the satellite orbit radius.
Following the Hufnagel-Valley model, the refractive index structural constant $C_n^2(h)$ is:

$$C_n^2(h) = 0.00594(v/27)^2(h10^{-5})^{10}e^{-h/1000} + 2.7 \cdot 10^{-16}e^{-h/1500} + Ae^{-h/100} \tag{2.6}$$

where v $[m/s]$ is the rms wind speed at high altitude, A $[m^{-2/3}]$ defines the turbulence strength at the ground level.
For a general case analysis we can assume the following values of $A = 1.7 \cdot 10^{-14}m^{-2/3}$ and $v = 21m/s$ ([23]) The short-term beam radius can be estimated as:

$$w_{ST}^2 = w_0^2\left(1 + \frac{L^2}{Z_0^2}\right) + 2\left\{\frac{4.2L}{kr_0}\left[1 - 0.26\left(\frac{r_0}{w_0}\right)^{1/3}\right]\right\}^2 \tag{2.7}$$

In the former equation and in (2.3) it clearly appears that the turbulence effects are summarized by an additive factor added to the Gaussian beam size equation for propagation in vacuum.
An accurate pointing system can ideally completely compensate the dominant beam displacement in equation (2.2), leading to a long-term width that reduces to short-term width. On the other hands, the turbulence compensation is effective only if β is higher than w_{ST}. As shown by [85]), for a real space link, the beam displacement is related to the residual tracking error and the co-alignment error due to turbulence, hence a fine pointing and tracking system converges in $w_{LT} \simeq w_{ST}$. In our simulation and analysis we deal with a worst-case scenario, where the beam displacement is uncompensated.
We can summarize the effects of turbulence in a redistribution of the beam energy. The power P collected by a receiver can be estimated as:

$$P = 2\pi I_0 \int_0^R \rho e^{-2(\rho^2/^2_{LT})} d\rho \tag{2.8}$$

where R is the entrance aperture radius. The link-efficiency η, that represents the link attenuation or in a "single photon point of view" the probability that a photon is collected by the receiver follows from the ratio between the power collected and transmitted:

$$\eta = \eta_0\left(1 - e^{2R^2/w_{LT}^2}\right) \tag{2.9}$$

taking into account the detection efficiency, the pointing losses and the atmospheric attenuation: the factor η_0 can be set to 0.1 at the zenith ([25]). More in general η_0 can be related to the zenith angle by the following equation ([58]) that is an accurate approximation up to 70°:

$$\eta_0 = L_P L_{TX} L_{RX} \cdot 10^{\left(-\frac{4.34\tau(0)sec(\Theta_{zen})}{10}\right)} \tag{2.10}$$

where L_P, L_{TX}, L_{RX} are the pointing losses, the transmitter losses and the receiver losses that from [25] can be set respectively at 0.2, 0.8 and 0.8. τ is the depth of path at the zenith, that given the atmospheric transmittance ($\simeq 0.8$ at $800nm$) can be evaluated by:

$$T = e^{-\tau} \tag{2.11}$$

In *downlink* the beam travels through the atmosphere only in the last path of the channel: the turbulent eddies appear to be much smaller than beam diameter. Its size is then large enough to make the beam wandering effect negligible compared to the beam spreading due to the short-term effect. . Moreover, compared with the uplink, the beam spreading appears to be less strong.
This consideration implies a reduced attenuation for the downlink with respect to the uplink.

2.2 Noise source

Attempting to characterize the optical quantum channel, our discussion inevitably has to lead with sources of noise, that can disturb the communication. The scenario varies from: night time, day time and uplink and downlink.

2.2.1 Uplink-day time

The main source of background noise in a day time operation uplink scenario is the Sun: its light diffused by the Earth is collected by the receiving telescope (see Fig. 2.1).

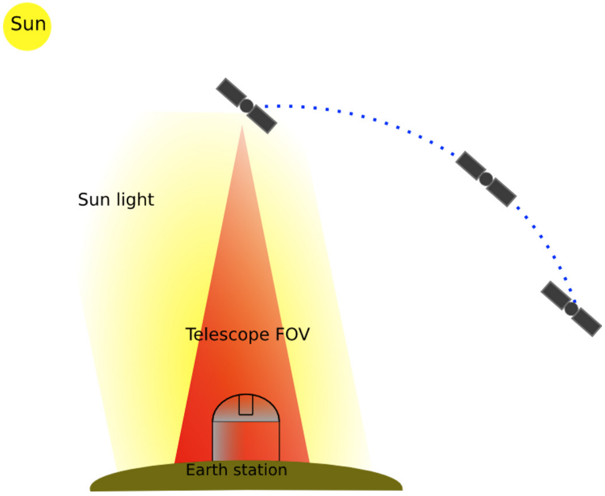

Figure 2.1: Model for the uplink day-time operation. The same model can be adapted for night-time considering the Moon as source of noise.

Lambertian diffusion can simply model this process: taking into account the Earth albedo[1], coupling the related model equation [30] and doing the math, we obtain the number of background photons collected by the receiver system as a function of bandwidth and time units $\Delta\nu[nm]$, $\Delta[s]$:

$$N_{DAY} = a_E R^2_{@S}(IFOV)^2 H_{Sun} \tag{2.12}$$

---

[1] Albedo: Is the portion of radiation reflected back in all directions by a surface

where $R_{@S}$ is the radius of the telescope in space, a_E is the Earth albedo, IFOV is the telescope field of view and H_{Sun} is the solar spectral irradiance (photons s^{-1} nm^{-1} m^{-2})

2.2.2 Uplink-night time

The background noise for a night-time operation uplink can be analysed in the same way. At this time, the noise sources are: Earth black-body emission, diffused moonlight and scattered light from human activities. The noise related by moonlight can be evaluated by:

$$N_{NIGHT} = a_E a_M R_M^2 R_{@S}^2 \frac{(IFOV)^2}{d_E^2 M} H_{Sun} \tag{2.13}$$

where R_M is the Moon radius, a_M is the Moon albedo and d_{EM} is the Earth-Moon distance. For a real QKD system, as shown by [30], the noise component due to Earth black-body radiation can be negligible : the numerical estimation shows that it is three order of magnitude smaller than that of moonlight. Also the human light is negligible for QKD experiments, in which the working sites are astronomical observatories located in suitable positions.

2.2.3 Downlink noise

In a downlink scenario: a receiver telescope based on an Earth station, points at a satellite in the sky. Following [30] and [43], the noise power received by the telescope is:

$$P_b = H_b \Omega_{fov} \pi R_{@E}^2 \Delta\nu \tag{2.14}$$

where Ω_{fov} is the telescope field of view in $[sr]$, H_b is the sky background brightness in $[W\ m^{-2} sr^{-1} \mu m^{-1}]$, $R_{@E}$ is the receiving telescope radius at the Earth station, $\Delta\nu$ is the optical bandwidth in $[\mu m]$.

2.3 Signal to noise ratio

In the previous sections, we have seen how to estimate the portion of power received by a telescope and the background noise sources. To complete the analysis of a quantum communication channel, we still have to evaluate the signal to noise ratio (SNR). The SNR is defined as the ratio between the single photons of signal and the noise photons at the receiver, from (2.9) becomes:

$$SNR = \frac{\eta}{\epsilon_N} \tag{2.15}$$

where ϵ_N is the number of noise photons at a detection time Δt for a bandwidth $\Delta\nu$. For the uplink in night time operation we have:

$$SNR = \frac{\eta_0 (1 - exp(-2R_{@S}^2 / w_{LT}^2)) d_{EM}^2}{a_E a_M R_M^2 IFOV^2 H_{Sun}} \tag{2.16}$$

and in the same way for the downlink in night-time operation:

$$SNR = \frac{\eta_0 (1 - exp(-2R_{@E}^2 / w_{LT}^2)) h\nu}{H_b \Omega_{fov} \pi R_{@E}^2 \Delta\nu \Delta t} \tag{2.17}$$

where h is the Planck constant. The contribution due to an imperfect QKD system is neglected in this SNR definition.
We omitted in this section the math for day-time operation because QKD, due to the high level of noise, is de facto unfeasible.

2.4 QKD from satellite simulations

The model presented is the base to evaluate the feasibility of satellite-earth QKD links. We simulated the link parameters (beam size, noise, attenuation, SNR) with MATLAB, for various families of satellite:

- Low Earth Orbit (LEO)
- Medium Earth Orbit (MEO): Europe global positioning system (Galileo), USA global positioning system (GPS)
- Geostationary Earth Orbit (GEO)

The orbit of a satellite seen from an Earth station, can be represented as a set of terns (zenith angle, azimuth angle, link distance) evolving in time. The analysis of the link as a function of the zenith angle, will be useful to estimate the link budget in a real scenario. In our simulation we focused on: a real Earth station (MLRO observatory) which has a telescope radius of $75cm$ and an IFOV of $0.016°$, and on a reasonable (for the actual state of the art) space terminal with a telescope diameter of $20cm$ and an IFOV of $100\mu rad$. We chose a bandwidth $\Delta\nu = 1nm$, a detection time $\Delta t = 1ns$ and a wavelength $\lambda = 800nm$.

2.4.1 Beam propagation simulations

As first we simulated the effects of the atmosphere on the beam propagation for uplink and downlink. As we previously said, the long term beam width represents intuitively the beam width seen over a long time exposure picture: it is due to the integration of the beam wandering effect.

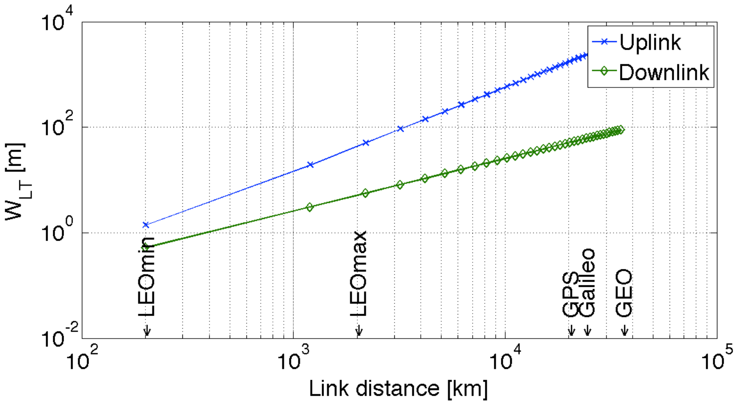

Figure 2.2: Long term beam width w_{LT} as a function of the link distance L. Simulation with an Earth telescope radius $r_T = 75cm$ and a space telescope radius $R = 10cm$.

A beam affected at the start of its path by the degradation induced by atmosphere will arrive at the receiver plane far away from the unperturbed expected position. On the same way, a beam affected at the end of its path will be barely modified. This results, highlighted in Fig. 2.2, shows that the effect of beam wandering is strongly different for the uplink and downlink, up to about two orders of magnitude. A few ten thousand meters of beam radius are reached in a very long distance (like GEO satellite) in the uplink, while a beam radius on the order of few hundred meters

is calculated in the case of downlink.
The simulation of the beam displacement β in Fig. 2.3 is reported: it is clearly negligible for downlink in which the main input affecting the beam is the broadening due to turbulence eddies, therefore related to short term beam effects. Instead for the uplink the beam displacement appears monotonically increasing with the distance, due to the atmosphere at the beginning of the path.

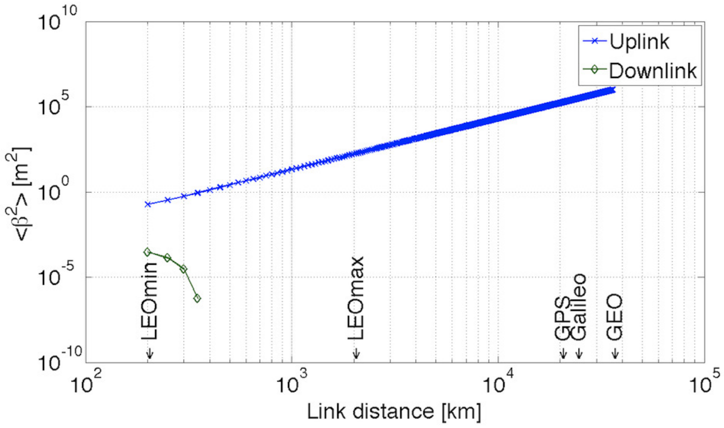

Figure 2.3: $\langle\beta^2\rangle$ as a function of the link distance L. Simulation with an Earth telescope radius $r_T = 75cm$ and a space telescope radius $R = 10cm$.

2.4.2 Uplink simulations: Attenuation and SNR

In this section we will simulate the scenario in which the earth station plays the role of transmitter and the space terminal is the receiver. The most suitable time operation to establish a space to Earth quantum link is the night time both for up and down links, mainly due to the achievable low level of background noise (Sky brightness is on the order of: $1.5 \cdot 10^{-5} Wm^{-2}Sr^{-1}\mu m^{-1}$). After presenting the results on beam propagation will be reported the simulations for SNR: Fig. 2.4 and Fig. 2.5 represent respectively the long term beam effect and the beam deviation as a function of the zenith angle.

Increasing the zenith angle, the beam deviation, and hence the long term effect grows up compared to a link at zenith. This is mainly due to a longer path over the atmosphere layer.
For a LEO satellite, and for satellites in general, the zenith angle defines a boundary angle for which a quantum link at angles greater than this is unfeasible. This is evident in the link attenuation Fig. 2.6 and the SNR Fig. 2.7: the SNR falls below zero preventing QKD at 40° of zenith angle for higher LEO. Only the portion of sky delimited by the cone formed by the zenith direction and the zenith boundary angle is suitable for quantum communication. Quantum communication for the simulated transmitter and receiver with GPS, Galileo and in general GEO satellites, is unfeasible for any zenith angle (Fig. 2.7).

The dependence of the link budget to the zenith angle leads to the following consideration:

- the key generation rate of a QKD system varies with the zenith angle; a high data rate is needed to obtain a sufficient key length and overcome the losses if the "zenith-cone" is too narrow.

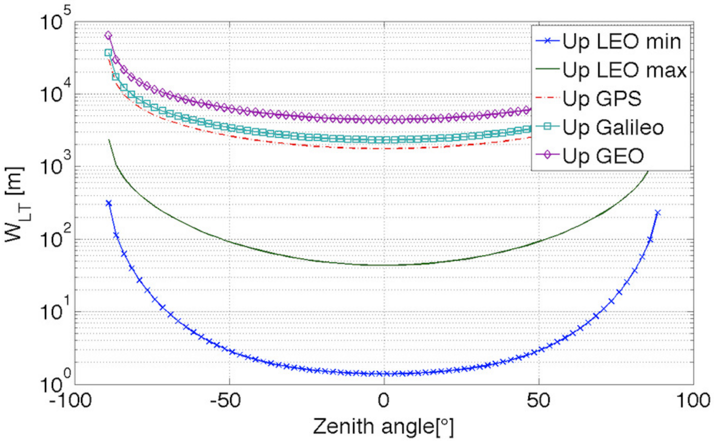

Figure 2.4: Long term beam width w_{LT} as a function of the zenith angle for different satellites in uplink. Simulation with an Earth telescope radius $r_T = 75cm$ and a space telescope radius $R = 10cm$.

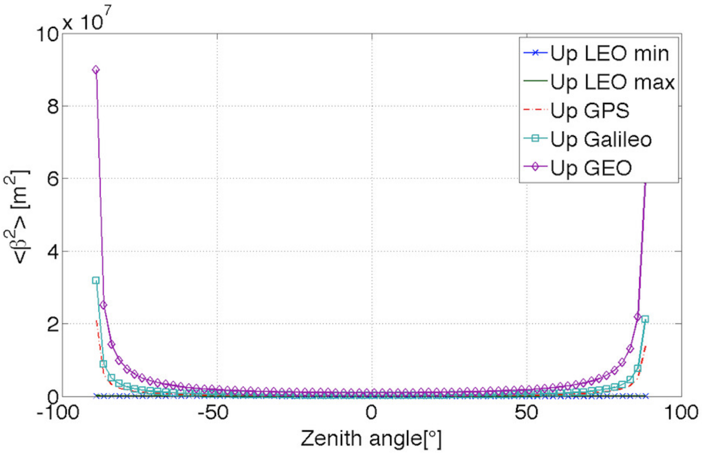

Figure 2.5: $\langle \beta^2 \rangle$ as a function of the zenith angle for different satellites in uplink. Simulation with an Earth telescope radius $r_T = 75cm$ and a space telescope radius $R = 10cm$.

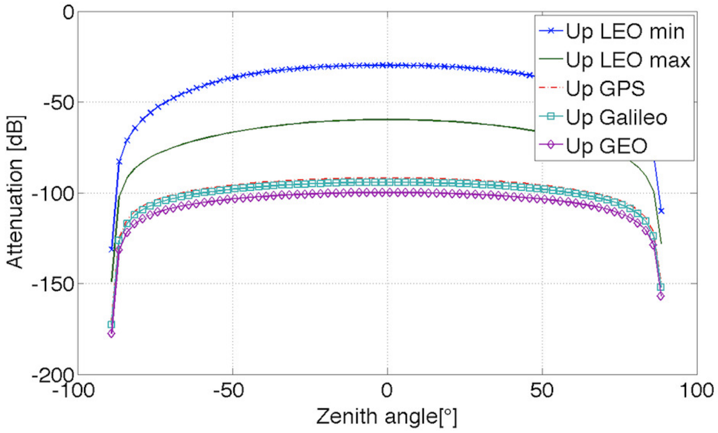

Figure 2.6: Attenuation η as function of the zenith angle for different satellites in uplink. Simulation with an Earth telescope radius $r_T = 75cm$ and a space telescope radius $R = 10cm$.

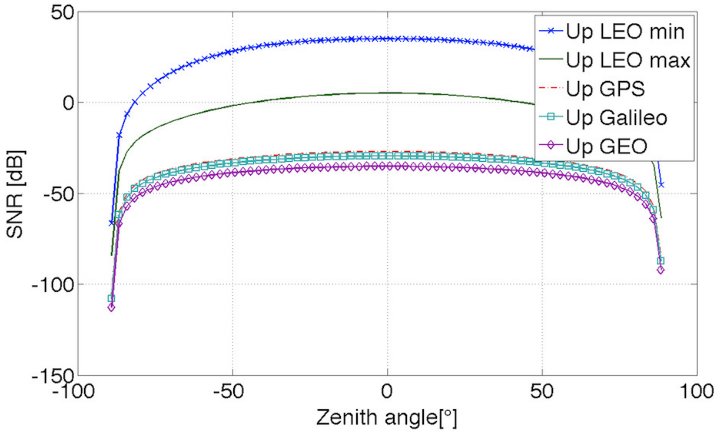

Figure 2.7: SNR as function of the zenith angle for different satellites in uplink. Simulation with an Earth telescope radius $r_T = 75cm$ and a space telescope radius $R = 10cm$

- the time interval between the rise of satellite and arrival at the point in which the SNR allows QKD must be optimized for pointing, tracking and synchronization to take advantage on quantum link when the satellite goes on the "good SNR cone" (Fig. 2.8).
- the zone out of the good SNR cone, in which the satellite is however visible from the earth station would be used for classical communication: not only for establishing the link with the satellite but also to perform the public exchange of polarization basis as expected in the BB84 and B92 QKD protocols.

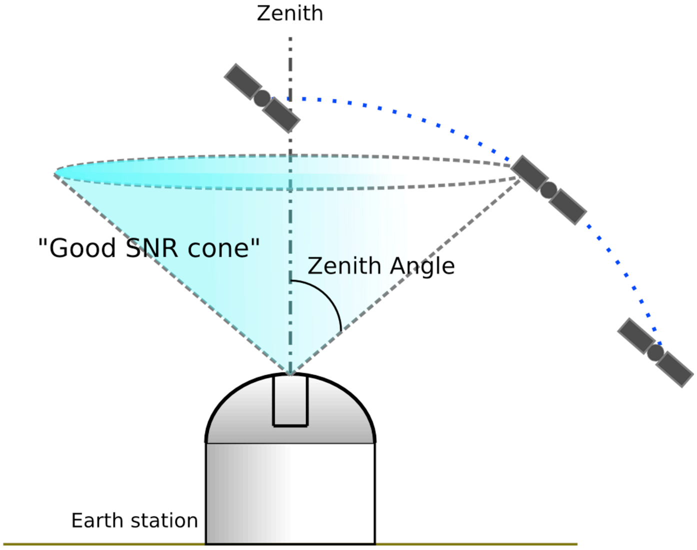

Figure 2.8: Model of the "good SNR cone" seen from the Earth station.

A narrow field of view and a relatively short link, in the case of night time operations, lead to much more promising results. However is quite difficult to do QKD in every conditions, more for far satellites as MEO and GEO; LEO satellites seem to be the best candidate. The challenge to decrease the IFOV has to deal with the precision of pointing and tracking.

2.4.3 Downlink simulations: Attenuation and SNR

Extending the results obtained above for the atmosphere model we can study the case of a downlink in which the transmitter is on space. The downlink scenario is more promising than in the uplink: the beam displacement is negligible because the beam is only broadened. Fig. 2.9 and Fig. 2.10 show this effect on beam propagation at different zenith angle for different satellites. The trend reported in Fig. 2.10 for a LEO satellite, shows that the effect due to altitude variations is dominant if compared to the increased layer thickness at higher zenith angle.

The SNR appears to be almost constant at $36dB$ for satellites orbiting at the lower limit of LEO: in Fig. 2.11 and Fig. 2.12 respectively the simulation results for attenuation and SNR are reported.

For a downlink a greater portion of sky compared to uplink falls in the "good SNR cone", allowing a longer time-slot for quantum communication (see Fig. 2.12). The SNR is closed to $0.7dB$ at zenith for Galileo satellites; the situation is most promising for GPS satellites in which the SNR is around $2.2dB$. In both cases the values, de facto prove the unfeasibility of quantum

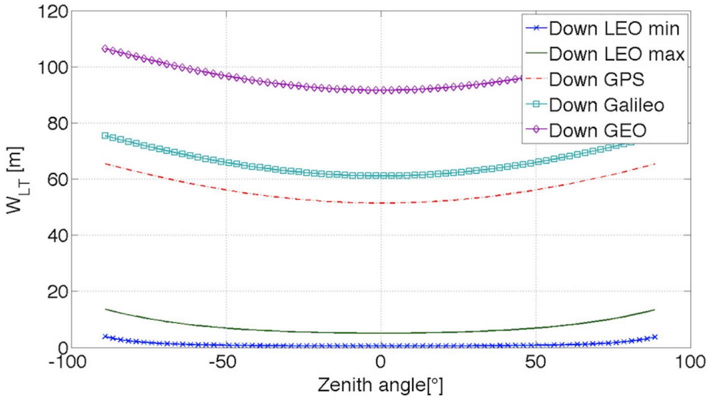

Figure 2.9: Long term beam width w_{LT} as function of the zenith angle for different satellites in downlink. Simulation with an Earth telescope radius $r_T = 75cm$ and a space telescope radius $R = 10cm$.

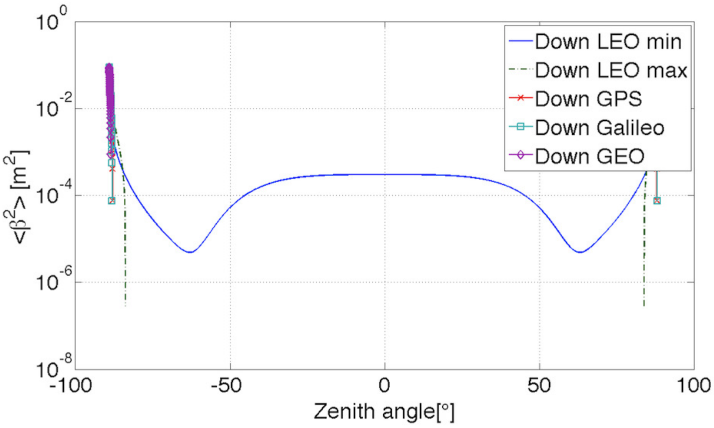

Figure 2.10: $\langle \beta^2 \rangle$ as function of the zenith angle for different satellites in downlink. Simulation with an Earth telescope radius $r_T = 75cm$ and a space telescope radius $R = 10cm$.

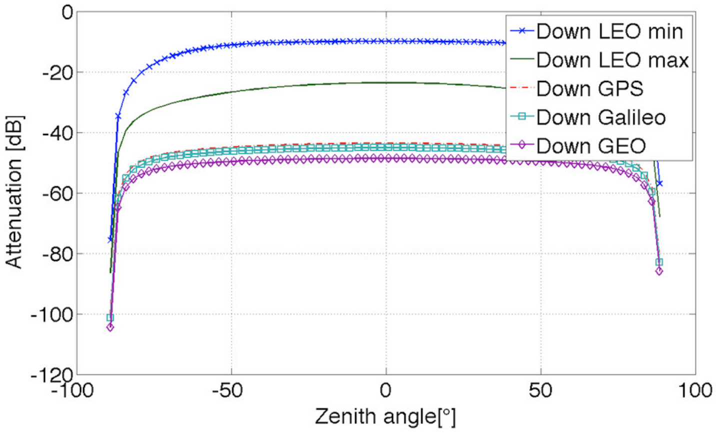

Figure 2.11: Attenuation η as function of the zenith angle for different satellites in downlink. Simulation with an Earth telescope radius $r_T = 75cm$ and a space telescope radius $R = 10cm$.

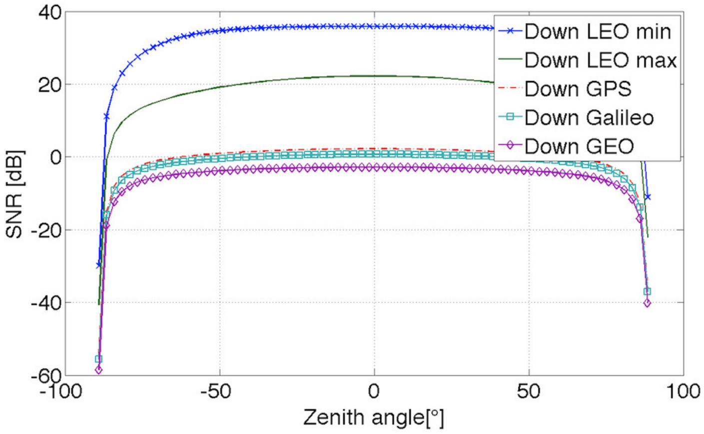

Figure 2.12: SNR as function of the zenith angle for different satellites in downlink. Simulation with an Earth telescope radius $r_T = 75cm$ and a space telescope radius $R = 10cm$.

communication with the simulated setup, but gives good wishes related to further technological improvements.

The actual feasibility of QKD is related to link distances in the range of LEO orbits, a good SNR can be achieved without stretching the telescope field-of-view to the technological limit. Small improvements on IFOV can shift the link distance feasibility limit toward higher orbits, allowing quantum communication even with GPS and Galileo satellites.

Chapter 3

Free-space long distance horizontal optical link

The results obtained from this work has been published in [35] and in the experimental reports.
In the perspective of the extension of Quantum Communication (QC) in free-space to long distances, the analysis of the phenomena that occur to a visible or near-infrared beam in the propagation in atmosphere and their understanding is of crucial importance for devising the most convenient optical terminal. The investigation on the ground-ground case is used also to envisage the space QC, along with a vast area of research in satellite Classical Communications [58].
More in details, optical propagation in atmosphere in the case of links length of over $100km$ is affected by several transformations of the beam parameters, resulting in an increase of the link losses. Moreover, the long range optical communication at the single photon limit exploiting the quantum protocols, on the other side, differs from the classical protocols in that the signal to be transmitted cannot be intensified, being a train of very weak pulses with an average about one photon per pulse.
The understanding of the effects induced by the propagation in both the irradiance at the receiver as well as in the temporal statistics is crucial to assess the quality of the communication and eventually the feasibility of the link. Moreover, for the very long links, fading and losses are induced by the decoupling of the beam with the receiver due to large wandering of the beam spot, as it was also investigated for the space channel [86].
In this perspective of free-space long range single-photon quantum link, we planned a set of experimental campaigns to study the propagation of a single or twin optical beams in scale length of several tens to a few hundreds kilometres.
We address in this work the study of the phenomena induced in very long propagation by using of laser beams to investigate links whose length is of several tens to a few hundreds kilometers. In the experiments, the observation of the whole beam combined to the measure of the local irradiance at the receiver side are performed and then projected to the case of single photons links. In addition, with the aim to stabilize the centroid position at the receiver, the propagation of two beams forming a small mutual angle is studied in the framework of the isoplanatic angle spread for low and high orders of the beam spatial modes.
The experimental models were realized in Alpine links as well as between the Tenerife and La Palma link in the Canary archipelagos. The whole beam at the receiver was acquired and the scintillation analysis carried out and compared to models including the meteorological data from the Canary Observatories.
The design of the optical setup for long range quantum communications is crucial, and we addressed

this issue by developing an optimized telescope for the experiments.
The literature on horizontal propagation is quite poor mainly because for decades of years the interest was focused on vertical propagation -for astronomical purposes-.
As first we needed to understand the effects of atmospheric turbulence in beam propagation: like wandering, spreading and scintillation. This led us, as last step, to identify the best design parameters for transmitters and receiver and for communication protocol.
With the gained data we want to define a model or a set of criteria to be considered in designing an optical quantum link and to predict the link losses for a realistic receiver and, possibly to envisage the exploitation of the time-varying losses for the selection of the portion with the highest signal-to-noise ratio [77].

Three main experiments were realized in three different localities:

- a first link of $2.2km$ between the roof of the building of the Department of Information Engineering (DEI) and the Specola tower in Padova,
- a second link of $13km$ between two locations in the Dolomiti Bellunesi (Italian Alps),
- and the link of $144km$ between Tenerife and La Palma islands at Canaries.

The first two to be considered preliminary studies will be just briefly mentioned.

3.1 Experimental Campaign Description

The experimental campaigns are temporally distributed in the months of: May 2010, September 2010, May 2011, September 2011.
The first runs were oriented on scenario identification and data acquisition for future design of a telescopes that were tested in May and September 2011.

In May 2010 we investigated the following issues:

- *Diffraction limits of transmitting and receiving apertures:* an aperture of size D produces at distance l a diffraction limited spot of diameter $2.44\lambda l/D$ so in principle the larger the aperture, the smaller the diffraction limited spot. On the other side the receiving aperture is the power collector, the bigger the better.
- *Turbulence of air-fluctuation, wandering and broadening of the spot at the receiver:* there are several reasons that cause the spot at the receiver to move: drift in temperature along the path, fast atmospheric effects, instrument vibrations. Those movements can finally move away the spot from the receiving aperture or/and decrease the collected power.

In September 2010 we investigated for:

- *Beam-stabilization method:* for the optimization of the beam pointing in the link between Tenerife and La Palma. Also studied was the use of a Laguerre-Gauss beam generated with a fork hologram.
- *Measuring the power at the receiver side:* using different beam size at the transmitter: $120mm$, $200mm$ refractor and the OGS (Optical Ground Station)[1] $1m$ reflector, and to scale-up to assess the link budget using the OGS.

---

[1] OGS is a telescope of ESA installed in the Teide Observatory

- *Measuring the temporal fluctuation of the signal and to model the irradiance statistics and the spatial correlation.*
- *Designing of the setup in order to aim a second beam with slight pointing offset or of different wavelength:* the purpose here is to investigate the extent of cross-stabilization, that is the correlation of the pointing stabilization on the one beam with the second beam.
- *Setting up the transmission in La Palma, using the* $120mm$ *f/7.5 refractor telescope.* In this scheme, the inter-island link is propagating in the opposite direction. This is to investigate the asymmetry in the turbulence effects, due to the proximity of the La Palma *caldera* to the position of JKT (Jacobus Kapteyn Telescope). This phase was not possible due to bad weather conditions.

And in May 2011:

- *Checking the symmetry of the optical channel.* In the previous experiment we demonstrate that a $2m$ like spot could be achieved shouting at OGS with a $20cm$ aperture (the OGS finder) and receiving at JKT. This has to be verified in the opposite direction since the final experiment will be done in this configuration due to the bigger collecting area of OGS in Tenerife. For this purpose we designed and tested a new transmitting telescope based on an aspheric singlet optics of $23cm$ of diameter.
- *Measuring the channel losses in several conditions.* Measure the losses of a known sent beam possibly at different wavelength. We would like also to measure scintillation by means of a photodiode.
- *Checking the guiding system.* In the previous report we described the used guiding system. This is based on the detection of the green spot at the receiver and on the correspondent correction movements given to the motors at the transmitter sending correction data over the internet.

And as last in September 2011:

- Testing the optical setup stability and pointing procedure. The transmitter based on the singlet $230mm$ refractor telescope has been tasted for row-manual motorized-fine pointing and for stability.
- Measuring the link losses in order to characterize the channel. The telescope was tested for a long time to assess the best performance achievable. Target losses are below $30dB$.
- Verifying the automatic pointing control based of the beacon coming from Tenerife.
- Getting data on turbulence and link properties.

3.2 Preliminary test

The firsts preliminary investigations with both static and adaptive optics, were realized with an exploratory set up for DEI-Specola $2km$.
The transmitting aperture was a refractor SkyWatcher Black Diamond Telescope [14] with $120mm$ diameter $f/7.5$ ($f = 900mm$) whereas the receiving aperture was a Meade reflecting telescope[13] with diameter $203mm$, $f/10$ ($f = 2030mm$).

Figure 3.1: The 2.17km link from the DEI Department roof to the Specola tower.

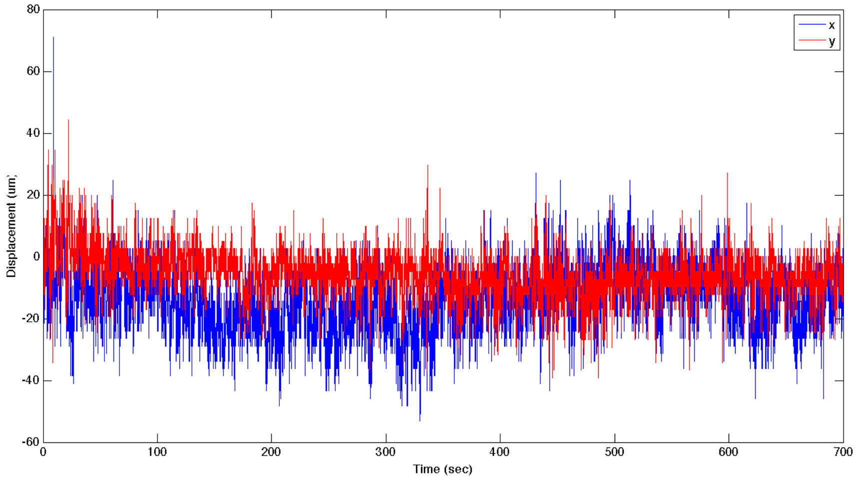

Figure 3.2: X and Y in μm it the Specola 2km link measured with the PSD. The average power is 174μW.

We performed measurement with a lateral effect Position Sensitive Detector (PSD) from Duma [8] which characteristics are resumed in Table 3.1; images of the spot taken using digital cameras were used to acquire the whole spot, which is obviously much larger than the beam profiler sensors.

Starting from the latter we could see a diffraction limited spot of about $3cm$ (Fig. 3.3), and it was also clearly visible the whole beam propagating and bending as a chord over the roofs with a frequency of about 5 to $20Hz$.

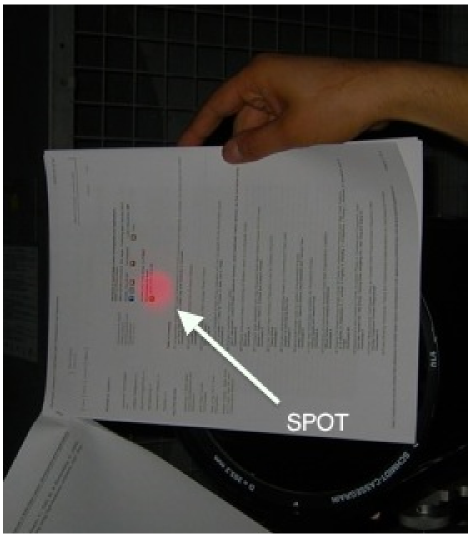

Figure 3.3: Spot received in the $2km$ link sent through the $120mm$ SkyWatcher. The spot is about $3cm$ wide and wandered of about its diameter with a frequency quite higher that once per second.

The beam was moving of a quantity comparable to about its diameter. Measurement with the PSD (Fig. 3.2) showed a displacement of the beam centroid with respect to the mean value with standard deviation of $6.5\mu m$ and range of about $40\mu m$ corresponding due to the focal length of the telescope to $3.2\mu rad$ and $19.7\mu rad$ in the far field. Taking the former value yields to a deviation over $2.17km$ of about $7cm$ thus confirming the observation by eye.
The $2km$ link has been a good first trial to understand the effects on the beam propagating in the atmosphere although the distance was quite small and the city environment is very different and peculiar with respect to others.

Parameter	Value	Units
Active area	9×9	mm
Beam Size Range	$50 - 8000$	μm
Position Resolution	better that ± 1	μm
Position Accuracy^2	± 25	μm
Calibrated Spectral Range	$350 - 1100$	nm
Input Power Range	$1 - 250$	μW
Power Accuracy	± 5	%
Data Update Rate	30	kHz in Analog Mode

Table 3.1: Parameters of the DUMA Positioning Sensing Detector as available in the data sheet downloadable from [8]

Another link that we realized has been between two location in the Dolomiti Bellunesi.

Figure 3.4: Link of 13km in the Dolomiti near Belluno.

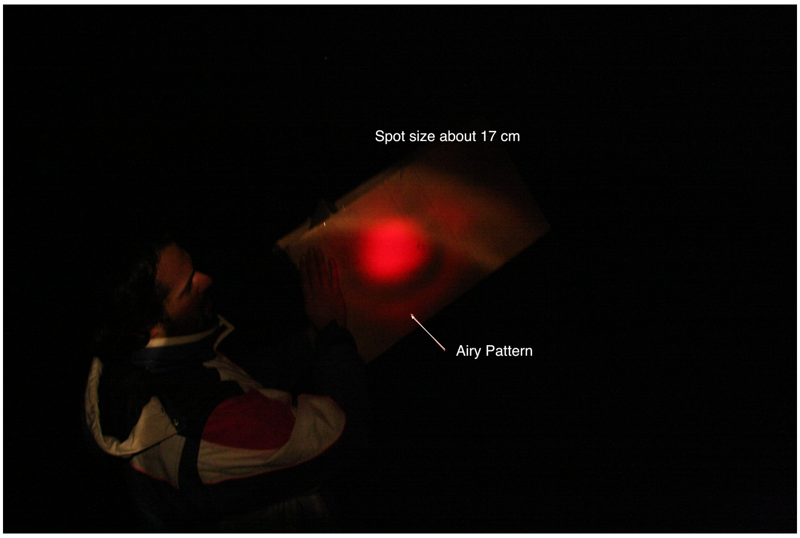

Figure 3.5: Spot size on the 13km link.

The link was $13km$ long at the height of about $1400m$ over sea-level (Fig. 3.4). In this case, we could not see the diffused light along the beam propagating, as in the previous case. At the receiver, a clear diffraction limited spot of about $17cm$ with Airy pattern was observed (Fig. 3.5). The beam was moving in this case also of about its diameter.
In this case we measured the received beam with a Shack Hartmann wavefront sensor from OkoTech with sampling of $25Hz$ in order to monitor the presence and power distribution of Saidel aberrations. As we expected the major contribution come from tilt, with a prevalence on one axis, as shown in Fig. 3.6.

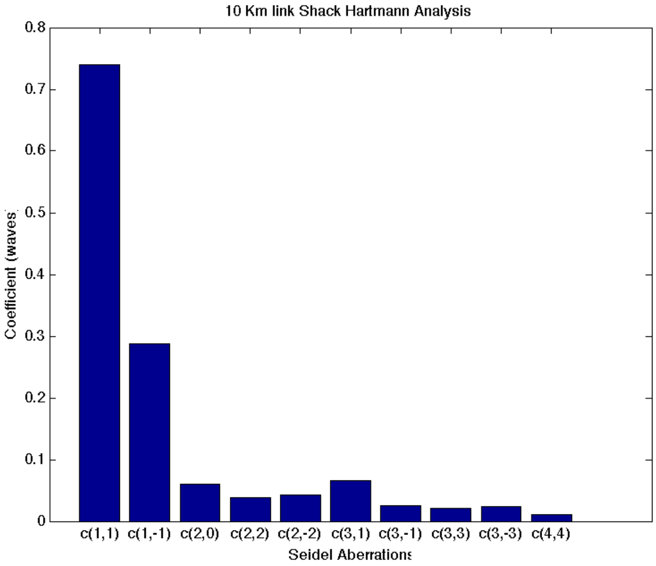

Figure 3.6: Shack Hartmann analysis in the $13km$ link. The data has been collected at a frequency of $25Hz$. The first two terms represent the tilts terms.

Some comments to these results:

- the spot obtained were diffraction limited for both links, this may be due to the good weather conditions, big fried parameter ($> 10cm$), good transmitting optics.
- the spot moved around of a quantity comparable with its diameter with a frequency similar to the $2km$ link ($5 - 20Hz$). This was not a problem when dealing with a few cm spot compared to $20cm$ aperture whereas it was not easily handled for the $10km$ link since the beam, at its minimum size, dropped out of the receiving aperture when bouncing around.

3.3 Canary Islands Tests

After the short-link preliminary tests, that highlighted the importance role played by the quality of the transmitting optics. We extended the link distance up to $144km$ at Canary Islands.
The purpose of the Canary setup was to optimize the transmission of an infrared (IR) laser ($810nm$) from La Palma to Tenerife, using a green laser from Tenerife as pointing guide; it born from the practical need of the researcher of IQOQI[3] from Vienna to get a stable optical link for quantum

---

[3] Institute for Quantum Optics and Quantum Information of the Austrian Academy of Sciences

experiments like: teleportation, etc.
Various schemes, and technological solution were taken into account: they were based on hypotheses that test after test were either verified or refused and that eventually led to the final setup. We can summarize the main experimental setup used in the various runs as:

1. $810nm$ IR laser from La Palma to Tenerife using a $532nm$ laser beam coming from Tenerife as pointing and turbulence probe. (LINK DIRECTION- La Palma: transmitter/ Tenerife: receiver)
2. $532nm$ and $640nm$ lasers from Tenerife to La Palma (LINK DIRECTION- Tenerife: transmitter/ La Palma: receiver)
3. $810nm$ and $532nm$ from La Palma to Tenerife using a dedicated telescope design for this purpose (LINK DIRECTION- La Palma: transmitter/ Tenerife: receiver)
4. $810nm$ from La Palma to Tenerife using a $532nm$ laser from Tenerife as pointing guide (LINK DIRECTION- La Palma: transmitter/ Tenerife: receiver)

3.3.1 (1) May 2010

In this first run we guessed that the link between Tenerife to La Palma is symmetric in propagation and it's not affected by the different orography of the two islands. An adaptive optic loop was used to compensate the atmospheric turbulence effects then to stabilize the beam at receiver

The issues addressed in this run were the following:

- ***Beam-wander correction and stabilization with adaptive optic system***

In La Palma the $120mm$ Skywatcher was used as receiver (of a green beacon) and as sender of the main infrared laser.
The OGS's finder telescope was chosen as transmitter of a green laser (beacon) used as pointing and turbulence probe.
According to the optical design of the OGS Observatory, the finder parameters are: $D = 200mm$ and $f = 2900mm$). The advantages gained from this choice were: on the ocular side, a precise alignment system is available, which turned out to be very useful for the fine adjustments of beam aiming. Other advantages of this choice are the stable optical mount, the intrinsic alignment with OGS, the possibility of use the OGS guide and the fact that it is a refractive optics without unwanted obstructions. About using other telescope from Tenerife, we faced harsh problems in finding a shelter from strong - and cold - wind or to place an additional optical board on top of OGS.
The whole setup is represented in Fig. 3.7.
The green beacon light from Tenerife is collected by the $120mm$ telescope and collimated with a $f = 65mm$ lens to yield a beam of about $8.7mm$ diameter. The beam is deviated by a dichroic mirror after the deformable mirror and it is focalized into the PSD. The deformable mirror is an Adaptica[5] PAN membrane DM driven with pre loaded tilt deformations in closed loop with the PSD.
The infrared laser is sent out from a single mode fiber from behind the dichroic filter collimated such as its propagation path is the same as the green beacon throughout the system. The analog signal from the PSD is collected and digitalized via a Picoscope four channels digital oscilloscope and the loop is closed using a C++ graphical interface. The overall closed loop refresh rate is about $300Hz$.

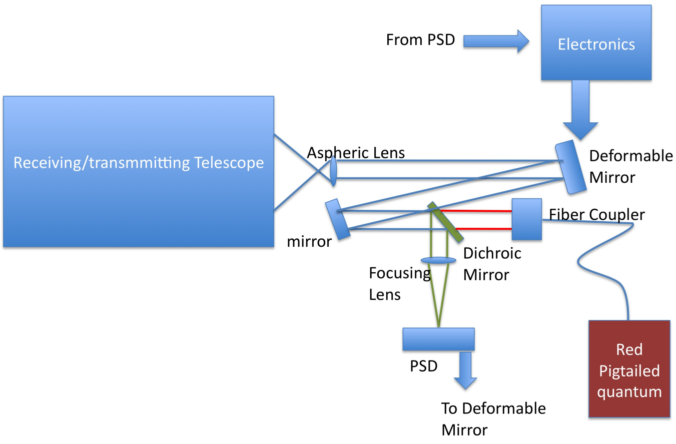

Figure 3.7: Schematic of the receiver setup used at Canaries

Measurements experimental results

Average and instantaneous beam size at JKT

With our $150mW$ laser [4], mounted on the $20cm$ diameter OGS finder telescope at La Palma we could clearly see a spot which size was about $1.8m$ (Fig 3.8). The size of the spots was not the same every night, nevertheless using the OGS finder and working a bit on the focus we could reach a beam of about 2 to 3 meters in diameter.
For comparison during this campaign we tried also the $8W$ guide star laser of OGS and a $20cm$ Meade reflective telescope.
In the first case, since there was no optics at the laser output there was a huge spreading of the energy due to diffraction. It is hard to quantify the size of the spot: we walked many meters away (about 100m) form the JKT to the right and we could clearly see a bright spot coming from Tenerife.
In the last one we cannot be sure of the cause of the degradation of the spot that seemed to have a diameter of more than $20m$, the more probable drawback is represented by the obstruction present in the telescope that causes the outgoing spot to be far from gaussian by cutting the central part of its profile.

Motion of the beacon beam at JKT

The observation of the spot, referring to the smallest we could get with the OGS finder, revealed two kind of motions: a movement of the whole spot and a speckle pattern inside the spot.
The slow continuous movement, with time scale of 5 to 15 seconds, has effect to change the beam position of an amount of about $5m$ away from its initial position. In order to appreciate the movement we asked to switch off the tracking of OGS. It is interesting to notice that even when the OGS tracking was turned on the movement of the spot was present, we noticed only a different behaviour in the velocity of the displacement, but not enough to impute it to the OGS tracking. It

---

[4] Opto Engine[3] MGL-III-532-100 Laser DPSS [3], multi-mode, nominal $100mW$@$532nm$, power stability $< 5\%$

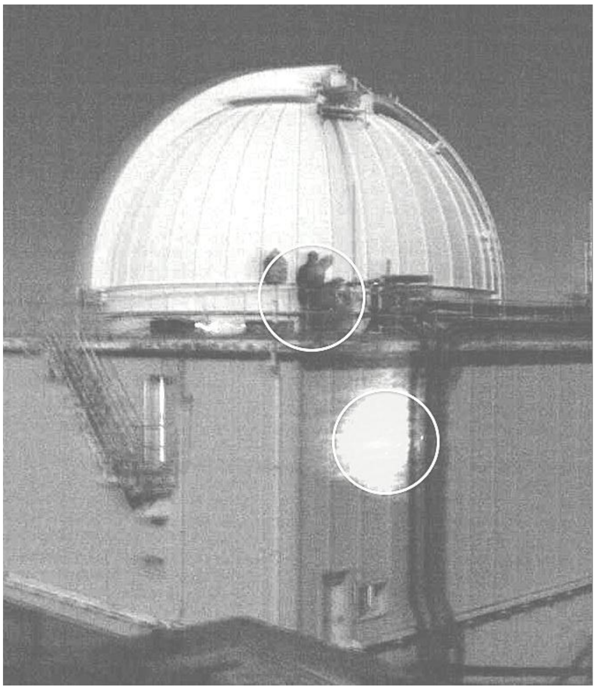

Figure 3.8: Spot size at Johan Kapteyn Telescope JKT, La Palma from 20cm OGS finder. The two circles are of same diameter 1.85m. 500ms Exposure Time

was indeed clear to us that the frequency of OGS tracking was not enough to compensate for the spot movement and keep it stable.

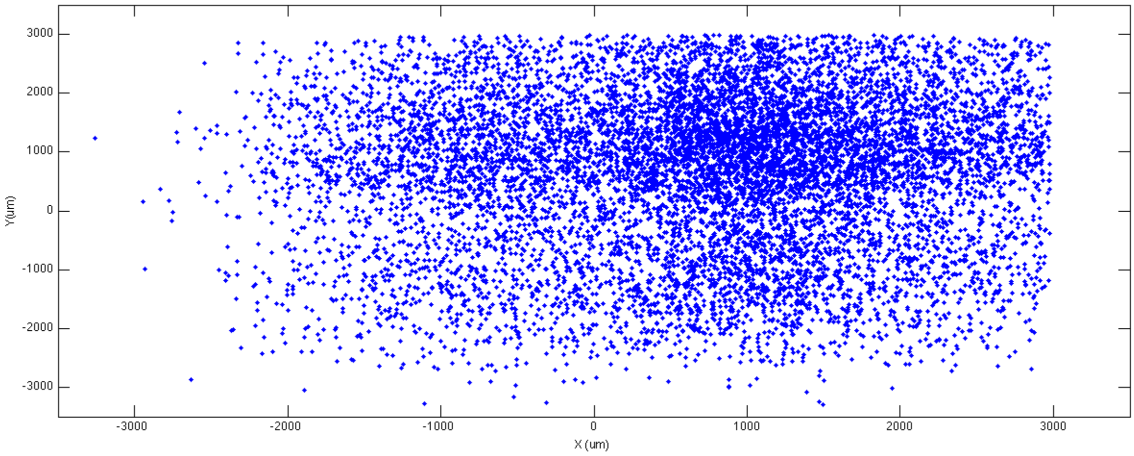

Figure 3.9: X and Y positions registered with the PSD around the center. The mean angle is 29.5°.

Another explanation that we cannot prove but is interesting to think about is the fact that we added a weight of bout $2-3kg$ to OGS installing our setup and there were no more balancing weights to put on OGS. In this way the motors of the telescope were continuously sinking current.

We do not know if this could cause a slow drift in the position of the telescope that would have induced a movement in the spot at JKT nor we know the amount of it.
In order to verify the empirical observation we use the data collected with PSD. Since the receiving aperture is small ($12cm$) compared to the spot size and the effect of speckling was very strong we received enough power to our PSD only in a fraction of the time. This problem has conditioned also the performances of the adaptive optics setup that will be described later on. In this case we simply took the signal and binned with different time bin in order to verify the observation obtained by eye about the spot movement and to argue if there was some type of correlation between the data collected at JKT and the OGS tracking system (see Par. 3.3.1).
The positions acquired during 30 minutes are represented in Fig 3.9 as well as the histogram of the angles in Fig 3.10.

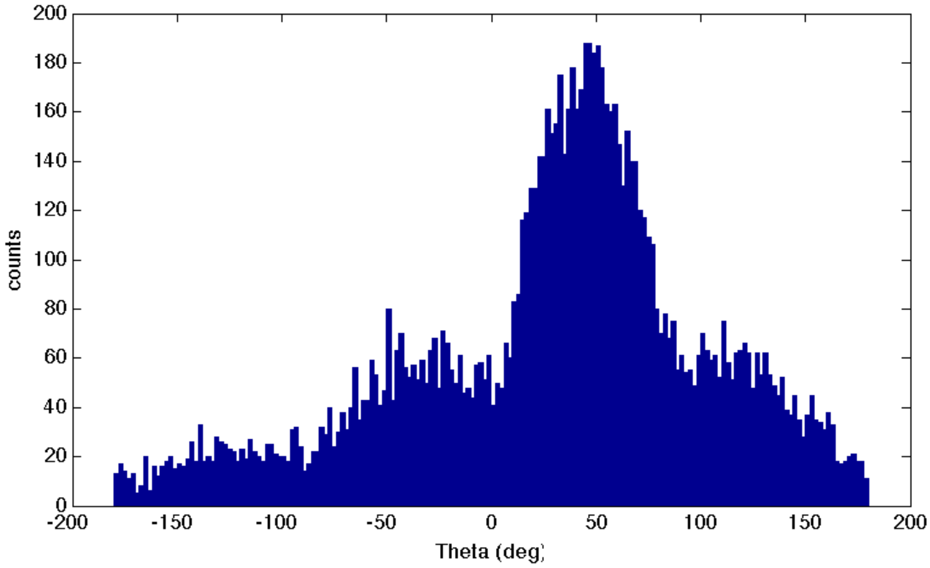

Figure 3.10: Histogram distribution of the angle o the received spot. The mean angle is 29.5°. The peak is centered at 50° and has a FWHM of 40°.

In order to appreciate the movement on the time scale of about 10 seconds we extrapolated several clusters of 90 seconds of acquisition and tried to fit the data to appreciate such a slow drift. It happened that due to such a movement we lost the signal from our PSD but later on manually or by the movement applied by the OGS tracking the spot was placed again so that the PSD could acquire. In this sense we were sampling the signal for its slow temporal drift and spatially in the sense of taking only a part of the spot with our $12cm$ lens. Taking only our $12cm$ subset of the spot. The spatial sampling revealed the fast movement induced by the speckle, that in our analysis seems to be much stronger than the movement caused by the slow drift. The temporal sampling does not influence the measurement: the movement imposed by hands or by OGS are not in phase with respect to the spot movements.
The result is showed in Fig 3.11. The mean tilt deviation of the slow drift is about $500\mu m$ which corresponds to an angle at the entrance of the telescope of about $40\mu rad$ that corresponds to a displacement over $144km$ of $5.5m$. As already mentioned it has to be noticed (Fig. 3.12) that the spatial sampling of the speckle caused a much grater angle at higher frequencies. This is also caused by the fact that the PSD is sensitive also to the energy distribution, so then two spots arriving in

the same position but with different energy distribution inside the focal spot could cause a different distribution of the generated photo-electrons among the four cathodes of the sensor[5]

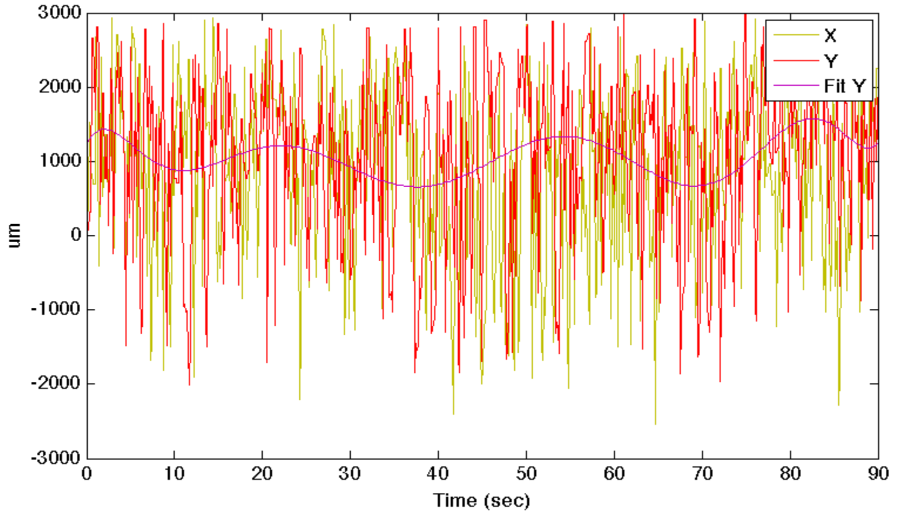

Figure 3.11: Sample of 90 second where the slow drift is represented as a fit of the data. The fast tilt is due to the speckle and is superposed and much higher than the slow drift.

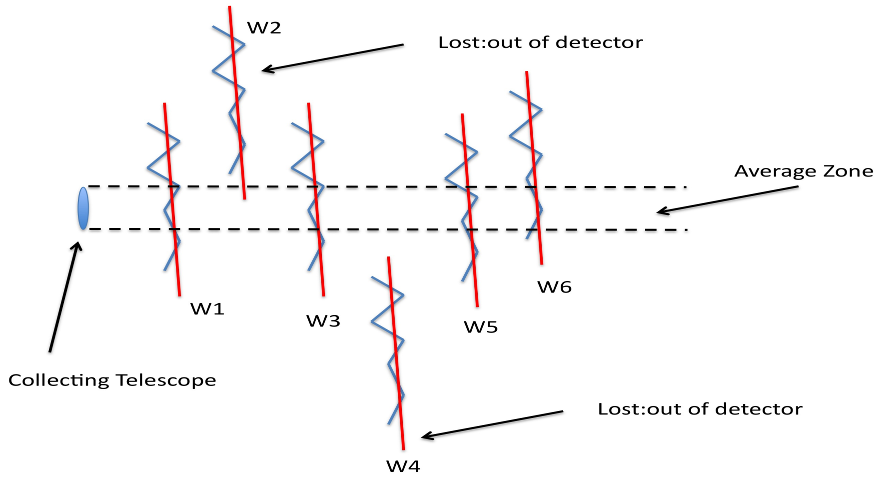

Figure 3.12: Different wavefront entering the collector at different times with the same global inclination. The speckle (blue) that varies from every wavefront is much more tilted locally than the global tilt.

---

[5] Lateral effect PSD works on the following principle: the distributions of photo-electrons among four cathodes positioned in a cross configuration causes four different currents detected. The differences in these currents is used for calculating the position of the spot.

Correlation of beam centroid at OGS and JKT

Regarding the OGS tracking we have collected some data and tried to correlate them with the measurements taken at JKT. First of all it has to be remarked that by observing the $1.8m$ spot by naked eye when the OGS was tracking it is clear that the tracking frequency is insufficient because the spot is not stable in the same position and it keeps moving with a frequency comparable with OGS tracking ($0.1Hz$). This has been a major problem for us and our setup since we could not have always enough energy on the PSD for the control tip tilt loop.
In spite of the slow feedback we were able to collect data about the OGS tracking. First of all the distribution of the correction angle (Fig. 3.13) which reveals the fact that the angles of correction are consistent with the movement seen by the PSD (Fig. 3.10). There is a reflection with respect to the vertical axis if we considered that the OGS and our PSD where facing each other.

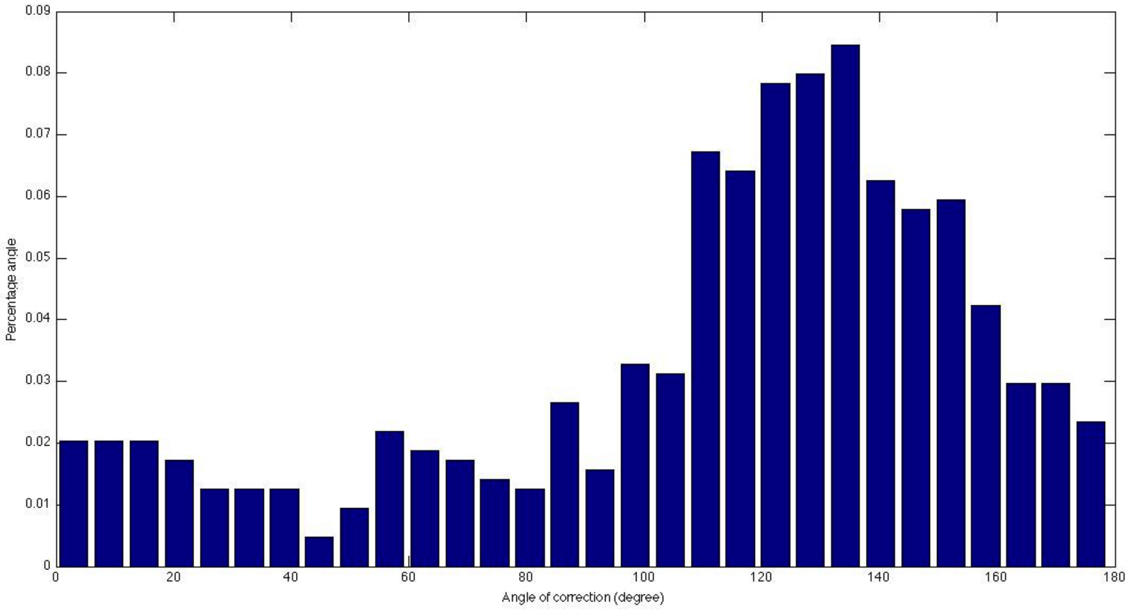

Figure 3.13: Distribution of correcting angle at OGS. The peak is centered at 135° with FWHM of about 40°.

The other interesting thing is the average FWHM of the correction represented in Fig. 3.14 which indicates an average correction of $6arcsec$ that corresponds over $144km$ to a displacement of about $4.2m$ consistent to what we measured and saw by naked eye.

Effect of Deformable Mirror in the link

We performed some measurements of the performances of the adaptive optics (AO) setup during two nights. We must first notice a couple of important remarks.

1. Since we lost the spot frequently because either we could not keep it stable by hands or the tracking of the OGS was too slow the actual correcting time was only 18% of the time the loop was on. This causes of course a degradation of the measurement but not necessarily a degradation of performances.

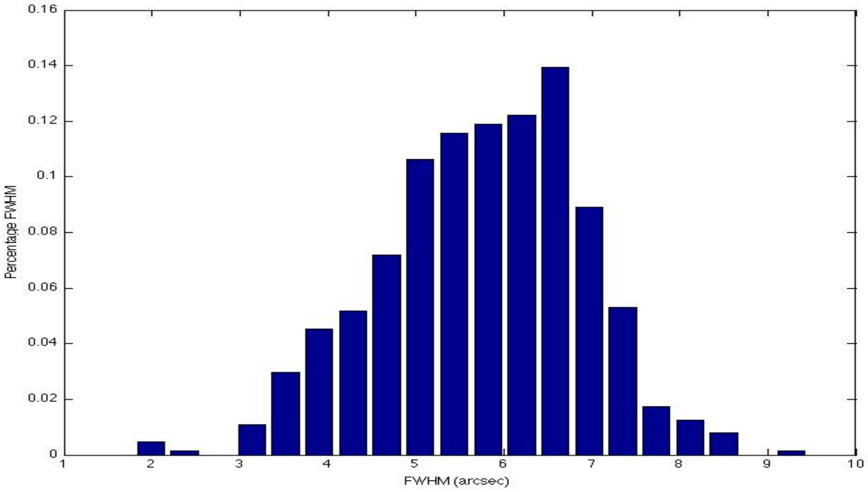

Figure 3.14: Distribution of the FWHM of the OGS corrections.

2. Since we was sampling the spot we collected only a fraction of the energy affected by the fast speckle. As mentioned the tilt of such cells was, according to our measurements (Motion of the beacon beam at JKT Sec. 3.3.1) very high compared to the average tilt. We can assume that fast fluctuations were related to local turbulence (at receiver) that degraded the wavefront inducing speckle. The deformable mirror (DM) have a maximum tilt scaled at the entrance of the telescope of about $40 \mu rad$. This means that the mirror worked mostly at the maximum stroke since it could not handle such high tilt.

   Due to weather conditions it was unfortunately not possible to establish a much slower corrected link filtering out the speckle effect by mediation of the spot position over a longer time.

To evaluate the AO performance we did some measurements of the receiver power (single photons count rate) at Tenerife: using the green beacon sent from the OGS finder as sensing/atmosperic turbulence probe, we sent back to Tenerife a $808nm$ infrared $3mW$ fiber coupled laser and measured the count rate of a single photon counter mounted in the focal plane of the OGS.
In Tab. 3.2 the measurements results are reported: we can see a mean improvement of 29.7% with a peak of 68% compared to the case without AO.
In Tab. 3.3 another set of measurements is reported, with a mean improvement of 11.3% and a peak of 22.7%.

cycle	counts AO on	counts AO off	AO percentage improvements
1	1717381	1020507	68%
2	1805167	1657218	8.9%
3	1853505	1654182	12%

Table 3.2: First set of AO measurements. Average improvement 29.7%, peak 68%.

For this second measurement, the mean displacement from the relative center of the PSD during correction and non correction operation reveals a mean improvement of 22%.

cycle	counts AO on	counts AO off	AO percentage improvements
1	7880919	7508668	$4,9\%$
3	7695923	6269970	$22,7\%$
4	6488807	5980040	$8,5\%$
5	7445284	6783109	9.7%

Table 3.3: Second set of AO measurements. Average improvement 11.3%, peak 22.7%.

Conclusions and consideration gained from the first experimental session

From the first experimental session we got more information on the atmospheric turbulence effects and on the optical link that had guided the future runs and solutions adopted.

1. *The beam wandering is evident and has a few-second timescale* $\Longrightarrow$ A SLOW DRIFT (WANDERING) CORRECTION SYSTEM IS NECESSARY The transmitted (single-photon) beam will be under the guide of the system at JKT that is much faster (at least 1Hz) than the guide system of OGS. The tracking of OGS will be used to maintain aligned the OGS with the JKT and this is good if the field of view coupled to the detector is enough to handle the imprecision induced by the slow guiding;

2. *The beam broadening is an inverse function of transmitter pupil diameter and varies with the night atmospheric conditions*$\Longrightarrow$ THE TRANSMITTER OPTICS MUST HAVE A SUFFICIENT LARGE DIAMETER TO REDUCE THE BEAM SIZE AT RECEIVER: a 12 to $20cm$ doublet or triplet lens (f/3 to f/7). This choice of optics would create a much smaller spot at the OGS, from about $2m$ in the case of $20cm$, to about $4m$ in the case of the $12cm$. The effect of this is a significant reduction of the coupling losses with OGS, which can be estimated on the basis of the square of spot/telescope diameter ratio. Using actual parameters, an improvement of a factor up to about 10 in link efficiency should be expected from this optics.

3. *The coupling of the small scale fluctuations with the receiver optics, induces a fast fluctuation of the position of the spot on the receiver focal plane much more evident with a small receiving aperture.* The size of the deviation has to be considered carefully by a pointing stabilization system. The PSD data appears to represent a beam displacement much larger of what actually observed on the spot, by averaging the scale and by naked eye observations. These fluctuations are not the real displacements, but coherent combination of the gathered portion of the beam by the telescope pupil. They are also the cause of the broadening of the spot produced by the telescope with the gathered light. In some cases the power collected is not enough to be sensed by PSD $\Longrightarrow$ A DETAILED DESIGN OF THE GATHERED FIELD OF VIEW OF THE ACTUAL RECEIVER IS NEEDED, TO AVOID SIGNAL LOSS AT THE DETECTOR LEVEL. A STABILIZATION AND POINTING AO SYSTEM MUST REJECT OR DISCRIMINATE BETWEEN FAST LOCAL FLUCTUATION AND WANDERING ON THE GLOBAL BEAM SPOT. The correction at high speed and driven by the fast fluctuations due to speckle, appears as not effective for the beam stabilization, that evolves on a second-time scale. Moreover, as the acquired tilts are relatively large, it drives the mirrors to a unnecessary large correction. An adaptive optics system will be used for either the correction of static aberrations induced by actual optical components and their mounts and alignment non-idealities and for the active tracking at the tip-tilt level on a Hz frequency scale. In this way, the continuity of the link in time would be improved. The matching of the detector with the incoming beam aperture - including the fast-scale fluctuations - has to be implemented.

The methods here is to properly design the front end optics. This part also has to pre compensate for the initial deformation of the deformable mirror.

4. *A correlation between JKT and OGS beam wandering was observed using the data acquired.* $\Longrightarrow$ EITHER THE BEAM POSITIONS INFORMATION AT LA PALMA OR TENERIFE CAN BE USED TO STABILIZE THE BEAM AT THE RECEIVER

3.3.2 (2) September 2010

In this second run we implemented a conceptually different stabilization system in a reversed link: an outdoor camera collects the beam centroid received at La Palma and sends the positioning error to the transmitter at Tenerife to pre-compensate the position deviation induced by the atmospheric turbulence. In this new configuration the pointing beam and the signal beam co-propagates in the same direction in the range of isoplanatic angle: the signal beam (a red laser) and the pointing beam (a green laser) are separated at the source by a small quantity that is enough to make the beam spatially separated at the receiver but subjected to the same atmospheric effects. As transmitter was used the OGS's finder, that simplified the pointing procedures.

Two main facts of the previous run inspired this new solution:

- The feedback signal used to drive the AO system was a sample of the whole beam, and provided only a partial information on the instantaneous wavefront deformation. Moreover, the very long path actually induces an involved transformation of the optical wavefront, which requires a formidable computation speed and modeling capacity to be analysed and inverted in real-time. This signal is not suitable and effective for the link optimization.
- The slow drift of the spot and signal was observed, with a temporal scale of the centroid swings of 5-20 seconds. This drift should have been corrected by a slow tracking system based on the observation from both sides of a "guide star" laser shooting from the other side. This method was acceptable as long as the spot had been very big ($> 20m$) but failed when, using the OGS finder, the spot reached the dimension of a few meters, as the reference itself is subjected to fading.

The issues addressed in this run were the following:

- ***Beam-wander correction with a merit function from the whole spot:*** the new correction system is based on a CCD camera that acquires the entire spot at the JKT (as soon the dimensions are $< 10m$). A computer elaborates the image and sends back the error signal to the corrections setup attached to the OGS finder from where the laser beams are sent. In this setup two stepper motors are present with the aim of moving the outgoing direction in two axes. In this way the correction of OGS is no longer necessary for the spot stabilization and the correction itself is based on global information of the spot and not on partial sampled information. The setup is depicted in Fig. 3.15.
- ***Study of the spot characteristics and power sampling:*** we wanted to analyse also the spot in terms of collected power and temporal and spatial scintillation with different collecting apertures. The aim is a comparison of these data with models in the literature of irradiance statistics for turbulent propagation as well as with the weather data.

The signal laser source is a continuous (CW) single mode pigtailed red laser diode, while the pointing source is formed by two similar green lasers (used together or as single source), mounted at the telescope focal-plane on a rigid cage.

Considering the losses of the transmitting telescope at OGS the outgoing powers where about $40mW$ for the red and $100mW$ for a single green laser.

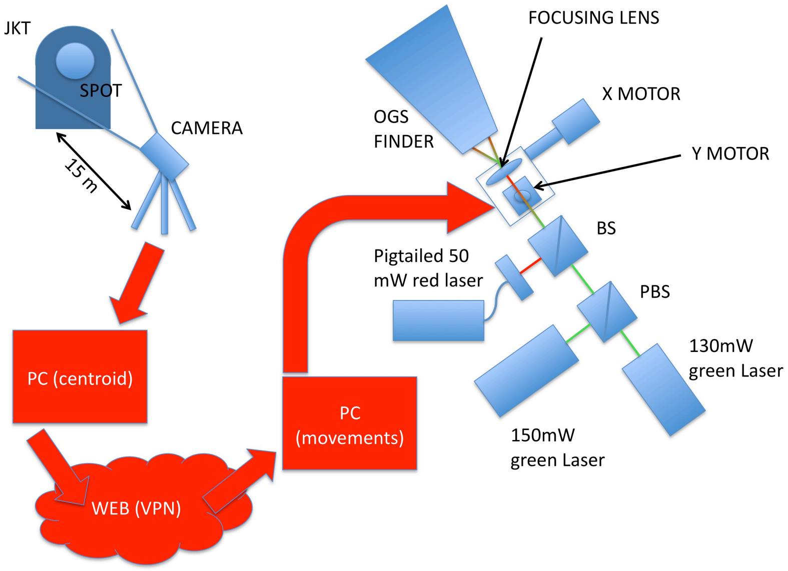

Figure 3.15: Link setup and feedback loop used at Tenerife (OGS) and La Palma (JKT)

Measurements and experimental results

The measurements we have performed can be summarized as follows:

- *Beam wander correction:* stabilization of the beam centroid with a correction setup based on a whole spot acquisition via a CCD camera on the JKT and a feedback transducers implemented by a stepper motors system that moves the secondary lens at OGS.
- *Power Measurement of the beam:* while the beam centroid is maintained fixed using the method above, we measured the collected power with a power meter and a fast photodiode with different apertures: i) $22cm$, ii) $10cm$ and iii) $5cm$.
- *Measurement of spatial features of the beam:* we have acquired the spatial scintillation dynamics by filming the whole beam in different conditions of the transmitter.
- *Separation of two laser beams:* we aimed the beams of two green laser beam from OGS with a different angle, in such a way to separate their spots in the JKT dome. We acquired a film of the evolution.

Beam wander correction

As stated above, the correction system is based on the whole information of the spot at JKT that we registered with Thorlabs camera positioned about $15m$ away from the JKT and looking at the JKT dome nearly parallel to the incoming beam to minimize parallax.
Due to the camera performance the overall step correction time was about from 2 to 4 seconds

depending on the intensity of the spot. And since the spot is in fact a series of smaller blobs as depicted in Fig 3.16, the sensitivity of the camera adds an error in the determination of the centroid.

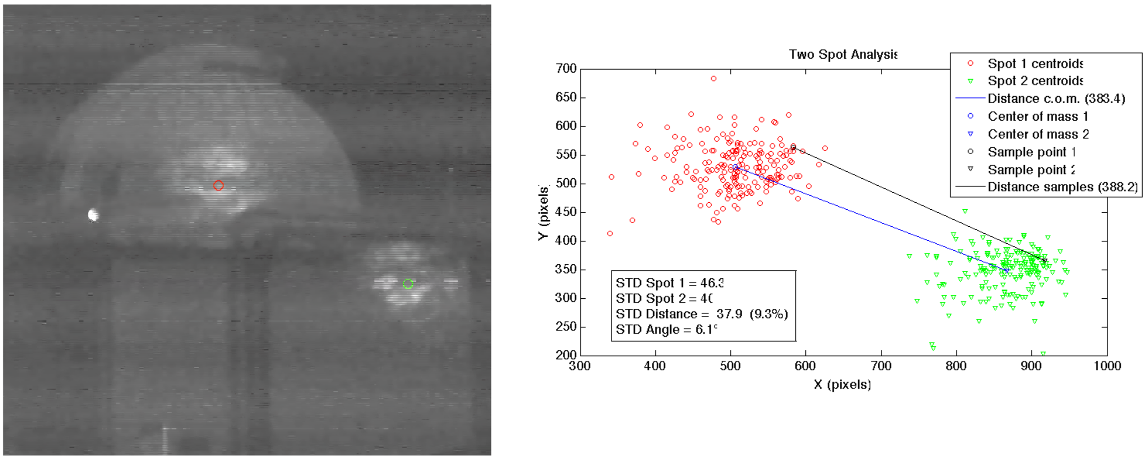

Figure 3.16: Spot of the two green lasers sent from Tenerife in the dome of OGS during the second night and temporal analysis. $50 pixels = 1$ meter.

This larger noise appeared to not alter the effectiveness of the correction algorithm.
An optical setup with three different lasers and a motorized x-y stage in order to change the point source position was attached at the OGS finder.
The software at JKT calculates the position of the laser spot and sends back to OGS the coordinates to move the motors accordingly.
In the figures 3.17 and 3.18 two examples of non corrected and corrected conditions in terms of short time position of the found centroid used for the correction and calculated by the control software.

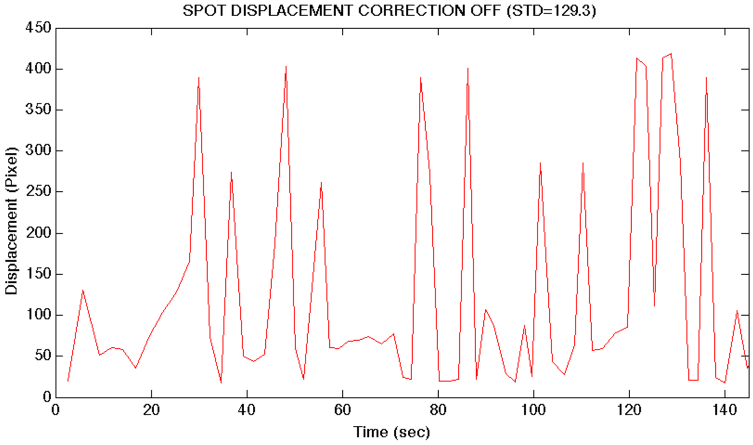

Figure 3.17: Centroid displacement with respect to the desired position with correction off. STD=129.3. Scale: $1m = 50 Pixels$

Notice that the non corrected samples span 150 seconds whereas the corrected samples reach 2000 seconds. This discrepancy on acquisition time is due to the long time scale beam movements: without correction, after a while the beam is completely lost due to wandering. This effect cannot

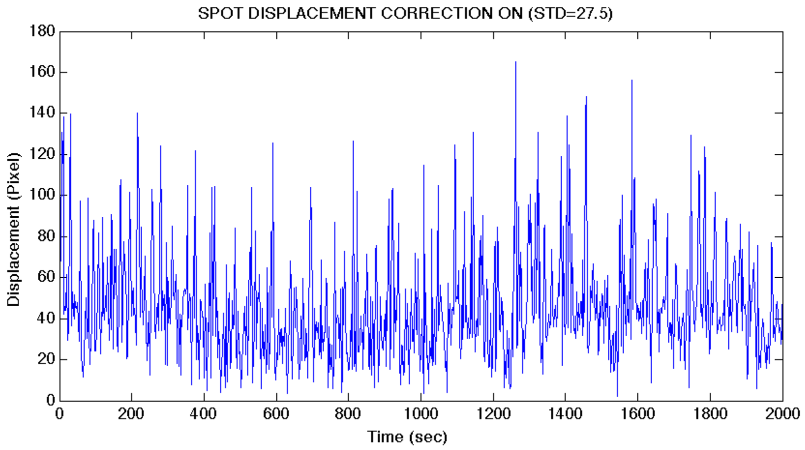

Figure 3.18: Centroid displacement with respect to the desired position with correction on. STD=27.5. Scale: $1m = 50Pixels$

be followed calculating the centroid because the spot goes out of the JKT dome and cannot be seen by the camera.
The time needed for the beam to go completely away from the JKT dome varies even during the same night from 30 second to a few of minutes. When we measured the effect with the power meter as one can see (Fig. 3.19 and 3.20) the spot was completely lost in about 2 minutes.

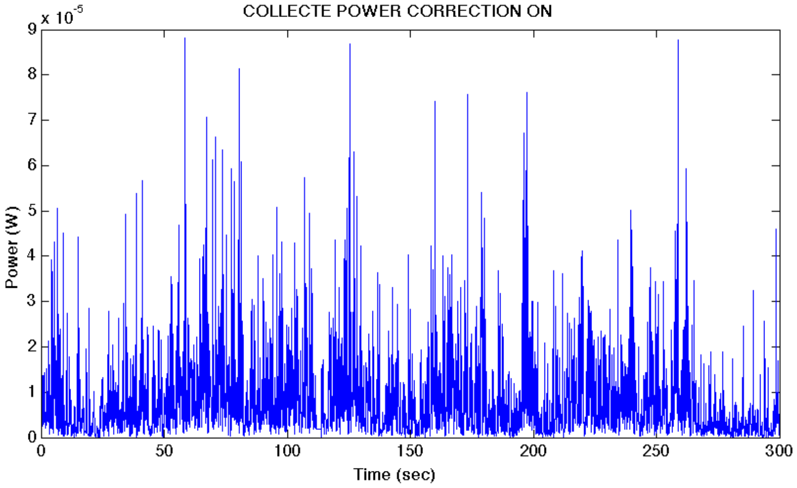

Figure 3.19: Irradiance with active stabilization.

Trying to understand the link model and the causes of beam wandering we correlated the error signal with the wind direction during the first night. In one night the wind was blowing from about 300° both at JKT and OGS at a mean speed of about $30km/h$ whereas the line of sight between the two telescopes is about at 290° so there was indeed a wind component blowing from JKT to OGS and one weaker component blowing from right to left following the transmission direction. The situation is depicted in Figure 3.21.

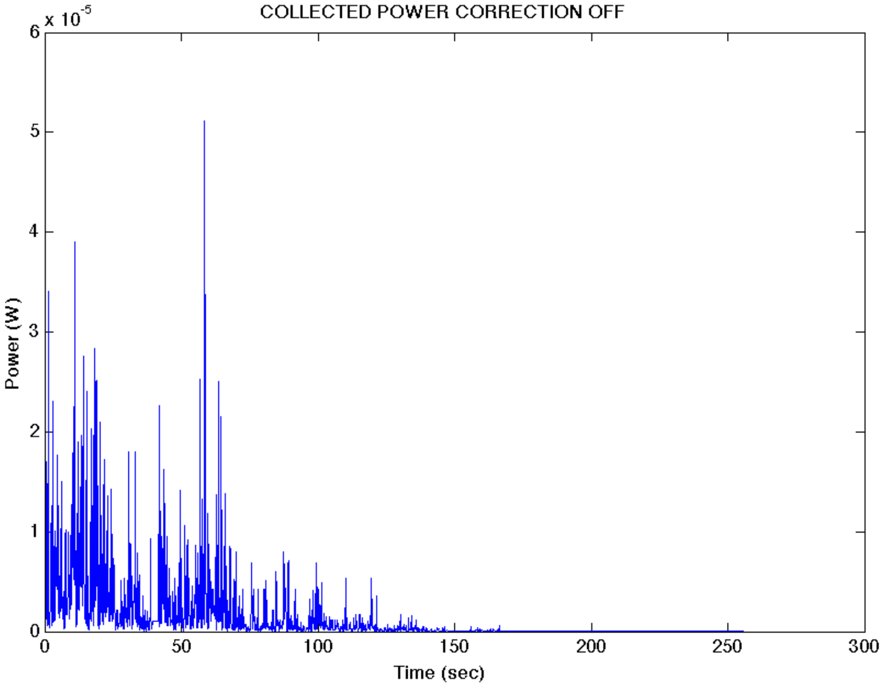

Figure 3.20: Irradiance without active stabilization.

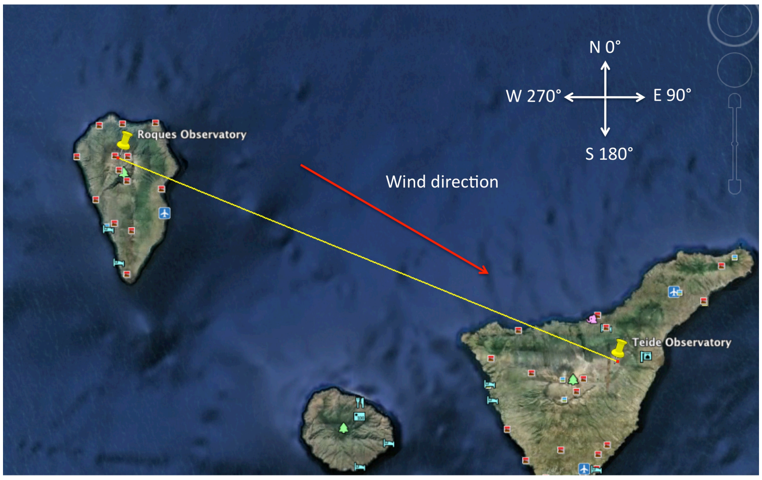

Figure 3.21: Wind direction (about 300°) during the first night.

If one looks at the correction data it is clearly present a predominant movement of the spot, here is reported one case (see Fig. 3.22)of 149° but other measurements during the same night had angles of 153°, 154° and 150°. This angles refers to the position of the spot on the JKT dome with respect to the center (black cross on the figures) and is calculated anti-clock-wisely.

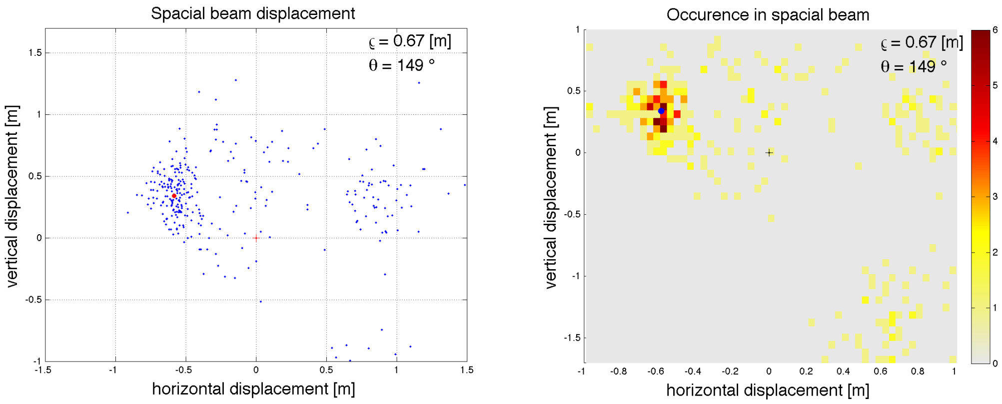

Figure 3.22: Samples and histogram of predominant correction angle. Data refers to centroid displacements at JKT.

Analysis of beam size and scintillation at the receiver

The analysis of the spatial characteristics of the beam has been done analysing the various video clips recorded. Although the spot was clearly visible, its dimensions and characteristics changed in the various nights. In figure 3.23 a snapshot of the spot of the green laser during two different nights is shown. The observations were made from a location that minimized parallax, in such a way that the curved dome is not significantly influencing the extraction of the error function or the spot distribution.

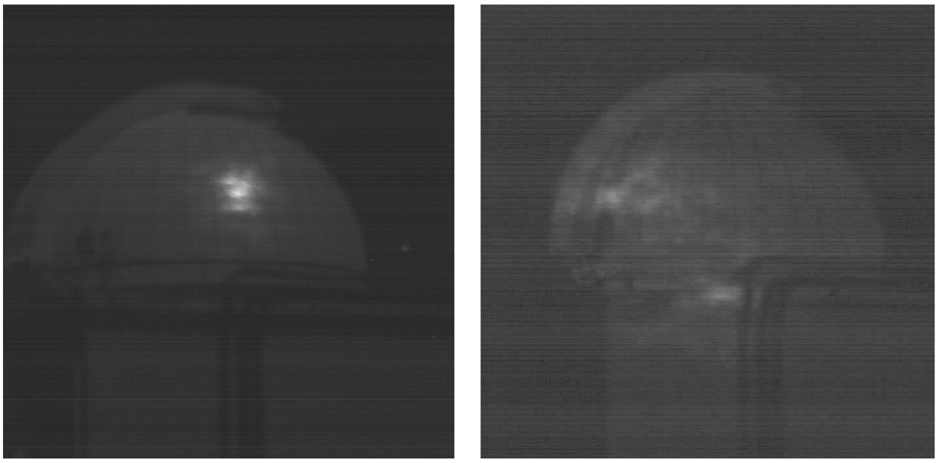

Figure 3.23: Left: spot of the green laser sent from Tenerife in the dome of OGS during the first night. Right: spot of the green laser sent from Tenerife in the dome of OGS during the second night.

We did some measurements combining different laser sources to study the effect on beam scintillation:

- a 1st $150mW$ Green Laser (named Green A)
- a 2nd $150mW$ Green Laser (named Green B)
- a 3rd $40mW$ Red Laser (named Red)

The following table resumes the analysis on the movies that have been carried out manually and with a fully automated software for comparison.

Date	Laser	Auto D.	Man. D.	Min. Blob	S. SI	T. SI
1st Night	Green A	$2.39m$	$2.02m$	$12cm$	1.57	3.67
2nd Night	Green A	$5.08m$	$4.28m$	$17cm$	0.45	2.83
2nd Night	Green B	$5.36m$	$4.16m$	too weak	0.40	n.m.
2nd Night	Green A+B	$4.59m$	$5.52m$	$15cm$	0.67	n.m.
2nd Night	Red	$5.17m$	$4.52m$	$18cm$	0.45	n.m.
2nd Night	Red + Green A	$5.09m$	$4.04m$	$29cm$	0.47	n.m.
2nd Night	Red + Green B	$4.97m$	$4.92m$	$35cm$	0.55	n.m.
2nd Night	Red + Green A+B	$4.99m$	$5.1m$	$32cm$	0.58	n.m.

Table 3.4: Parameters of the beam extracted from the movies. The first measurement is the only taken in the first night, all the other have been taken in the second night. Auto D. = Automatic Diameter, Man. D. = Manual Diameter, Min. Blob. = minimum blob size, S. SI = Spatial Scintillation Index, T. SI = Temporal Scintillation, n.m = not measured. Index.

Data analysis

The algorithm for the *automatic determination of the diameter* takes the image and threshold it after having applied a noise reduction filter. The value of the threshold has been retrieved with a series of calibrations. The diameter is then obtained as the value of the $1/e^2$ value inside a box centered on the centroid of the thresholded image. The size of this box has been also calibrated. Box size and threshold value are the same for all the calculations.
The *manual diameter* is instead calculated by averaging the measurement taken by the operator (who did not know the values of the automatic measurements) on 5 frames opportunely distributed throughout the video clips.
Also the *minimum blob* value is determined in this way and refers to the size of the smallest structure clearly distinguishable on the various frames.
The *spatial scintillation index* is calculated as $< I^2 > / < I >^2 -1$ where I is the pixel-wise intensity.
The *temporal scintillation index* is calculated as $< I^2 > / < I >^2 -1$ where I is the instantaneous collected intensity. The latter has been calculated only for one measurement each night. It is interesting to notice that the first night, when the diameter was smaller, the spatial scintillation index was much higher and this is confirmed (of course with the reserve of hand taken measurement) by the size of the smaller blob.

Measurement of spatial features of the beam

The best probability distribution which fits the data is clearly a log-normal function, as one may expect from previous findings on atmospheric propagation (Fig. 3.24).

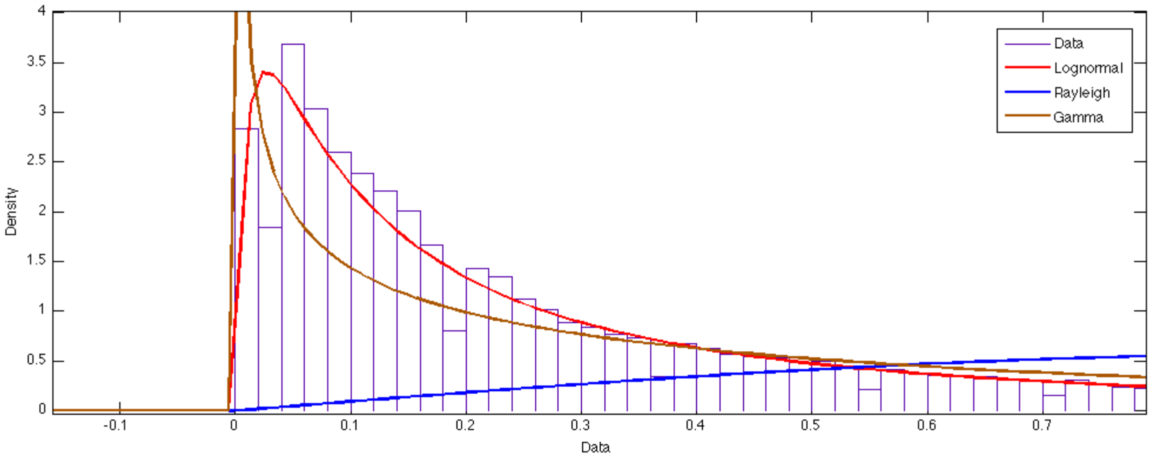

Figure 3.24: Various fits of the statistic of the data collected in the first night. The log-normal distribution is the best fit.

We estimated the behaviour of the transmission coefficient at single photon level by using the approach described by Hughes[67]. The probability $p(n,T)$ of counting n photons in a time interval T is given by the Mandel formula

$$p(n,T) = \langle \frac{\xi^n}{n!} X^n(t,T) e^{-\xi X(t,T)} \rangle \tag{3.1}$$

where ξ characterize the detection efficiency and, considering $I(t')$ the intensity at time t',

$$X(t,T) = \int_t^{t+T} dt' I(t'). \tag{3.2}$$

Under the approximation that $X(t,T)$ is independent of the starting time of successive intervals we obtain

$$p(n,T) = \frac{q^n}{n!} e^{-q}, \qquad q = \xi \int_t^{t+T} dt' I(t') \tag{3.3}$$

where q represents the mean number of photons counted in an interval T. In this case hence the photon statistic depends on the modulation of the mean photon caused by the propagation $P(q)$:

$$p(n) = \int_0^\infty dq \frac{q^n}{n!} e^{-q} P(q) \tag{3.4}$$

where the dependence on T is implicit.

Using this approach we considered $P(q)$ the statistic derived from our data considering a $T = 20ns$ and a poissonian transmission statistic with a mean value of 1 photon per time bin. We derived then the photons statistic for a sample run during the first and the second night. $P(q)$ is considered as the number of photon per time bin received i.e.the losses of the channels that is indeed a time variable process. In this calculation background noise and detector non idealities such as dead time have not taken into consideration. Under this hypothesis the $p(n)$ for the first and second night are reported in Fig. 3.25.

These probability give a mean photon detection rate lower than a photon per second. We will see in sec. 3.3.2 how these values become when the system is scaled to an OGS like telescope instead

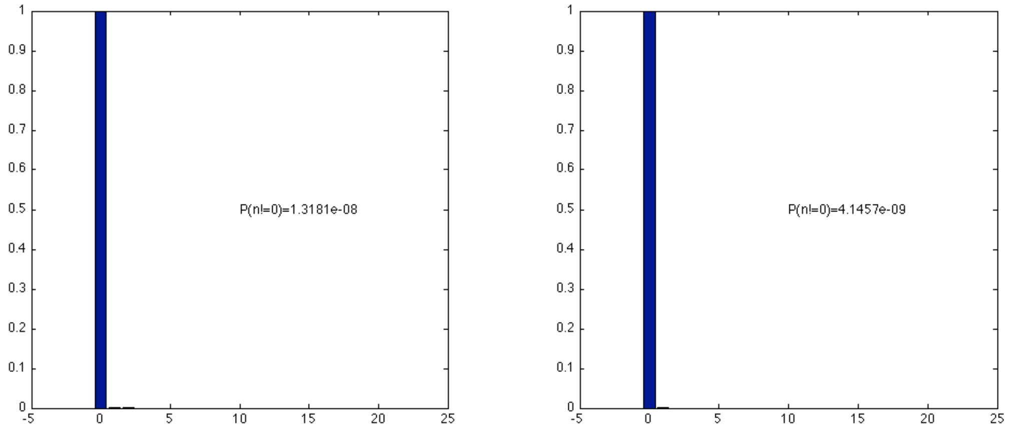

Figure 3.25: Probability of photon detection estimated from the density function of losses in the channel during the first nigh (left) and second night (right). $P(n! = 0)$ is the probability of finding at least one photon in the time bin.

of a $20cm$ receiving aperture.
A last comment on the statistic of the data collected concerns the hypothesis made by Semenov and Vogel in their work [77] "Entanglement transfer through the turbulent atmosphere" where they use a model in which the fluctuating atmospheric efficiency is log normally distributed with mean atmospheric losses θ and variance σ. He then states that the model used can only be applied if $\sigma << \theta$. This is not true in our set of data where the mean and variance of the logarithmic intensity are inversely related (respectively 0.6 and 0.4).

Separation of two laser beams

In figure 3.16 a snapshot of the transmission of two out of axis green beams is reported.
The two beams where clearly visible with a diameter of about 4 meters and a separation of about 7 meters. From the Fig. 3.16 it is possible to see how the beams moved in a similar way with a standard deviation of $5.2\mu rad$ concerning angle and of 37.9 pixels ($75cm$) on a mean distance of $770cm$.
It seems that at this separation of about $50\mu rad$ ($12arcsec$) the two beams are correlated at least in a common mode that involves the wander of both beams. This should be true even for higher order spatial fluctuations if the separation angle is less than the isoplanatic angle for this situation. The isoplanatic angle θ_0 is the angle that defines an equal behaviour of the turbulent atmosphere and depends on atmosphere strength, path length, angle of observation and lambda. A formulation for vertical propagation can be written as follows:

$$\theta_0 = [2.914k^2(sec\xi)^{8/3} \int_h dhC_n^2(h)h^{5/3}]^{-3/5} \tag{3.5}$$

The angle θ_0 decrease as the spatial mode increase as been already noticed[26], it values can span from 1.5 to $3.5arcsec.$[49] but if one consider only tilt this value can be of also more than $20arcsec^6$.
Our results show a strong correlation in the spot movement that means that the separation angle

---

[6] Data from the TNG site[4]

is less than the isoplanatic tilt angle. Regarding the higher spatial mode correlation it is hard to state how much the beams are correlated, for sure there is a correlation as one can see from sample images in Fig. 3.26.

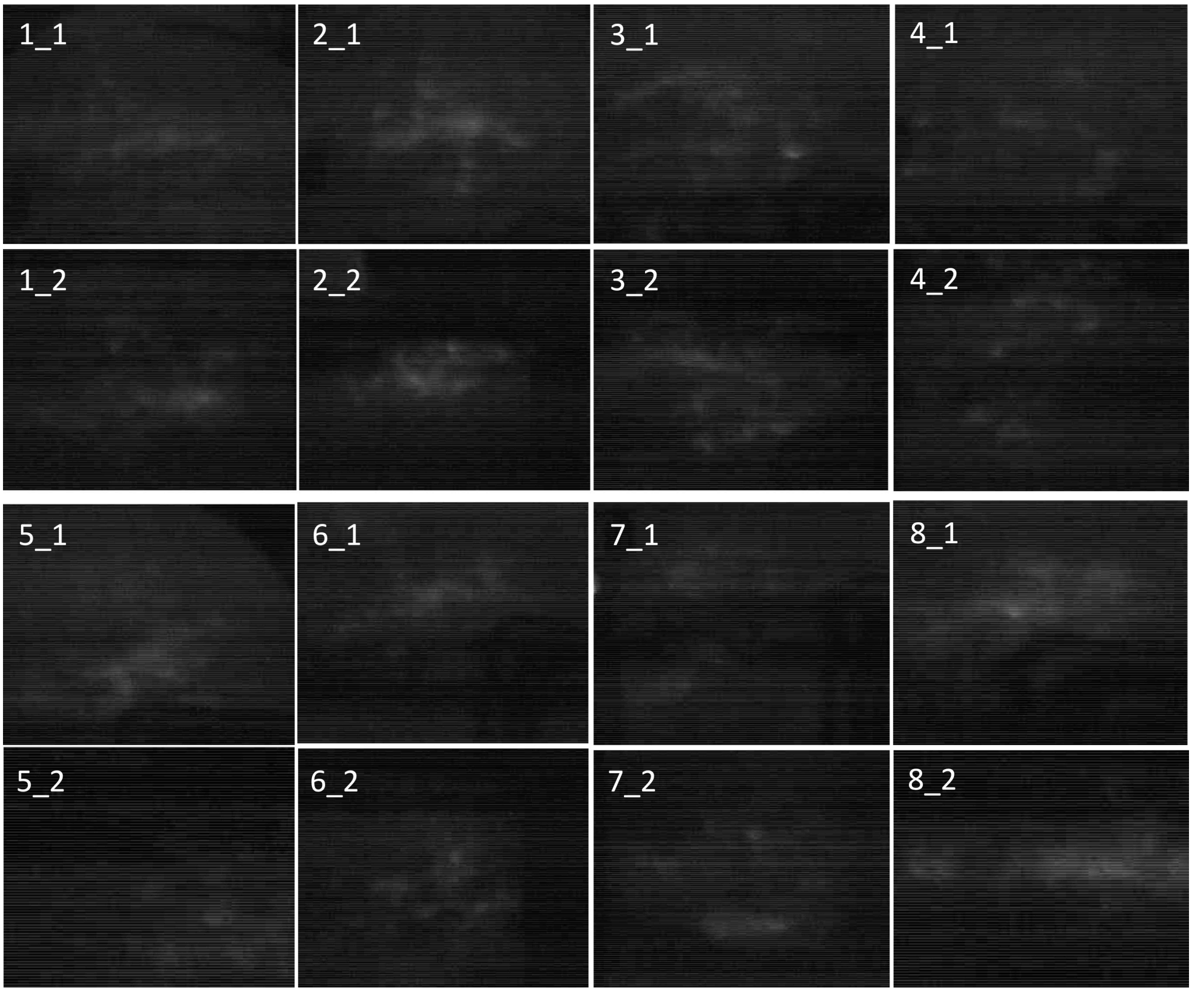

Figure 3.26: Some image samples of the two beams during two beams transmission. They are correlated in position and at least on the first few spatial modes.

From our analysis it looks like in this particular case of $144km$ transmission the two spots, even if separated by an angle that is grater than the commonly accepted isoplanatic angle for high spatial order fluctuation show a not negligible correlation both in wandering and shape. The application of this method and the technological challenges are discussed later on in sec 3.3.2.

Power Measurement of the beam

We calculated the attenuation coefficient during the first night when we took a series of measurements with the power meter at different apertures with one of the green laser from OGS that had a outgoing power of about $100mW$ considering the setup and telescope losses. We also did the calculation of the theoretical scale factor when moving to an OGS like receiving telescope, obstruction

included. Since we were collecting power with a Fresnel lens that has poor imaging performances we considered for link budget the smallest aperture of $10cm$ obtained vignetting the lens. In this case the mean collected power has been $< I >= 4.5\ \mu W$ corresponding to an attenuation of $43.5dB$. The attenuation value change if we consider the same transmitter and a different receiver. In particular for an OGS like telescope the attenuation become $24.0dB$ considering $1m$ primary mirror and a $30cm$ obstruction.
If we calculate the single photon probability distribution using the method and assumptions described in section 3.3.2 we found a probability of receiving at least one photon of $P(n \neq 0) = 1.2 \times 10^{-6}$.

Fried Coherence length and size of Transmitting Telescope

Remembering that the transmitter was the Zeiss refractive telescope that is the OGS finder telescope, which is based on a doublet of $200mm$ diameter and f/15 aperture, acting as a laser beam expander for a $100mW$ $532nm$ CW laser the profile of the outcoming beam is shown in the following Fig. 3.27
The beam expansion has been made such to avoid the clipping of the beam, according to the "$D = \pi\omega$" criterion [79]. Therefore, the beam waist is estimated as $60mm$, with flat front at the telescope exit. The observations done in this two experimental runs are suitable for the extraction of Fried parameter from the spot analysis. Indeed, the spot on the wall of JKT was observed and the minimum FW1e2 after an integration of about 1 s was estimated as 2 m, in both May and September shifts. On September, the weather conditions were such that with identical transmitter conditions, the minimum diameter in the second night was significantly larger, FW1e2 of 4.5 m, due to poorer seeing conditions.

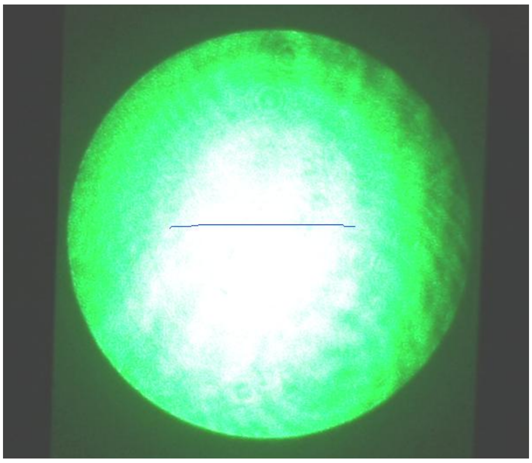

Figure 3.27: Spot after the OGS finder telescope. To scale the beam size, the screen is a A4 paper.

The model for the beam propagation is derived by the early work of Fante [45] then recalled in the analysis of Dios et al. [40] and Tomaello et al.[83]
The value of the Fried coherence parameter r_0 can be derived from the long term spot radius w_{LT} as derived from:

$$w_{LT}^2 = w_0^2(1 + \frac{L^2}{Z_0^2}) + 2(\frac{4L}{k_0 r_0})^2 \tag{3.6}$$

where w_0=60 mm is the beam waist, $Z_0 = \frac{\pi w_0^2}{\lambda}$ is the Rayleigh range, $L = 144km$ is the link length and $k_0 = \frac{2\pi}{\lambda}$.

From graphical interpolation of the curve from Eq. 3.6 (see Fig. 3.28) for the values of the two beam widths, the best value for r_0 was found to $80mm$, while for the second night, it is of $33mm$. The corresponding seeing conditions in the two cases are of $6.5\mu rad$ ($1.3arcsec$) and $16\mu rad$ ($3.2arcsec$), which are reasonable values for the site conditions.
From this analysis, for the best conditions of the site, it is possible to observe that the final spot radius curve, in the Figure below, is near to the minimum, which occur to about $w_0 = 140mm$. This latter waist corresponds to an optics of over $400mm$ of diameter, which is very hardly feasible from technical point of view.

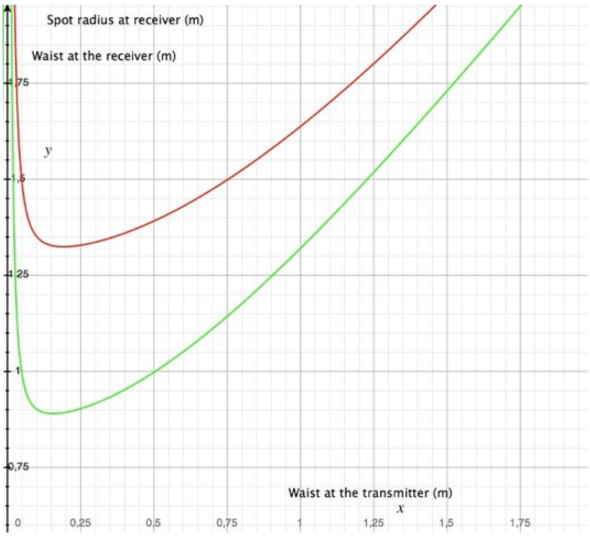

Figure 3.28: Model of the spot from the OGS finder to JKT wall in the best weather conditions, $r_0 = 80mm$. In green $532nm$, in red $800nm$.

Conclusions and consideration gained from the second experimental session

The main results of the champaign are the following:

1. *Correction system:* with the implemented beam correction position system,the spot remains stable. This scheme have also the advantage that the guide system of the OGS is not required. In order to address the issue of the beam wandering, we note that it is significant but can be stabilized by mean of a secondary beams: one quantum signal beam and one bright reference beam for stabilization with a small parallax. With reference to the sketch in Fig. 3.29, the two beams shall be overlapped by means of an optical element before the beam steering element, namely a lens. This scheme requires a dedicated telescope holder in the JKT terrace. It does not require OGS active tracking, provided that its FOV is suitably large.

2. *Beam statistic:* the statistic of the data sampled with our apertures (more than 10 times smaller that the beam size) showed a log normal distribution. The data collected do not meet the Semenov-Vogel hypothesis on the relation between the mean and variance of the log intensity fluctuation.

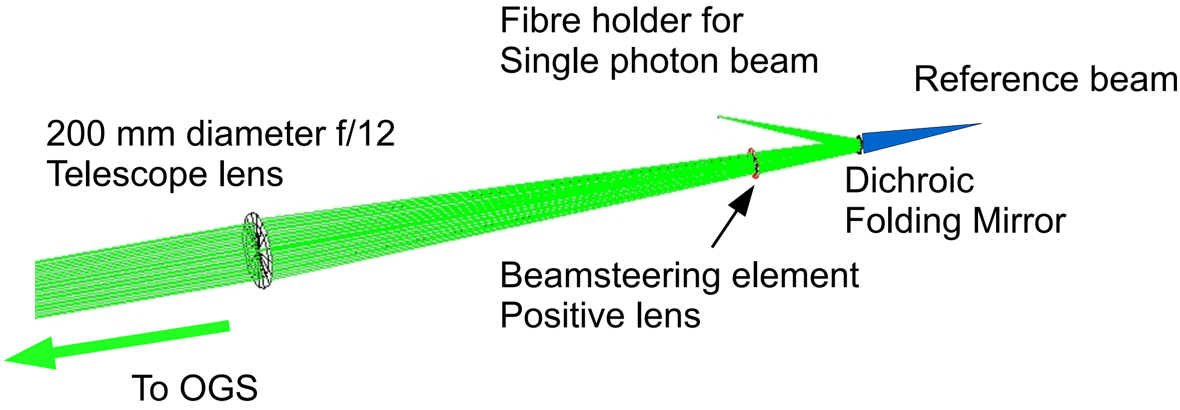

Figure 3.29: Layout of the quantum channel. The beacon laser will be inserted through the folding mirror, at the far right. The beam steering lens is in red

3. *Link budget:* resumed in section 3.3.2, the link budget showed that with a transmitter with $20cm$ aperture and with a receiver with an aperture as that of the OGS telescope, the attenuation is on the order of $25dB$. The measure has been made OGS to JKT. This represent a significant increase of the single photon detection probability. The caldera may introduce an asymmetry that we had not the possibility to measure due to bad weather. The atmospheric conditions in the case of clear nights are suitable to exploit a transmitter diameter of $200mm$, like that we effectively used, or larger up to about the double $\Longrightarrow$ REALIZATION OF A TRANSMITTER WITH A $200mm$ DIAMETER AND ASTRONOMICAL OPTICAL QUALITY.

4. *Two spot analysis:* it showed that it is possible to transmit two beams - at the same wavelength maintaining a small angle between them which is kept almost as constant. Provided that this is also the case of two near wavelengths, this fact allows the application of our beam wander correction system: one beam can be used for pointing while the other as signal. Indeed, this should be done with different wavelengths for the signal and reference beams in order to avoid unwanted background noise effects.

5. *Aperture size:* the value of Fried coherence parameter resulting from the measurements is of the order of $80mm$. A beam propagation analysis based on Fante approach is shown in the Fig. 3.28, in which the two colors are for $800nm$ and $532nm$ case. The minimum of the waist at the receiver corresponds to beam diameter at the transmitter side of the order $400mm$, which are hardly feasible using a refractor telescope. This point tells us that we should implement the bigger possible feasible optics up to that range.

6. *Adaptive Optics:* the use of adaptive optics is not useful when using as feedback signal a small portion of the spot at the receiver. Only the real-time knowledge of an extended portion of the wavefront may enable the implementation of the phase conjugation procedure.

3.3.3 (3) May 2011

The results obtained with the OGS finder leads us to develop a similar optical system to be used at La Palma as transmitter: a telescope with a primary lens of $23cm$ *of diameter, since the final set* *up the receiver will be at La Palma*

Optical setup

The telescope structures is formed by three aluminium flanges aligned by four pipes: a first flange is the lens holder, a second flange in which the optical breadboard at the focal plane is placed and a third flange for structure stabilization. The whole telescope is secured to two additional breadboards that guarantee the movement. The orientation is achieved with two screws at the back flange. A picture of the setup is reported in figure 3.30.

Figure 3.30: Picture of setup at the transmitter.

The optical setup is reported in figure 3.31 where in particular it is possible to see the focal plane of the transmitting telescope. Two sources were used: a green $130mW$ laser and a pigtailed $50mW$ red laser. The latter is collimated with a $8mm$ aspheric lens to reach a dimension of about $2mm$ comparable with the green free space laser. The red and green needs separated lens to be focalized since the transmitting telescope is not achromatic. We put on a motorized stage then two aspheric lenses with the same focal length of $18.4mm$, in this way we compensated the difference in focal between the two wavelengths and could move the source point in the same manner inducing the same movement on the two beams. The collimating and focusing stages have been verified with Zemax. The green and the red beams are then put together with a dichroic window. In normal conditions the beams on the lens should have gaussian distribution and be of the order of $20cm$ at $1/e^2$.

Lens Design

The lens, manufactured by a Venetian optician,is a plano-convex single lens. The optics is then affected by chromatic aberration. The following focal lengths for the wavelength of interests are reported in table 3.5 as well as the distance of the focal point that minimizes the spot after $144km$.

The lens is depicted in figure 3.32 whereas surface characteristic of the lens surface and distortions are reported in the following pages, figures 3.33 and 3.34.

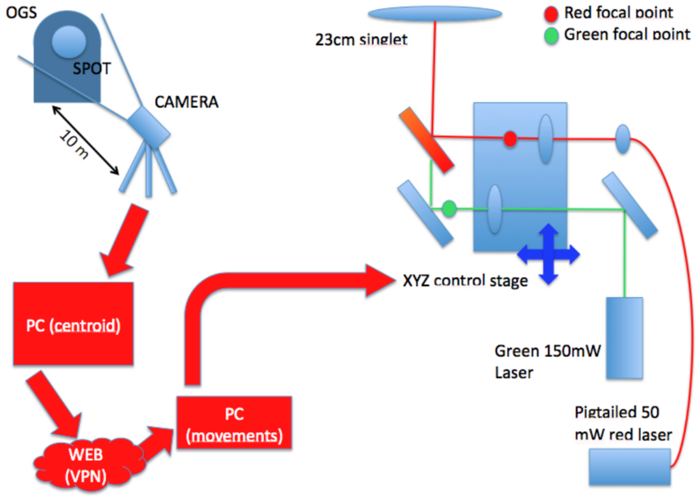

Figure 3.31: Setup at the transmitter and receiver.

Wavelength	Direct Focus	Focus for best $144km$ spot
$532nm$	$2164.22mm$	$2164.25mm$
$632nm$	$2182.61mm$	$2182.64mm$
$819nm$	$2202.07mm$	$2202.11mm$

Table 3.5: Focal lengths at the wavelengths of interests for the $23cm$ singlet.

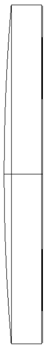

Figure 3.32: The $23cm$ singlet.

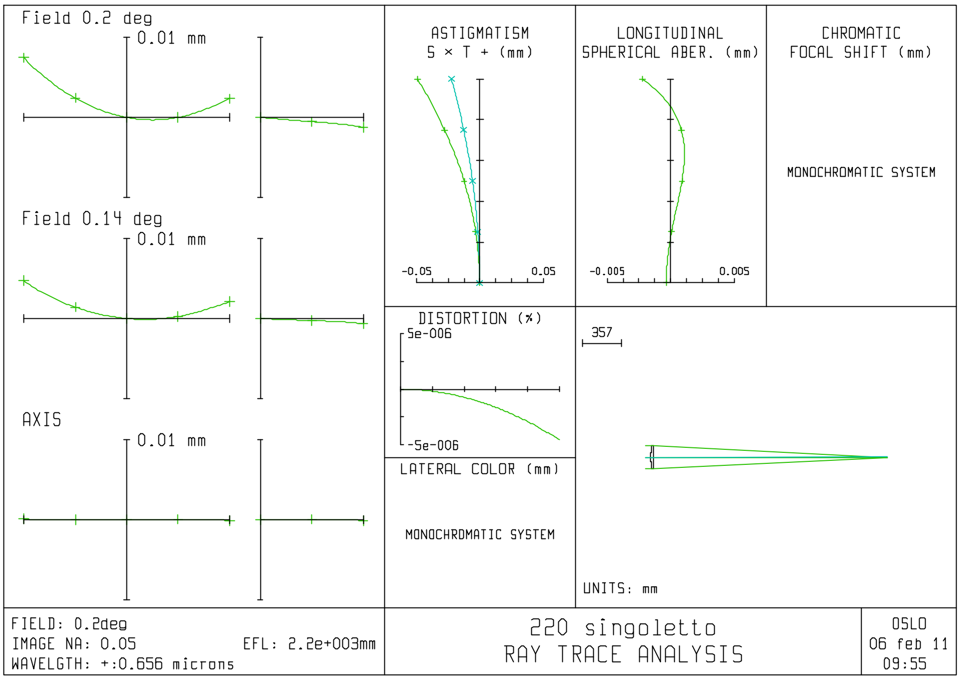

Figure 3.33: Ray tracing of the 23cm singlet.

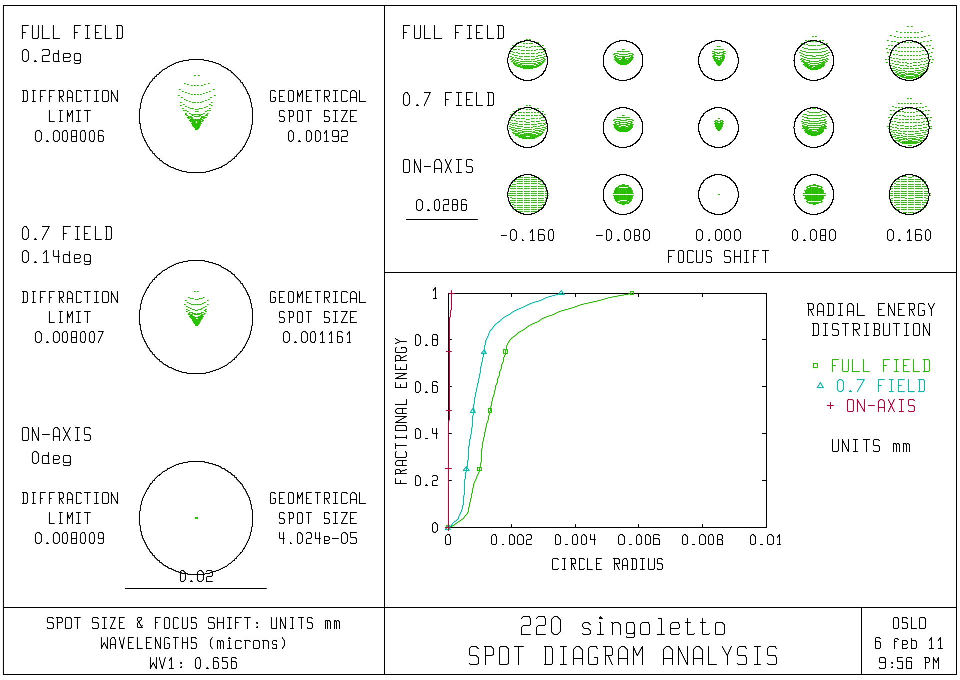

Figure 3.34: Spot diagram of the 23cm singlet.

Guiding

The pointing and stabilization system is the same used in September 2010: the problem of beam stabilization is solved acquiring the entire spot displayed on the OGS building with a CCD camera (as soon the dimensions are $< 10m$). A computer elaborates the spot image and sends back the error signal to the correction setup at La Palma where a motorized lens (the secondary of the telescope) is moved to change the beam wavefront propagation direction and then keep it stable at the receiver.

Measurements and experimental results

Spot size

In figures 3.35 and 3.36 the green laser spots obtained at Tenerife with the new transmitting telescope are reported . Looking at the two references, the dome aperture and the window it can be seen that the spot is about 3 m in diameter. This let us say that the link is symmetric when the conditions are not critical since last time we could get a 2 meter spot from OGS to JKT sending the beam out of the OGS finder, a $20cm$ telescope similar to the one we are using.

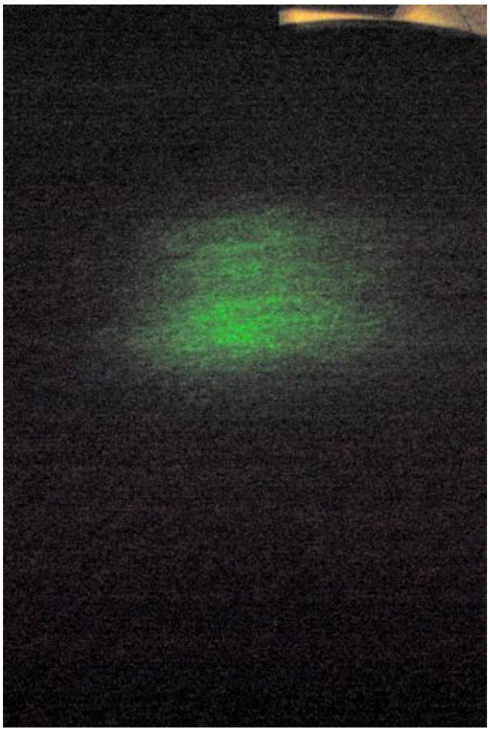

Figure 3.35: Spot at the OGS dome. The size is about 3 m.

The spot profile extracted from fig.3.36 is depicted in fig. 3.37 showing a shape measuring less that 3 meter in the vertical section.

Attenuation

We did a comparative measurement of attenuation for our setup and Vienna IQOQI-setup. Unfortunately we could not perform a measurement with the two system (Padova and Vienna) during

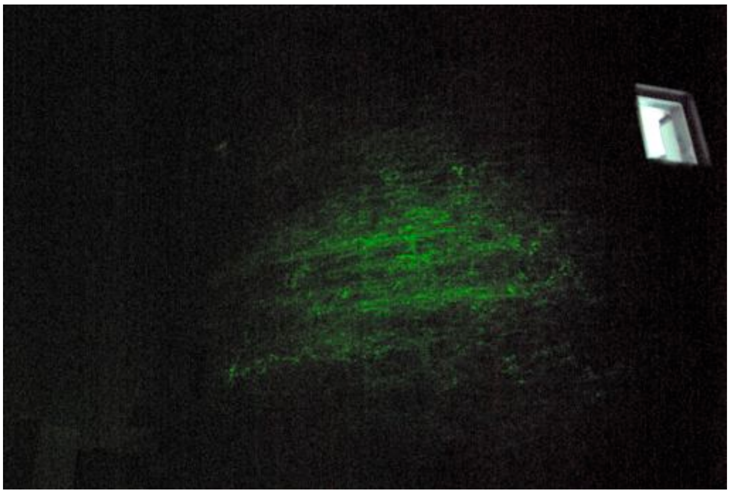

Figure 3.36: Spot at the OGS dome. The size is about 3 m.

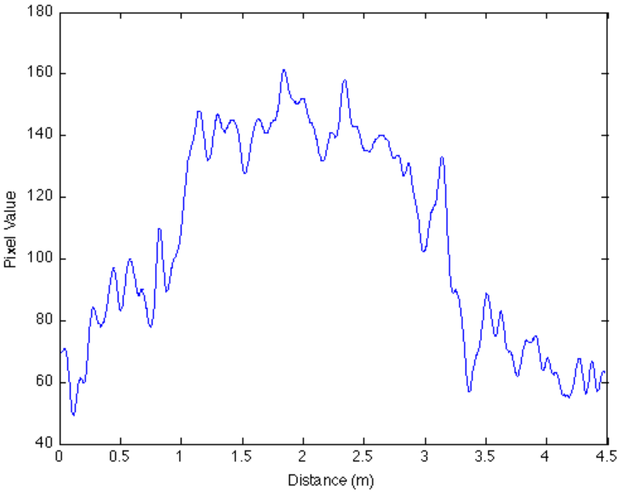

Figure 3.37: Spot profile at the OGS dome. The size is about 3 m.

the same night. We have a measure from Vienna during the night between the 17th and the 18th and two from Padova during the nigh between the 19th and 20th. These two night has been quite similar in terms of seeing and other atmosphere characteristics that is why we think that the results are still worth of comparison. To be precise is was a little more windy at La Palma during the Padova measurement ($40km/h$ vs. $32km/h$) (In tables 3.6 and 3.7 the meteo data for the two considered nights are reported).

Day	Temp	Humidity	Wind Speed	Wind Dir
17/18	10.3°	3%	$18.5km/h$	270°
19/20	6°	35%	$18km/h$	305°

Table 3.6: Weather in Tenerife.

Day	Temp	Humidity	Wind Speed	Wind Dir	Seeing	r0
17/18	$6,1°$	22%	$32km/h$	315°	$0.85arcsec^7$	$10.7cm$
19/20	7°	30%	$40km/h$	170°	$0.9arcsec^8$	$10.9cm$

Table 3.7: Weather in La Palma

The total transmitter attenuation, considering the used lenses and the coating mismatch (optimized for $810nm$), was about 37.2%. The output power laser in the Vienna case was $32mW$ whereas in our case was $63mW$. Having taken this into considerations we compared a measurement of 5 minutes with the Vienna setup with a 10 minute measurement with the Padova setup. The results are reported in figure 3.38. The mean value are respectively $-40.2dB$ for the Vienna setup and $-37.4dB$ for Padova setup. In fig.3.39 another shorter measurement of about 90 seconds of our setup with mean value attenuation of $-34.98dB$.

Conclusions and consideration gained from the third experimental session

The main results of the champaign are the following:

- *Spot size and link symmetry:* the spot size at the OGS that we could get was of the size of 3 meter. This shows that the link can be considered symmetric if compared with the results obtained in the second session. We noticed that there is a strong correlation between the wind speed at the receiver side and the size of the spot since the first two nights when it was very windy the best spot was bigger than the OGS itself. This shows also that a bigger lens leads to a smaller spot in good conditions. When the conditions are bad and the Fried length decreases the spot degrades as we expected. Fante [45].

- *Guiding system:* although in the second run the guiding system was tested with promising results it is clear that it will work only when the spot is small enough to guarantee a centroid measurement on the OGS dome. $\Longrightarrow$ FOR A RELIABLE AND EFFECTIVE TRANSMITTER AN AUXILIARY GUIDING SYSTEM IS NECESSARY TO REDUCE THE DEPENDENCE OF LINK PERFORMANCE WITH WEATHER CONDITIONS

- *Losses:* we measured the losses of our optics and compared them with the Vienna setup. The data, taken in two different but comparable nights in terms of weather conditions show an average gain of 3 to $5dB$ using the $23cm$ lens as transmitter without any guiding.

- *Pointing and mechanics:* A fine and rough alignment system is necessary in the final transmitter setup to make the system reliable and simplify the pointing procedure $\Longrightarrow$ A MANUAL

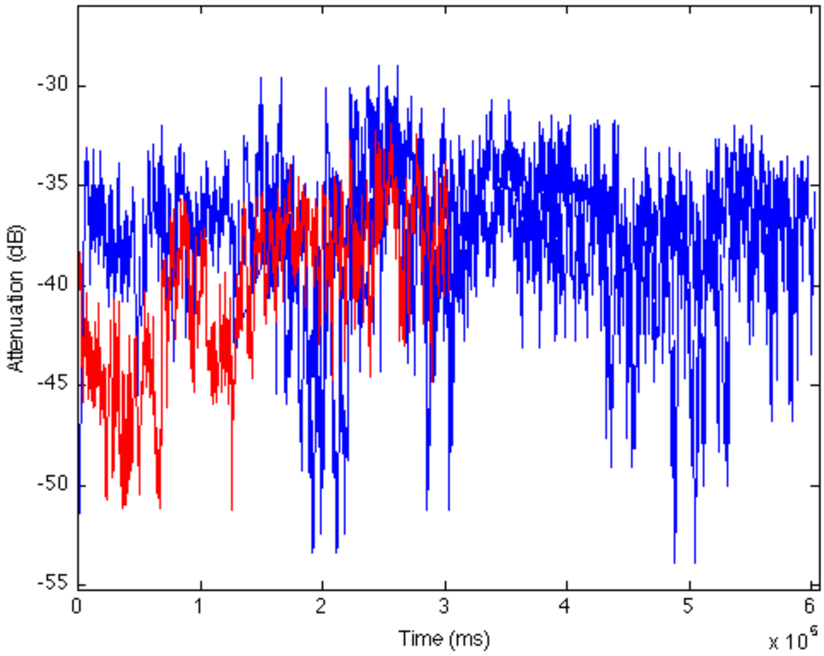

Figure 3.38: Attenuation. Red: five minutes of Vienna laser. Blue: ten minutes of Padova laser.

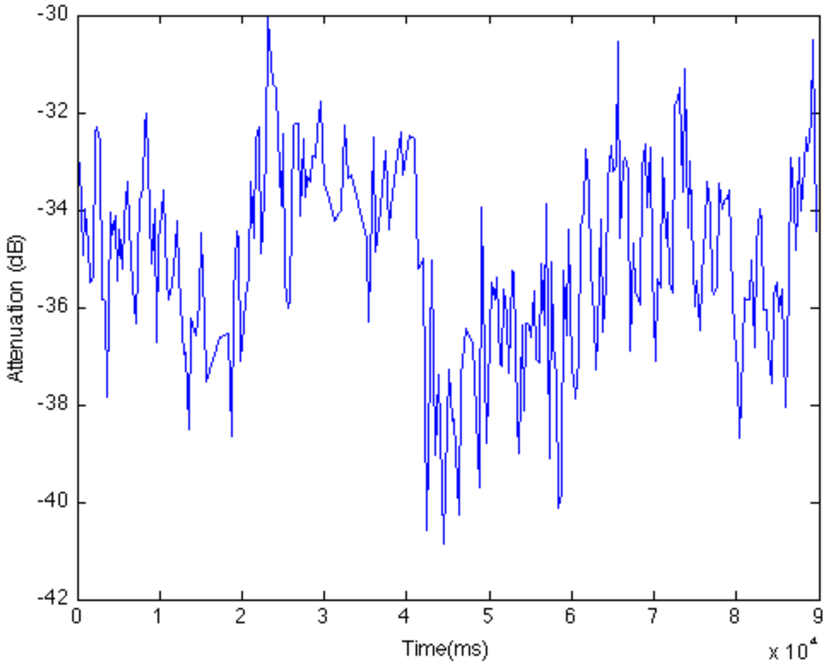

Figure 3.39: Another sample of the attenuation of the Pd system. Mean value $34.98dB$.

ROUGH POINTING STAGE FOR COARSE MOVEMENTS TO BE COUPLED WITH THE FINE MOTORIZED STAGE REMOTELY CONTROLLED THAT ACTUATES THE SECONDARY OF THE TELESCOPE

3.3.4 (4) September 2011

Optical setup

The optical setup has been modified since the last run in May 2011 in order to stabilize it although the main characteristics of the optical setup are unchanged. In order to facilitate the raw pointing a new XY stage has been added. This stage moves all the telescope that is $2.5m$ long. A picture of the setup is reported in figure 3.40.

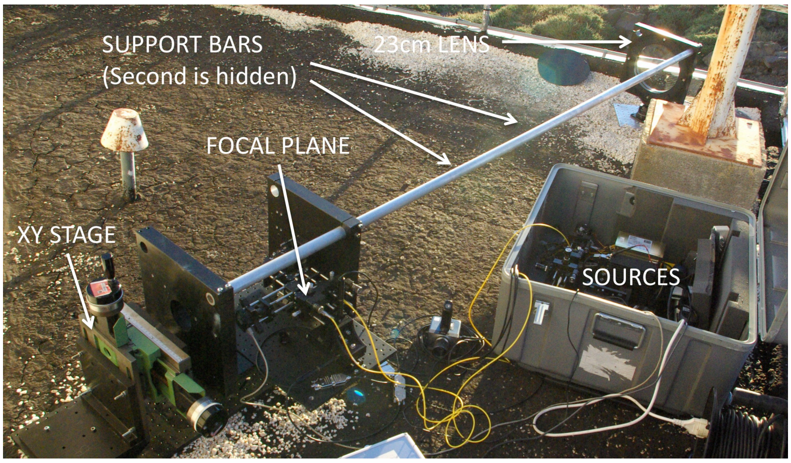

Figure 3.40: The telescope and its mounts.

All the structure is assembled by three aluminium flanges, one holds the lens, one the focal plane and the other is attached to the X-Y back stage. The lens is fixed to an articulated mount to prevent bending of the structure. A scheme of the optical setup is depicted in figure 3.41. We have two sources: one green coupled into fiber with a total output power of about $40mW$ and an infrared diode at $808nm$ coupled into fiber with a output power of about $6mW$.

The green and IR sources have been aligned so they share the output optical axis by means of a mirror and a dichroic window. In this way the green laser can be used for first alignment and switched off in a second moment when the IR needs to be operative. The raw alignment that we performed took about 1 hour, from scratch to the aligned IR. Since the singlet is chromatic the green and IR have two different focal points and this had to be corrected. The focal plane that comprises the focusing lens, the collimating lens and the fiber port for both green and IR can be moved by a fine X-Y-Z system based on stepped Thorlabs motors. In this way the beam can be slightly steered by moving the focal spot at the singlet focus. In the optical setup at the focal plane we added also a CCD for the control. The system in fact can be controlled in two ways:

1. In the first way a beacon laser is sent front the OGS (receiver) to the JKT (transmitter) and acquired with the CCD camera after passing through the same path of the outgoing IR laser. The position of the spot at the CCD are sampled about once a second and averaged for a number of frames and this data feeds a control software that calculates the movement for the fine X-Y stage in order to compensate slow drift in beam direction.

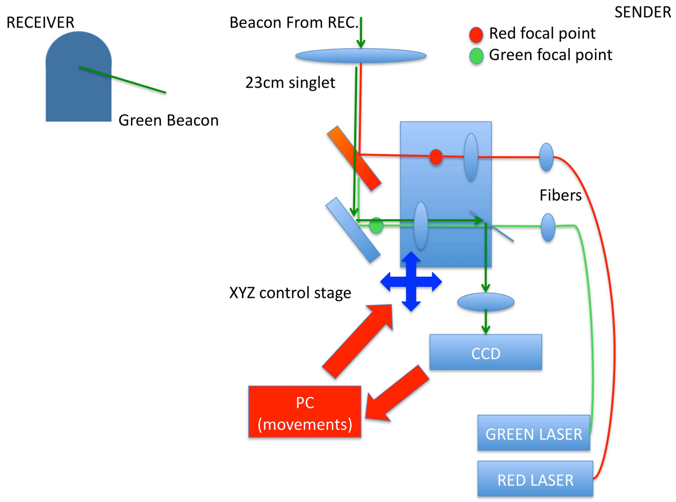

Figure 3.41: Schematic of the optical setup.

2. The other correction system is based on a CCD camera that acquires the entire spot at the OGS (provided that the spot dimensions are $< 10m$). The camera is positioned some meters away from the telescope dome. A computer at the receiver elaborates the images, calculates the position of the laser spot and sends back the error signal to the sender by means of a VPN network. The sender takes care of moving the fine XY stage accordingly. This control strategy needs a beacon that propagates in the same direction of the quantum signals.

In this campaign we only set up the system for the first control type (see section 3.3.4). The green beacon laser was sent either from the OGS finder using a $150mW$ green solid state laser, or by means of a small portable $5mW$ laser module directly pointed towards La Palma without any optics. The beacon sent through the OGS finder serves also as night tester: with that optics, that is very close to the one we build for the JKT setup, it is possible to see at La Palma the spot dimensions in order to evaluate the average link conditions based also on our experience when we used the OGS finder in other campaigns in 2010.

Spot profile at Transmitter

We measured the spot profile along two orthogonal singlet diameters during the night in order to see the mode and also the attenuation of the optics. An example of beam profile fit and reconstruction is presented in figures 3.42 and 3.43.

The data relative to the power measured at the transmitter during the various nights are reported in table 3.8.

Meteo Conditions

In table 3.9 the average meteorological data of the two sites during the observing nights are reported.

The determination of r_0 is obtained starting from the vertical seeing. First we estimate the value $r_0^{(V)}$ i.e. the freed coherence length for the vertical propagation that is given by [10]

$$r_0^{(V)} = 2.013 \times 10^5 \cdot \lambda / seeing \tag{3.7}$$

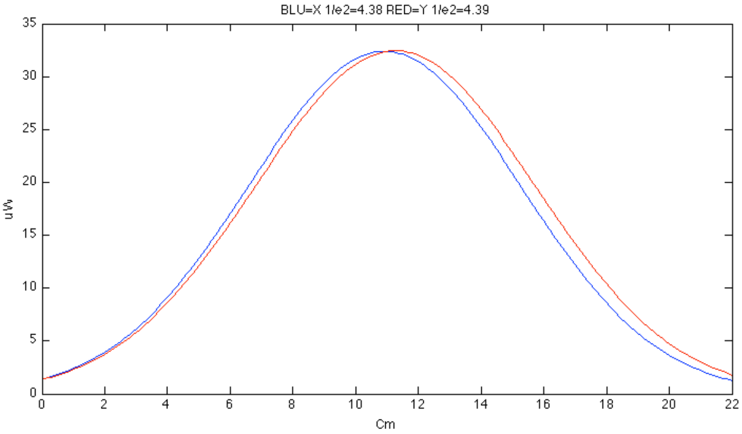

Figure 3.42: Fitting of the profile in x and y on the transmitting aperture during the 7th night. Notice how the $1/e^2$ criteria is met.

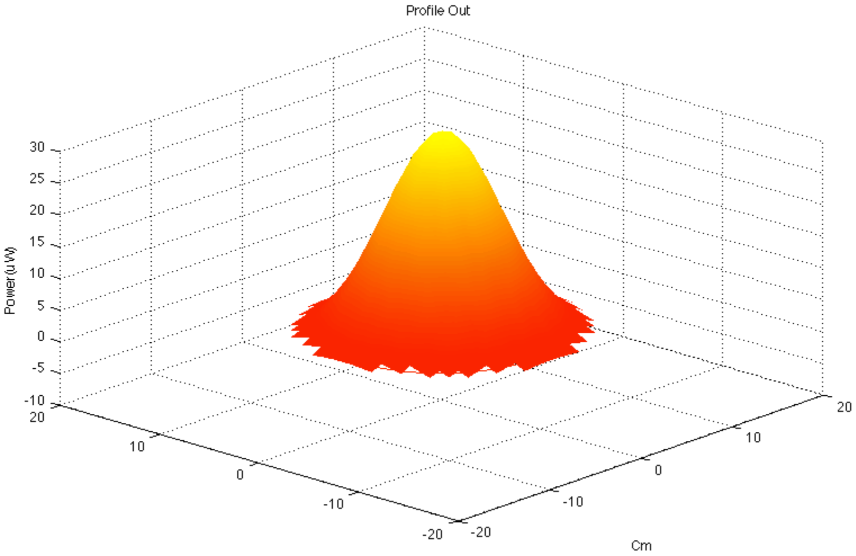

Figure 3.43: 3D profile of the outgoing beam on 7th night.

Night	Fiber Out	Lens Out	Optics Transmission
1st (17-18)	n.a.	n.a.	n.a.
2nd (18-19)	$4.5mW$	n.a.	n.a.
3rd (19-20)	$7.37mW$	$4.98mW$	0.67
4th (20-21)	$5.7mW$	$3.86mW$	0.68
5th (21-22)	$5.4mW$	$4.23mW$	0.78
6th 22-23)	n.a.(rain)	n.a.	n.a.
7th (23-24)	$5.7mW$	$3.99mW$	0.7
8th (24-25)	n.a.	n.a.	n.a.

Table 3.8: Output power measured at JKT.

Night	ws(T)	wd(T)	H(T)	ws(R)	wd(R)	H(R)	seeing(R)	r_0(R)	Cn^2(R)	C
1st	14.31	328	4	23.55	271	0.5	0.9	3.4	0.19	G
2ns	15.17	186	6.5	31.6	221	6	1.165	2.6	0.3	G
3rd	5.9	129.5	4.5	12.4	151	3	1.75	1.7*	0.59	P
4th	15.4	241.5	18.5	18.6	98.5	7.5	0.695	4.4	0.12	M
5th	13.35	155	52.5	16	96.5	52	n.a.	-	-	
6th	30.31	198	82	31.05	170	93	n.a.	-	-	
7th	7.57	193.5	21	24.95	229.5	26	0.775	3.9	0.15	M
8th	8.82	250.5	27	4.55	233	36	n.a.	-	-	

Table 3.9: Meteo Data on both sites (T=Teide, R=Roque) for all the observing nights. Wind Speed is in $[km/h]$, wind direction in degrees, humidity in percent whereas r0 in $[cm]$. The value of Cn^2 is to be intended as explained in the text multiplied by 10^{-14} for $1km$ along the path and by 10^{-16} for the others $143km$. C is the validity index for seeing based on the number of seeing data: Poor, Medium, Good. Value with * has been recalculated with video data, see text.

then we estimate two Cn^2 using the Hufnagel-Valley (H-V) model [91] , the first for the first 100m (L_{v1}) and the second for the rest of the vertical propagation (L_{v2}). This is done by resolving the system given by this equations:

$$Cn^2_{(2)} = \frac{(r_0^{(V)})^{-5/3}}{0.423(\frac{2\pi}{\lambda})^2(L_{v2} + Cn^2_{(1)} L_{v1})} \tag{3.8}$$

and the equation derived from the mean ratio of Cn^2 close to ground and far above the ground in the H-V model.

$$Cn^2_{(1)} = 100 Cn^2_{(2)} \tag{3.9}$$

At this point the value of r_0 for the horizontal propagation is easily obtained with the standard formula using the two distances $L_{h1} = 1km$ e $L_{h2} = 143km$. In this way it is better taken into consideration the fact that for some km the beam travel close enough to the ground especially in Tenerife.

$$r_0 = 0.423(2\pi/\lambda)^2(L_{h1} * Cn^2_{(1)} + L_{h2} * Cn^2_{(2)})^{-3/5} \tag{3.10}$$

This approach is a good one when the meteo conditions are acceptable in the sense that the approximation of the Cn^2 can be considered valid even for horizontal propagation using the formulas above. Moreover in the table a *validity index* in three levels is reported indicating whether the r_0 approximation is good or poor. This index takes into consideration the amount of seeing data available for the calculation. In a particular case, the 3rd night we had only one value of seeing obtained not a ING (Isaac Newton Group, meteo stations close to JKT) but at the TNG site. In that night we have recorded also a number of videos with our system that allow us to estimate directly the value of Cn^2 and r_0 from a measure of the spot size at the CCD and considering the optical setup. These values are: $Cn^2 = 3 \times 10^{-17}$ and $r_0 = 3.76cm$.

Link Budget

As already mentioned the goal of the campaign was to demonstrate the capability of the system to maintain low attenuation and high stability along the night. Although the control has been not automated (see section 3.3.4 for further details on system control) we collected data with the power meter during three days namely 3rd, 4th and 7th. We tried also to correlate the losses data with the meteo conditions and noticed that there is a fairy strong correlation with the wind speed and humidity: as expected a calm night low humidity is a better night in terms of power transfer. In the following figure the results are reported, first the dependence on the wind speed: figure 3.44, 3.45, 3.45. Following then the dependence on the humidity: figure 3.47, 3.48 and 3.49.

During the best night with the best conditions we reached and maintained an attenuation below $30dB$ for a considerable time. The other nights the attenuation was between $30dB$ and $35dB$.

Comparison With Other Runs

We would like to compare our results with two previous run, the first is the campaign of May 2011 and the second is the runs reported in the "Technical Note 5B: Experimental evaluation of proof-of-concept demonstrator" QIPS document.
Regarding the first, we could get an average value of attenuation of $37.4dB$ in the night between the 19th and 20th that we compared with the attenuation of $40.2dB$ obtained on a similar night (17th-18th). In figure 3.50 the graph of attenuation of the May run are reported. The meteo conditions of the two night are summarized in Table 3.10 and 3.11. The value of horizontal r_0 is calculated as in section 3.3.4.

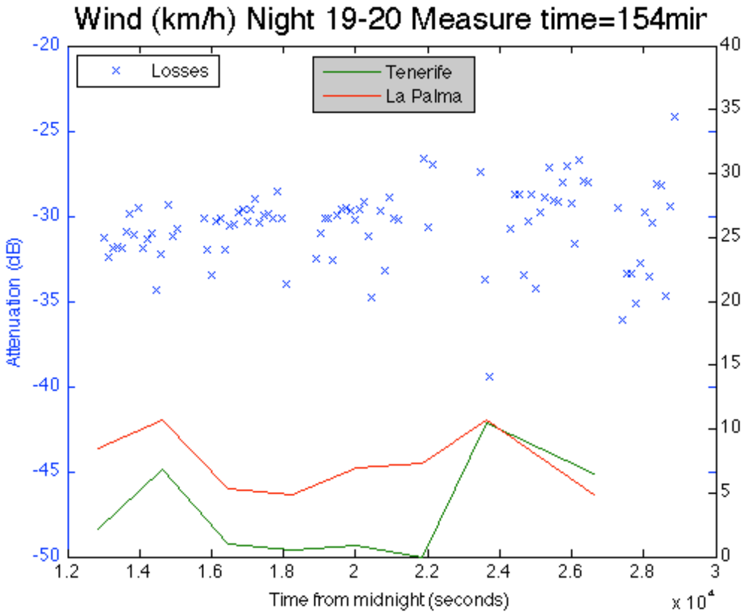

Figure 3.44: Attenuation and wind speed dependence. Each sample is a 2 minutes average.

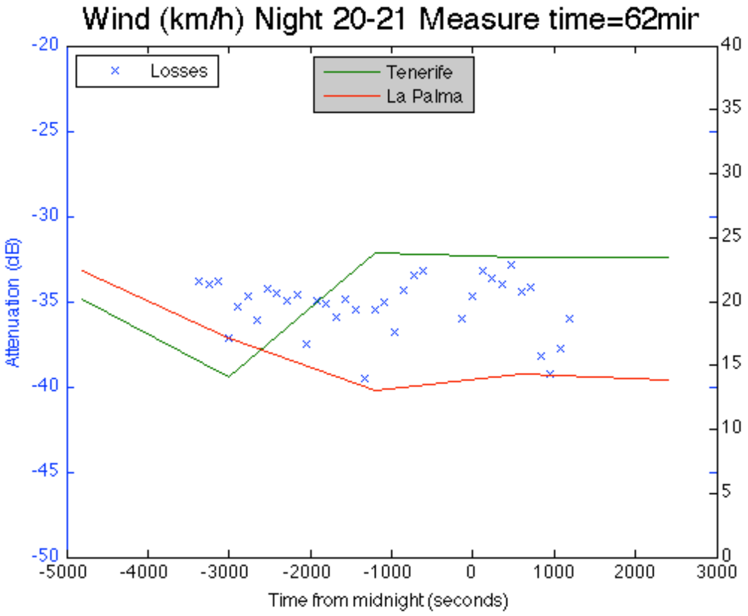

Figure 3.45: Attenuation and wind speed dependence. Each sample is a 2 minutes average.

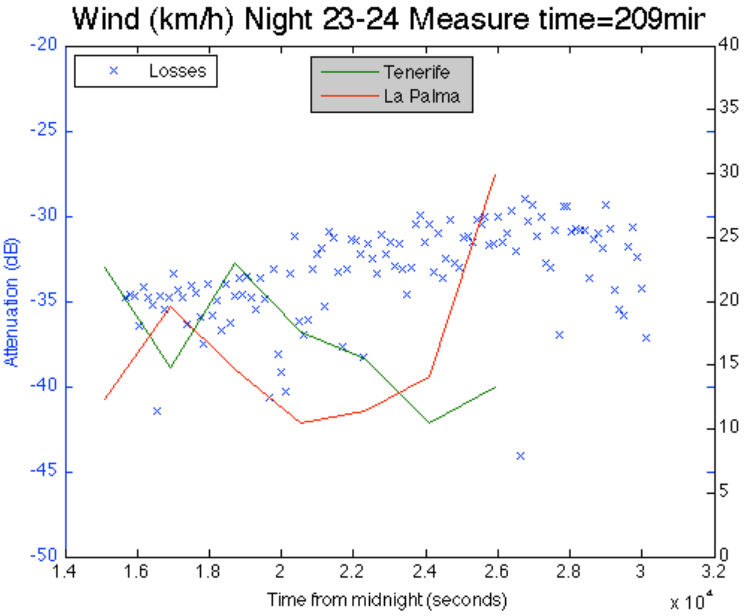

Figure 3.46: Attenuation and wind speed dependence. Each sample is a 2 minutes average.

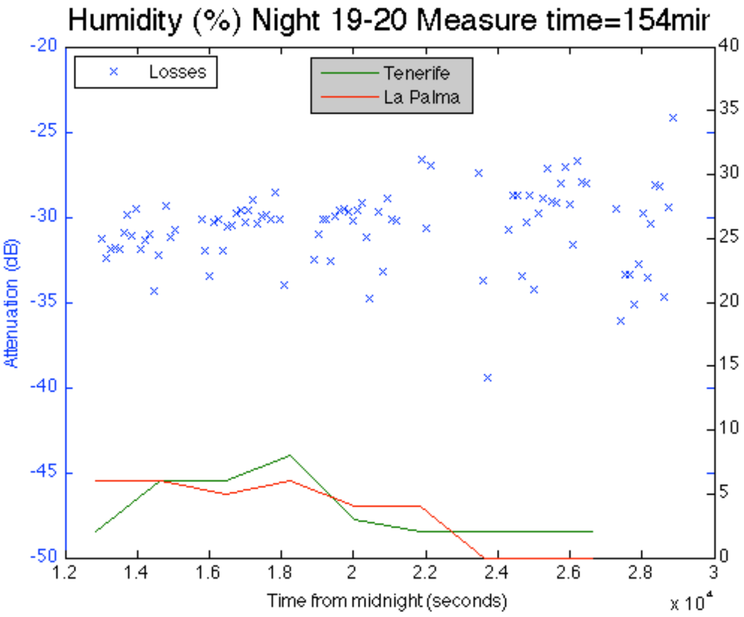

Figure 3.47: Attenuation and humidity variations. Each sample is a 2 minutes average.

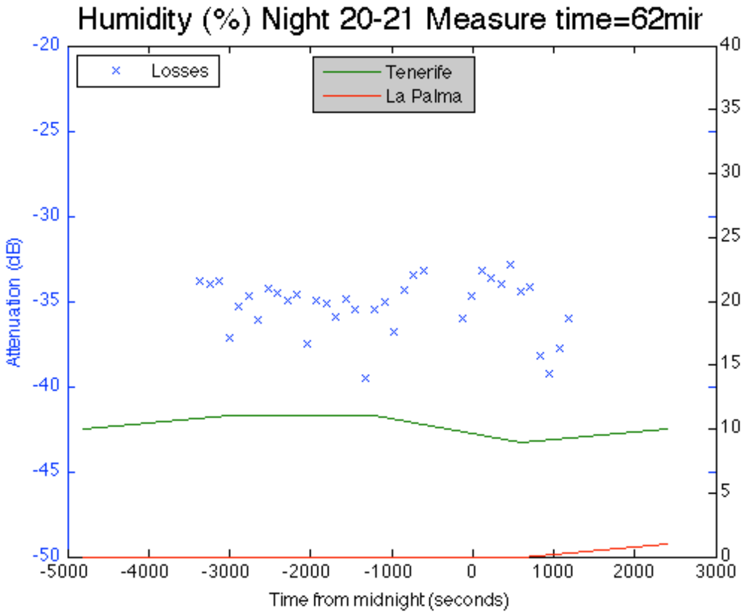

Figure 3.48: Attenuation and humidity variations. Each sample is a 2 minutes average.

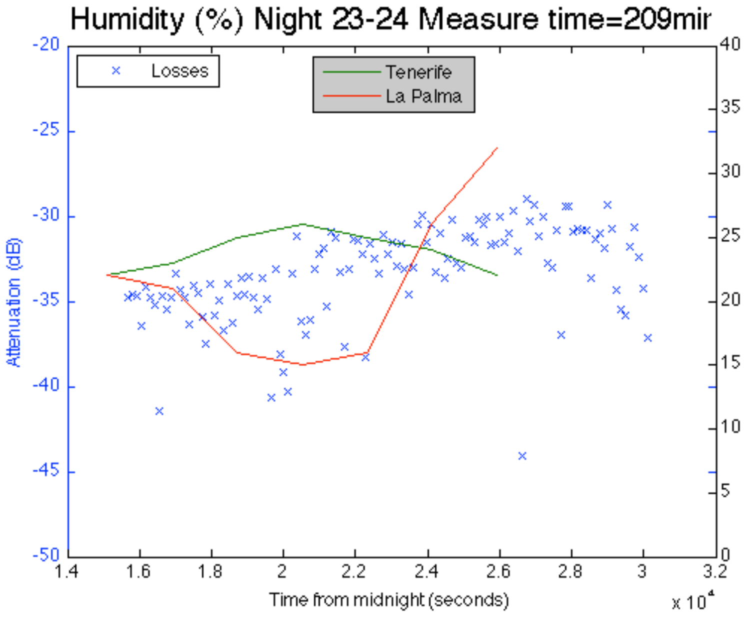

Figure 3.49: Attenuation and humidity variations. Each sample is a 2 minutes average.

It is evident from the data that **with the same night conditions ($r_0 = 3.4$ in May vs. $r_0 = 3.76$ in this run) we have an attenuation that is in average $5dB$ better in this run. This results demonstrate the improvements of the system in terms of focalization (we added a focus motor), alignment (we added a new X-Y stage) and beam mode (we used fibers and a better optical system).**
Regarding the comparison with the QIPS Technical Note 5B, in such note it is stated that the best $r_0 = 6cm$ whereas the worst $r_0 = 1cm$ and that the best attenuation reached had been $26dB$ and the worst $43dB$. It is also mentioned that the lens used in the setup is not the one used in this and in the May run, the lens is in fact a $150mm$ diameter lens with $400mm$ focal length (f/2.7). **Given those data the results of such a report and our results are comparable even regarding other system parameter such as the spot size at the receiver even though we did not have any night with r_0 grater than $4.4cm$.**

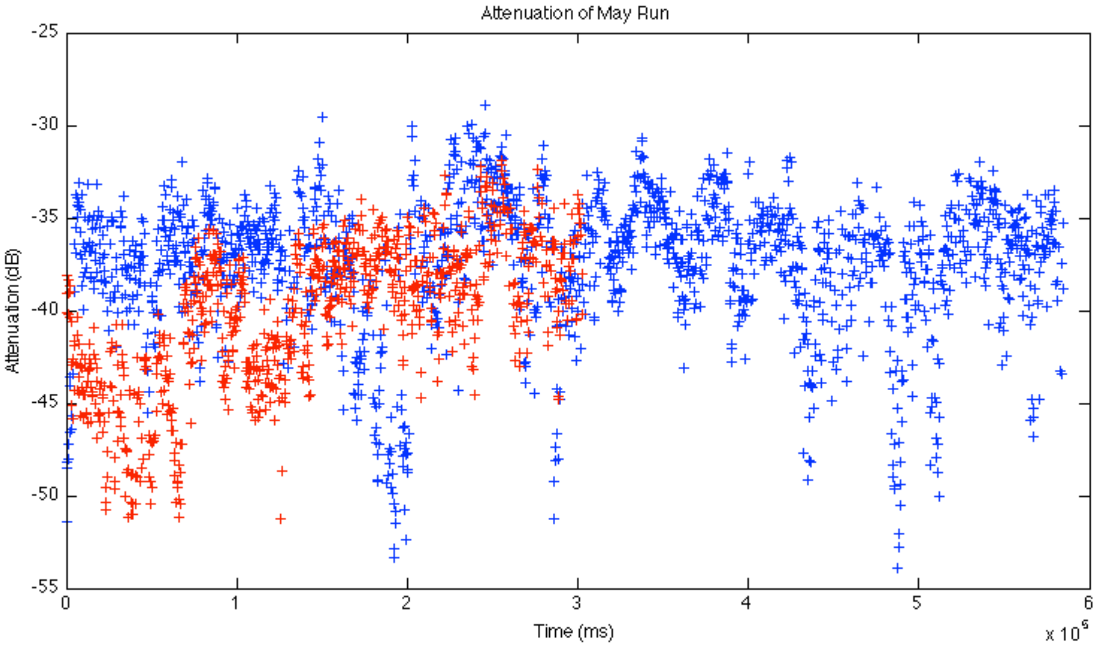

Figure 3.50: Attenuation during the May run. Red: five minutes of Vienna laser. Blue: ten minutes of Padova laser.

Day	Temp	Humidity	Wind Speed	Wind Dir
17/18	10.3°	3%	$18.5km/h$	270°
19/20	6°	35%	$18km/h$	305°

Table 3.10: Weather in Tenerife.

Beacon Signals and Control

As already mentioned the control system that we implemented was based on a beacon coming from Tenerife. In this run we gave priority to the link losses and so we could not calibrate the control unless during the last night that unfortunately turned cloudy and foggy. The data collected for

Day	Temp	Humidity	Wind Speed	Wind Dir	Seeing	r0
17/18	$6,1°$	22%	$32km/h$	315°	$0.85arcsec$	$3.6cm$
19/20	7°	30%	$40km/h$	170°	$0.9arcsec$	$3.4cm$

Table 3.11: Weather in La Palma

calibration are anyway useful to understand the possibility and limits of a such type of control if compared with the collected power at OGS.
We were recording the beacon signal with a camera in the focal plane of the sender telescope, the sensitivity of the system, due to optical leverage is about $3\mu rad/px$. Meanwhile the IR was transmitted to Tenerife in order to measure the power received. The first interesting plot (Fig. 3.51) shows the different averages of the beacon position sampled by the camera in order to beat the scintillation due to atmospheric turbulence.

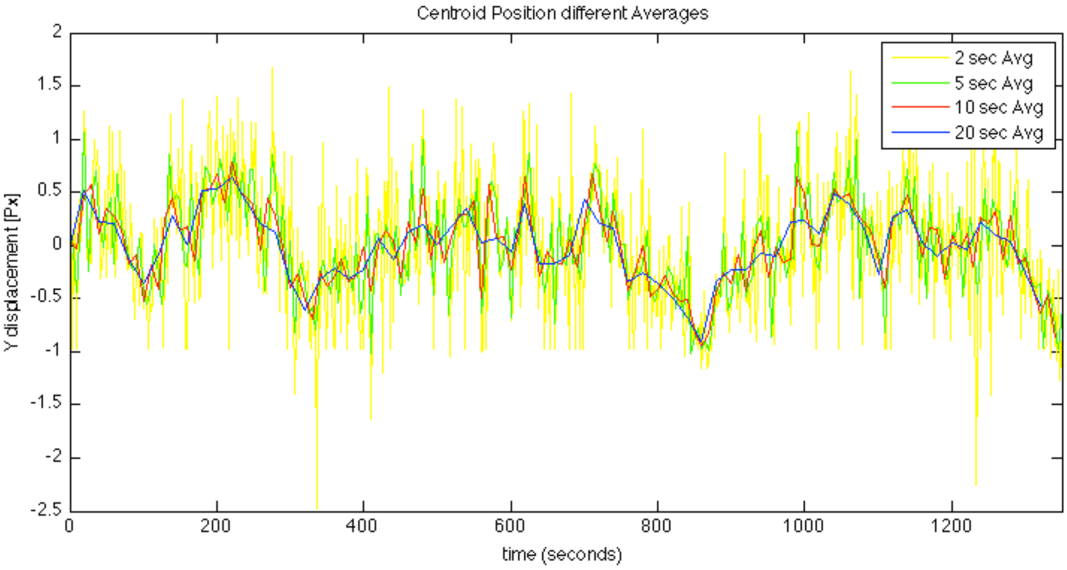

Figure 3.51: Y centroid position night 3rd 8:01 am. Averages at different times in order to eliminate the effect of short term turbulence.

Now we can compare the 20 seconds averaged plot with the power record at Tenerife. We have in total 4 data sets for comparison all in the nights between 19th and 20th at 5:22 am , 5:52 am, 6:19 am and 8:01 am. The result are reported for the last two respectively in figure 3.52 and 3.53. As one can see there is a strong correlation between the power collected and the position of the centroid distance from best position. There is indeed a strong dependence from the Y direction that has been observed during all the nights since the most frequent manual correction where done in that direction. It has to be noticed that during the morning and also after sunrise the signal becomes more stable and the dependence is almost all related to the Y axis.

From this analysis it is clear then that it is possible to correct with such a system given the proper average on the centroid in order to overcome the turbulence effect.
Another important consideration is the following, we used the green laser that arrived from OGS finder to check the spot dimensions and expect our IR spot to be similar in dimensions at Teide observatory (apart from wavelength discrepancy) due to the similar optics used. The green spot received at JKT the night of the 19th-20th was about 2 meters. The graph 3.52 shows that

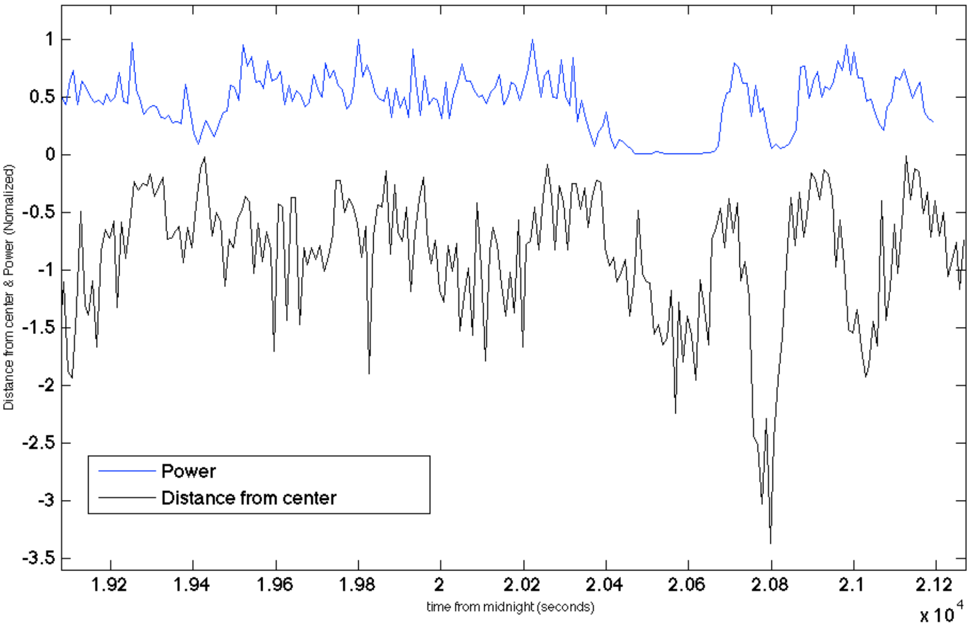

Figure 3.52: Centroid distance from center (with minus sign) with respect to the collected power at OGS 3rd night 6:19 am.

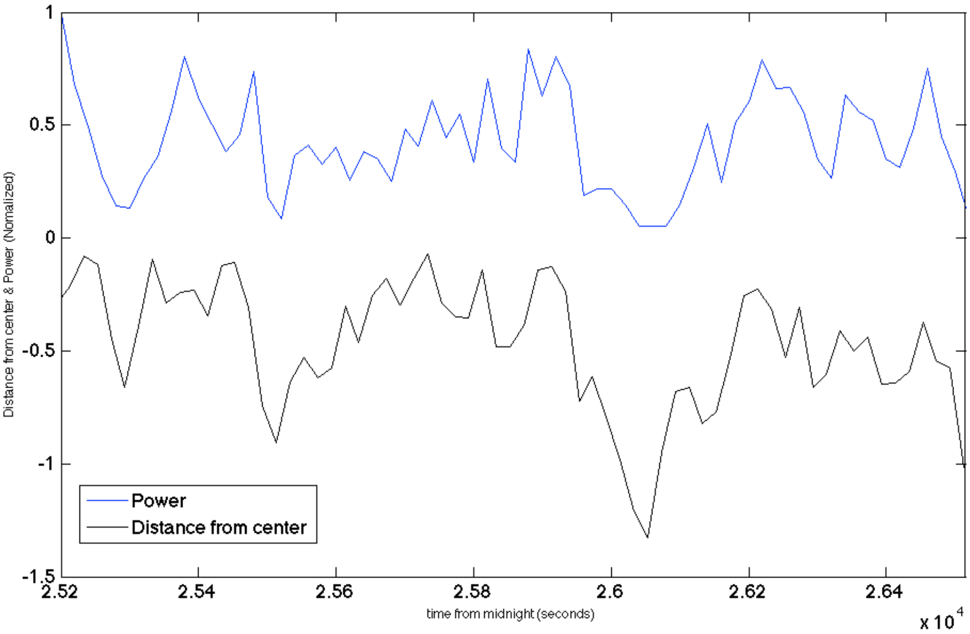

Figure 3.53: Centroid distance from center (with minus sign) with respect to the collected power at OGS 3rd night 8:01 am.

the collected power is nearly completely zero with a movement of about 2.5 pixels. Now from system calibration it turns out that the focal spot moves of about $3\mu m/pixel$ that corresponds to a displacement of about $70cm$ at OGS compatible with the observations.

Temporal Analysis

We collected data with a photodiode both at La Palma and Tenerife in order to measure temporal scintillation and analyse the temporal structure of the signal. At JKT we used a Fresnel lens of $20cm$ diameter with the photodiode on the focal point. At OGS we placed the photodiode directly in the Coude' focus. Moreover at the OGS we collected also data with a single photon [15] detector. The table 3.12 summarizes the measurements.

Night	PD at OGS	SP at OGS	PD at JKT
1st (17-18)	-	-	-
2nd (18-19)	ok	-	-
3rd (19-20)	-	-	-
4th (20-21)	ok	-	-
5th (21-22)	-	ok	ok
6th (22-23)	-	-	-
7th (23-24)	ok	ok	ok
8th (24-25)	-	-	-

Table 3.12: Measurements with photodiode (PD) and single photon detector (SP) at La Palma (JKT) and Tenerife (OGS).

Since the night of 23th-24th we have data for all sites and instruments the following plots refers to that night. In figure 3.54 the photodiode temporal distribution, the power spectrum, the distribution and the log normal probability are reported. The scintillation index evaluated using the formula:

$$SI = < I(t)^2 > / < I(t) >^2 - 1 \tag{3.11}$$

is equal to 2.67.

The plots relative to the photodiode signal collected at OGS are reported in figure 3.55. The scintillation index in this case is 1.19 compatible with much greater aperture.
We have collected also data with a single-photon avalanche diode (SPAD) with a $1ms$ counting time bin. The analysis is reported in figure 3.56 that included the SPAD temporal distribution, the power spectrum, the distribution and the log normal probability plot. Scintillation index in calculated in this case is 2.22.

Aperture Averaging

Using the images used in section 3.3.4 about spatial analysis we tried also to evaluate the temporal scintillation index for each pixel or group of pixels using 21 images representing different realizations of the beam at the JKT site.
For each block size we calculated the sum of the intensities and the temporal scintillation of the block. This is done for each block of the image and then the mean value is calculated. The result shows (Fig. 3.57) the aperture averaging effect, as the block size increases the scintillation index decreases eventually going to nearly 0 when the full sized image is used for the calculation.

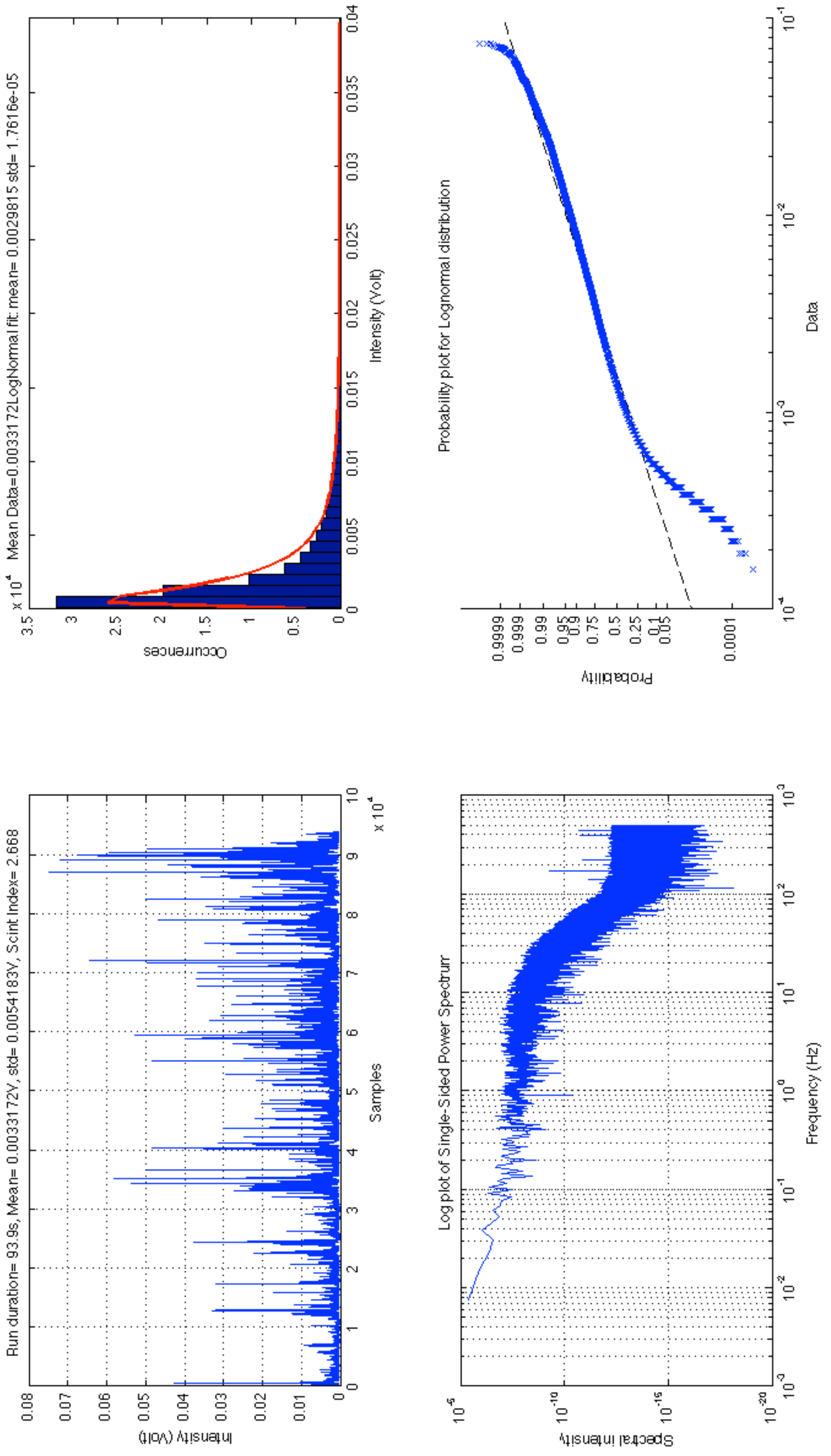

Figure 3.54: Photodiode temporal distribution, power spectrum, distribution and the log normal probability plot. Data from JKT at La Palma.

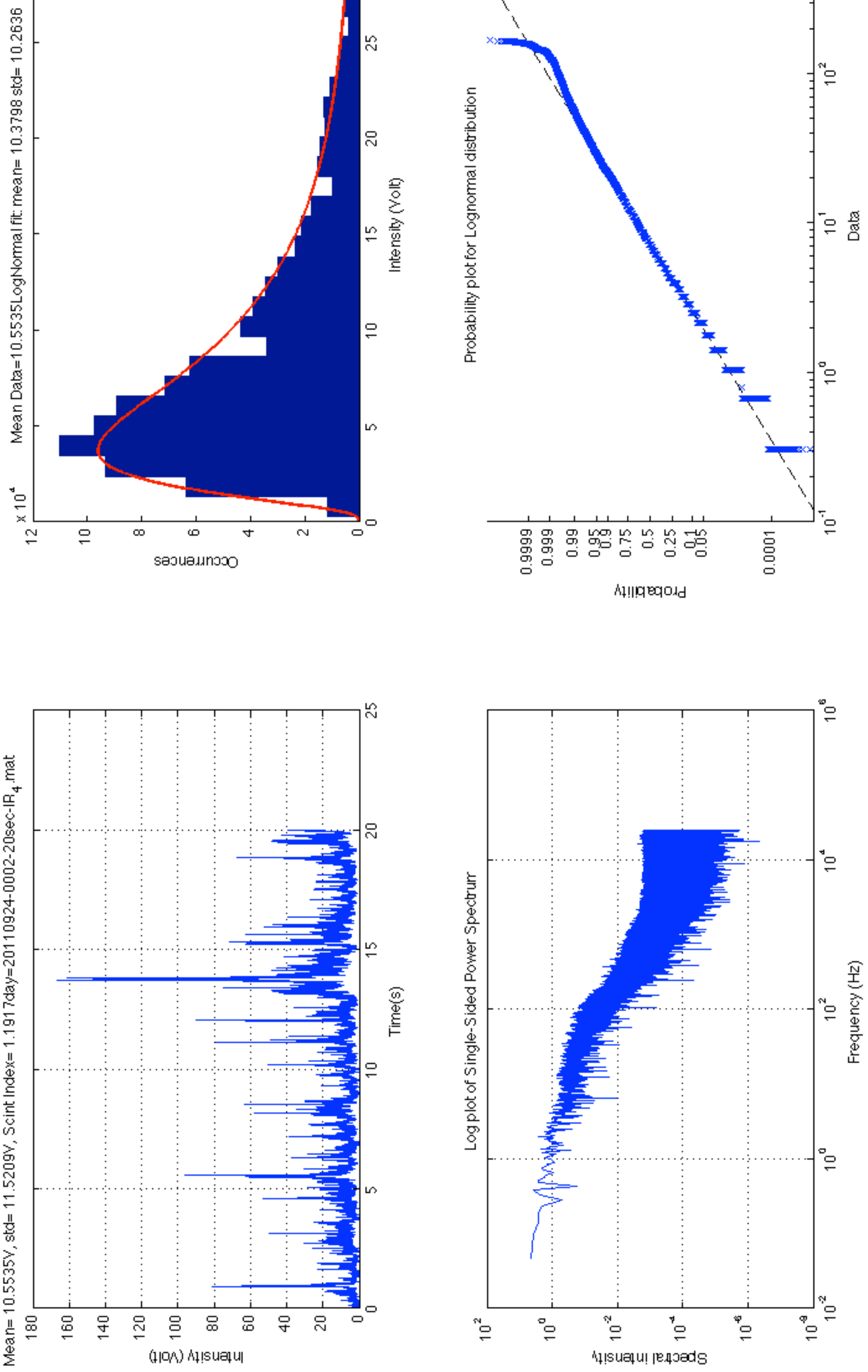

Figure 3.55: Photodiode temporal distribution, power spectrum, distribution and the log normal probability plot. Data from OGS at Tenerife.

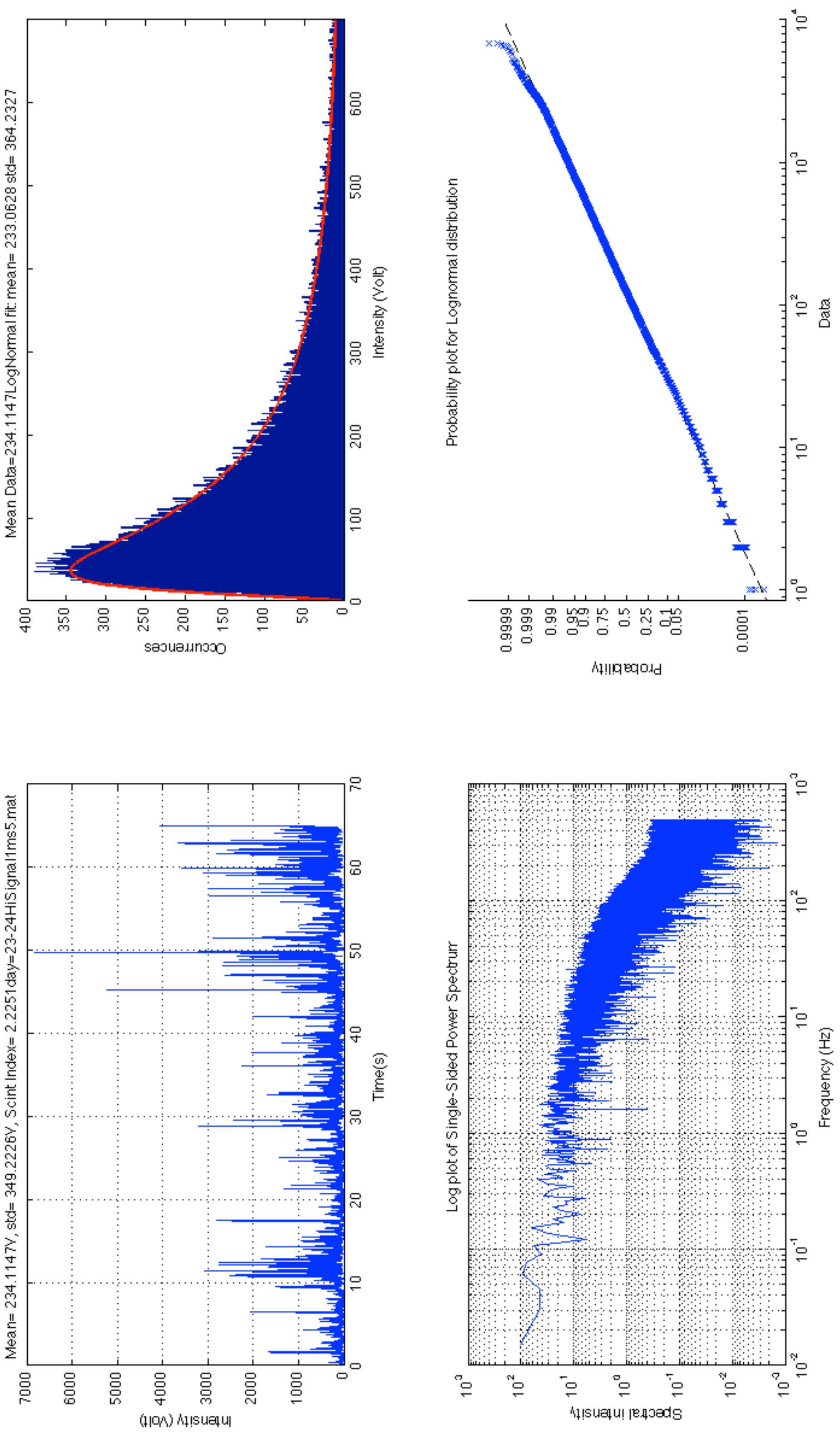

Figure 3.56: SPAD temporal distribution, power spectrum, distribution and the log normal probability plot. Data from OGS at Tenerife

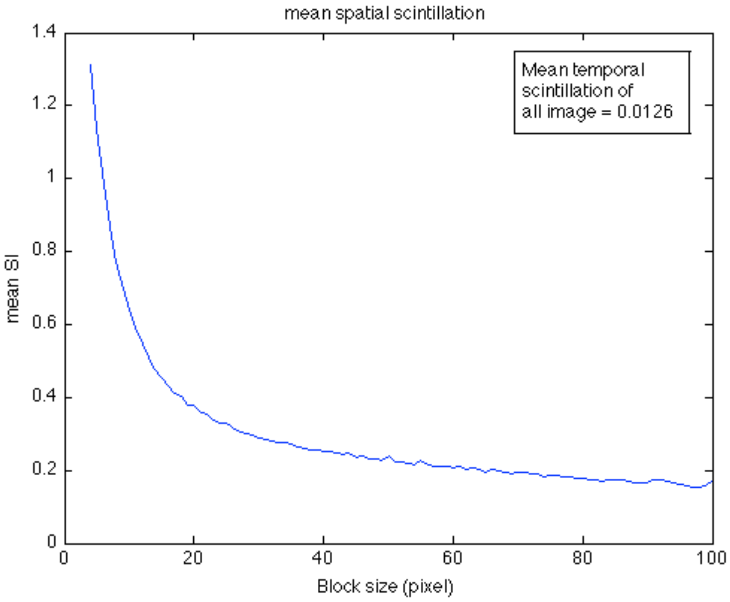

Figure 3.57: Mean temporal scintillation variation versus the block size on which the SI is calculated. This is the effect of aperture averaging.

Spatial Analysis

We performed an analysis of the beam in order to retrieve the spatial information of the beam. First of all the spatial scintillation index is calculated by applying the formula of the scintillation pixel-wise on each image at different exposure time. The general equation for the scintillation index is the following:

$$SI =< I(x,y,t)^2 > / < I(x,y,t) >^2 -1 \tag{3.12}$$

when an integral over t is taken (exposure time) and the mean is over x and y we get the spatial scintillation index, otherwise when we integrate along x and y in our aperture and the mean is taken against t we have the temporal scintillation index.

On figure 3.59 the scintillation index is plotted versus the exposure time of the image. Another feature of the spot is that it is composed by a number of blobs and it is interesting to evaluate the size of such blobs with respect to the exposure time, in this case we evaluated the global blob size at each exposure time so not taking into account smaller structures inside the blob. In figure 3.58 the dimension of the blobs are reported with respect to the exposure time. In table 3.13 a resume of the features described is reported. This can be related also to the blob size calculated considering the autocorrelation of the images at different exposure times. In this case the full width half maximum is considered and the results are compatible with the blob size in table 3.13.

The autocorrelation function is calculated for a MxN image using the following:

$$C(i,j) = \sum_{m=0}^{M-1} \sum_{n=0}^{N-1} A(m,n)A(m+i,m+j) \tag{3.13}$$

The FWHM blob size with respect to the exposure time calculated using the autocorrelation method is reported in figure 3.60.

Texp	Samples	Blob Diameter (px)	Scintillation Index	$\sigma(SI)$
1/30	13	193	0.987	0.2625
1/20	15	248.9	0.79	0.3005
1/15	18	258.8	0.86	0.3161
1/8	13	386.1	0.82	0.2776
1/4	7	460.5	0.38	0.1013
0.7	5	511.8	0.35	0.1002
1	7	575.4	0.342	0.1343
1.5	6	610.2	0.427	0.1530
2	2	613.2	0.299	0.0129
8	1	788.5	0.193	0

Table 3.13: Spatial analysis of the beam. The pixel size in the image is about $6mm$ i.e. about $166px/m$

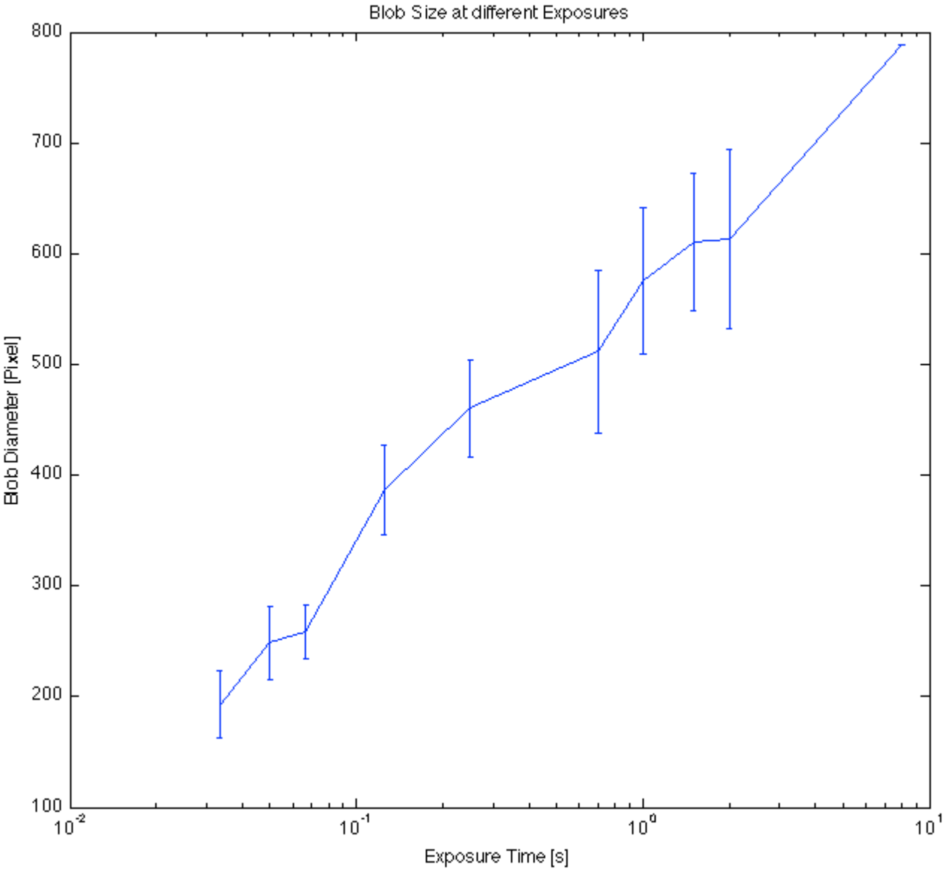

Figure 3.58: Diameter of the maximum blob v.s the exposure time.

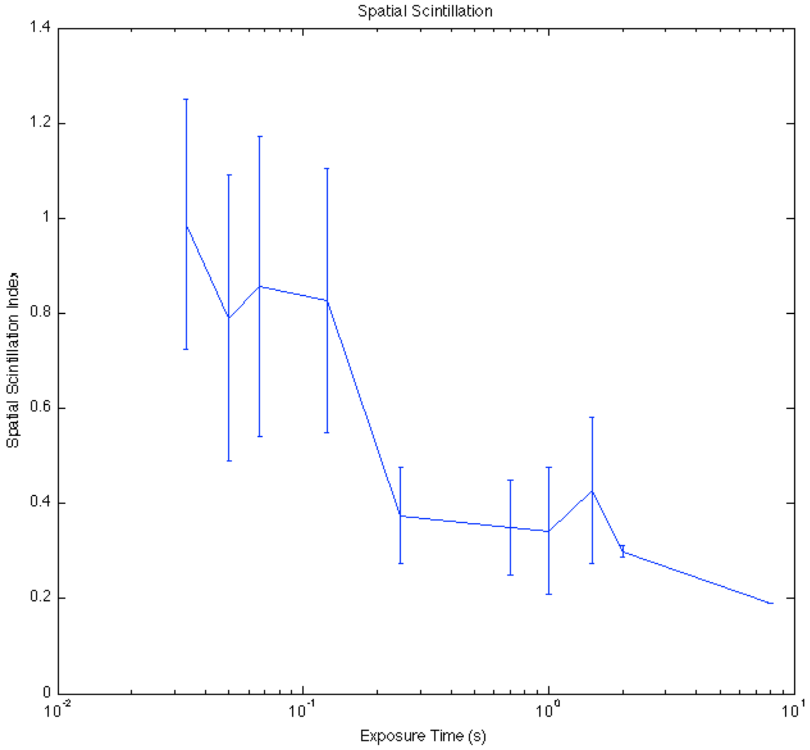

Figure 3.59: Spatial Scintillation Index v.s the exposure time.

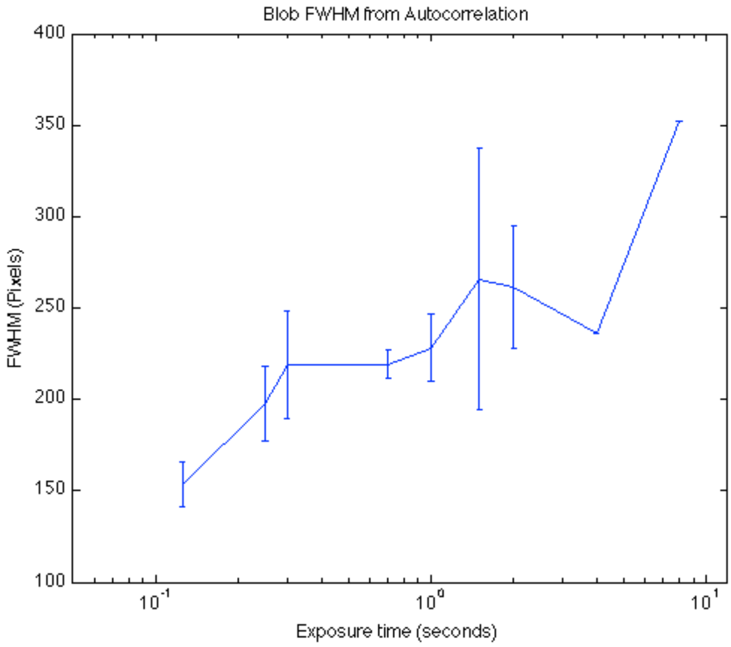

Figure 3.60: FWHM blob size calculated using the autocorrelation method.

Wandering Index

We found useful to introduce a coefficient that takes into account the short term spot movement and shape with respect to its long term shape, we called it wandering index (WI), defined as follows: suppose you fix an exposure time T and take a series of realization of the spot with this exposure time $R_n(x,y,T)$ where n goes from 1 to the number of realization considered, say N and x and y span the image domain D. Now the long term spot associated with this realizations is given by:

$$S(x,y,NT) = \sum_{n=1}^{N} R_n(x,y,T) \tag{3.14}$$

At this point it is possible to define the wandering index for every realization R_n as:

$$WI_n = \frac{< (S(x,y,NT)\gamma_n - R_n(x,y,T))^2 >}{< (S(x,y,NT)\gamma_n)^2 >} \tag{3.15}$$

where γ_n is a normalization factor:

$$\gamma_n = \frac{\int\int_D R_n(x,y,T)}{\int\int_D S(x,y,NT)} \tag{3.16}$$

chosen such as if R_n is gaussian with sigma σ and it is located σ away from the S center the coefficient WI is constant over all σ. Now examining the meaning of this coefficient WI_n as absolute value it is clearly seen that if the shape of any realization R_n is equal to the shape of S then WI_n=0. Moreover with a simple calculation it turns out that WI is composed of two terms, the first that depends only on the dimension of the realization R and the second that depends on both dimension and position of the realization.

$$WI_n = 1 + C_1(dim(R_n)) - C_2(dim(R_n), pos(R_n)) \tag{3.17}$$

From further analysis it turns out that if the dimension of the realization is smaller than about 5 times the dimension of the long term spot S the coefficient C_1 is much significative that C_2. In our case we did the calculation with two different exposure times, 1/15 (18 samples) and 1/30 (13 samples). The dimensions of the realizations are respectively about 2.5 and 3 times smaller than the long term spot. In figure 3.61 is represented a realization of the signal and the sum S resulting from the sum of all realization.

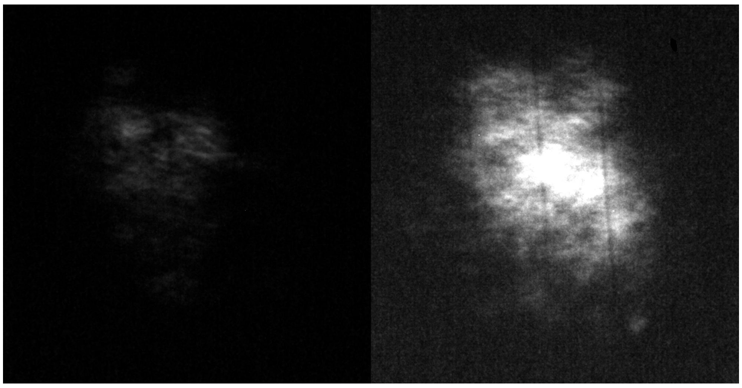

Figure 3.61: Left: a single realization with 1/15 exposure time. Right: the sum off all realizations.

In figures 3.62 and 3.63 the value of WI_n is reported for two different T: mean and variance are respectively $\mu = 1.7$ $\sigma = 0.49$ for $T = 1/15$ and $\mu = 1.63$ $\sigma = 0.28$ for $T = 1/30$.

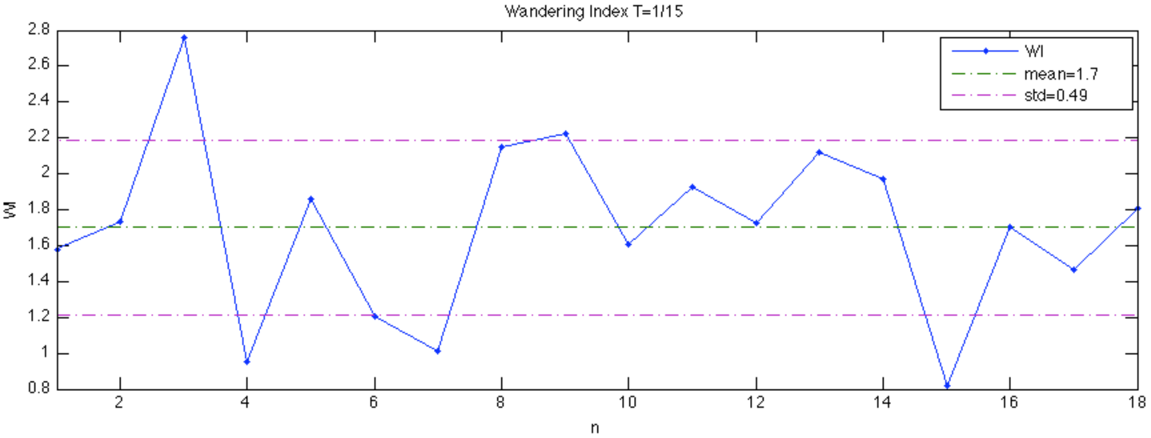

Figure 3.62: Wandering Index coefficient for T=1/15. $\mu = 1.7$ $\sigma = 0.49$.

As a verification of the meaning of WI we did the calculation incrementally summing the realizations R_n up to the long term exposure spot. The result is depicted in figure 3.64.

It is interesting to plot also the WI with respect to the SI (Spatial Scintillation Index) in order to see the differences between the two (Figure 3.65).

Notice how the scintillation index does not goes to zero. This is due to the fact that the beam considered is not flat but has a gaussian shape. This means that even in absence of turbulence the

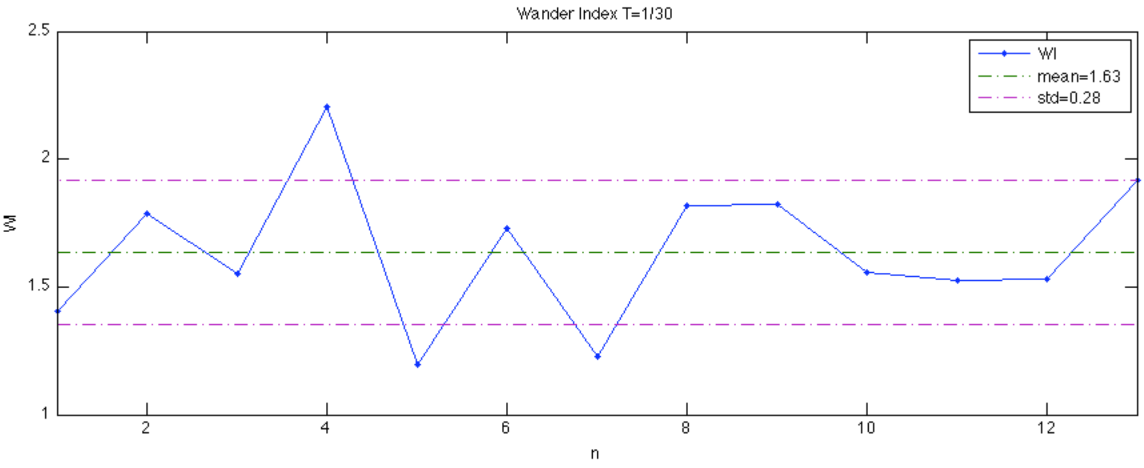

Figure 3.63: Wandering Index coefficient for T=1/30. $\mu = 1.63$ $\sigma = 0.28$.

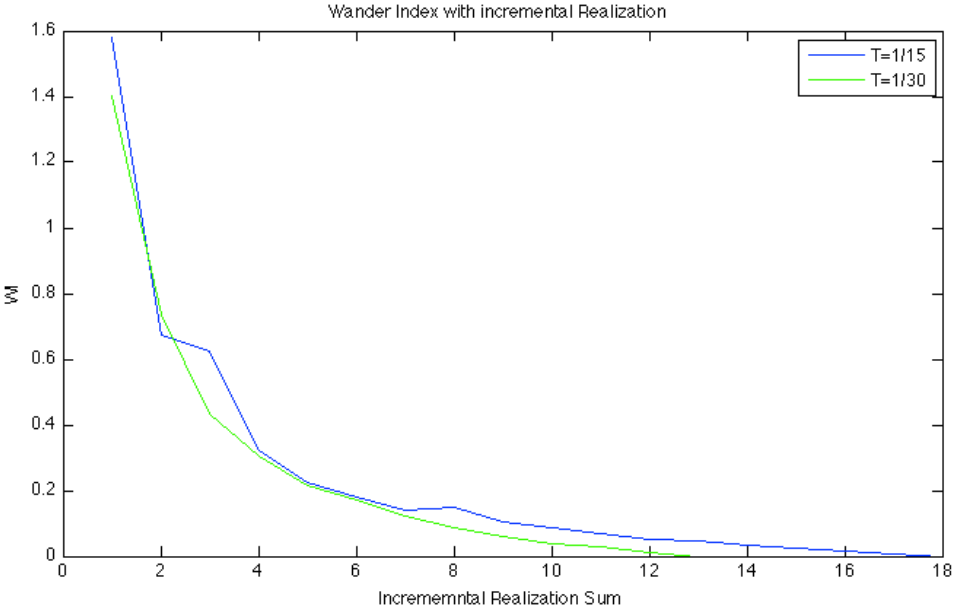

Figure 3.64: Incremental WI. It is clear that approaching the long term spot the WI goes to 0 as expected.

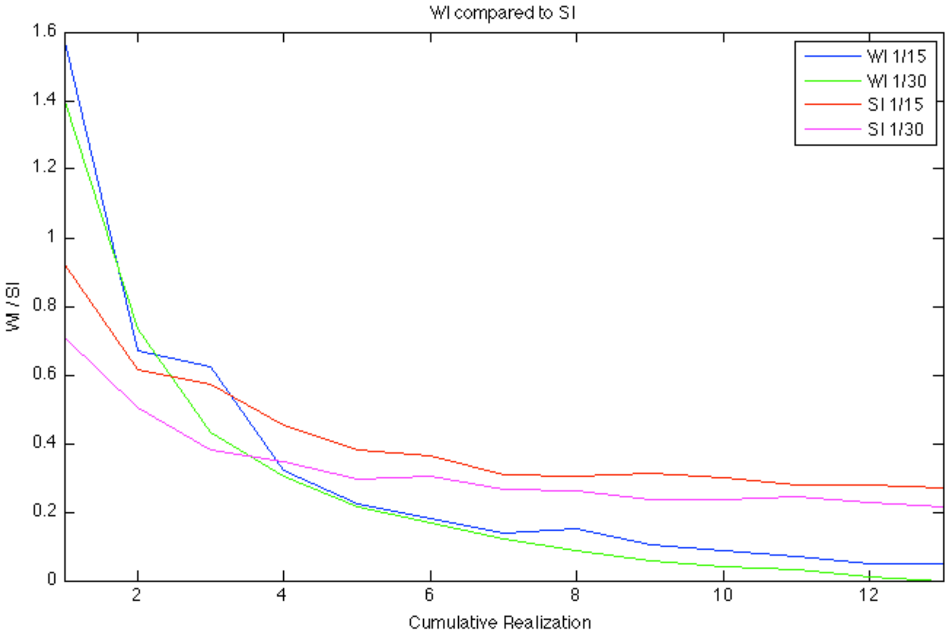

Figure 3.65: Incremental WI and SI. It is appreciable the difference between the WI and the SI.

scintillation index is not zero. These consideration will be part of further analysis.

Conclusions and consideration gained from the fourth experimental session

In conclusion we would like to stress a number of points:

1. *Our system is much more stable than the last run. It is possible to align the IR from scratch in less that one hour and the system stays aligned among nights without power supply.*
2. *The optical plane of our system is flexible and allow the insertion of IR fibers as well as green fibers for alignment.*
3. *The attenuation obtained is at least* $5dB$ *better that the previous run in May and it has been below* $30dB$ *for many times during the run with peaks of* $24dB$ *averaged over 2 minutes.*
4. *The pointing control algorithm, even though it has not been completely exploited, and the analysis on the beacon signal demonstrate its usability.*
5. *We performed a deep analysis of temporal and spatial analysis on the beam.*

3.4 Summary of the whole experimental study

Single beam propagation

The optical link between distant terminals may be modeled by combining the diffraction, attenuation and turbulence effects. This latter has been intensively investigated for decades and is suitably parametrized according to the geographical and meteorological conditions [82, 45, 46, 22, 58]. However, for what concerns the spatial distribution of the spot and its coupling with a receiver in the case of very long path, of tens or hundreds of kilometres, the knowledge of actual atmospheric parameters along the whole path is hardly feasible in practice. Therefore, the spatial effects induced by the turbulence, that in principle have to be expected significantly larger that the diffractive ones, call for direct testing.

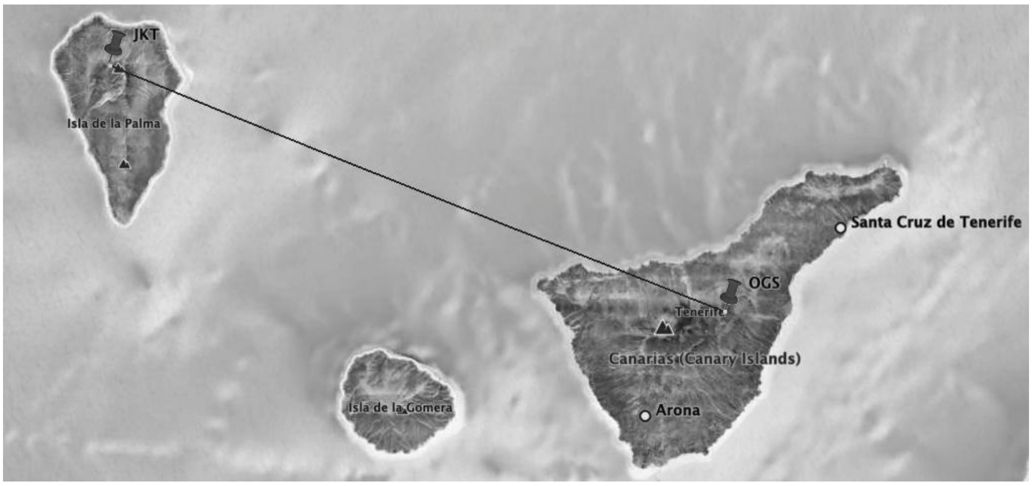

Figure 3.66: Bidirectional path from the Optical Ground Station OGS of ESA in Tenerife and the Johan Kapteyn Telescope JKT, of ING in La Palma.

We set up the conditions to analyse the parameters of the beam by extending the acquisition of the gathered signal in the time domain to the capture of images at different integration time of the whole beam, in order to point out the effect of the spatial scintillation and the coupling to the receiving telescope.

The use of a refractor telescope is convenient in order to avoid the severe cut of the central portion of the gaussian beam by the central obstruction in the case of the reflecting telescopes. For this reason, transmitting refractors have been used in all the trials.

We used different types of optics to investigate the propagation. In the design of these instruments, the spherical aberration was always corrected. Due to the on axis use of the instrument, no further Seidel aberrations are acting, beside defocus. The use of an apochromatic lens was tested in order to simplify the transmission of two beams with different wavelength. When not possible, the chromatic aberration was cancelled by separating the optical origin of the beams using a beamsplitter.

We have used three different instruments:

1. a commercial $120mm$-f/7.5 refractor, SkyWatcher Black Diamond Telescope, that use an apochromatic design and have a $120mm$ optical aperture;
2. the secondary telescope of Optical-Ground-Station (OGS), thank to the kind permission of ESA, that is a $200mm$-f/15 doublet telescope from Zeiss;
3. a $230mm$-f/10 aplanatic telescope realized with a custom aspheric singlet from Costruzioni Ottiche Zen, Venezia, Italy [7].

In the case of both urban and mountain links up to $13km$, we have observed that an Airy-pattern may be obtained in clear nighttime conditions.

In particular, the urban link of $2.2km$ between the DEI building roof and the Specola tower of Padova Astrophysical Observatory, across downtown Padova, was investigated with refractor telescopes of different diameter. In the case of telescope n.1 above, the direct observation of the spot shows an Airy pattern of about $30mm$ between the two first zeros and with a beam wandering extension of about the spot radius. The Airy pattern is due to beam clipping. These conditions are well described in the case of weak turbulence[45, 46, 22].

We investigated the case of longer lengths, finding that the beam is subjected to significant transformation that ends up to an irregular spot distribution [45, 46, 22]. In the case of the Canary link, we initially studied the propagation from OGS to JKT using the telescope n. 2. The JKT location is fortunate in that it is in direct sight of Tenerife top and the Observatory building results nearly normal to the link, so that it may be used as a screen for the spot detection.

The telescope was used to transmit toward La Palma one or two beams, at the wavelength of $532nm$, from single mode laser CW laser source, realized from an $Opto\,Engine\,MGL-III-532-100$ DPSS laser. An optical front-end was designed to realize a gaussian beam of about $65mm$ of waist and with a wavefront of adjustable curvature. The detection in La Palma was done with a refractive optic of $230mm$ diameter equipped with both a power meter and a photodiode. In addition, the whole spot was imaged on the JKT wall with different exposure times.

The meteo conditions may change radically the results of the propagation, due to a series of causes. Some of these may block the propagation, as in the case of rising of clouds, which due to the local atmospheric conditions are usually lower than the link altitude, which is about $2300m$ over the Atlantic Ocean, or the presence of *calima* that is sand from central Africa, brought by high-altitude winds and that invades the link altitude with enough density to diffuse completely the beam. The presence of strong wind or high level of humidity are often cause of widening of the spot but that remains still clearly visible. However, with fair weather condition, a remarkable small spot was observed.

With optimal meteo conditions the diameter of the spot was of $1.85m$. From this observation, we may assess the diameter of the integrated spot to about 2 m. This particular condition was observed for and extended period of several hours in that night. For observations with clear sky but with stronger wind, the observed spot diameter was larger by typically smaller that $3 \pm 0.5m$, with an increase of about 50%. In the best case, the full angle subtended by this spot is of $14\mu rad$.

The diffraction limited full angle of a collimated beam may be calculated from and estimate of the beam waist at the transmitter of $w_0 = 60mm$, as follows:

$$2\theta = \frac{2}{\pi}\frac{\lambda}{w_0} = 5.6\mu rad. \tag{3.18}$$

The comparison of these two values shows that the observed spot in optimal conditions is less than a factor three of the diffraction limit, in the hypothesis that the beam is collimated at the telescope.

The dimension of the spot at distance $x = 144km$ may be described in terms of the mean-square long-term beam radius $< \rho_L^2 >$ by the combined effect of the propagation in vacuum and the turbulence effect, expressed in Eq.37 of the 1975 paper of Dr. Fante[45]:

$$< \rho_L^2 > \cong \frac{4x^2}{k^2D^2} + \frac{D^2}{4}\left(1 - \frac{x}{F}\right)^2 + \frac{4x^2}{k^2\rho_0^2} \tag{3.19}$$

in which D is the beam diameter at the transmitter, that is defined in the case of a gaussian beam of radius w as $D = \sqrt{2}w$, that have an initial curvature of radius $-F$ and k as the wave vector, and ρ_0 is the turbulence coherent radius. This parameter is a function of the local value of the structure constant of the refractive index C_n^2 along the path length. It is computed using different approximations relative to the type of beam. Again, using the previous reference, ρ_0 is expressed by the following equation:

$$\rho_0 = \left[1.46\, k^2 x \int_0^1 (1-\xi)^{\frac{5}{3}} C_n^2(\xi x) d\xi\right]^{-\frac{3}{5}}, \tag{3.20}$$

where it is evident that the link is in general asymmetric if the value of C_n^2 is not uniform. We have verified that in the case of realistic values of this value, it is verified the inequality $x \ll (k^2 C_n^2 l_0^{\frac{5}{3}})^{-1}$, where l_0 is the inner scale size of the turbulent eddies [45]. We may note that the expression for the ρ_L as a function of ρ_0 and of ρ_0 itself are defined differently in Dios $et\,al.$[40] as they are discussed in the case of collimated beam only. However, an adequate up scaling by a factor $\sqrt{8}$ provides a similar overall description.

In the optimal condition for the propagation, the value of ρ_0 that results from inverting Eq. 3.19 is of $28mm$. From this estimate, we may note that the propagation corresponds to the fourth case described by Fante, as $k\rho_0^2 \ll x$ and it effectively corresponds to a beam that at the receiver plane breaks up in multiple spots [45].

The dependence of ρ_L on the radius of curvature F of the beam at the transmitter in eq. 3.19 has been verified in the experiment by varying the position of source of telescope n.2 from the front focal length. By observing the back-scattering of the beam with an auxiliary telescope $100mm$ diameter - f/10 mounted beside the n. 2, it was possible to assess the actual focal position. The feedback from the observer at the receiver end allowed to optimize the focal position in order to minimize ρ_L. This condition was observed in the experiment corresponding to the focus at the path end, and corresponds to the minimum of the term $\frac{D^2}{4}\left(1-\frac{x}{F}\right)^2$.

The asymmetry of the link was tested by using telescope n.3 located on the top of JKT in La Palma pointing the building of OGS in Tenerife. In this new instrument, we designed the beam shaping in order to exploit the $230mm$ diameter of the primary singlet lens using the maximum on-axis irradiance criteria in the Prof. Siegman book (Ch. 18), obtained with the waist-to-aperture-radius rate at 0.89[79]. With not optimal meteo conditions, we had recorded a spot of about $3.5 \pm 0.5m$. Anyway, this observation indicates that the two directions may provide a comparable spot. Telescope n.3 in the final configuration, was optimized using fiber lasers (green and IR lasers) hence imposing a pure Gaussian spatial mode and with a row manual alignment combined with a fine motorized focus and pointing system: at OGS was estimated an IR spot of $1.4m$ comparable with the green one measured at La Palma using the OGS finder as transmitter.

Link losses estimate

We calculated the attenuation coefficient between OGS and JKT (Telescope n.2), using a series of measurements with receiving optics realized by a Fresnel lens (Fresnel Technologies, $267mm$ square Fresnel lens) and a power meter ($Thorlabs\, TC130D$). With an aperture of $10cm$ we observed an attenuation value of $43 \pm 5dB$. By scaling to the size of the OGS telescope as receiver, the attenuation my be predicted to be of $24 \pm 5dB$, considering the size of the 1 m primary mirror and a central obstruction of $300mm$. This results has been validated with Telescope n.3 in its final configuration, that allows to get an attenuation below $30dB$ with best weather conditions and to limit it between $30 - 35dB$ in the other nights.

Twin Beam-Propagation: isoplanatic angles for different modes

We have analysed the propagation of two beams along the same path, to study the correlation of the beam centroids. The application of this technique would be to use one beam for the quantum channel - thus for the single-photon exchange - and the other with a weak laser beam to be used as beacon for the beam steering, in the same direction of propagation. In this way, if the two beams are correlated in their centroids, the instantaneous beam wandering introduced by the turbulence

may be compensated by using an error signal from the acquisition of the second beam.
With the two green beams, the average separation is of 7.7 ± 0.5 meters, corresponding to a subtended angle of $\theta = 53\mu rad$.
From the analysis of the centroids we have seen that the beams movements are correlated with a standard deviation of 37.9 pixels, equivalent to $0.75m$. We may conclude that at this separation θ, the two beams are correlated at least in a common mode that involves the wander of both beams. This results is not valid for the higher order spatial fluctuations as the centroid is the first order momentum of the distribution. Indeed, the separation angle is compared with the set of reference values introduced in adaptive optical corrections of phase front, as the isoplanatic angle θ_0 and the independence angle $\theta_{\psi\, ind}$. The former is the largest angle between two paths for which the turbulence-induced wavefront variations in the two paths are relatively similar. The latter quantify the angle over which the phase effects between the propagation paths of two point sources are nearly uncorrelated [48, 74, 49, 63, 64].
The angle θ_0 decrease as the order of the spatial mode of interest increase [27], and its values for vertical observations spans from 7 to $17\mu rad$[49, 63], even if values of tilt alone as large as $100\mu rad$ are reported by the TNG Observatory. Direct calculation of these two values were obtained using the condition of the experiment as follows: wavelength $\lambda = 532nm$, link length $L = 144km$, $C_n^2 = 2 \times 10^{-17} m^{-\frac{2}{3}}$, transmitting aperture $D = 200mm$, wind speed $V = 10m/s$, outer scale $L_0 = 70$ m and inner scale $l_i = 7.5mm$, where for the turbulence parameters we extracted the values from the various meteo stations of the Instituto de Astrofisica de Canarias (IAC). The results are:

$$\theta_0 = 0.18\mu rad \qquad and \qquad \theta_{\psi_{ind}} = 3.1mrad. \tag{3.21}$$

Our results show a strong correlation in the spot movement, which results in agreement with the following interpretation: the separation angle is greater than the isoplanatic angle. This can be deduced from the different scintillation patterns and the centroid relative motion. However the separation is significantly lower that the independence angle, thus attesting the feasibility of the above described type of control.

3.4.1 Beacon signal

The pointing system based on the "Twin Beam Propagation" is effective only if the weather condition do not strongly degrade the beam and hence it is closed up to $10m$ diameter spot a receiver, otherwise with the current system is not possible to reconstruct the centroid position. For this purpose, in addition we tested a pointing system based on a beacon beam, coming from the receiver. The beam is acquired at transmitter by a CCD camera and its position is elaborated to control the transmitter motorized pointing system.
Our system is capable of a sensitivity of $3\mu rad/px$ and the comparison between the position information of the beam at the transmitter and the power at receiver has shown a strong correlation between them, proving the effectiveness of this pointing system.

The correlation is clearly visible (see fig. 3.67) integrating the signal over 20 seconds: this means that the information has to be properly processed before used as feedback system to overcome the high frequency fluctuation induced by atmosphere.

3.4.2 Conclusions

The observation of the propagation of a single or a pair of beams along very long paths of over $100km$ have shown that the beam is subjected to splitting into multiple spots but that its long-term

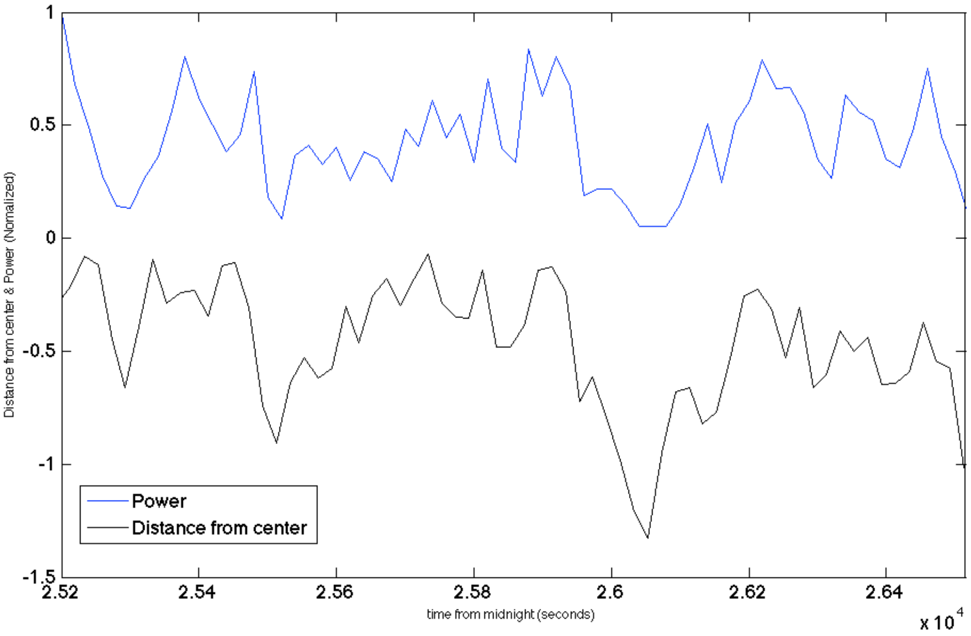

Figure 3.67: Centroid distance from center (with minus sign) with respect to the collected power at OGS

diameter may be confined to a spot that is only a factor 3 to 5 the diffraction limit. This results have been obtained by using a suitable large aperture aplanatic refractive transmitter. In this way a significant reduction of the link losses for quantum communication channels in this extreme conditions are possible by the implementation of such scheme. This setup was used in both the OGS-to-JKT propagation and the reverse.
The losses reduction is a fundamental aspect to improve the communication effectiveness and reliability. In single photon quantum communications link losses require to stretch the communication time: in fact, unlike the classical channel in which high losses can be compensated increasing the transmitter power, in quantum communication we can only iterate the single photons transmission until a sufficient amount of data is reached. The correlations of the two spots in the twin beam propagation and in opposite propagation (beacon signal from receiver) have demonstrated the possibility of the centroid control of the quantum channel by the use of an auxiliary co-propagating beam or by the use of an intense beam from the receiver. Alternative or combined use of both systems is the winning solution for an effective and stable quantum link. The system presented and tested aims to be a reliable solution to establish a free space quantum channel. The techniques described allow the transmission of an intense laser (the so called "auxiliary") for turbulence probing and compensation while simultaneously being exchange single photons.

Chapter 4

Polarization of the light

This chapter is an introduction to the polarimetry, for more details see: [44] and [55]. Polarization is a property of electromagnetic waves, describing shape and orientation of the locus of the electric field vector extremity as a function of time. This property of the light is used in single photon quantum communication as a degree of freedom to encode information. To preserve the information, is crucial to understand what happens to light when passes trough or is reflected by a medium. A polarimetry analysis of the communication channel is therefore necessary to control and monitor the communication link performance.

4.1 Polarized and unpolarized light

The classical concept of polarized light, refers to the wave polarization state as a time evolving function of its electric field vector $\overrightarrow{E}$. If the extremity of the vector describes a stationary curves during the observation time, the wave is defined as *polarized*, otherwise if the vector takes random positions the wave is defined *unpolarized.*

4.2 Polarization formalism

The electric field vector of a monochromatic or quasi-monochromatic wave, can be expressed in terms of three orthogonal components in the right-handed Cartesian coordinate system. For a wave propagating over the z direction, the instantaneous electric field vector, can be expressed as:

$$\overrightarrow{E}(z,t) = \begin{bmatrix} E_x(z,t) \\ E_y(z,t) \end{bmatrix} = \begin{bmatrix} E_{0x} cos(\omega t - kz + \varphi_x) \\ E_{0y} cos(\omega t - kz + \varphi_y) \end{bmatrix} \tag{4.1}$$

where E_{0x} and E_{0y} are respectively the amplitudes of the components $E_x(z,t)$ and $E_y(z,t)$ and φ_x, φ_y their phases. In the plane $z = 0$ can be simplified as:

$$\overrightarrow{E}(z,t) = \begin{bmatrix} E_x(z,t) \\ E_y(z,t) \\ E_z(z,t) \end{bmatrix} = \begin{bmatrix} E_{0x} cos(\omega t - kz + \varphi_x) \\ E_{0y} cos(\omega t - kz + \varphi_y) \\ 0 \end{bmatrix} \tag{4.2}$$

4.2.1 Ellipse of polarization

From (4.2) we can obtain the locus of the extremities of the electric filed vector:

$$\left(\frac{E_x}{E_0x}\right)^2 + \left(\frac{E_y}{E_0y}\right)^2 - 2\frac{E_xE_y}{E_{0x}E_{0y}}cos\varphi = sin^2\varphi \tag{4.3}$$

where $\varphi = \varphi_x - \varphi_y$. The equation can degenerate in a circle or in a line. The corresponding polarization will be defined as: elliptical, circular and linear. The following case can be found:

- $-\pi < \varphi < 0$ Elliptical right-handed
- $0 < \varphi < \pi$ Elliptical left-handed
- $\varphi = 0, \pi$ Linear
- $\varphi = \pm\pi/2$ Circular

In the figure above is reported the polarization ellipse. It lies in a rectangle of dimension $2E_{0x} \times 2E_{0y}$:

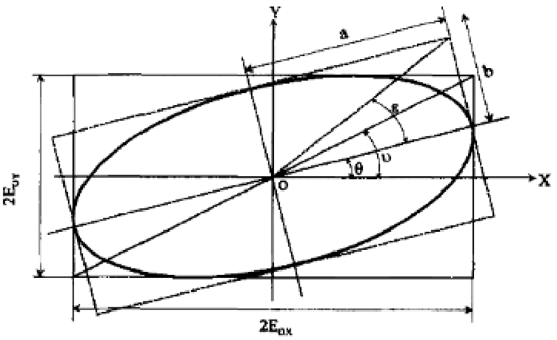

Figure 4.1: Polarization ellipse. Image from [44]

Through the geometric parameters of the ellipse, each polarization state can be unequivocally described:

$$\left\{\begin{array}{ccc} \eta & = & ellipticity \\ \theta & = & azimuth \\ \nu = tan\nu & = & \frac{E_{0y}}{E_{0x}}(0 \leq \nu \leq \pi/2) \end{array}\right. \tag{4.4}$$

This parameters are related to the electric field vector by the following equations:

$$\left\{\begin{array}{ccc} tan2\theta & = & tan2\nu cos\varphi \\ tan2\epsilon & = & \pm sin2\theta tan\varphi \\ tan\epsilon & = & \frac{\pm b}{a}(-\pi/4 < \epsilon \leq \pi/4) \end{array}\right. \tag{4.5}$$

where

$$\begin{array}{rcl} tan2\nu & = & 2\frac{E_{0x}E_{0y}}{E_{0x}^2 - E^2 0y} \\ a^2 + b^2 & = & E_{0x}^2 + E_{0y}^2 \\ \pm ab & = & E_{0x}E_{0y}sin\varphi \end{array} \tag{4.6}$$

4.2.2 Jones formalism

A representation of the electric field vector can be obtained using column complex vector:

$$\overrightarrow{E}(z) = \begin{bmatrix} E_{ox}e^{j\varphi_x} \\ E_{oy}e^{j\varphi_y} \end{bmatrix} \tag{4.7}$$

With this math structure, each optical system, can be modelled through a 2×2 complex matrix, called Jones matrix.
If $\overrightarrow{E_i}$ denotes the Jones vector of an incident wave to an optical system, described by its Jones matrix J, the outgoing waves $\overrightarrow{E_o}$ is related to that incident by:

$$\overrightarrow{E_o} = J\overrightarrow{E_i} \tag{4.8}$$

The resultant electric field vector, of an electromagnetic wave passing through a complex optical system, formed by more than on optics: can be easily expressed by the product of the Jones matrices of each single optical device. Following the wave propagation direction:

$$\overrightarrow{E_o} = J_n J_{n-1} ... J_2 J_1 \overrightarrow{E_i} \tag{4.9}$$

where J_1 is the first crossed device and n is the n^{th}. Usually the Jones vector are written in normalized form, so that the sum of the intensities of the two components gives one.

4.2.3 Stokes parameters

To complete the representation of the polarization states of real waves, we have to take into account also the depolarization. In fact, the Jones formalism, seen in the previous section, deal only with polarized light. To extend the model we need more degree of freedom in the vectorial representation: this is done by the Stokes parameters.
A Stokes vector, is a vector formed by four parameters: S_0, S_1, S_2, S_3. They are to represent the amplitude, phase and polarization of a wave. Are defined by:

$$\begin{cases} S_0 &= \left\langle E_x^2 \right\rangle + \left\langle E_y^2 \right\rangle \\ S_1 &= \left\langle E_x^2 \right\rangle - \left\langle E_y^2 \right\rangle \\ S_2 &= 2\left\langle E_x E_y cos\varphi \right\rangle \\ S_3 &= 2\left\langle E_x E_y sin\varphi \right\rangle \end{cases} \tag{4.10}$$

where $\varphi = \varphi_x(t) - \varphi_y(t)$ is the difference in phase between x and y components, and $\langle\rangle$ is a temporal average on the measurement time. The four parameters are real quantities that represent energies:

- S_0 is proportional to the total density of power of the wave,
- S_1 is proportional to the density of power in the linear horizontal or vertical polarization components,
- S_2 is proportional to the density of power in the linear 45° or 135° polarization components,
- S_3 is proportional to the density of power in the left-handed or right-handed polarization components.

Completely polarized waves

In the case of a completely polarized wave, the vector parameters (4.10) become:

$$\begin{cases} S_0 &= E_{0x}^2 + E_{0y}^2 \\ S_1 &= E_{0x}^2 - E_{0y}^2 \\ S_2 &= 2E_{0x}E_{0y}cos\varphi \\ S_3 &= 2E_{0x}E_{0y}sin\varphi \end{cases} \tag{4.11}$$

it follows that $S_0^2 = S_1^2 + S_2^2 + S_3^2$.

S_0 is usually normalized, so the parameters of the polarization ellipse seen in section 4.2.1 can be expressed by the Stokes parameters as:

$$\begin{bmatrix} 1 \\ S_1/S_0 \\ S_2/S_0 \\ S_3/S_0 \end{bmatrix} = \begin{bmatrix} 1 \\ cos2\epsilon cos2\theta \\ cos2\epsilon sin2\theta \\ sin2\epsilon \end{bmatrix} \tag{4.12}$$

From which:

- ellipticity ϵ $(-\pi/4 < \epsilon \leq \pi/4)$

$$sin2\epsilon = \frac{S_3}{S_0} \tag{4.13}$$

- azimuth θ $(0 \leq \theta < \pi)$

$$tan2\theta = \frac{S_2}{S_1} \tag{4.14}$$

- relative phase φ $(-\pi \leq \varphi \leq \pi)$

$$tan\varphi = \frac{S_3}{S_2} \tag{4.15}$$

Unpolarized waves

For an unpolarized wave, the position of the electric field vector is undetermined. Considering a temporal average on the measurement time we can write:

$$\begin{aligned} \langle E_{0x}^2 \rangle &= \langle E_{0y}^2 \rangle \\ \langle E_{0x}E_{0y}cos\varphi \rangle &= \langle E_{0x}E_{0y} \rangle \langle cos\varphi \rangle \\ \langle E_{0x}E_{0y}sin\varphi \rangle &= \langle E_{0x}E_{0y} \rangle \langle sin\varphi \rangle \end{aligned} \tag{4.16}$$

The phase variation are equally distributed between $-\pi$ and π, hence the average values of the *sin* and *cos* therms are zero. From these, follows:

$$\begin{bmatrix} S_0 \\ S_1 \\ S_2 \\ S_3 \end{bmatrix} = S_0 \begin{bmatrix} 1 \\ 0 \\ 0 \\ 0 \end{bmatrix} \tag{4.17}$$

Theorem of decomposition

The Stokes vectors can be used both with polarized and unpolarized waves. The formalism enables to express the incoherent superposition of two light waves. The Stokes vector S^i of a partially polarized waves (PP) can be decomposed into a completely polarized (CP) part, and a non-polarized part (CD); this decomposition is unique:

$$\begin{bmatrix} S_0 \\ S_1 \\ S_2 \\ S_3 \end{bmatrix} = \begin{bmatrix} S_0 - \sqrt{S_1^2 + S_2^2 + S_3^2} \\ 0 \\ 0 \\ 0 \end{bmatrix} + \begin{bmatrix} \sqrt{S_1^2 + S_2^2 + S_3^2} \\ S_1 \\ S_2 \\ S_3 \end{bmatrix} \tag{4.18}$$

$$PP = CD + CP$$

Coherency matrix and degree of polarization

In the former section we saw how a wave can be decomposed into its polarized and unpolarized components. Now we will see how to define quantitatively the degree of polarization of a wave.
The coherence matrix, also called polarization matrix, is define as the temporal average of the product of a Jones vector by its Hermitian conjugate:

$$\Phi = \left\langle \overrightarrow{E} \otimes \overrightarrow{E^+} \right\rangle = \begin{bmatrix} \langle E_x E_x^* \rangle & \langle E_x E_y^* \rangle \\ \langle E_y E_x^* \rangle & \langle E_y E_y^* \rangle \end{bmatrix} \tag{4.19}$$

The coherency matrix can be connected to the Stokes parameters by the following relationship:

$$\Phi = \frac{1}{2} \sum_{i=0}^{3} S_i \sigma_i \tag{4.20}$$

where the Pauli matrices are:

$$\sigma_0 = \begin{bmatrix} 1 & 0 \\ 0 & 1 \end{bmatrix}, \sigma_1 = \begin{bmatrix} 1 & 0 \\ 0 & -1 \end{bmatrix}, \sigma_2 = \begin{bmatrix} 0 & 1 \\ 1 & 0 \end{bmatrix}, \sigma_3 = \begin{bmatrix} 0 & -i \\ i & 0 \end{bmatrix} \tag{4.21}$$

The degree of polarization is defined by the ratio between the intensity of the polarized part and the total intensity:

$$P = \frac{I_{pol}}{I_{tot}} = \left[1 - \frac{4det(\Phi)}{Tr(\Phi)^2} \right]^{1/2} \tag{4.22}$$

that can be written in:

$$P = \frac{\sqrt{S_1^2 + S_2^2 + S_3^2}}{S_0}, \; 0 \leq P \leq 1 \tag{4.23}$$

If $P = 0$ the wave is not polarized, otherwise if $P = 1$ the wave is completely polarized.

4.3 Poincaré sphere

An useful graphical representation of the polarization states is the Poncaré sphere. Each point of the sphere is uniquely associated to a Stokes vector. The vector coordinates S_1, S_2, S_3 correspond to the coordinates of the 3-axes of the sphere.
Given the quadratic relation 4.11, and considering its normalized form, it follows that for a completely polarized wave the radius of the sphere is unitary.

A deflated sphere or a squeezed sphere, has points with radius that is less than one: for a real optical device, this is related to depolarization.
Since each point of the sphere is strictly related to a Stokes vector, also, from the sphere is possible to get the polarization ellipse parameters.
The equatorial circle represents the linear polarization states, and the poles correspond to the circular states: respectively right-handed at the South pole and left-handed at the North pole. The North hemisphere corresponds to the elliptical left-handed polarization states, otherwise for the South hemisphere.

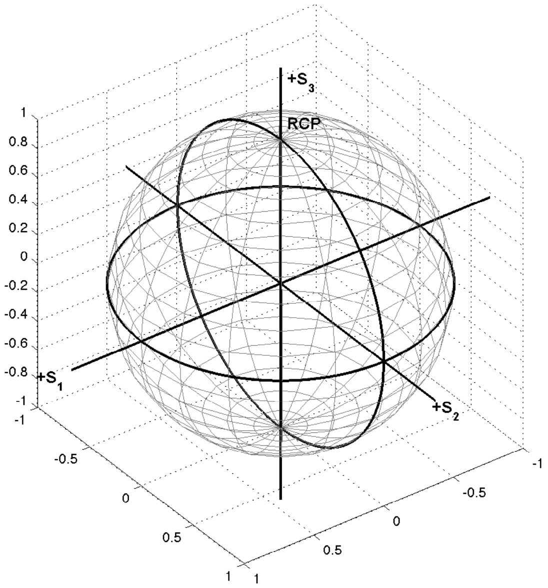

Figure 4.2: Poincaré sphere

4.4 Mueller matrix

The Mueller matrix is a 4 × 4 matrix, that describes completely the polarimetric behaviour of an optical device. It can be seen as an operator that maps each polarization input state, represented by a Stokes vector, to an output Stokes vector, corresponding to a defined polarization output state:

$$S_o = MS_i \tag{4.24}$$

An optical system is represented by 16 coefficients. Each Jones matrix (4.2.2) can be rewritten as a Mueller matrix by:

$$m_{ij} = \frac{1}{2}Tr(J\sigma_j J^+ \sigma_i) \tag{4.25}$$

As for the Jones matrices, a complex system can be represented in the Mueller matrices via the products of the Mueller matrices of each subcomponent of the device:

$$M = M_n M_{n-1} ... M_2 M_1 \tag{4.26}$$

Unlike the Jones matrices, the Mueller matrices better suit the experimental analysis since the involved quantities are intensities and hence measurable. The equation (4.25) can be rewritten as:

$$M_J = A(J \otimes J^{+})A^{-1} \tag{4.27}$$

where A is the matrix:

$$A = \begin{bmatrix} 1 & 0 & 0 & 1 \\ 1 & 0 & 0 & -1 \\ 0 & 1 & 1 & 0 \\ 0 & i & -i & 0 \end{bmatrix} \tag{4.28}$$

Chapter 5

Space Quantum Communications

About a decade ago, several groups endeavoured the porting of quantum communication in general and Quantum Key Distribution (QKD) as first example outside the cradle of the lab, in the adverse outdoor conditions: [34], [62]. The natural extent of free space Quantum Communication (QC) is space, due to the restrictions imposed on the Earth surface by the Earth curvature as well as atmospheric turbulence.
The experimental demonstration of the feasibility of single photon exchange between space and a ground receiver has been also demonstrated in our group recently [94]. The demonstration of the control of the polarization state along the space channel is important to pave the way to further steps in space QC based on polarization of photons.

5.1 Problems in the transmission of photons

Polarization analysis for an Earth-Space link as first, start with the problem of modelling a real quantum link on space. Physically, we have to deal with a free-space dynamic optical link through the atmosphere. Dynamic means the fact that transmitter and receiver are in relative motion between them. We can identify the following main issues, that have to be addressed:

- Effects due to atmospheric turbulence that causes attenuation and fluctuations in the signal received.
- Background noise: due to sunlight, moonlight and every source of photons that can be collected by the receiver.
- The relative motions between transmitter and receiver, that is the main source of misalignment in the polarization references of the transmitter and receiver.
- Non ideal optics that can cause depolarization, attenuation and distortion.

5.2 Channel polarization analysis

The polarization properties of an optical system can be generally described through the use of the Mueller matrix and the Stokes formalism. The interaction between a polarized beam and a polarizing device can be described by:

$$S = MS' \tag{5.1}$$

where S' and S are respectively the Stokes vectors of the incident beam and of the outgoing beam; M is the 4×4 Mueller matrix of the optical system.
A common way to retrieve the Mueller matrix of an optical device is to test it by measuring the outcoming light from$n$ differently polarized beams (with $n \geq 4$). The input state can be generated through the rotation of a quarter-wave plate at a determined angle θ starting from a vertical polarization state. Given the Mueller matrix of a rotated quarter-wave plate retarder :

$$M_q = \begin{bmatrix} 1 & 0 & 0 & 0 \\ 0 & cos^2 2\theta & sin2\theta cos2\theta & -sin2\theta \\ 0 & sin2\theta cos2\theta & sin^2 2\theta & cos2\theta \\ 0 & sin2\theta & -cos2\theta & 0 \end{bmatrix} \tag{5.2}$$

from a vertical polarization, the states generated via the half-wave retarder are:

$$J = \begin{bmatrix} 1 \\ cos^2 2\theta \\ sin2\theta \\ sin2\theta \end{bmatrix} \tag{5.3}$$

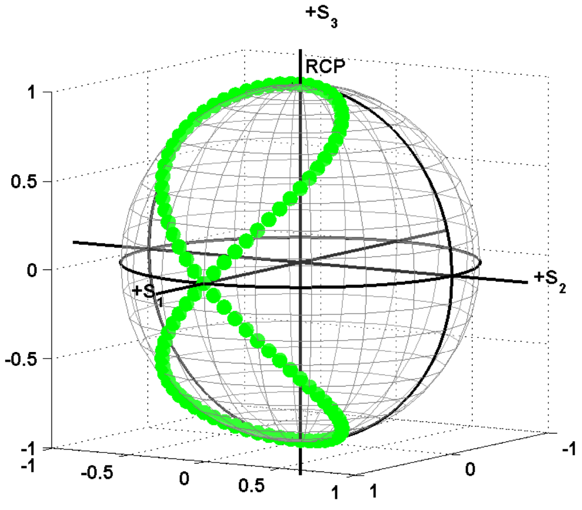

Figure 5.1: Polarization states of a rotated half-wave plate retarder

For n different input states the equation (5.1) can be rewritten in matrix form:

$$\mathbf{S} = \mathbf{MA} \tag{5.4}$$

where **S** is the matrix of the output Stokes vectors:

$$\mathbf{S} = \left[S^{(0)} S^{(1)} ... S^{(n)} \right] \tag{5.5}$$

and **A** is the matrix of the input states vectors:

$$\mathbf{A} = \left[J^{(0)} J^{(1)} ... J^{(n)} \right] \tag{5.6}$$

Inverting the equation (5.4), it is possible to retrieve the Mueller matrix **M**:

$$\mathbf{M} = \mathbf{SA}^{+} \tag{5.7}$$

where $\mathbf{A}^{+}$ is the pseudo-inverse matrix of **A**.

5.2.1 Feedback control in quantum communication system

An important feature of a quantum communication system is the polarization preservation. This is in general not realized in present systems, due to the non-idealities of real channels. It is however possible to study the polarization properties of the channel by the use of Mueller matrices formalism, and it allows to compensate the distortions induced by the channel. In fact defined the Mueller matrix of the channel it is possible to prepare an input state so that it is received in the desired state. Using the cascade of an half-wave plate and a quarter-wave plate retarder, it is possible to choose any kind of polarization states in the Poincaré sphere.

In the Mueller formalism the matrix of a rotated half-wave retarder is:

$$M_h = \begin{bmatrix} 1 & 0 & 0 & 0 \\ 0 & cos4\theta & sin4\theta & 0 \\ 0 & sin4\theta & -cos4\theta & 0 \\ 0 & 0 & 0 & -1 \end{bmatrix} \tag{5.8}$$

Combining the matrix (5.2) for a quarter-wave retarder, can be proved that starting from a vertically polarized state we can choose the suitable rotation angles to get the desired state.

Considering all the transmitting system together with the channel the equation (5.1) becomes:

$$S = MM_q(\theta_q)M_h(\theta_h)V \tag{5.9}$$

where V is the Stokes vector of the input vertical polarized state. A simple way to find the two suitable rotation angles is to minimize the norm[1] of the difference between the sent state and that expected at the receiver:

$$(\theta_q, \theta_h) = min_{\theta_q,\theta_h} ||S - MM_q(\theta_q)M_h(\theta_h)V||_F \tag{5.10}$$

In this way, knowing the Mueller matrix of the channel we can pre-compensate any effect introduced by the channel. In a typical transmitting system: channel probing and information exchange share the same medium, this implies that the Mueller matrix measure should not affect the single-photon exchange in the quantum channel. Two possible solutions are: time-multiplexing and wavelength-multiplexing proposed by [30].

With a system like that idealized if figure 5.2 we can predict the evolution of a time-varying quantum channel and compensate for changes in the polarization by means of a feedback control.

---

[1] Frobenius norm: is a matrix norm, defined as: $||A||_F = \sqrt{\sum_{i=1}^{m} \sum_{j=1}^{n} |a_{ij}|^2}$

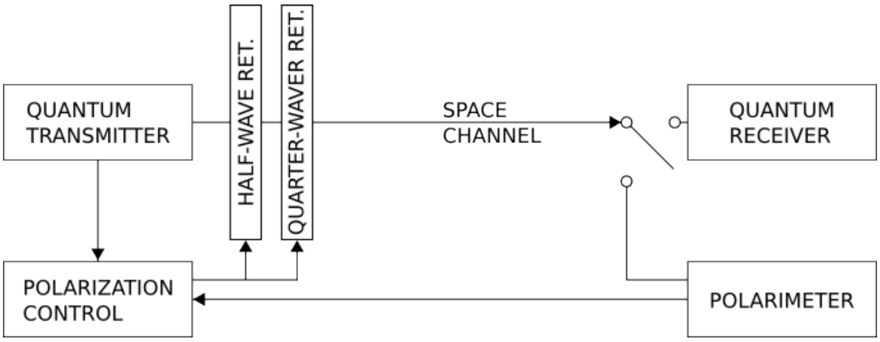

Figure 5.2: Quantum communication system, compensated in polarization

5.3 Laser ranging network

To study and implement a quantum space link a transmitter/receiver on space is needed: this requires an hosting satellite. Unfortunately, the availability of satellites is related to space agencies programs, and the availability of satellite is almost always a challenge. For this purpose we can take advantage from the satellite laser ranging network. It is the easiest way to achieve a quantum space link using yet existing facilities: obviously, properly adapted and integrated with new instrumentations.
In satellite laser ranging (SLR) a global network of stations measure the round trip time of flight of ultrashort pulses sent to satellites equipped with retro reflectors. This provides instantaneous range measurements with millimeters accuracy that can be used to provide careful measurements of orbits and important scientific data.
Through SLR we have at hand an optical Earth-space-Earth link, an on Earth facility able to point and track satellites and also a system able to send and detect laser pulses.

5.3.1 Laser ranging earth stations

A Laser ranging earth station is usually provided with:

- an high-speed telescope, able to point and track the laser ranging satellite, normally orbiting in the LEO (low earth orbit) range
- an high energy pulsed laser
- a detector to receive the retro reflected laser pulses
- a pointing and tracking system, able to predict the satellites orbits and control the telescope to follow them
- a data logger system to collect the ranging data

In table 5.1 are reported the specifics of the Matera Laser Ranging Observatory (MLRO): identified as a suitable site for our space link experiments.
The parameters are given from NASA in [1]. More information on laser ranging and our previous quantum experiments can be found in [39] and [94].

Telescope diameter	$1.5m$
Laser pulse energy	$100mJ$
Laser pulse repetition rate	$10Hz$
Laser wavelength	$532nm$
Beam divergence angle	$45\mu rad$
Transmission optical efficiency	0.75
Receiving optical efficiency	0.39 (with pass-band filter)
Elevation	$536.9m$
Telescope effective area	$1.7662m^2$

	Min	Max
One-way atmospheric transmission T_a	0.14	0.89
One-way transmissivity of cirrus clouds T_c	0.31	1
Beam pointing error θ	$14.6\mu rad$	$32.4\mu rad$
Transmitter gain G_t	$1.4 \cdot 10^9$	$3.2 \cdot 10^9$

Table 5.1: MLRO site specifics

5.3.2 Laser ranging satellites

The laser ranging satellites are provided with retro reflectors that are usually made by corner cubes. While a mirror reflects a beam back in the same direction of arrival only at normal incidence, a corner cube prism, with its three internal reflections, can reflects it back onto itself, regardless of the prism orientation. Because they work even at very large angles of incidence, corner cubes are valuable in applications where it is difficult or time - consuming to attain precision alignment.

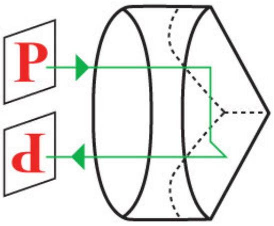

Figure 5.3: Corner cubes scheme

In figure 5.3.2 and following are reported some photos of satellites used in laser ranging.

In our experiment, the Earth station, will be the Matera Laser Ranging Observatory (MLRO). Taking into account the visibility of the satellite from the station, the capability of tracking and its altitude and the type of corner cubes we drafted a list of best candidates for our optical link:

5.4 Satellite Laser ranging-Link model

The standard mathematical model used to analyse and estimate the performance of a Satellite Laser Ranging Link is based on the Radar Link Equation, given by Degnan [39].
Via its classical form, is possible to estimate the mean photon flux recorded by a detector:

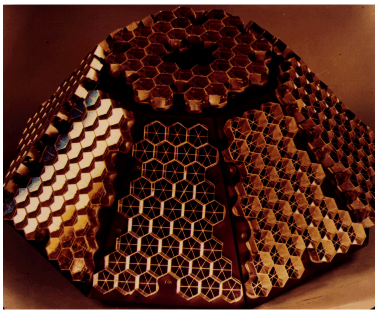

Figure 5.4: Beacon C

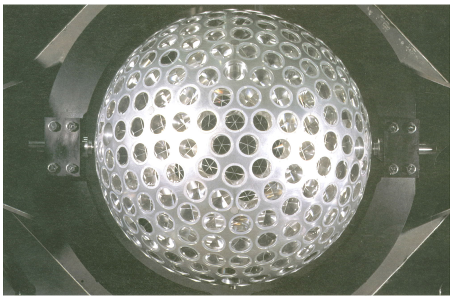

Figure 5.5: Lageos

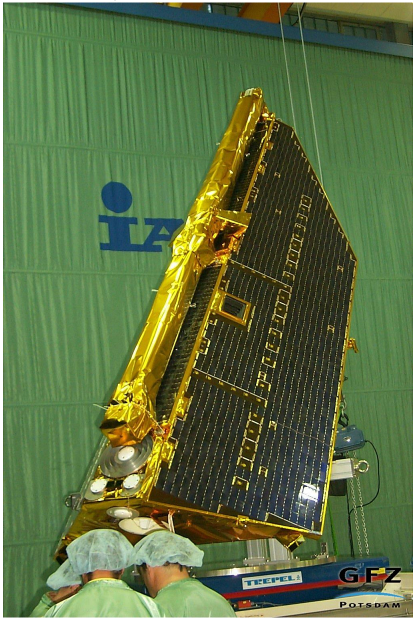

Figure 5.6: Champ

Figure 5.7: Giove B

Satellite	Altitude $[km]$	Retro reflectors	Cross-section $[10^6 m^2]$
Goce	295	7 aluminium coated corner cubes	≥ 0.7
Beacon C	927	160 coated corner cubes	13
ADEOS 2	803	9 corner cubes. Uncoated	
Jason-1	1336	9 corner cubes. Uncoated	0.8
Jason-2	1336	9 corner cubes. Uncoated	0.8
Larets	691	60 corner cubes	
OICETS	610	6 corner cubes	
SOHLA	666	12 corner cubes. Uncoated	
Stella	800	60 corner cubes. Coated	1.8
Starlette	800	60 corner cubes. Coated	1.8
TerraSAR-X	514	4 Aluminium coated corner cubes	
CHAMP	474	4 Aluminium coated coated corner cubes	1
BLITS	832	One spherical coated retro reflector	
ERS 1	780	9 corner cubes	0.85
ERS 2	780	9 corner cubes	0.85
Envisat	796	9 corner cubes	0.85
Glonass	19000	Coated	80-240

Table 5.2: Satellite candidate for quantum optical link

$$N_{pe} = \eta_q \left(E_T \frac{\lambda}{hc} \right) \eta_t G_t \sigma \left(\frac{1}{4\pi R^2} \right)^2 A_r \eta_r T_a^2 T_c^2 \tag{5.11}$$

in which the factors are: η_q is the detector quantum efficiency, E_T is the laser pulse energy, λ is the laser wavelength, h is the Planck constant, c is the speed of light, η_t is the transmission optical efficiency, G_t is the transmitter gain, σ is the satellite optical cross-section, R is the slant range to the target, A_r is the effective area of the telescope - receiver aperture, η_r is the efficiency of the receiver optics, T_a is the one-way atmospheric transmission and T_c is the one-way transmissivity of the cirrus clouds.

The cross section is the most important parameter that takes into account the satellite properties: mainly the corner cube geometry and optical properties. For a single unspoiled retroreflector, at normally incident light, we have a peak optical cross-section, defined by:

$$\sigma_{cc} = \rho A_{cc} \left(\frac{4\pi}{\Omega} \right) \tag{5.12}$$

where: ρ is the corner cube reflectivity, A_{cc} is the light collecting area of the corner cube, Ω is the effective solid angle occupied by the far field diffraction pattern of the retroreflector.

As defined in [39], for a circular entrance aperture, the cross section becomes:

$$\sigma(x) = \sigma_{cc} \left(\frac{2J_1(x)}{x} \right)^2 \tag{5.13}$$

in which:

$$x = kR_{cc} sin(\theta) \tag{5.14}$$

and R_{cc} and θ are respectively the radius of the collecting area of the corner cube and the angle from the cube face normal. J_1 is a Bessel function. The slant distance R can be evaluated by:

$$R = -(R_E + h_t)cos\theta_{ZEN} + \sqrt{(R_E + h_t)^2 cos^2\theta_{ZEN} + 2R_E(h_s - h_t) + h_s^2 - h_t^2} \tag{5.15}$$

where: R_E is the Earth radius, h_t is the SLR station height above the sea level, h_s is the satellite altitude above the sea level and θ_{ZEN} is the zenith angle of the satellite as observed from the station.

The transmitter gain for a mode-locked laser (the most useful for modern SLR) is given by the expression:

$$G_t(\theta) = \frac{8}{\theta_t^2} e^{-2(\frac{\theta}{\theta_t})^2} \tag{5.16}$$

in which θ_t is the far field divergence half-angle between the beam center and the $1/e^2$ intensity point and θ is the beam pointing error.

5.4.1 Model of the measurement setup

A real Stokes parameter measurement setup involves four simultaneous measures on four different polarization bases. This means that incoming photons are splitted on four differents optical paths (one for each polarization base) ending on an avalanche photodiode (APD).

Taking into account the real optical efficiency, the photon flux at the entrance aperture of each APD becomes:

$$N_{APD} = \eta_0 \frac{N_{pe}}{4} \tag{5.17}$$

5.4.2 SNR

To complete the link analysis, we are going to introduce the signal-to-noise ratio (SNR). This parameter will play an important role to establish the goodness of the measurements and so the experiment feasibility. As defined in [50] for an optical receiver based on APDs the SNR is defined as:

$$SNR = \left(\frac{m_1 - m_0}{\sigma_1 + \sigma_0} \right)^2 \tag{5.18}$$

in which m_1 and m_0 are the mean electron-hole pairs per pulse respectively when a pulse is detected or not and σ_1^2 and σ_0^2 are their variances.

The mean values can be evaluated by:

$$m_1 = (N_{APD} + \lambda_0 T + N_b T)G \tag{5.19}$$

$$m_0 = (\lambda_0 T + N_b T)G \tag{5.20}$$

where λ_0 are the pairs spontaneously generate in the APD, that are not related to photons, N_b is the pairs flux due to background noise and G is the mean APD gain. In the same way, the variances, in a Gaussian approximation are:

$$\sigma_1^2 = (N_{APD} + \lambda_0 T + N_b T)G_2 + N_A^2 \tag{5.21}$$

$$\sigma_0^2 = (\lambda_0 T + N_b T)G_2 + N_A^2 \tag{5.22}$$

where G_2 is the variance on the APD gain and N_A is the merit figure of the amplifier. In some cases is known the ionization coefficient γ that is related to the APD gain by:

$$F = \frac{G_2}{G^2} = \gamma G + \left(2 - \frac{1}{G}\right)(1-\gamma) \tag{5.23}$$

and the noise spectral density R_i from which the merit figure becomes:

$$N_A = \frac{\sqrt{R_i T}}{e} \tag{5.24}$$

5.4.3 Simulation results

To complete the experiment scenario and do simulations, we also need the informations related to the Stokes parameters measurement setup (polarimeter). For our measurement setup we can assume an optical efficiency η_0 of 0.9 and for APDs we can use parameters in table 5.3:

Quantum efficiency η_q	0.7
Gain G	100
Ionization coefficient γ	0.05
Detection time T	$10ns$
Dark pairs generated on APD λ_0	$3.12 \cdot 10^8 pairs/s$
Noise spectral density R_i	$10^-24A^2/Hz$
Pair due to background noise N_b	$20pairs/s$

Table 5.3: Measurement set up parameters

With these data, we estimated the link budget for the Matera station. The results helped us in designing the polarimeter. The simulations performed for Goce are reported in table 5.4: SNR at the minimum and maximum satellite visibility.

Satellite	SNR min	SNR Max
Goce	25.92	56.12

Table 5.4: Matera-Goce-Matera link budget

The high values of SNR obtained, assure the experiment feasibility . The simulation results can be properly extended for others satellites.

Chapter 6

SPOLAR-M experiment

In the previous chapter we introduced the problem of light polarization preservation for single photons space QC. After a theoretical analysis of the problem, we modeled and simulated the space channel, taking advantage of the yet existing laser ranging facilities (SLR) to experimentally realize a quantum channel on space scale.
The simulation showed the link budget required for Earth-space and space-Earth single photon channel, and justify the use of Laser Ranging sites to experimentally test the link. In this chapter after a brief introduction on Stokes Polarimetry (for more details see [55]), will be presented the polarimeter used at the MLRO: designed and developed at the Luxor Laboratory.

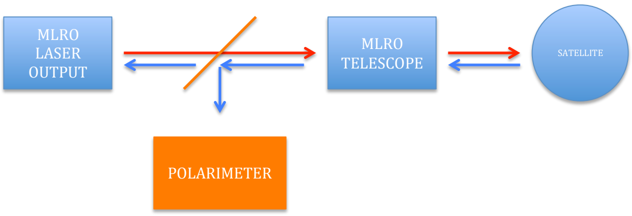

Figure 6.1: Schematic of the polarimeter with the laser ranging facility

6.1 Stokes polarimetry

A set of elements that analyses the polarization state of incoming light is called polarization state analyser (PSA).
A Stokes polarimeter is a PSA able to measure the Stokes parameters or some of them. A Stokes polarimeter is defined complete if it measures all the four elements of the Stokes vector, and incomplete if it measures less than four. In the sections below are reported a set of techniques used to realize polarimeters.

6.1.1 Division of Wavefront Polarimetry

Wavefront division relies on analysing different parts of the wavefront with separate polarization elements. This has been done using a pair of boresighted cameras that were flown on the space shuttle [96], [41]. A linear polarizer was placed in front of each camera where the polarizers were orthogonal to each other. Chun et al. [36] have performed wavefront division polarimetry using a single infrared camera. Metal wire-grid polarizers were formed on a substrate using microlithography in the pattern shown in figure 6.2. This wire-grid array was placed in front of the detector array so that light from different parts of the object space pass through different polarization elements and on to different detectors. Each detector element of the infrared focal plane array has its own polarizer. These polarizers are linear polarizers at four different orientations, as shown in figure 6.2, and the pattern is repeated up to the size of the array. There are no circular components measured and thus this is an incomplete polarimeter.

The advantage of this polarimetric measurement method is the simultaneous measurement of the Stokes vector elements available from the polarization element array. The reduction in resolution of the detector by the number of different polarization elements and the spatial displacement of information within the polarization element pattern are disadvantages.

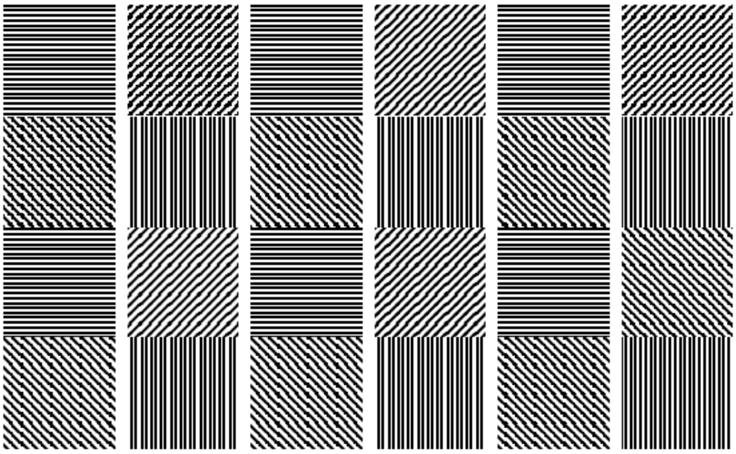

Figure 6.2: Pattern of micropolarizers in a wavefront division polarimeter.

6.1.2 Division of Amplitude Polarimetry

In amplitude division polarimetry, the energy in the entire wavefront of the incident beam is split and analysed before passing to detectors. The detectors should be spatially registered so that any detector element is looking at the same point in space as all other detector elements. This method can employ as few as two detectors with analysis of two orthogonally polarized components of light, or it can measure the complete Stokes vector using four detectors. There are a number of variations of division amplitude polarimeter.

Four-Channel Polarimeter using Polarizing Beam Splitters

A diagram of a four-channel polarimeter is shown in figure 6.3. This polarimeter uses three polarizing beam splitters and two retarders. Readings are made at four detectors. The input Stokes vector is determined from the four detectors measurements and from use of a transfer Mueller matrix found during the calibration procedure. The polarizing beam splitters have transmissions of 80% and 20% for the parallel and perpendicular components. A quarter-wave retarder before detectors 1 and 2 is oriented at 45° and the half-wave retarder before detectors 3 and 4 is oriented at 22.5°.

The advantage of this system is the simultaneous measurement of all four Stokes components for each point in object space. Care must be taken to ensure spatial registration of the detectors and equalization of detectors responses.

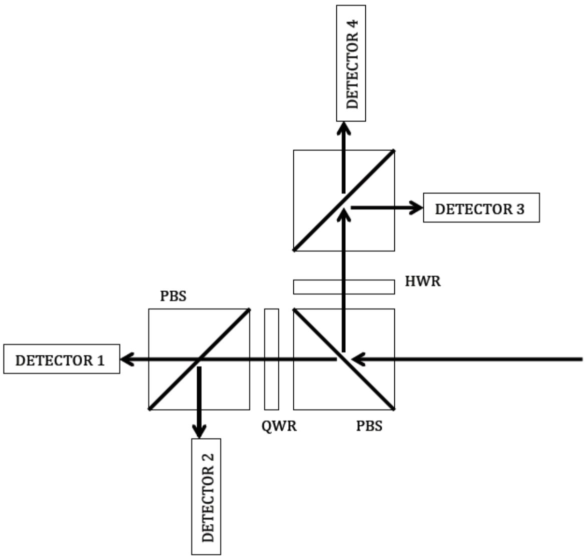

Figure 6.3: A four-channel polarimeter. PBS is a beam splitter, QWR is a quarter-wave retarder, and HWR is a half-wave retarder.

Four-Channel Polarimeter using Non Polarizing Beam Splitter

This is the set-up chosen for the SPOLAR-M experiment. This polarimeter use two non polarizing beam splitters, a quarter-wave retarder, a polarizing beam splitter and two linear polarizers. Readings are made at four detectors. The input Stokes vector is determined from the four detector measurements and from use of a transfer Mueller matrix found during the calibration procedure. In figure 6.4 the optical scheme is reported: the polarizer in front of channel 3 is rotated at 45°, also the quarter wave plate of channel 4, followed by an horizontal linear polarizer, is rotated at 45°.
The intensity at the four channel of the polarimeter are respectively: I_H the horizontal component at channel 1, I_V the vertical components at channel 2, I_+ the linear 45° at channel 3, and I_R the circular right-handed at channel 4.

The signals read by the four channels are related to the Stokes vector of the incoming state as follows: in each channel the initial polarization state, pass trough a set of polarizing optics. Detectors at the end of the polarimeter arms, read the intensities on the four polarization bases. The overall outgoing intensity, corresponds to the S_0 parameter of the output Stokes vector.
For the moment we will consider the same intensity at the input of each arms of the polarimeter, as if the splitting action does not affect the power level of the wave. In the first channel the light pass trough a linear polarizer, hence the output state will be:

$$S_H = M_H S_i = \frac{1}{2}\begin{bmatrix} 1 & 1 & 0 & 0 \\ 1 & 1 & 0 & 0 \\ 0 & 0 & 0 & 0 \\ 0 & 0 & 0 & 0 \end{bmatrix}\begin{bmatrix} S_0 \\ S_1 \\ S_2 \\ S_3 \end{bmatrix} \tag{6.1}$$

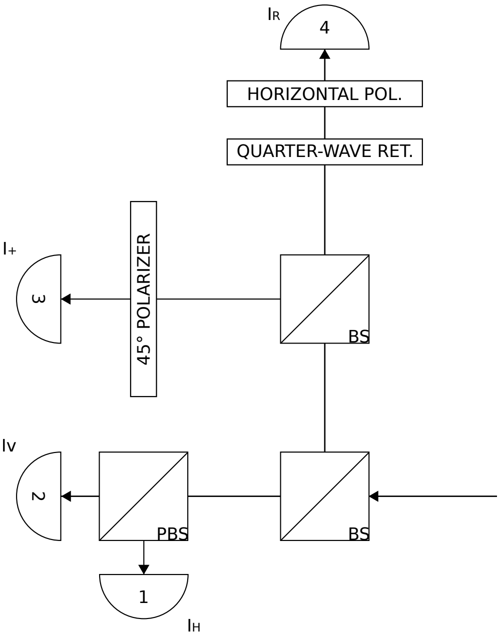

Figure 6.4: Scheme of the polarimeter for SPOLAR-M experiment. PBS is a polarizing beam splitter, BS is a beam splitter.

where S_i is the Stokes vector of the input state, and M_H is the Mueller matrix of an horizontal polarizer.
The intensity at the detector will be:

$$I_H = \frac{1}{2}(S_0 + S_1) \tag{6.2}$$

The second channel is formed by a vertical polarizer and the corresponding output state will be:

$$S_V = M_V S_i = \frac{1}{2}\begin{bmatrix} 1 & -1 & 0 & 0 \\ -1 & 1 & 0 & 0 \\ 0 & 0 & 0 & 0 \\ 0 & 0 & 0 & 0 \end{bmatrix}\begin{bmatrix} S_0 \\ S_1 \\ S_2 \\ S_3 \end{bmatrix} \tag{6.3}$$

where M_V is the Mueller matrix of a vertical polarizer.
The intensity at the detector will be:

$$I_V = \frac{1}{2}(S_0 - S_1) \tag{6.4}$$

The third channel is formed by a 45° linear polarizer, the output state will be:

$$S_+ = M_+ S_i = \frac{1}{2}\begin{bmatrix} 1 & 0 & 1 & 0 \\ 0 & 0 & 0 & 0 \\ 1 & 0 & 1 & 0 \\ 0 & 0 & 0 & 0 \end{bmatrix}\begin{bmatrix} S_0 \\ S_1 \\ S_2 \\ S_3 \end{bmatrix} \tag{6.5}$$

where M_+ is the Mueller matrix of a 45° linear polarizer.
The intensity at the detector will be:

$$I_+ = \frac{1}{2}(S_0 + S_2) \tag{6.6}$$

The fourth channel is formed by an half-wave retarder at 45° followed by an horizontal polarizer, its output state will be:

$$S_R = M_H M_{HV} S_i = \frac{1}{2}\begin{bmatrix} 1 & 1 & 0 & 0 \\ 1 & 1 & 0 & 0 \\ 0 & 0 & 0 & 0 \\ 0 & 0 & 0 & 0 \end{bmatrix}\begin{bmatrix} 1 & 0 & 0 & 0 \\ 0 & 0 & 0 & -1 \\ 0 & 0 & 1 & 0 \\ 0 & 1 & 0 & 0 \end{bmatrix}\begin{bmatrix} S_0 \\ S_1 \\ S_2 \\ S_3 \end{bmatrix} \tag{6.7}$$

where M_{HV} is the Mueller matrix of an half-wave retarder at 45°and M_H is the Mueller matrix of an horizontal polarizer .
The intensity at the detector will be:

$$I_R = \frac{1}{2}(S_0 - S_3) \tag{6.8}$$

In matrix form, we can relate the input Stokes vector to the outputs intensities, by:

$$I = AS_i = \frac{1}{2}\begin{bmatrix} 1 & 1 & 0 & 0 \\ 1 & -1 & 0 & 0 \\ 1 & 0 & 1 & 0 \\ 1 & 0 & 0 & -1 \end{bmatrix}\begin{bmatrix} S_0 \\ S_1 \\ S_2 \\ S_3 \end{bmatrix} \tag{6.9}$$

where A is the matrix that maps the Stokes parameters to the channel intensities.
Inverting this relation, we can reconstruct the input Stokes parameters, known the vector of the intensities of the 4 channels:

$$S_i = A^{-1} I \tag{6.10}$$

from which we obtain the following relation:

$$\begin{bmatrix} S_0 \\ S_1 \\ S_2 \\ S_3 \end{bmatrix} = \begin{bmatrix} I_H + I_V \\ I_H - I_V \\ 2I_+ - I_H - I_V \\ I_H + I_V - 2I_R \end{bmatrix} \tag{6.11}$$

Now, considering the splitting action, that reduces the power at channels 1 and 2 by a factor 1/2 and the power at channels 3 and 4 by 1/4, the equation 6.9 becomes:

$$I = AS_i = \frac{1}{8}\begin{bmatrix} 2 & 2 & 0 & 0 \\ 2 & -2 & 0 & 0 \\ 1 & 0 & 1 & 0 \\ 1 & 0 & 0 & -1 \end{bmatrix}\begin{bmatrix} S_0 \\ S_1 \\ S_2 \\ S_3 \end{bmatrix} \tag{6.12}$$

from which we obtain the following relation:

$$\begin{bmatrix} S_0 \\ S_1 \\ S_2 \\ S_3 \end{bmatrix} = \begin{bmatrix} 2(I_H + I_V) \\ 2(I_H - I_V) \\ 2(4I_+ - I_H - I_V) \\ 2(I_H + I_V - 4I_R) \end{bmatrix} \tag{6.13}$$

6.2 Polarimeter design

In this section will be discussed the design of an intensity polarimeter to be integrated with the Matera laser ranging facility. The design will be oriented in order to reduce the changes to the existing setup and to ensure the normal operation of the station. The polarimeter is formed by three sections:

- Optics
- Electronic
- Mechanical

6.2.1 Optical design

By designing the polarimeter, as first, we had to take into account this requirements, related to Laser Ranging technologies and limits and :

- The dimension of the laser ranging beam ($\varnothing = 45mm$)
- The velocity aberration: it is the tilt of the wavefront of the ranging beam compared to the telescope optical axis. This effect is induced by the satellite movements that require a continuous tracking. The unavoidable inaccuracy on this operation cause a tilt on the wavefront collected that appears as movements on the detectors focal planes.

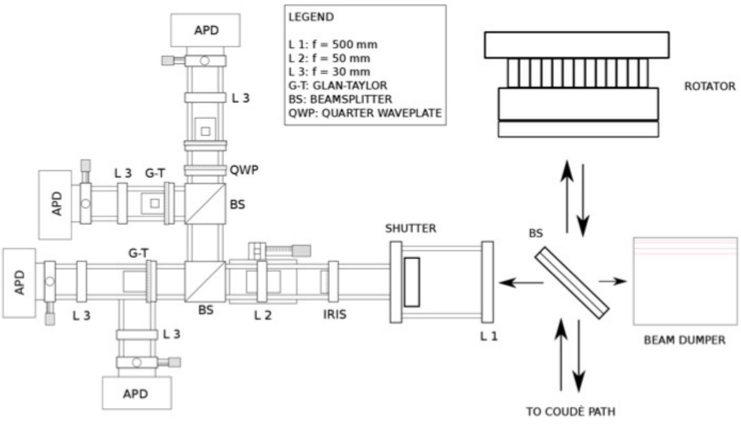

Figure 6.5: Polarimeter optical scheme

For this reasons the incoming beam is reduced in size by a $5X$ Keplerian beam reducers formed by two positive lenses ($f = 500mm \varnothing = 2”$, $f = 100mm \varnothing = 1”$). In the final setup the lenses distance has been setted to $l = 450mm$ to get a collimated beam of $d = 3mm$ from the uncollimated MLRO telescope. A non polarizing beam splitter (NPBS) send the collimated beam into two orthogonal direction: the transmitted portion into the *Horizontal-Vertical* channels and the reflected one into the *Right Circular*-$+45\circ$ *linear* channels. In the former case a Glan-Taylor polarizer split the beam into the *Horizontal* channel -the transmitted portion - and *Vertical* channel -the reflected portion. The reflected portion is in turn splitted again by an other NPBS for the *Circular* and $+45\circ$ *linear* channels: respectively formed by a quarter wave plate (QWP) followed

by a Glan-Taylor polarizer and by a Glan-Thomson polarizer. In the end, the light of each channel is focused with a $f = 50mm$ $\varnothing = 1$" lens into an avalanche photodiode (APD).
All the system is assembled in a cage system that simplify the assembly, alignment and operations and improve the portability of the instrument.

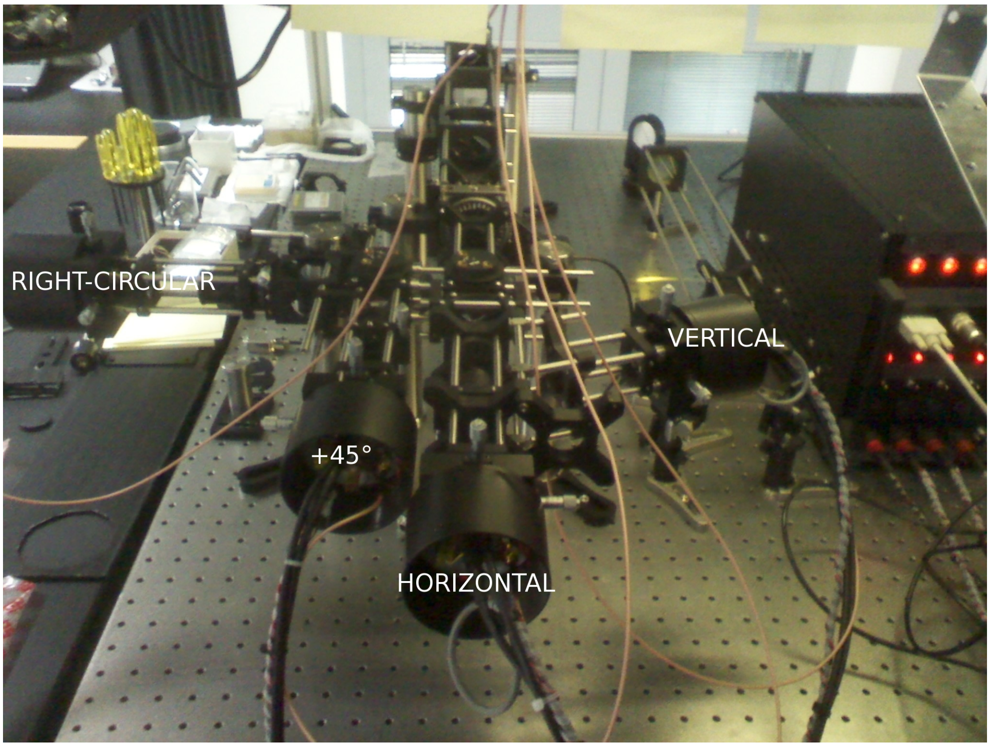

Figure 6.6: Photo of the polarimeter for SPOLAR-M experiment.

6.2.2 Mechanical design

The polarimeter has a set of mechanical components needed to integrate it with the Matera Laser Ranging Facility. The polarization state of the ranging laser is changed by rotating the quarter wave plate of the Matera facility, that in normal conditions transforms the linear polarization of the output laser into circular. At this purpose a new motorized holder has been designed and realized. Again, a beamsplitter has to be inserted in the output optical path to send the incoming light from satellite into the polarimeter and consequently a beam dump to stop the reflected portion of the high energy pulses. The mechanical parts are listed below:

- A beam splitter holder used to fix the output beam splitter to the Matera facility optical bench. In figure 6.7 its CAD design is reported.

  A photo of the installation at the MLRO motorized translator is reported in figure 6.8.

- A rotator for the Matera quarter wave plate retarder that allows us to change the output polarization state. In figure 6.9 the CAD design of the flange is reported.

  Coaxially with the central hole of the flange is mounted a crown with ball bearings, retained by a set of screws inserted around the hole. A separation gasket (see Fig.6.10) combines the

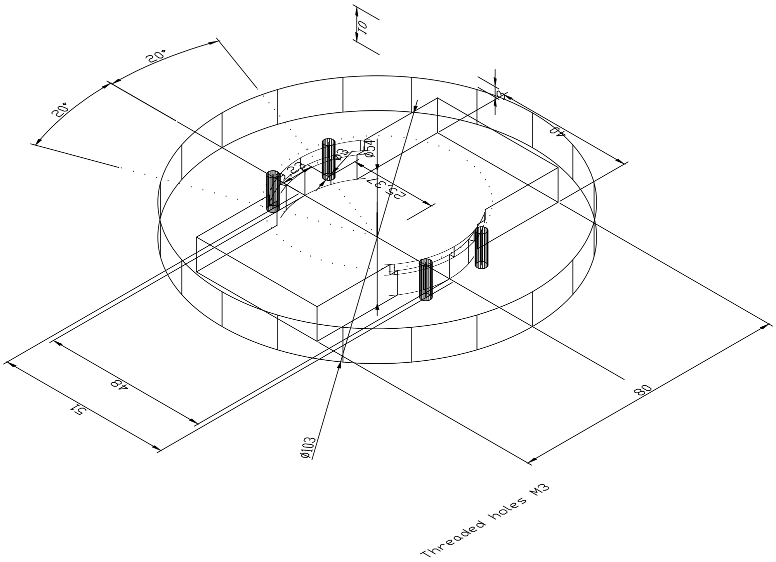

Figure 6.7: Beam splitter holder

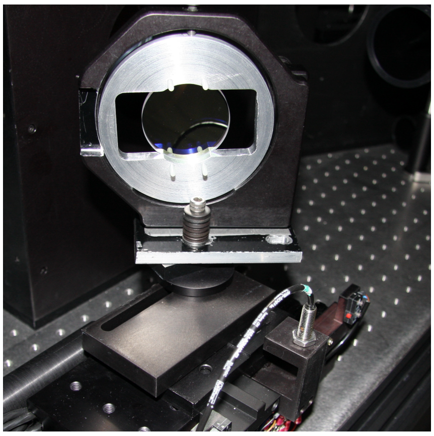

Figure 6.8: Beam splitter holder @ MLRO

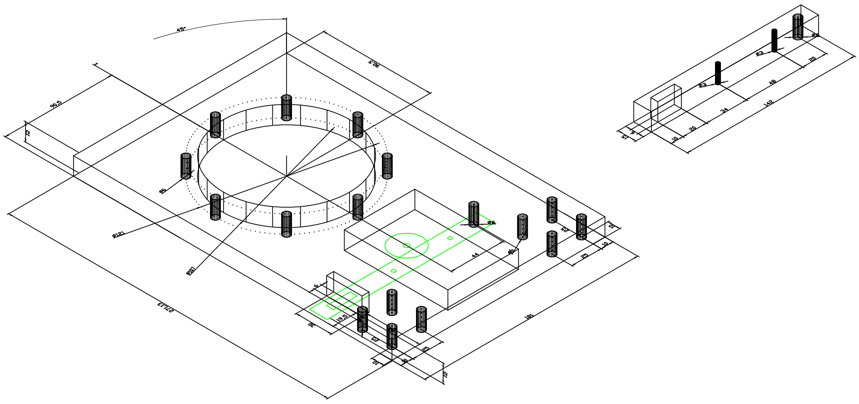

Figure 6.9: Rotator flange

ball bearing crown with a pulley (see Fig. 6.11) in whose head is mounted the quarter wave plate holder. The pulley, connected to the motor pulley, via a toothed belt transmits the motion to the wave plate holder, rotating it up to the desired position.

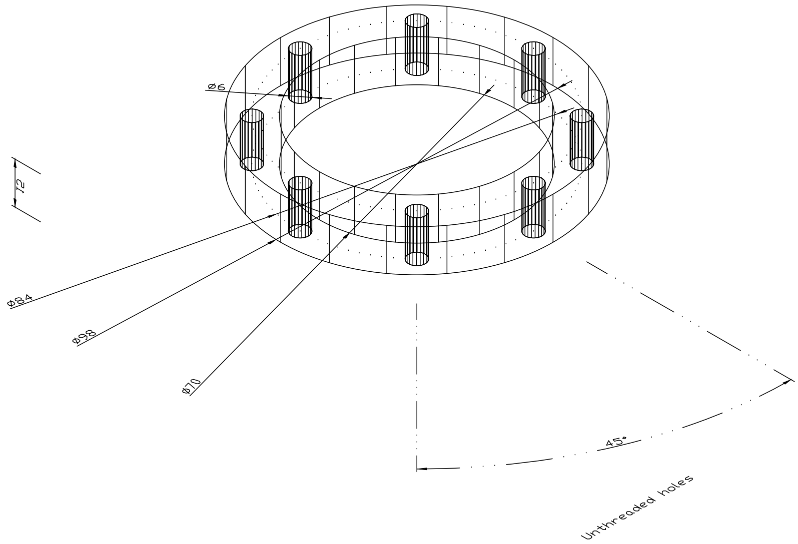

Figure 6.10: Separation gasket

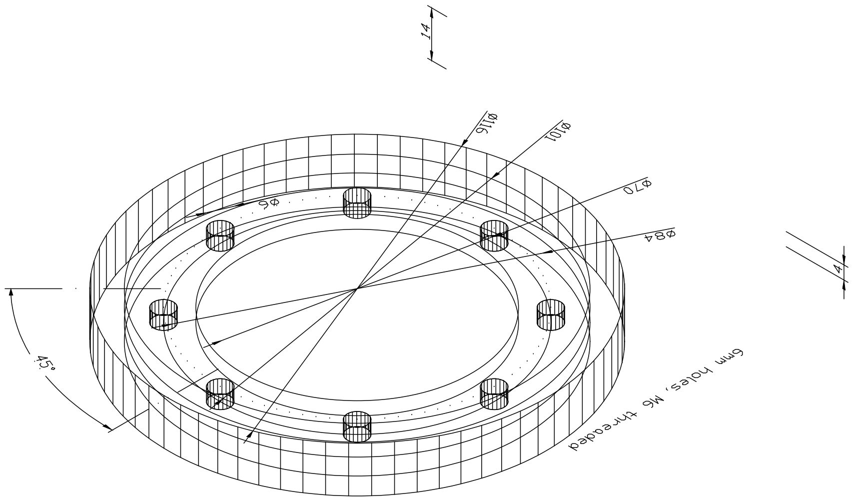

Figure 6.11: Pulley

- An holder for the Matera quarter wave plate retarder that protects the wave retarder and allows to mount it in the rotator.
- A beam dump from Standa [16], whose drawing is reported in figures 6.13, stops the portion of high energy laser light that inevitably is reflected by the output beam splitter. If the light is not blocked it should be a source of noise for detectors and should damage them.

  Pictures of the beam dump in the MLRO optical bench is reported in figure 6.14.

A stepper motor remotely controlled allow the rotation of the waveplate during the measurement. The stepper motor whose connection scheme is reported in figure 6.15

is a 4 phases (6 wires) motor with 600 steps per rev., the maximum holding torque is of $53.6Ncm$ and operating in uni-polar mode the maximum current per phase is of $0.55A$. The internal gear ratio is of 25 : 2. This kind of motor can be used in unipolar or bipolar mode. The motor controller (see figure 6.16) provides a PC remote control via an RS232 interface and an optoisolated driver section. The motor can be driven remotely, specifying also the "electronic gear" or microstep and the current profile. The step frequency can span from $63Hz$ up to $60kHz$. To operate the motor in bipolar mode, according with figure 6.15, the phases common terminations are not connected. The first phase corresponds to leads 1 and 2 and the second one to leads 3 and 4.

Motor Lead	1 (Yellow)	2 (Orange)	3 (Brown)	4 (Black)
Control Driver PIN	C2	C6	C4	C8

Table 6.1: Motor to Controller driver connections

The motor power supply applies to pins C10-C12 a voltage of $8V$.

With our gear system, described in figures (6.9, 6.10, 6.11) the rotation to step ratio is of $1/640[°/step]$

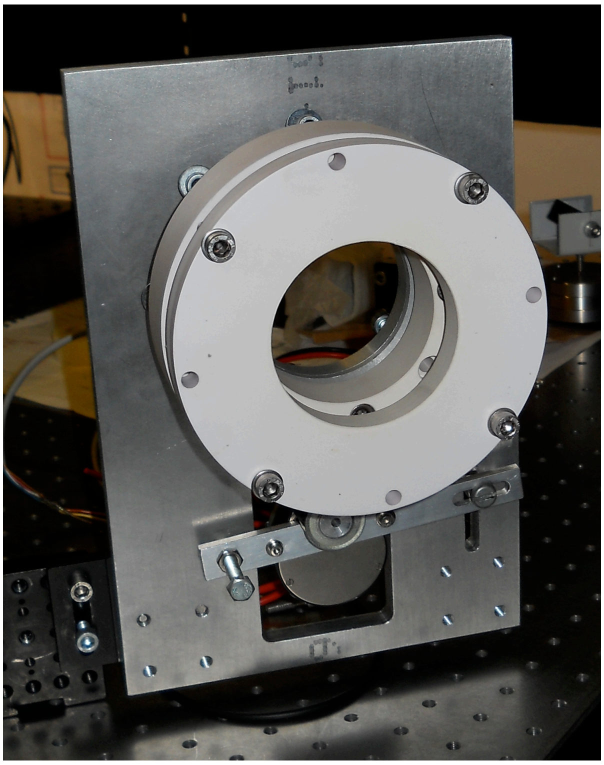

Figure 6.12: Picture of the quarter wave plate holder

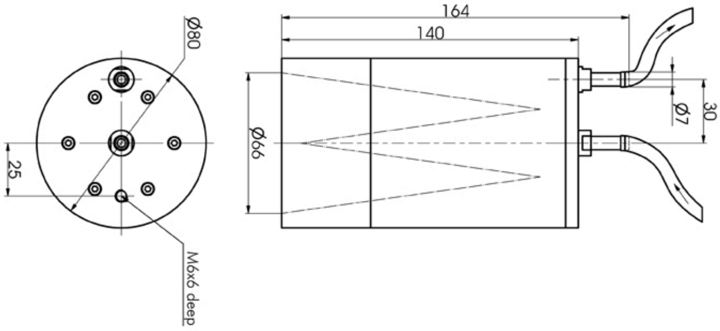

Figure 6.13: Beam dump

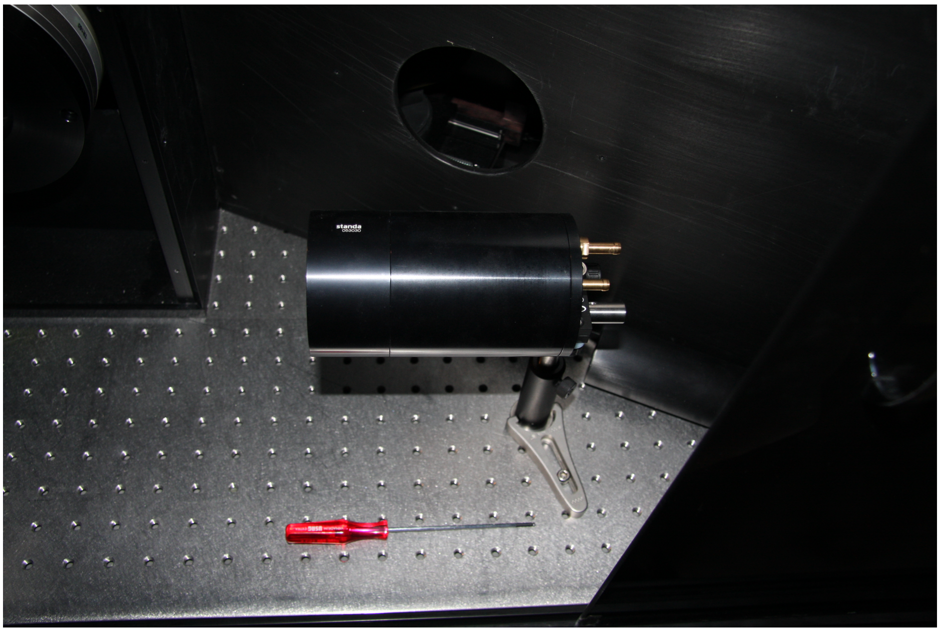

Figure 6.14: Beam dump top view

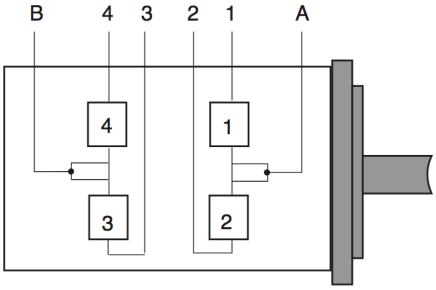

Figure 6.15: Stepper motor connection scheme

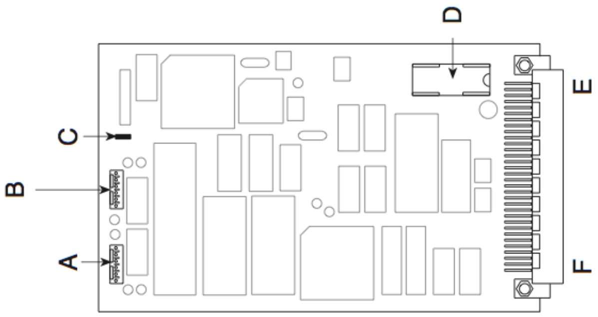

Figure 6.16: Motor controller scheme

6.2.3 Electronic design

For each channel of the polarimeter we have a laser pulse whose intensity is proportional to the level of polarization of the incoming light. To reconstruct the polarization state we need to measure the relative intensities of the four channels. The detectors have to satisfy the following requirements:

- High sensitivity to detect the faint signal retroreflected from the satellite
- High bandwidth to detect the short pulses of the laser ($40ps$)
- Large active area to compensate the velocity aberration

The avalanche photodiodes are the solution that meet all these requirements. We chose the SAR3000 T6 from Laser Components [11] for their short rise time of $500ps$ corresponding to a bandwidth of $700MHz$ and for the large sensitive area of $3mm$ of diameter. Furthermore they have an avalanche gain of 100 that means that a single photon can give rise to 100 electrons. In the table below are summarized the technical specifications of this device.

APD

The avalanche photodiodes (APD) are high speed and high sensibility photodiodes, that exploit an internal avalanche amplification system, based on high voltage reverse biasing.

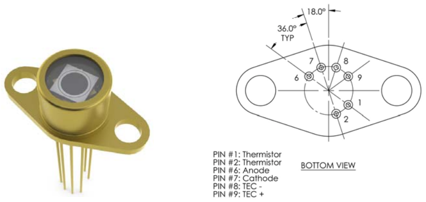

(a) Picture (b) Pin out

Figure 6.17: APD SAR3000T6

Some common definitions that describe the photo-conversion performance are:

- *Photo sensitivity:* is the ratio between the radiant power [W] and the photocurrent [A]: $S = A/W$. If it is normalized for the sensitivity at the peak wavelength it represent a relative sensitivity.
- *Quantum Efficiency:* the ratio between the electrons or holes detectable as photocurrent and the incidents photons $QE = (S \cdot 1240/\lambda) \cdot 100$
- *Spectral response:* the photocurrent generated depends on wavelength. Compared with a photodiode, the spectral response of an APD is subjected to the wavelength dependance of the avalance multiplication effect.
- *Dark current:* is the current that flows in a biased photodiode in absence of incident light.
- *Shunt resistance:* is the ratio voltage over current in the proximity of $0V$. $R_{sh} = 10[mV]/I_D$ where I_D is the dark current at $10mV$.
- *Terminal capacitance:* is the capacitor formed in the p-n junction, and it is the main factor affecting the time response of the photodiode.

- *Cut-off frequency:* is the frequency at which the photodiode output decreases by $3dB$ from the output at $100kHz$ with a load resistance of 50Ω $f_c = 1/(2 * \pi C_t R_L)$
- *Rise time:* is the time required to the output to change from 10% to 90% of the steady output level $tr = 0.35/f_c(CR)$
- *Noise Equivalent Power (NEP):* is the light intensity equivalent to the noise level of the device, is the level of light required to obtain a signal to noise ratio of unity.

The APD, whose internal structure is reported in 6.18, is bases on a PN junction like each other photodiodes but differs from them for the use of avalanche effects to get amplification of the generated photocurrent. This gain is related to the generation of electron-hole pairs via high energy electrons that give rise to an avalanche discharge process.

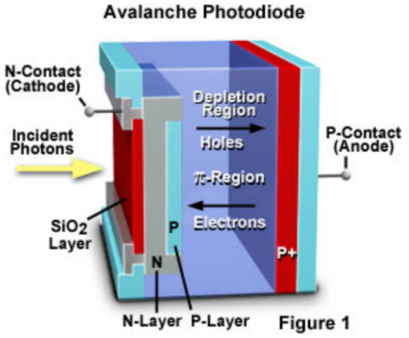

Figure 6.18: APD internal structures. Image from [2]

The photons enter from the Silicon Dioxide interface and in the PN region generates electron-hole pairs that migrate respectively towards the anode and the cathode. The high biasing voltage increases the kinetic energy of the electrons giving rise to collisions with the lattice which ionizes and generates other electron-hole pairs that in turns form other pairs with a multiplication avalanche effects, that is defined by the gain M. The number of electron-hole pairs generated by the carrier when they pass through a certain distance is called ionization rate: α for electrons and β for holes. The ratio $k = \beta/\alpha$ called ionization rate is useful to define the noise level of the device.
The amplification factor M of an APD is related to the electric field applied to the layers in which the avalanche takes place: it increases with the bias voltage.
Over a certain bias voltage the photocurrent loses its proportionality with the intensity of the incident light: this effect, due to lowering in voltage in the avalanche region imposes a limit in the bias voltage. It is caused by the current that flows in the load and series resistance of the photodiode.
The gain is also dependent to temperature: infact, the lattice of the photodiode vibrates more increasing the temperature. Consequently the carries collide with the lattice before having reached the energy for ionization and avalanche.
To maintain a constant output response, it is necessary to adjust the bias voltage according to temperature variations or keep the temperature constant. The multiplication process is subjected to statistical fluctuations and generates noise ("excess noise"), the APD noise current can be expressed as:

$$I_n^2 = 2q(I_L + I_{dg})BM^2F + 2qI_{ds}B \tag{6.14}$$

where:

- q is the electron charge
- I_L is the photocurrent at $M = 1$
- I_{dg} is the dark current component subjected to the multiplication process
- I_{ds} is the dark current component not subjected to the multiplication process
- B is the bandwidth
- F is the excess noise factor

In figure 6.19 is reported the noise characteristic of the APD.

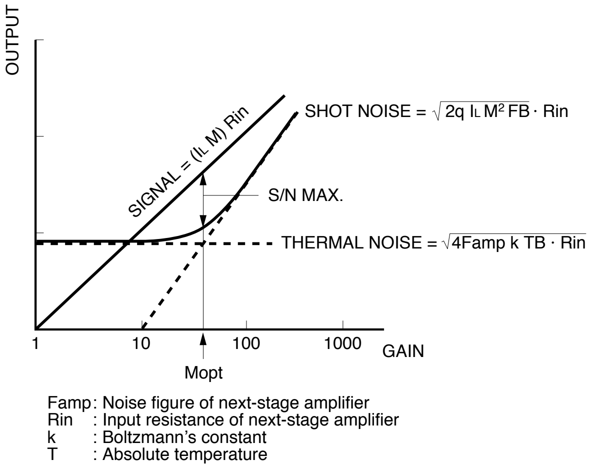

Figure 6.19: APD noise characteristic From Photodiode technical information-Hamamatsu

In figure 6.20 the equivalent circuit of an APD is reported.

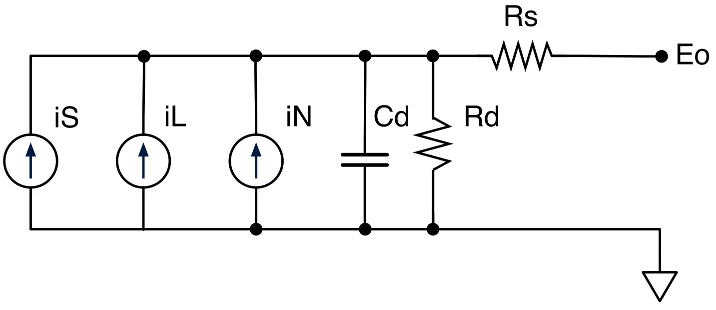

Figure 6.20: APD equivalent circuit

where

- iS is the signal current
- iL is the leakage current

- iN is the noise current
- Cd is the junction capacitance
- Rd parallel shunt resistance
- Rs series resistance

In the table below are summarized some specifications of the APDs SAR3000T6:

	Min	Typ	Max	Units
Wavelength Range	400		1000	nm
Peak Sensitivity		905		nm
Diameter		3		μm
Breakdown Voltage @ $I_d = 10\mu A$	200	300		V
Responsivity @ $\lambda(peak)$ & $M = 100$	50	60		A/W
$V_{br} Temperature Coefficient$		2	3.2	$V/°C$
Dark Current @ $M = 100$		1	10	nA
Noise Current @ $M = 100$		0.5	1.5	$pA/\sqrt(Hz)$
Capacitance @ $M = 100$		7		pF
Rise Time @ $M = 100$		500		ps

Table 6.2: Parameters of the SAR3000 T6 APD

In figure 6.21 is reported the APD gain as a function of the biasing voltage: few hundreds volts are required for a gain of 100. We have also to consider that the gain is strictly related to temperature. Power dissipation while operating or environmental temperature variation can induce gain variations and so affect the measured signal. An high voltage power supply and a temperature control system is required to get an effective and accurate measurement.
The SAR3000 T6 APDs are provided with an internal thermistor and a Peltier cell that must be driven properly to keep the junction temperature constant.

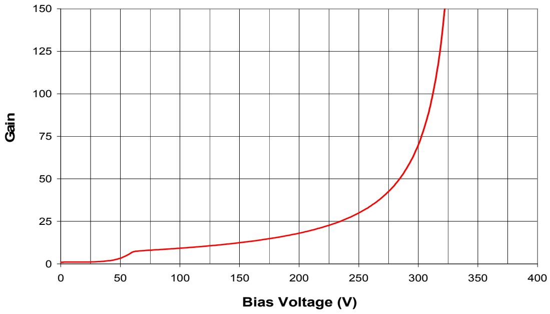

Figure 6.21: Gain vs Bias Voltage

Figure 6.21 indirectly also suggest the kind of electronic we will have to use to read the signal: the photocurrent. Variations on the APD biasing, that is the voltage across the photodiode, imply gain variations. A reading electronic should be able to detect the photocurrent without inducing voltage variations: this is done by a transimpedance amplifier also called: *Current to Voltage converter*. Using the information provided on the SAR3000 T6 datasheet we are going to roughly estimate some APD parameters; once defined the APD gain we can obtain the dark current from the dark noise density as:

$$I_{DK}(M) = N_D(M) * sqrt(BW) \tag{6.15}$$

The dark current I_{DK} at $M = 100$ is of $10nA$. At the temperature of 25° the bias voltage required for a gain of 100 is of $312V$ and for a constant gain the bias voltage must be decreased approximatively of $2V/°C$, so for a gain of 100 at $5/°C$ the bias voltage must be adjusted to $272V$.

APD biasing

The direct current (DC) APD biasing is simply realized trough a full bridge rectifier that converts the bipolar voltage of the power line into an unipolar one; a second stage with a linear regulator LR8 from Supertex [17] regulates the voltage within an adjustable range from $1.2V$ up to $330V$. The power supply PCB board provides four separated and independently adjustable output voltages, one for each APD.
A second sub PCB provides start up current limits and optoisolated switches for safely operations. In the figures 6.22 and 6.23 are reported the electrical schemes and the PCB layouts of the power supply.

APD signal reading

The APD photocurrent is collected by an high speed transimpedance amplifier whose electrical scheme is reported in figure 6.24. The amplifier is based on the AD8000 (Analog Devices [6]) CFB operational amplifier that has allowed to reach a bandwidth of $800MHz$.

In table 6.3 are reported the values of the components of the preamplifier circuits.
The transimpedance gain is related to the value of the feedback resistance R_F

	R_F (R1)	R_{BIAS} (R4)	R_{IN} (R2)	R_+ (R3)
Channel 1	139.2	1.237k	42.5	211
Channel 2	168.2	1.087k	41.8	207.3
Channel 3	137.9	1.119k	42.2	210.3
Channel 4	137.6	1.064k	42.9	210.6

Table 6.3: Parameters of the transimpedance amplifier

A screen shot of the acquisition oscilloscope TDS 6124C, displaying the signals of the four APDs is reported in fig. 6.25.

APD temperature stabilization

The temperature stabilization is implemented in each APD via a feedback loop: the temperature transducer is the NTC thermistor inside the APD package whose resistance-temperature curve is reported in Fig. 6.26

The APD SAR3000T6 also contains a thermoelectric cooler (TEC): a Peltier cell whose maximum ratings are: $1.9A$ and $0.8V$. The temperature controllers are TC LV-Series modules from Electron Dynamics [9]. They are USB programmable and can operate in differents control modes:

- On/Off temperature control.
- Proportional, Integral and Derivative that can be operated separately or together.

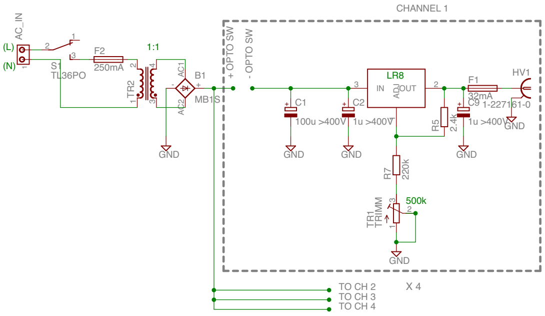

(a) High voltage power supply scheme

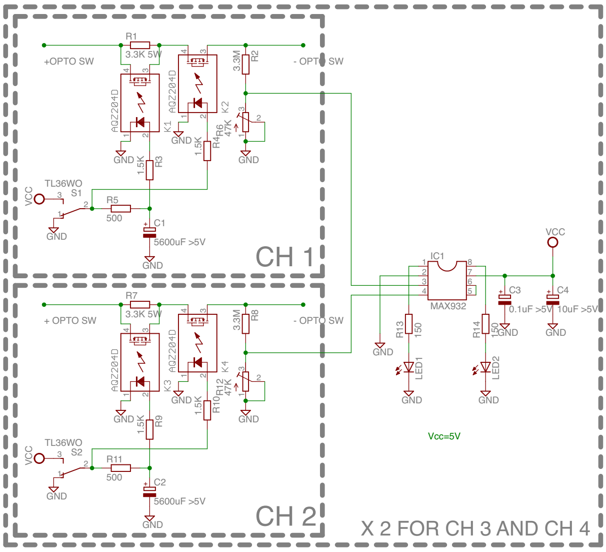

(b) Optoisolated switches scheme

Figure 6.22: Electrical schemes of the high voltage power supply and optoisolated switches

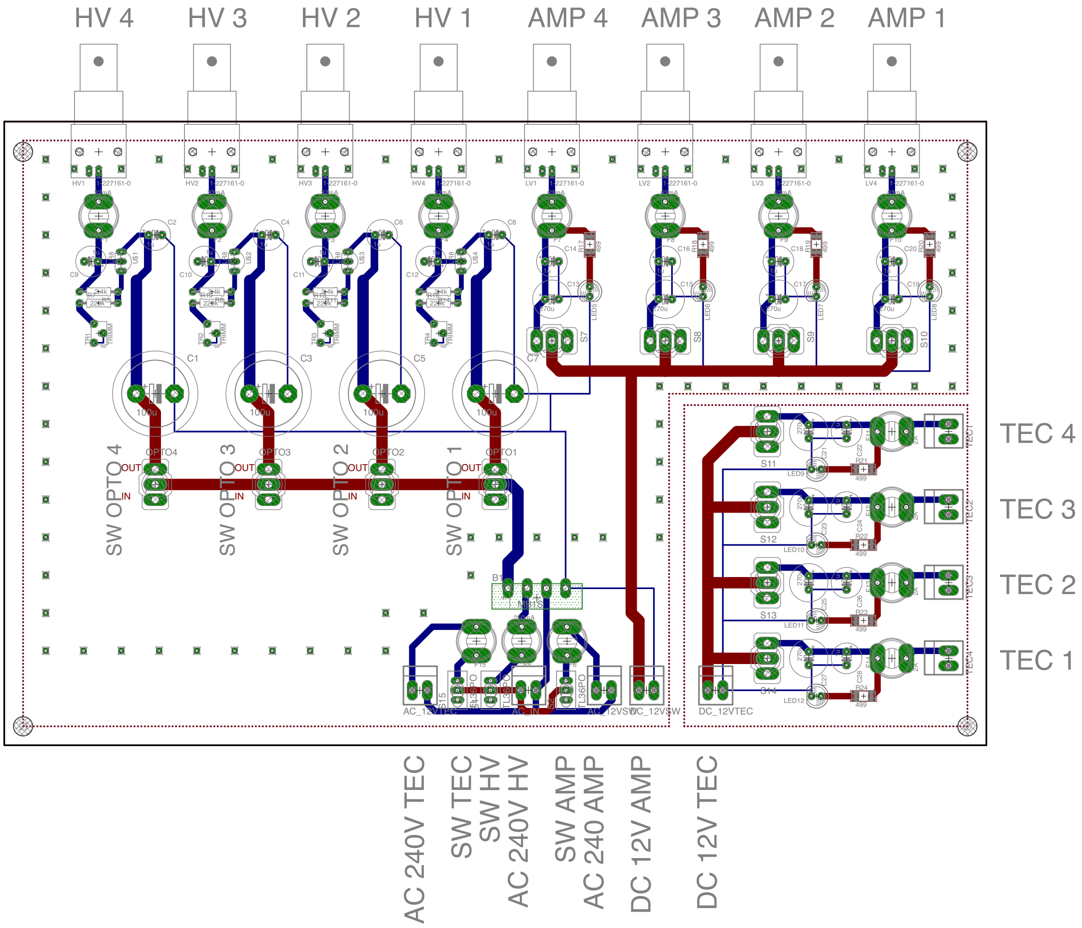

(a) High voltage power supply PCB layout

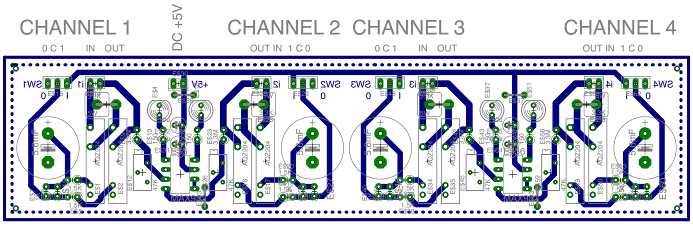

(b) Optoisolated switches PCB layout

Figure 6.23: PCBs of the high voltage power supply and optoisolated switches

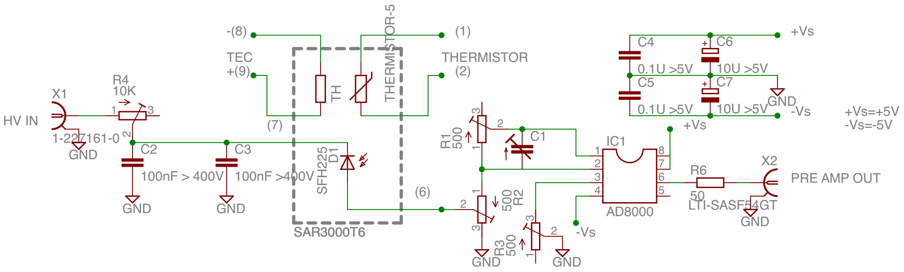

(a) Preamplifier scheme

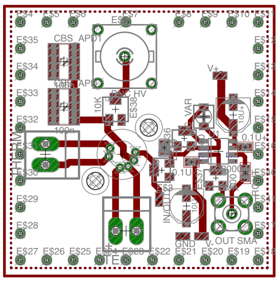

(b) Preamplifier PCB layout

Figure 6.24: Electrical schemes of the APD preamplifier and PCB layout

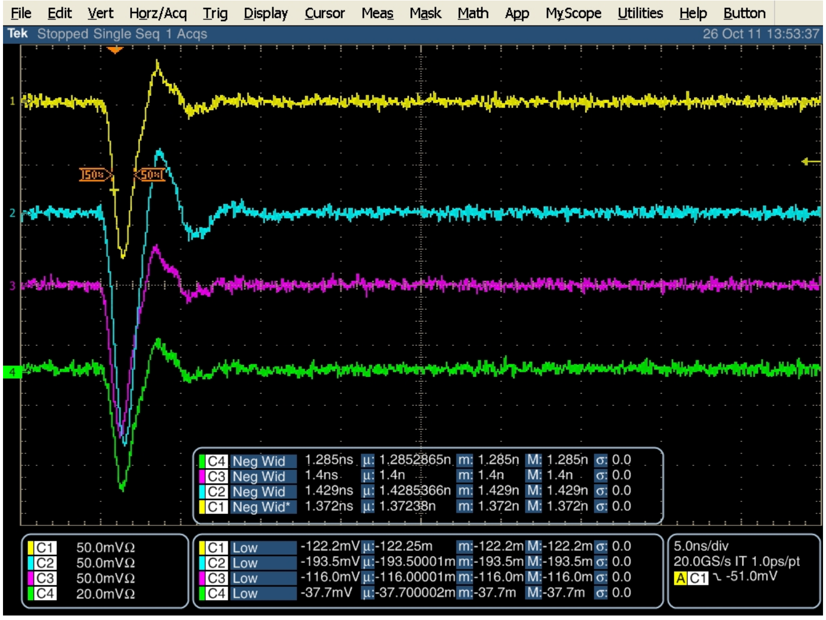

```
C4 Neg Wid   1.285ns  µ: 1.2852865n  m: 1.285n  M: 1.285n  σ: 0.0
C3 Neg Wid   1.4ns    µ: 1.4n        m: 1.4n    M: 1.4n    σ: 0.0
C2 Neg Wid   1.429ns  µ: 1.4285366n  m: 1.429n  M: 1.429n  σ: 0.0
C1 Neg Wid*  1.372ns  µ: 1.37238n    m: 1.372n  M: 1.372n  σ: 0.0

C1  50.0mVΩ    C1 Low  -122.2mV µ:-122.25m     m:-122.2m M:-122.2m σ: 0.0    5.0ns/div
C2  50.0mVΩ    C2 Low  -193.5mV µ:-193.50001m  m:-193.5m M:-193.5m σ: 0.0    20.0GS/s IT 1.0ps/pt
C3  50.0mVΩ    C3 Low  -116.0mV µ:-116.00001m  m:-116.0m M:-116.0m σ: 0.0    A C1 ⌊ -51.0mV
C4  20.0mVΩ    C4 Low  -37.7mV  µ:-37.700002m  m:-37.7m  M:-37.7m  σ: 0.0
```

Figure 6.25: APDs signals on TDS 6124C oscilloscope

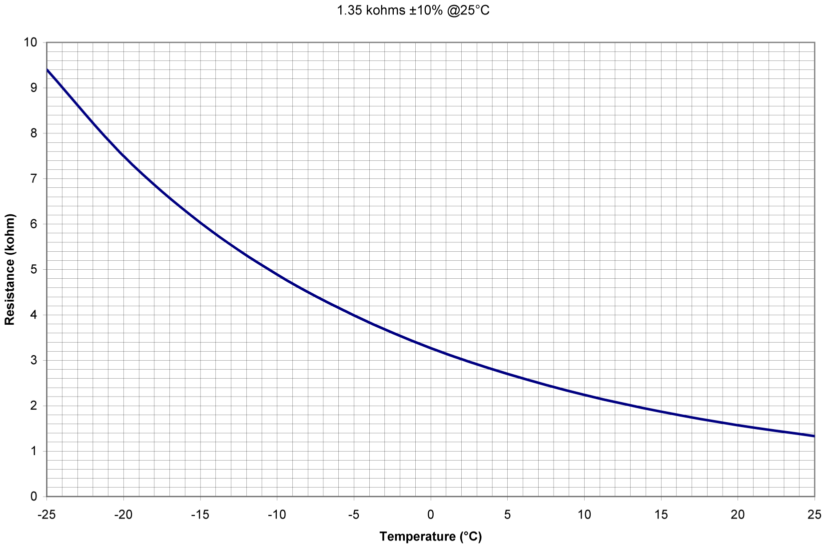

Figure 6.26: APD Thermistor curve

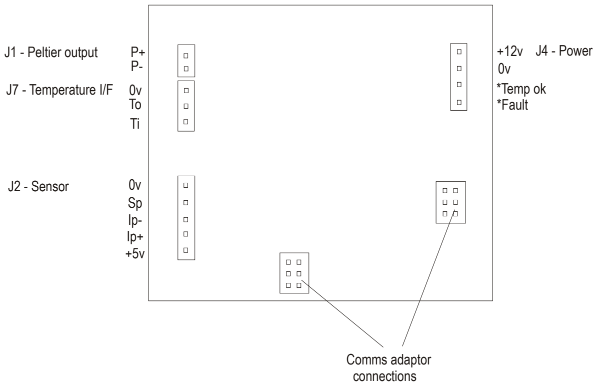

Figure 6.27: Thermoelectric cooling controller PCB scheme

A scheme of the controller PCB is reported in figure 6.27:

To set the control parameters the units provide an auto-tuning relay feedback, but in our case the most suitable tuning procedure was found to be the Ziegler-Nicholas closed loop - ultimate gain method. The actual temperature set point is $5 \pm 0.1°C$ and to avoid APDs damage the controllers outputs must be limited to ±12%. The controllers operating mode is easily settable via an USB connection and a GUI (see fig.6.28).

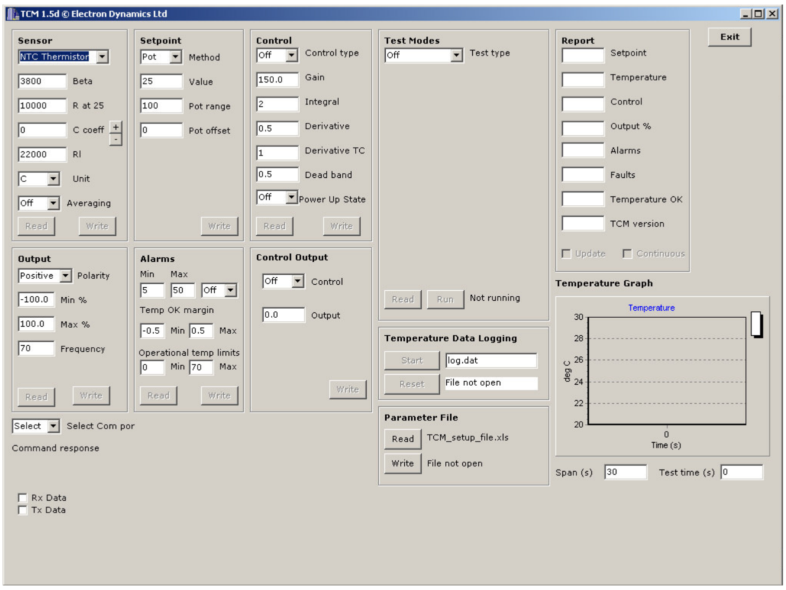

Sensor
NTC Thermistor
3800 Beta
10000 R at 25
0 C coeff
22000 Rl
C Unit
Off Averaging

Setpoint
Pot Method
25 Value
100 Pot range
0 Pot offset

Control
Off Control type
150.0 Gain
2 Integral
0.5 Derivative
1 Derivative TC
0.5 Dead band
Off Power Up State

Test Modes
Off Test type
Not running

Report
Setpoint
Temperature
Control
Output %
Alarms
Faults
Temperature OK
TCM version
☐ Update ☐ Continuous

Output
Positive Polarity
-100.0 Min %
100.0 Max %
70 Frequency

Alarms
Min Max
5 50 Off
Temp OK margin
-0.5 Min 0.5 Max
Operational temp limits
0 Min 70 Max

Control Output
Off Control
0.0 Output

Temperature Data Logging
log.dat
File not open

Parameter File
TCM_setup_file.xls
File not open

Span (s) 30 Test time (s) 0

Select Select Com por
Command response

☐ Rx Data
☐ Tx Data

Figure 6.28: Thermo cooling GUI

The setting parameters for thermoelectric cooling are reported in table 6.4.

sensor type	sensor x2	sensor x	sensor c	sensor Ri	sensor Rref	units	averaging	
6	2865	1350	0.0000	22000	0 C	0		
setpoint mode	pot range	pot offset	setpoint	setpoint change	temp control	PWM o/p		
5	100	0.0000	5	1,000,000	10,000	0.0000	1	0.000
control type	gain	integral	derivative	derivative TC	dead band			
4	7	2	0.5	1	0.5			
polarity	output min	output max	output freq	output rate				
1	-12	12	20	1				
alarm mode	temp alarm min	temp alarm max	temp ok min	temp ok max	temp ABS min	temp ABS max		
3	-5	40	-0.5000	0.5000	-5	40		

Table 6.4: TEC Driver Parameters

The NTC thermistor are setted to 1350Ω at 25°C with a β of 2865 and R_l of 22000.
The controllers outputs are limited to ±12% with a slew rate of $1\%/s$ and a frequency of $20Hz$ to suite the APDs-Peliter cells absolute maximum ratings.

Overall scheme

All the main electronic subsystem of the polarimeter, presented in the previous sections, can be summarized as:

- APD Biasing

- APD Temperature stabilization
- APD Signal reading

The overall scheme that provides a complete point of view of the electronic system and all the interconnections between the differents parts is reported in figure 6.29,

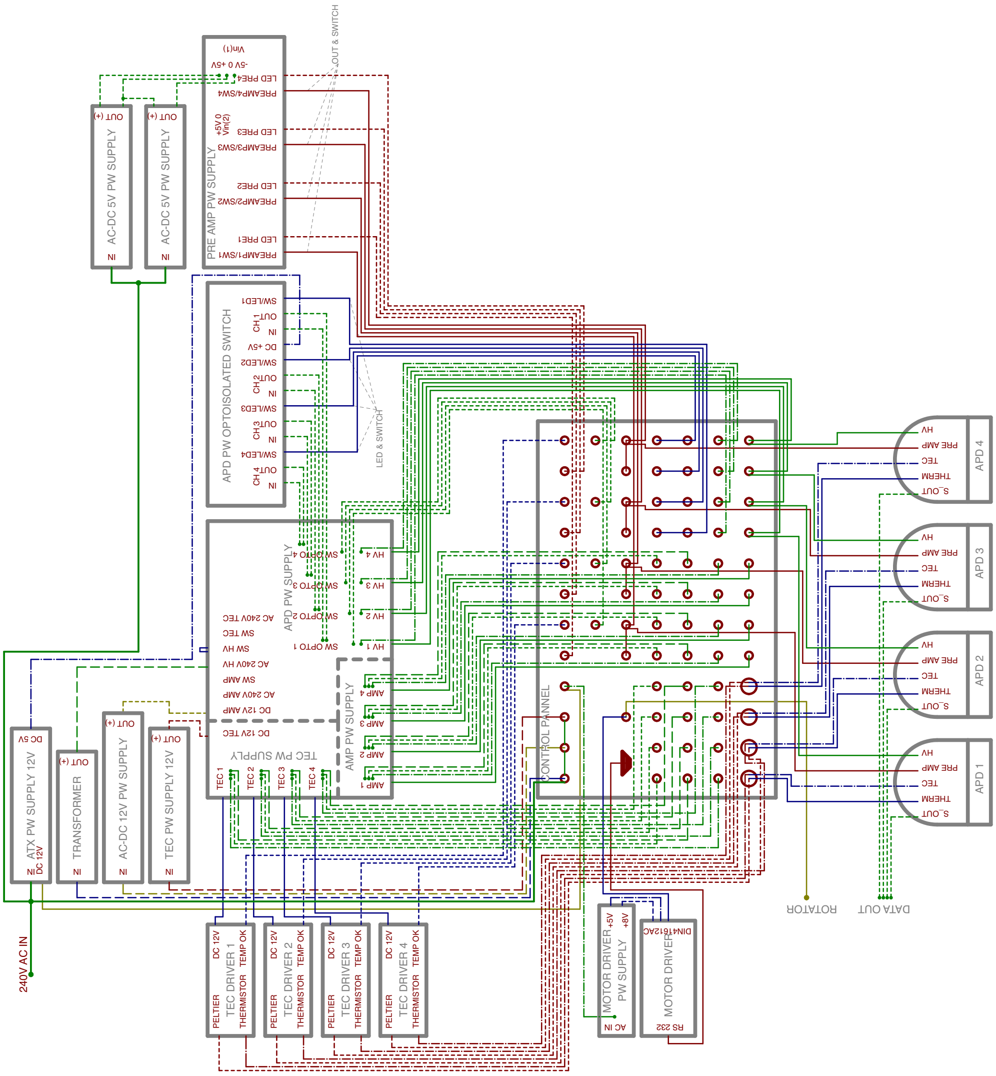

Figure 6.29: Polarimeter overall electric scheme

each of the PCB boards can easily be identified and all the interconnection toward the power supply stages or toward the control panel and hence to APDs are highlighted. The electric energy, provided by the power line is converted into a set of DC voltages, required for supply: the High Voltage biasing board (fig.6.22) and amplifiers, the APD preamplifiers (fig. 6.24), the temperature controllers for thermoelectric cooling (fig.6.27) and the quarter waveplate rotator.

Control Panel

The polarimeter control panel, a picture is reported in fig. 6.30, provides all the controls required for operations and adjustments.

Figure 6.30: Polarimeter control panel

The scheme reported in fig. 6.31 describes in detail the function of each section:

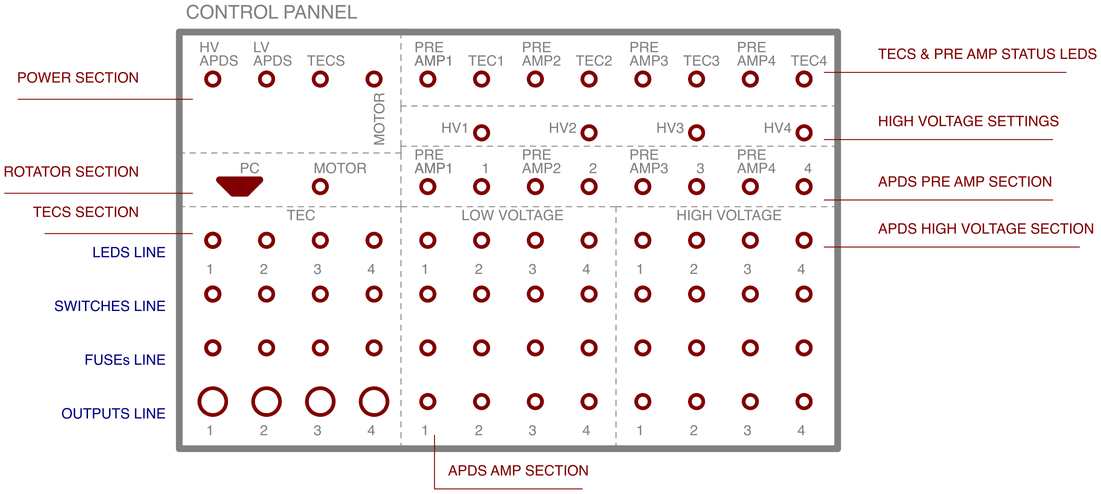

Figure 6.31: Polarimeter control panel

The main switches in the *power section* on the top-left of the panel control respectively the power supply for the *APDs high voltage section*, for the *APDs amp section*, for *TECs section* and for *rotator section*.
The *APDs high voltage section* provides power switches, output status LEDs and protection fuses to control the biasing voltage of each APD. Four potentiometers labelled in the scheme as *high voltage settings* allow to adjust the output voltage for each channel.
In the same way the *APDs amp section* and *TECs section* provide status LEDs, power switches

and protection fuses for each APD amplifier and for each thermoelectric cooling driver. In turn the *rotator section* provides an RS-232 port and a multipole connector respectively for the PC remote control of the quarter wave plate rotator and to connect the rotator motor.
The *APDs pre amp section* provides power supply outputs and switches for each APD preamplifier; the output status are displayed in the right-up LEDs line labelled *TECs & pre amp status LEDs*. In the same line TECs LEDs show when the APDs temperatures are out of range.

6.2.4 Polarimeter data acquisition and auxiliary systems

A complete scheme of the polarimeter as it is in the Matera Laser Ranging Facility is reported in figure 6.32.

In addition to the Optical and Electronic setup an high bandwidth digital oscilloscope by Tektronix, TDS6124C, acquires the analog signals outgoing from the APDs preamplifiers. The TDS6124C has a bandwidth of $12GHz$ and a real time sample rate of $20GS/s$ on the four channels. A GPIB IEEE-488 interface connect the instrument to the control/acquisition PC. The polarimeter presents other auxiliary devices:

- *Beam dump*: the output beam splitter that sends the light incoming from the telescope into the polarimeter, unfortunately split also the high energy laser pulse shot by the laser ranging system. To avoid noise, erroneous pulse detection by the APDs and dangerous reflections, the light escaping from the beam splitter must be collected and absorbed avoiding further reflections.

- *Shutter*: to prevent APDs damages the optical input path of the polarimeter is physically closed by a mechanical shutter when the ranging laser is shooting and is opened in the time interval in which the ranging signal is expected. To obtain the right trigger signal and synchronization for the shutter, in terms of signal level, delay and duty-cycle, a function generator triggered by the laser ranging system, synthesize the shutter trigger. The shutter and the controller are respectively the: SH05 and the SC10 from Thorlabs [18] (see fig.6.33). The controller is remotely driven from the control/acquisition PC via an RS232 interface.

- *Amplifier*: two stages of $3GHz$ $20dB$ RF amplifiers from Mini-Circuits [12] can be inserted between the oscilloscope and the APDs preamplifiers outputs to amplify the signals if they should be lower than the oscilloscope background noise.
  In figure 6.34 the PCB layout and the electrical scheme is reported.

- *control/acquisition PC*: a PC with a software developed in Matlab whose GUI is reported in figure 6.35, provides easy access to measurements settings.

  The software manages all the acquisition sequence: initializes the oscilloscope and the shutter and rotates the quarter wave plate to the first polarization state. According with the parameter chosen by the user it performs the measurements by operating the quarter wave plate and the oscilloscope. It is also devoted to data acquisition and remote storage so that each measure is directly store in the PC.

6.3 "Operation manual"

6.3.1 Installation

As presented in the previous section the polarimeter is formed by 4 subsystems:

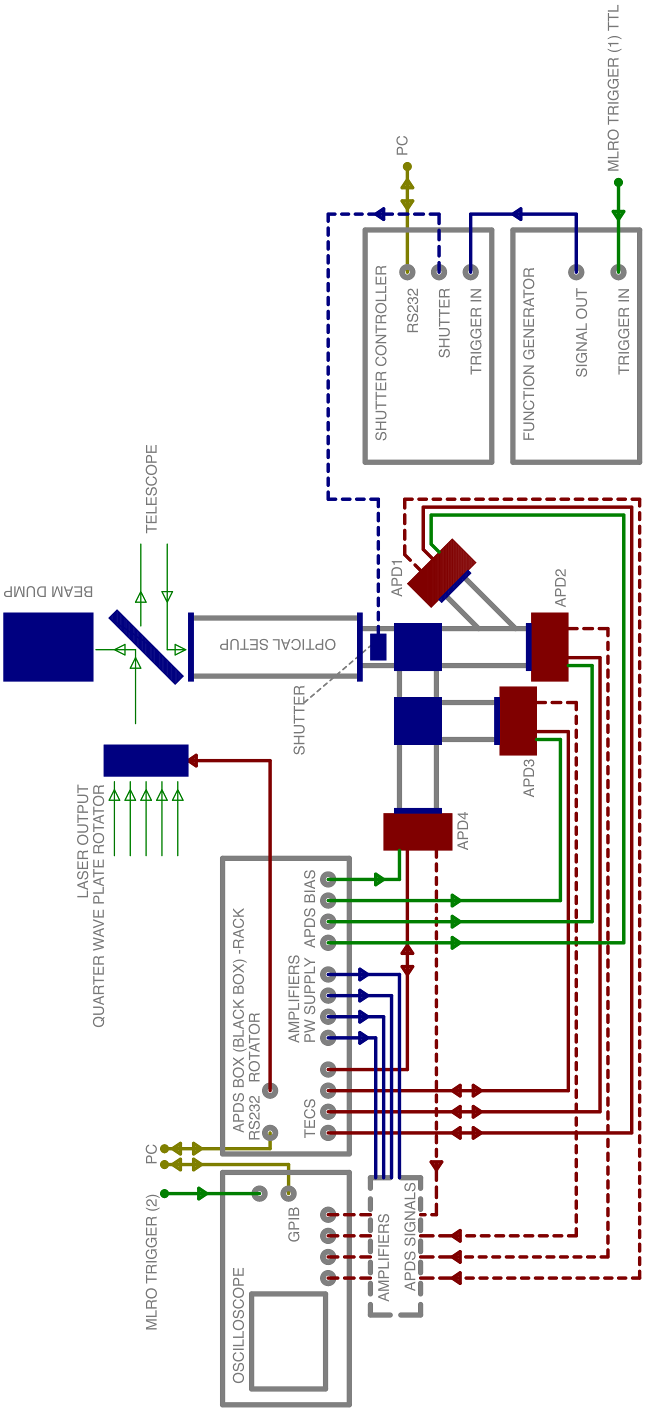

Figure 6.32: SPOLAR-M Polarimeter system

(a) Shutter SH05 (b) Controller SC10

Figure 6.33: Shutter SH05 and his controller SC10

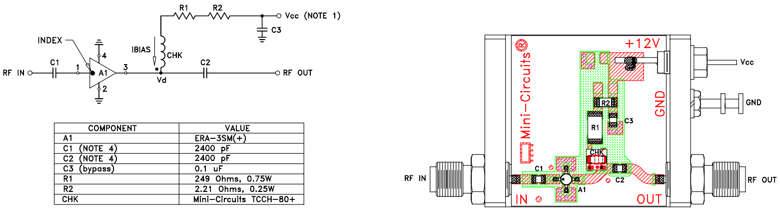

COMPONENT	VALUE
A1	ERA–3SM(+)
C1 (NOTE 4)	2400 pF
C2 (NOTE 4)	2400 pF
C3 (bypass)	0.1 uF
R1	249 Ohms, 0.75W
R2	2.21 Ohms, 0.25W
CHK	Mini–Circuits TCCH–80+

(a) Amplifier scheme (b) Amplifier PCB layout

Figure 6.34: Mini-circuits RF amplifier scheme and PCB layout

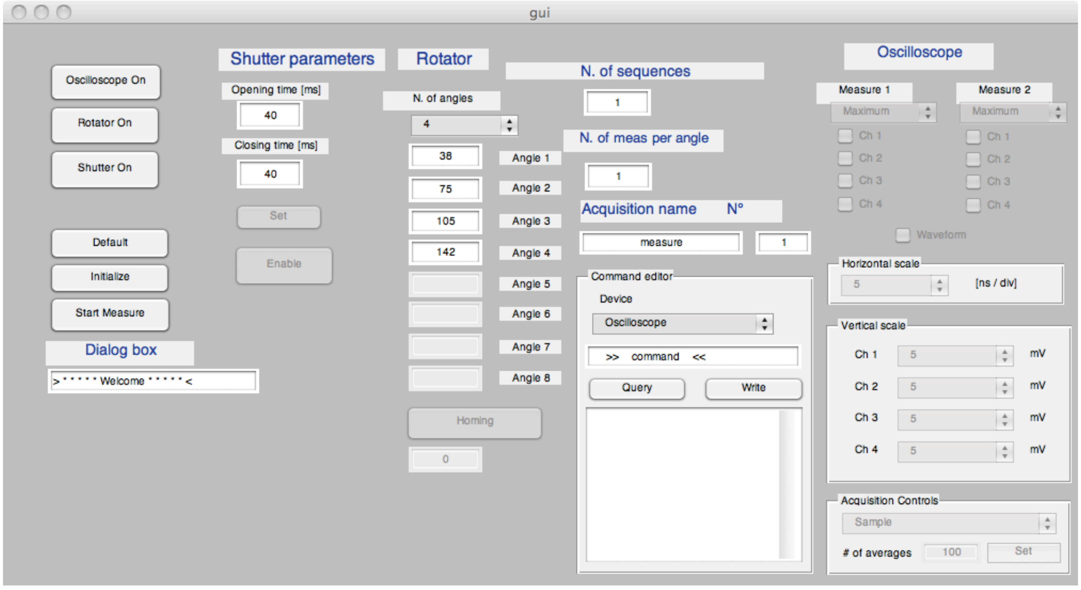

> * * * * * Welcome * * * * * <

Opening time [ms] 40

Closing time [ms] 40

N. of angles 4

38	Angle 1
75	Angle 2
105	Angle 3
142	Angle 4
	Angle 5
	Angle 6
	Angle 7
	Angle 8

0

N. of sequences 1

N. of meas per angle 1

Acquisition name N°

measure 1

Device Oscilloscope

>> command <<

Measure 1 Maximum
☐ Ch 1
☐ Ch 2
☐ Ch 3
☐ Ch 4

Measure 2 Maximum
☐ Ch 1
☐ Ch 2
☐ Ch 3
☐ Ch 4

☐ Waveform

Horizontal scale 5 [ns / div]

Vertical scale
Ch 1 5 mV
Ch 2 5 mV
Ch 3 5 mV
Ch 4 5 mV

Acquisition Controls Sample
# of averages 100

Figure 6.35: GUI acquisition software

- Optical setup that includes: the entrance beam reducer and all the optical components that split the beam in the four polarization components (four channels), the alignment mirrors between the beam splitter and the beam reducer.
- Electronic setup that includes the APDs and the black rack "APDS BOX"
- Optomechanical setup that includes the quarter wave retarder rotator and the output beam splitter
- Shutter and acquisition setup that include the oscilloscope, the control PC and the function generator

To assembly the polarimeter as first the optical setup has to be mounted and aligned in order to get that the light incoming in the entrance telescope (beam reducer) arrives in all the four optical outputs where the APDs will be inserted. To do this operation use only the degree of freedom given by the output beam splitter and the two mirrors interposed between the beam splitter and the entrance telescope of the polarimeter.
After this operation mount the four detectors and check that for each of them the beam is focused and centered in the sensitive are of the APD. As last step mount and align the beam dump at the right of the output beam splitter and insert the shutter in the entrance telescope of the polarimeter.
Plug all the connectors of the electronic system:

- the APDs connectors respectively into the APDS BOX - *High voltage section, High voltage settings, and TECs section*
- the rotator connector into the APDS BOX -*Rotator section*
- the shutter into the shutter controller
- the APDs SMA outputs into the oscilloscope inputs
- and into the remote PC the shutter controller (via RS232), the rotator controller (via RS232 from APDS BOX - *rotator section*) and the oscilloscope (via GPIB to USB)
- the trigger signals from MLRO facility into the oscilloscope and shutter controller "trigger aux" inputs

6.3.2 Startup and operation

Once the installation operations have been carried out, the polarimeter is ready for use. To startup: as first check and adjust the values of the APDs biasing voltages, turning on the "HV APDS" switch in the APDS BOX - *power section* and the respective switches in the *High voltage section* and acting with the knobs in the *High voltage settings* section - after having disconnected the BNC output connectors of the *APDs high voltage section*
After this check reconnect the APDs BNC connectors and turn on the switches: "HV APDS", "TECS" and "MOTOR" in the APDS BOX -*power section* and those related to *TEC* and *High voltage* in the *Switches Line.*
Wait until the TECs status LEDs in the *Tec & Pre Amp status LED* go off. Turn on the shutter controller, the "delay-function generator" and the oscilloscope. Adjust the function generator and the controller to get the right synchronization of the shutter according to the MLRO trigger signal. Start the acquisition software and set it for measurements and remote control of the: oscilloscope, shutter and rotator. Now the polarimeter is ready, when the MLRO system is shooting click on "Start Measure" and the measurement will start.
Similarly to turn the system off reversely repeat all the starting operations.

6.4 Polarimeter channels equalization

The polarimeter operates comparing the voltage signals of the four detectors: this consideration relax the constraints on the APDs responses. Infact, it not implies that the responses of the APDs must be linear as functions of the input power but that the responses must be linear between them. This means that the power-responses must have the same trends. In figures 6.36, 6.37, 6.38 are reported the output voltages of APDs 2, 3 and 4 for differents values of input power, compared to APD 1. All the detectors were tested with a biasing voltage of $192V$ at $5°C$

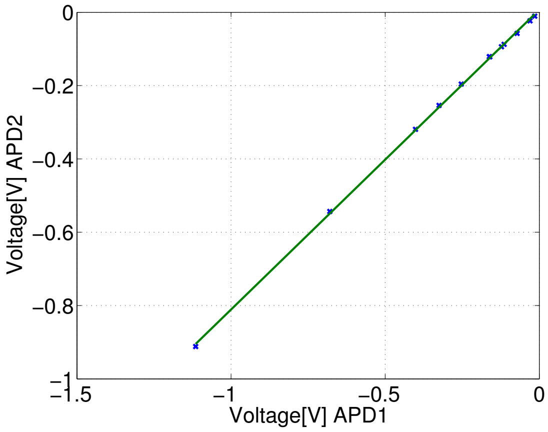

Figure 6.36: APD 2 output voltage vs APD 1 output voltage [$192V$ at $5°C$]

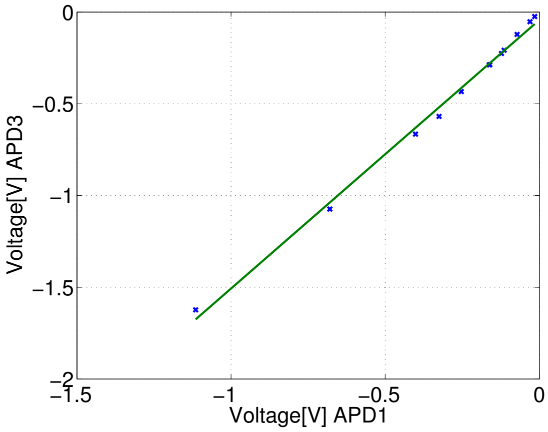

Figure 6.37: APD 3 output voltage vs APD 1 output voltage [$192V$ at $5°C$]

The responses of the APDs are clearly linear: this means that less then a proportionality factor the detectors have a similar response. This simplify the data reconstruction from measurements and not requires a calibration curve, because each channel differs from the others only by a proportional factor. In figures 6.39, 6.40, 6.41 are reported the APDs output voltages for a constant input power and differents biasing voltages at a temperature of $5°C$, measured with differents oscilloscopes to highlight a possible dependence with the sampler bandwidth. The figures show that there are

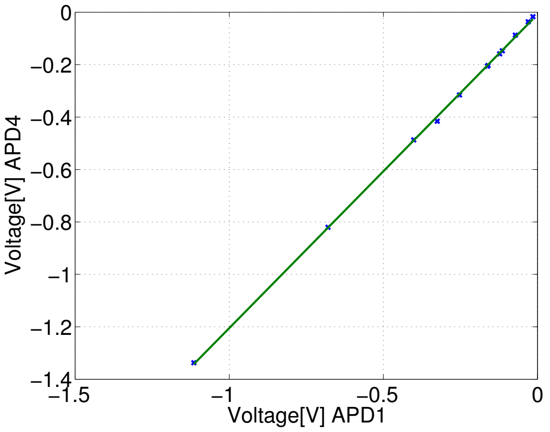

Figure 6.38: APD 4 output voltage vs APD 1 output voltage [$192V$ at $5°C$]

voltage regions in which the output responses change with the oscilloscope bandwidth a parity of biasing voltage.

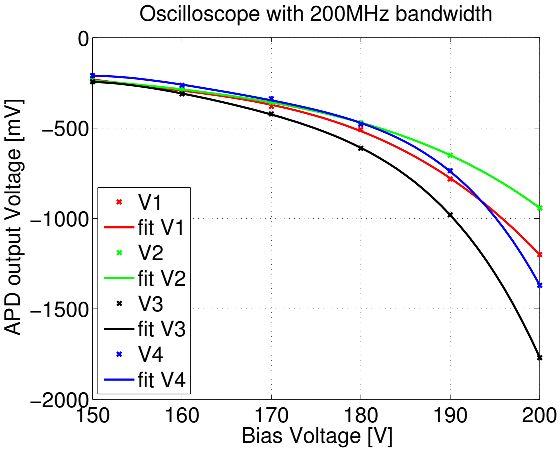

Figure 6.39: APDs output voltages vs biasing voltage $200MHz$ oscilloscope BW [$5°C$]

The previous analysis leads to the conclusion that the APDs are intrinsically differents and an initial equalization procedure is required to get the same output responses a parity of optical power. This procedure consists in the adjustment of the biasing voltages so that the output voltages become equals: operatively this consists in adjusting the bias voltages of the four APDs, testing them in the same optical channel of the polarimeter.

Also the optical setup requires calibration: it consists in the adjustment of each channel so that the light signal outgoing from it is minimized when the incoming light is orthogonally polarized respect to that ideally revealed from it. For vertical, horizontal and diagonal channels the calibration operations consist in the rotation of the optical axes of the Glan-Taylor polarizers respectively in a way in which the horizontal polarization is transmitted while the vertical is reflected and for the diagonal one: a $+45°$ polarization is transmitted. For the right-circular channel the quarter wave retarder and the linear polarizer (Glan-Taylor) have to be rotated to minimize the outgoing signal

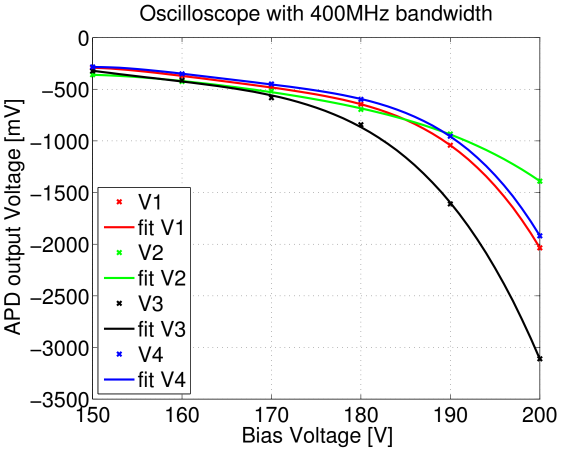

Figure 6.40: APDs output voltages vs biasing voltage $400MHz$ oscilloscope BW [$5°C$]

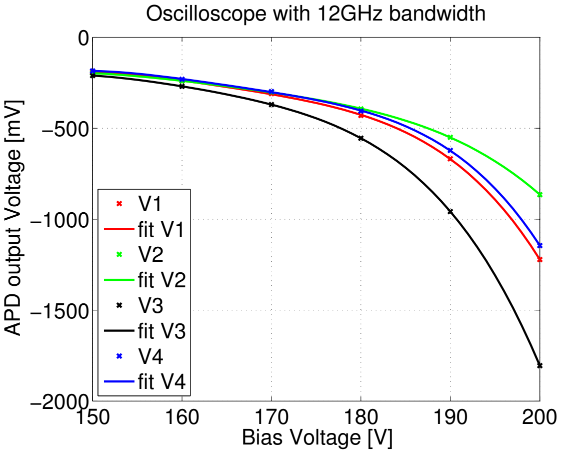

Figure 6.41: APDs output voltage vs biasing voltage $12GHz$ oscilloscope BW [$5°C$]

when the light polarization is left-circular.

6.5 Integration with the MLRO facility

The polarimeter was installed in the Matera facility in October 2011. See figures: 6.42, 6.43, 6.44.

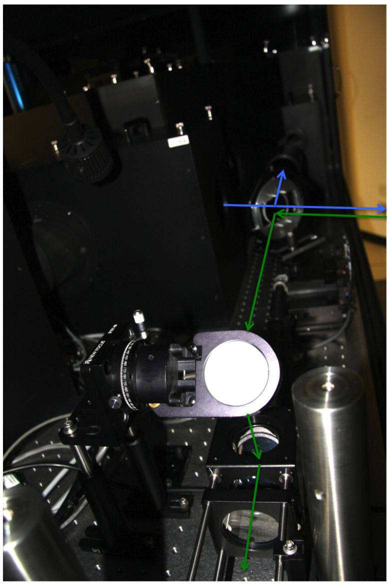

Figure 6.42: Polarimeter optical path (1) @ MLRO

In this experimental session, after the installation of the polarimeter we did a set of polarization measurements. Due to the bad weather conditions was not possible to open the telescope and hence shoot to satellites. We get however some measurements with the external target and with the internal target of the telescope.

6.5.1 Experimental results and considerations

We analysed the data collected during the installation and integration session at MLRO. Although we were unable to get space link measurements, we did some tests using an internal target on the secondary mirror of the telescope rotating it at differents pointing positions to simulate satellite tracking. We get interesting results that prove the proper functioning of the polarimeter. In particular the measurements show that the polarizations measured are in agreement with the phase displacement induced by the Coude' path of the telescope (see Fig. 6.45), infact different zenith and azimuth positions implies rotations between the mirrors of the Coude'.

To make sense of the data collected we simulated the effects of a mirror rotation on a circular polarization state and compared the results with the experimental data. For simplicity we simulated the rotation effects of only one mirror, using the mirror matrix:

$$M(\phi) = \begin{bmatrix} 1 & 0 \\ 0 & e^{-i\phi} \end{bmatrix} \tag{6.16}$$

and the rotation matrix:

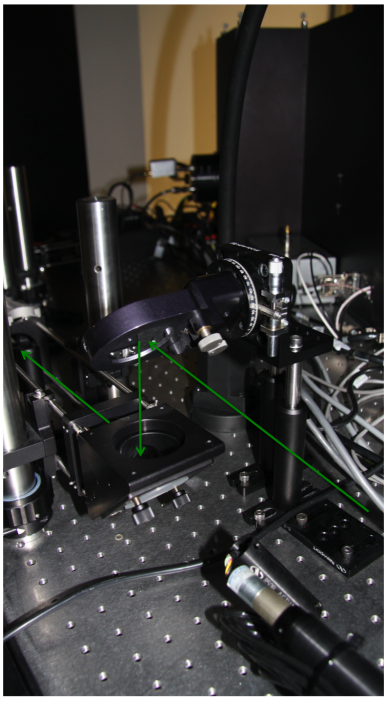

Figure 6.43: Polarimeter optical path (2) @ MLRO

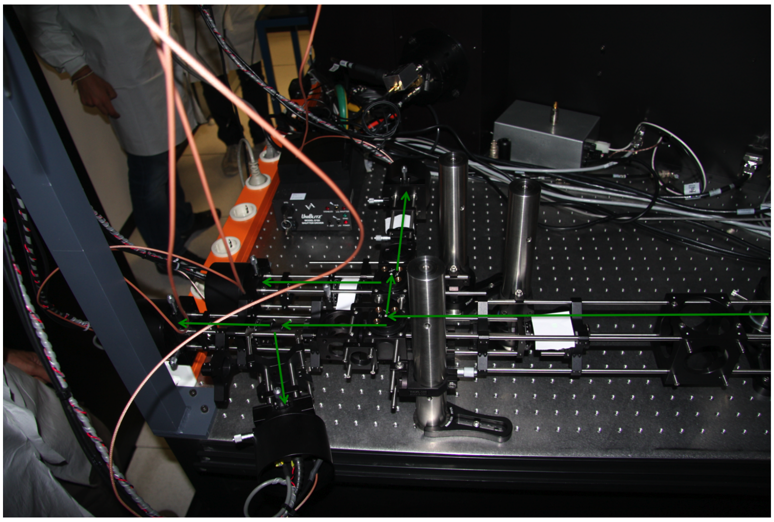

Figure 6.44: Polarimeter optical path (3) @ MLRO

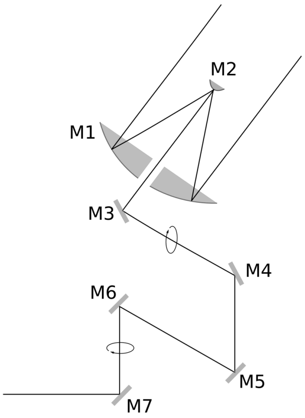

Figure 6.45: Coude' path model

$$R(\theta) = \begin{bmatrix} cos(\theta) & -sin(\theta) \\ sin(\theta) & cos(\theta) \end{bmatrix} \tag{6.17}$$

In figure 6.47 are reported the simulated point (represented in the circle) and the measured ones (the single dots).

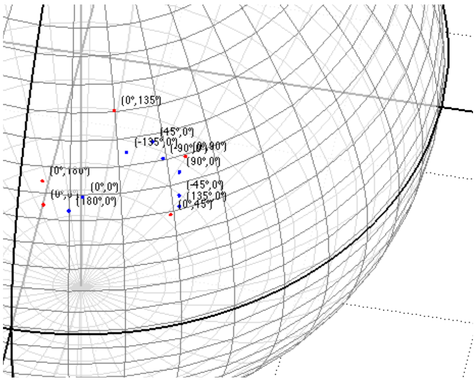

Figure 6.46: Polarization test results: internal target at different zenith and azimuth angles.

The polarimeter is ready to work and get data for a long time. This first test showed that it is able to measure polarization state. Now it is stable at MLRO.

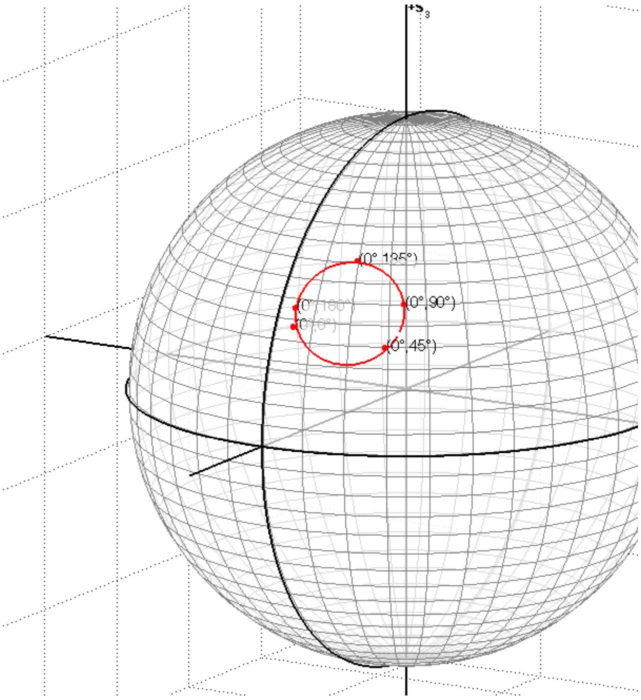

Figure 6.47: Polarization test results: internal target and simulated points (circle).

Chapter 7

Intersatellite link

In this last chapter, to complete the scenario of a global quantum communication network, will be analysed the feasibility of intersatellite quantum link.
In section 7.1 will me modelled the propagation of laser beam in a satellite to satellite link in order to get information on the link budget (attenuation, noise, SNR) and hence on its feasibility.

7.1 Optical link model

The communication scheme of an intersatellite link can be essentially based in the propagation model of a laser beam in vacuum: between a transmitter and a receiver hosted into satellites.
The propagation equation of a Gaussian beam in vacuum will be the starting point of our link model: it is the more common mode for laser sources and it has the least divergence θ compared to the other energy distribution-transverse modes, so it is the most suitable for long distance energy transfer:

$$\theta \simeq \frac{\lambda}{\pi w_0} \tag{7.1}$$

the lower is the divergence the higher will be the energy transferred per unit of area at the receiver and in a quantum point of view, and the higher will be the detection probability.
We may note that in Eq.7.1, where λ is the beam wavelength and w_0 is the beam waist: increasing the beam size and decreasing the wavelength, the divergence of the beam is reduced.
A Gaussian beam in vacuum enjoy the absence of the broadening effects due to atmosphere ([45], [22]), the simplified propagation equation becomes:

$$w_{LT}^2 = w_0^2 \left(1 + \frac{L^2}{Z_0^2}\right) \tag{7.2}$$

where L is the propagation (link) distance and $Z_0 = \frac{\pi w_0^2}{\lambda}$ is the Rayleigh parameter of the beam.
This relation leads us to the estimation of the power P collected by a receiver of radius R:

$$P = 2\pi I_0 \int_0^R \rho e^{-2(\rho^2/w_{LT}^2)} d\rho \tag{7.3}$$

To get a quantitative idea of the link energy-transfer we introduce η, defined as the ratio between the transmitted over received energy as:

$$\eta = \eta_0 \left(1 - e^{-2R^2/w_{LT}^2}\right) \tag{7.4}$$

In a real scenario we have to consider a set of unwanted quantities: such as the optical efficiency and the pointing losses. In our simulations all the involved non-ideality are combined in the factor η_0, set to 0.1 from [25]).
A beam waist of w_0 as expressed in Eq.7.2 requires an effective telescope diameter D that has to be significantly larger: the most effective criteria is maximum on-axis irradiance, introduced in the Prof. Siegman book (Ch. 18), with the waist-to-aperture-radius rate at 0.89, while the optimal ratio for reducing tail clipping require a waist-to-aperture-radius rate of $\pi/2$ ([79]).

7.1.1 Link Budget

The communication with single photons is feasible if the receiver is able to distinguish between signal photons and noise photons: this is related to the noise level, an useful communication like quantity is the ratio of signal photons over noise photons (SNR) at receiver:

$$SNR = \frac{\eta}{\epsilon_N} \tag{7.5}$$

the link efficiency in a quantum point of view represents the probability of a photon to be collected by the receiver, so the number of signal photons received, can be estimated from equation (7.4). For a fixed detection time $\Delta t = 1ns$ and a bandwidth $\Delta\lambda = 1nm$ [30], [83] we can evaluate the number of noise photons ϵ_N of an optical quantum receiver with a field of view Ω_{fov} and that aims a satellite that in the background has a portion of space, by:

$$\epsilon_N = H_b \Omega_{fov} \pi R^2 \Delta\lambda \Delta t \tag{7.6}$$

where:

- H_b is the brightness of the space background $[photons\ s^{-1} cm^{-2} nm^{-1} sr^{-1}]$
- Ω_{fov} is the field of view of the telescope in $[sr]$ - $[100\mu rad$ in the simulation$]$
- R is the telescope radius in $[cm]$
- $\Delta\nu$ is the optical bandwidth $[nm]$
- Δt is the detection time $[s]$

In a worst case study analysis, we have to consider the space background spectral irradiance in the Galactic Plane: the zone of the Galactic Coordinate System with the highest density level of dust.
In our simulation we considered a mean spectral irradiance of 10^6 $[photons\ s^{-1} cm^{-2} nm^{-1} sr^{-1}]$ in the region from $300nm$ to $800nm$, see [97]. The main sources of noise are Zodiacal light (ZL) -Zodiacal light is sunlight reflected by interplanetary dust- and integrated starlight (ISL) that comes from direct starlight and from starlight scattered by interstellar dust. Obviously,the noise source and photons ratio depend on the observation direction. The most sources and so the highest noise level are on the Galactic Plane from our galaxy.

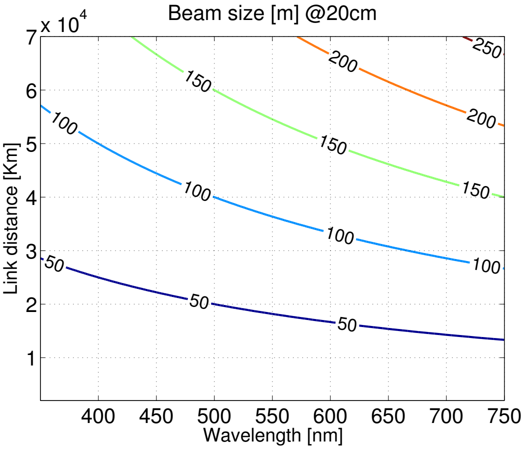

Figure 7.1: Beam size at the receiver - 20cm telescopes

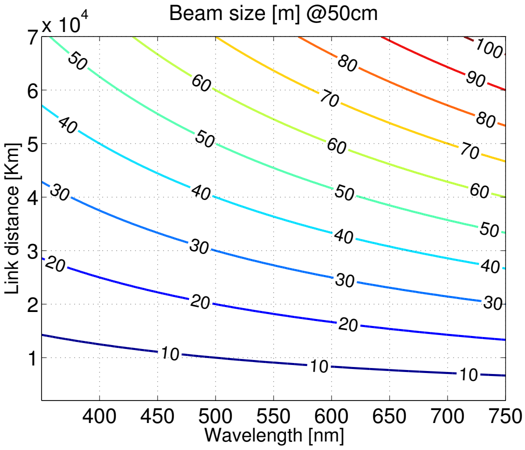

Figure 7.2: Beam size at the receiver - 50cm telescopes

7.1.2 Simulations

With the model presented in the previous section we did simulations to analyse the feasibility of an intersatellite quantum link and to identify the telescopes requirements. We spanned from Low Earth Orbit (LEO) to Medium Earth Orbit (MEO) satellites. We considered a set of wavelengths from 350nm up to 750nm and two telescopes diameters: 20cm and 50cm. In Fig. 7.1 and Fig. 7.2 respectively the beam sizes as functions of wavelength and link distance for telescopes diameter of 20cm and 50cm are reported. The simulations for different laser wavelength and telescopes radius show that decreasing the wavelength and increasing the radius, the beam size at the receiver is reduced: this is due to the dependence of the beam divergence with wavelength and telescope radius. In all the simulations we hypothesized the same diameters for transmitting and receiving telescopes, that is a reasonable condition for a real communication network in which the same terminal can operate in both direction as transmitter or receiver. In Fig. 7.3 and Fig. 7.4 respectively the link attenuations as functions of wavelength and link distance for telescopes diameter of 20cm and 50cm are reported.

In Figure 7.5 and 7.6 respectively the SNRs as functions of wavelength and link distance for telescopes diameter of 20cm and 50cm are reported.

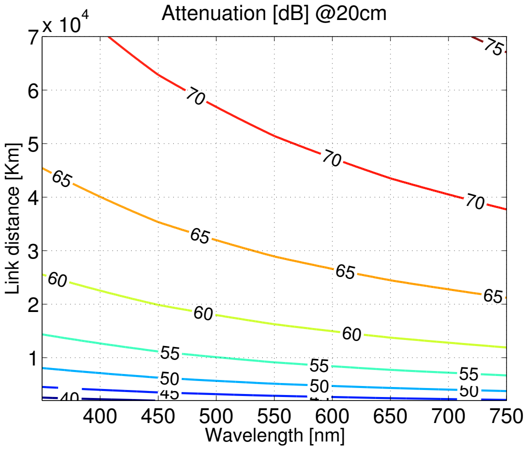

Figure 7.3: Link attenuation at the receiver - 20*cm* telescopes

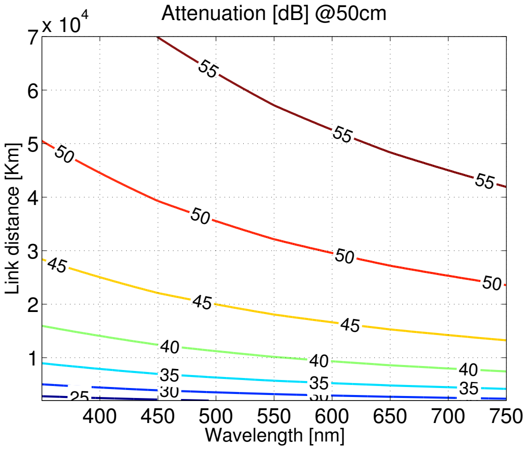

Figure 7.4: Link attenuation at the receiver - 50*cm* telescopes

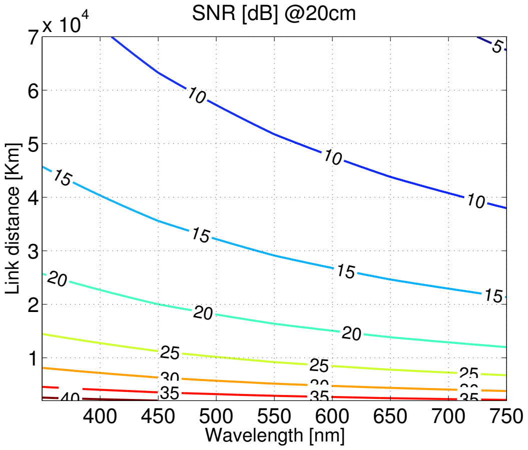

Figure 7.5: SNR - 20*cm* telescopes

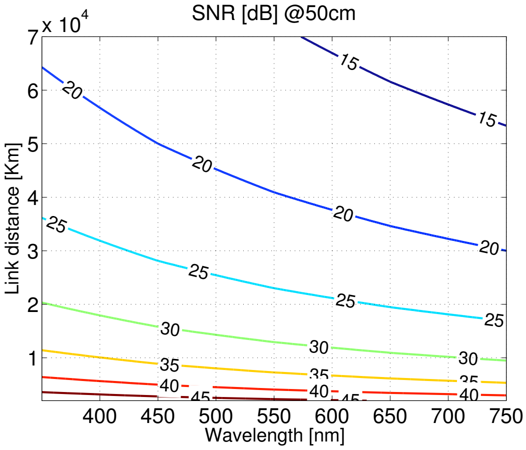

Figure 7.6: SNR - 50*cm* telescopes

7.2 Comments to simulations

As in chapter [2] for vertical link, the simulation results show that a real implementation of a QKD protocol in space, based on coherent states, requires a careful design of the transmitter: field-of-view, telescope pointing and tracking, efficient single photon detectors etc. From Fig. 7.1 and Fig. 7.2: the spot size at the target is of the order of a few tens of meter for short-wavelength transmission systems. The corresponding attenuation, from Figs. 7.3 and Fig. 7.4, is rapidly increasing from the relatively good conditions of closest approach of the satellites. The level of attenuation ranges between the cases of downlink and uplink in the case with a terminal on the Earth[30]. Anyway, using the part of the orbit in which the satellites are sufficiently close, the QKD appears feasible. In general, the level of losses that are associated with terminals equipped with optics up to $500mm$ in diameter makes hardly feasible the double simultaneous link for the distribution of an entangled pair. The background noise is here limiting the SNR to very low levels. The feasibility is also dependent on the capacity of orbital prediction and pointing accuracy over extended intervals. In conclusion, we have seen that in some conditions the extension of quantum communications and technologies appears feasible in the extreme scenario of the satellite optical quantum networks.

Conclusions

The work presented in this thesis has shown that quantum communication could become a reality in the future. The results show that quantum links are feasible in all the scenarios required in a global quantum communication network. Horizontal links, Earth-space links and satellite to satellite links are feasible under certain conditions. The models are starting points for: refine and define new models and predict the feasibility of experiment. Simulations highlighted that actual technology limits quantum communication to LEO satellites: field of view, pointing accuracy, are crucial issues for extension to upper links. The work to reach an effective communication system is still a lot and requires major technological efforts.
All the topics addressed can be considered still open points in which our contribution is only a little part compared to what required for a real working system and not for an experiment. For Earth-space, space-Earth and intrasatellite links the presented models and simulations are an important tools to proof the sense of research in this fields.
The simulations results also may be used to justify space missions for quantum communication. The experimental results and the knowledge and experience gained from the Canary sessions have shown the way to go to reduce the link losses. The collected data may be used to better understand the atmospheric turbulence and define a propagation model (still missing in literature) that should help the receiver and transmitter design. Moreover, new communication protocols that exploit the atmospheric turbulence as a resource can be defined. Our telescope should be used in future for single photons long distance free space experiments, like: teleportation, QKD, etc. The polarimeter SPOLAR-M is an useful tool that will help to better understand what happen on the photons polarization states on a quantum channel. It will remain at MLRO for long time and the collected data will help to experimentally demonstrate the feasibility of Earth-space quantum links. One more step toward global quantum network has been done.

Bibliography

[1] *http : //ilrs.gsfc.nasa.gov/stations/sitelist/matm*$_g$*eneral.html.*

[2] *http : //micro.magnet.fsu.edu/primer/digitalimaging/concepts/avalanche.html.*

[3] *http : //optoengine.com/default.aspx.*

[4] *http : //tngweb.tng.iac.es/weather/.*

[5] *http : //www.adaptica.com/site.*

[6] *http : //www.analog.com/en/index.html.*

[7] *http : //www.costruzioniottichezen.com/.*

[8] *http : //www.duma.co.il.*

[9] *http : //www.electrondynamics.co.uk/e/.*

[10] *http : //www.eso.org/public/.*

[11] *http : //www.lasercomponents.com/de − en/.*

[12] *http : //www.minicircuits.com/homepage/homepage.html.*

[13] *http : //www.miotti.it/index.php/item/sku/*17831*.html.*

[14] *http : //www.otticasanmarco.it/skywatcher_black_diamond_*120*_apo_ota.htm.*

[15] *http : //www.perkinelmer.com/.*

[16] *http : //www.standa.lt/.*

[17] *http : //www.supertex.com/.*

[18] *http : //www.thorlabs.com/.*

[19] IAC Proceedings A2.1.3 (2008), editor. *Space-QUEST: Experiments with quantum entanglement in space*, number arXiv:0806.0945v1, 2008.

[20] Jawad Elsayed Ahmad and Yoshitate Takakura. Estimation of physically realizablemueller matrices from experimentsusing global constrained optimization. *Opt. Express*, 16(18):14274–14287, Sep 2008.

[21] A. Aiello, G. Puentes, D. Voigt, and J. P. Woerdman. Maximum-likelihood estimation of mueller matrices. *Opt. Lett.*, 31(6):817–819, Mar 2006.

[22] L. C. Andrews and R. L. Phillips. *Laser Beam Propagation through Random Media, Second Edition (SPIE Press Monograph Vol. PM152)*. SPIE Publications, 2nd edition.

[23] L. C. Andrews, R. L. Phillips, and P. T. Yu. Optical scintillations and fade statistics for a satellite-communication system. *Appl. Opt.*, 34(33):7742–7751, Nov 1995.

[24] David A. Arnold. Cross section of ilrs satellites.

[25] M. Aspelmeyer, T. Jennewein, M. Pfennigbauer, W.R. Leeb, and A. Zeilinger. Long-distance quantum communication with entangled photons using satellites. *Selected Topics in Quantum Electronics, IEEE Journal of*, 9(6):1541 – 1551, nov.-dec. 2003.

[26] Lidia Bolbasova and Vladimir P. Lukin. Isoplanatic requirements for adaptive-optics systems. *SPIE Newsroom*, 2009.

[27] Lidia A. Bolbasova and Vladimir P. Lukin. Modal phase correction for large-aperture ground-based telescope with multiguide stars. volume 7476, page 74760M. SPIE, 2009.

[28] C Bonato, C Pernechele, and P Villoresi. Influence of all-reflective optical systems in the transmission of polarization-encoded qubits. *Journal of Optics A: Pure and Applied Optics*, 9(10):899, 2007.

[29] C. Bonato, A. Tomaello, V. Deppo, G. Naletto, and P. Villoresi. Feasibility analysis for quantum key distribution between a leo satellite and earth. In Alexander Sergienko, Saverio Pascazio, and Paolo Villoresi, editors, *Quantum Communication and Quantum Networking*, volume 36 of *Lecture Notes of the Institute for Computer Sciences, Social Informatics and Telecommunications Engineering*, pages 96–99. Springer Berlin Heidelberg, 2010.

[30] C Bonato, A Tomaello, V Da Deppo, G Naletto, and P Villoresi. Feasibility of satellite quantum key distribution. *New Journal of Physics*, 11(4):045017, 2009.

[31] Cristian Bonato, Markus Aspelmeyer, Thomas Jennewein, Claudio Pernechele, Paolo Villoresi, and Anton Zeilinger. Influence of satellite motion on polarization qubits in a space-earth quantum communication link. *Opt. Express*, 14(21):10050–10059, Oct 2006.

[32] Cristian Bonato, Andrea Tomaello, Vania Deppo, Giapiero Naletto, and Paolo Villoresi. Study of the quantum channel between earth and space for satellite quantum communications. In Kandeepan Sithamparanathan and Mario Marchese, editors, *Personal Satellite Services*, volume 15 of *Lecture Notes of the Institute for Computer Sciences, Social Informatics and Telecommunications Engineering*, pages 37–40. Springer Berlin Heidelberg, 2009.

[33] D. Bouwmeester, A.K. Ekert, and A. Zeilinger. *Physics of Quantum Information.* Springer, 2000.

[34] W. T. Buttler, R. J. Hughes, P. G. Kwiat, S. K. Lamoreaux, G. G. Luther, G. L. Morgan, J. E. Nordholt, C. G. Peterson, and C. M. Simmons. Practical free-space quantum key distribution over 1 km. *Phys. Rev. Lett.*, 81:3283–3286, Oct 1998.

[35] Ivan Capraro, Andrea Tomaello, Alberto Dall'Arche, and Paolo Villoresi. Long-range beam propagation for single-photon communications. volume 8161, page 81610C. SPIE, 2011.

[36] Cornell S. L. Chun, David L. Fleming, W. A. Harvey, and E. J. Torok. Polarization-sensitive infrared sensor for target discrimination. volume 3121, pages 55–62. SPIE, 1997.

[37] Alberto Dall'Arche, Andrea Tomaello, Cristian Bonato, and Paolo Villoresi. On the polarization analysis of optical beams for use in quantum communications between earth and space. In Mario Marchese, Marina Ruggieri, and Igor Bisio, editors, *Personal Satellite Services*, volume 43 of *Lecture Notes of the Institute for Computer Sciences, Social Informatics and Telecommunications Engineering*, pages 291–296. Springer Berlin Heidelberg, 2010.

[38] Mark de Burgh and Stephen D. Bartlett. Quantum methods for clock synchronization: Beating the standard quantum limit without entanglement. *Phys. Rev. A*, 72:042301, Oct 2005.

[39] John J. Degnan. Millimiter accuracy satellite laser ranging: A review. *Contributions of space geodesy to geodynamics: technology*, (25):133, 1993.

[40] Federico Dios, Juan Antonio Rubio, Alejandro Rodríguez, and Adolfo Comerón. Scintillation and beam-wander analysis in an optical ground station-satellite uplink. *Appl. Opt.*, 43(19):3866–3873, Jul 2004.

[41] M. J. Duggin, S. A. Israel, V. S. Whitehead, J. S. Myers, and D. R. Robertson. Use of polarization methods in earth resources investigations. In R. A. Chipman, editor, *Society of Photo-Optical Instrumentation Engineers (SPIE) Conference Series*, volume 1166 of *Society of Photo-Optical Instrumentation Engineers (SPIE) Conference Series*, pages 11–22. SPIE, 1989.

[42] A.S. Eddington. *The mathematical theory of relativity.* The University press, 1934.

[43] Miao Er-long, Han Zheng-fu, Gong Shun-sheng, Zhang Tao, Diao Da-sheng, and Guo Guang-can. Background noise of satellite-to-ground quantum key distribution. *New Journal of Physics*, 7(1):215, 2005.

[44] Le Roy-Brehonnet F. and Le Jeune B. Utilization of mueller matrix formalism to obtain optical targets depolarization and polarization properties. *Progress in Quantum Electronics*, 21(2):109–151, 1997.

[45] R.L. Fante. Electromagnetic beam propagation in turbulent media. *Proceedings of the IEEE*, 63(12):1669 – 1692, dec. 1975.

[46] R.L. Fante. Electromagnetic beam propagation in turbulent media: An update. *Proceedings of the IEEE*, 68(11):1424 – 1443, nov. 1980.

[47] Alessandro Fedrizzi, Rupert Ursin, Thomas Herbst, Matteo Nespoli, Robert Prevedel, Thomas Scheidl, Felix Tiefenbacher, Thomas Jennewein, and Anton Zeilinger. High-fidelity transmission of entanglement over a high-loss freespace channel. *NATURE PHYSICS*, 5:389, 2009.

[48] David L. Fried. Anisoplanatism in adaptive optics. *J. Opt. Soc. Am.*, 72(1):52–52, Jan 1982.

[49] Jesus J. Fuensalida, Sergio Chueca, Jose M. Delgado, Begona Garcia-Lorenzo, Jose M. Rodriguez-Gonzalez, Claudia K. Hoegemann, Esteban G. Mendizabal, Marcos Reyes, Manuel Verde, and Jean Vernin. Vertical structure of the turbulence above the observatories of the canary islands: parameters and statistics for adaptive optics. volume 5490, pages 749–757. SPIE, 2004.

[50] N. Laurenti G. Cariolaro, C. De Angelis. *COMUNICAZIONI OTTICHE.* Libreria Progetto, 2006.

[51] V. Giovannetti, S. Lloyd, L. Maccone, and M. S. Shahriar. Limits to clock synchronization induced by completely dephasing communication channels. *Phys. Rev. A*, 65:062319, Jun 2002.

[52] Vittorio Giovannetti, Seth Lloyd, and Lorenzo Maccone. Quantum-enhanced measurements: Beating the standard quantum limit. *Science*, 306(5700):1330–1336, 2004.

[53] Vittorio Giovannetti, Seth Lloyd, and Lorenzo Maccone. Quantum metrology. *Phys. Rev. Lett.*, 96:010401, Jan 2006.

[54] Vittorio Giovannetti, Seth Lloyd, Lorenzo Maccone, Jeffrey H. Shapiro, and Franco N. C. Wong. Conveyor-belt clock synchronization. *Phys. Rev. A*, 70:043808, Oct 2004.

[55] D.H. Goldstein and E. Collett. *Polarized light*. Optical engineering. Marcel Dekker, 2003.

[56] D. Gottesman, H.-K. Lo, N. Lutkenhaus, and J. Preskill. Security of quantum key distribution with imperfect devices. In *Information Theory, 2004. ISIT 2004. Proceedings. International Symposium on*, page 136, june-2 july 2004.

[57] H. Inamori, N. Lütkenhaus, and D. Mayers. Unconditional security of practical quantum key distribution. *Eur. Phys. J. D*, 41(3):599–627, 2007.

[58] H. Hemmati. *Near-Earth Laser Communications*. Optical science and engineering. CRC, 2009.

[59] Barton J. Howell. Measurement of the polarization effects of an instrument using partially polarized light. *Appl. Opt.*, 18(6):809–812, Mar 1979.

[60] Won-Young Hwang. Quantum key distribution with high loss: Toward global secure communication. *Phys. Rev. Lett.*, 91:057901, Aug 2003.

[61] M. T. Jaekel and S. Reynaud. Quantum limits in interferometric measurements. *EPL (Europhysics Letters)*, 13(4):301, 1990.

[62] C. Kurtsiefer, P. Zarda, M. Halder, H. Weinfurter, P. M. Gorman, P. R. Tapster, and J. G. Rarity. Quantum cryptography: A step towards global key distribution. *Nature*, 419(6906):450–450, 10 2002.

[63] James A. Louthain. *Integrated Approach to Airborne Laser Communication*. PhD thesis, Air Force Institute Of Technology, 2008.

[64] James A. Louthain and Jason D. Schmidt. Anisoplanatism in airborne laser communication. *Opt. Express*, 16(14):10769–10785, Jul 2008.

[65] Xiongfeng Ma, Bing Qi, Yi Zhao, and Hoi-Kwong Lo. Practical decoy state for quantum key distribution. *Phys. Rev. A*, 72:012326, Jul 2005.

[66] Norman Margolus and Lev B. Levitin. The maximum speed of dynamical evolution. *Physica D*, pages 188–195, 1998.

[67] Peter W. Milonni, John H. Carter, Charles G. Peterson, and Richard J. Hughes. Effects of propagation in air on photon statistics. volume 5111, pages 7–11. SPIE, 2003.

[68] Peter W Milonni, John H Carter, Charles G Peterson, and Richard J Hughes. Effects of propagation through atmospheric turbulence on photon statistics. *Journal of Optics B: Quantum and Semiclassical Optics*, 6(8):S742, 2004.

[69] L. Moli, A. Rodriguez, G. Seco-Granados, and J.A. Lopez-Salcedo. Quantum key distribution (qkd) using leo and meo satellites and decoy states. In *Signal Processing for Space Communications, 2008. SPSC 2008. 10th International Workshop on*, pages 1 –6, oct. 2008.

[70] Cheng-Zhi Peng, Tao Yang, Xiao-Hui Bao, Jun Zhang, Xian-Min Jin, Fa-Yong Feng, Bin Yang, Jian Yang, Juan Yin, Qiang Zhang, Nan Li, Bao-Li Tian, and Jian-Wei Pan. Experimental free-space distribution of entangled photon pairs over 13 km: Towards satellite-based global quantum communication. *Phys. Rev. Lett.*, 94:150501, Apr 2005.

[71] J. G. Rarity. Quantum communications and beyond. *Phil. Trans. R. Soc. Lond. A*, 361:1507–1518, 2003.

[72] J G Rarity, P R Tapster, P M Gorman, and P Knight. Ground to satellite secure key exchange using quantum cryptography. *New Journal of Physics*, 4:82.1–82.21, 2002.

[73] B.E.A. Saleh and M.C. Teich. *Fundamentals of photonics.* Wiley series in pure and applied optics. Wiley-Interscience, 2007.

[74] Richard J. Sasiela. *Electromagnetic Wave Propagation in Turbulence: Evaluation and Application of Mellin Transforms, 2nd Ed. (SPIE Press Monograph Vol. PM171).* SPIE Publications, 2 edition, May 2007.

[75] Valerio Scarani and Renato Renner. Quantum cryptography with finite resources: Unconditional security bound for discrete-variable protocols with one-way postprocessing. *Phys. Rev. Lett.*, 100:200501, May 2008.

[76] Thomas Scheidl, Rupert Ursin, Alessandro Fedrizzi, Sven Ramelow, Xiao-Song Ma, Thomas Herbst, Robert Prevedel, Lothar Ratschbacher, Johannes Kofler, Thomas Jennewein, and Anton Zeilinger. Feasibility of 300 km quantum key distribution with entangled states. *New Journal of Physics*, 11(8):085002, 2009.

[77] A. A. Semenov and W. Vogel. Entanglement transfer through the turbulent atmosphere. *Phys. Rev. A*, 81:023835, Feb 2010.

[78] A.V. Sergienko. *Quantum communications and cryptography.* Optical Science and Engineering Series. Taylor & Francis, 2006.

[79] A. E. Siegman. *Lasers.* University Science Books, 1986.

[80] ALENIA SPAZIO. Goce: Lrr procurement specification, 2003.

[81] Kiyoshi Tamaki. Unconditionally secure quantum key distribution with relatively strong signal pulse. *Phys. Rev. A*, 77:032341, Mar 2008.

[82] V. I. Tatarski. Wave propagation in a turbulent medium. *Science-McGraw-Hill, New York*, 134(3475):324–325, 1961.

[83] Andrea Tomaello, Cristian Bonato, Vania Da Deppo, Giampiero Naletto, and Paolo Villoresi. Link budget and background noise for satellite quantum key distribution. *Advances in Space Research*, 47(5):802 – 810, 2011. Scientific applications of Galileo and other Global Navigation Satellite Systems - II.

[84] Masahiro Toyoda. Intensity fluctuations in laser links between the ground and a satellite. *Appl. Opt.*, 44(34):7364–7370, Dec 2005.

[85] M. Toyoshima, S. Yamakawa, T. Yamawaki, K. Arai, M.R. Garcia-Talavera, A. Alonso, Z. Sodnik, and B. Demelenne. Long-term statistics of laser beam propagation in an optical ground-to-geostationary satellite communications link. *Antennas and Propagation, IEEE Transactions on*, 53(2):842 – 850, feb. 2005.

[86] Morio Toyoshima and Kenichi Araki. Far-field pattern measurement of an onboard laser transmitter by use of a space-to-ground optical link. *Appl. Opt.*, 37(10):1720–1730, Apr 1998.

[87] Morio Toyoshima and Kenichi Araki. Far-field pattern measurement of an onboard laser transmitter by use of a space-to-ground optical link. *Appl. Opt.*, 37(10):1720–1730, Apr 1998.

[88] Morio Toyoshima, Hideki Takenaka, Yozo Shoji, Yoshihisa Takayama, Yoshisada Koyama, and Hiroo Kunimori. Polarization measurements through space-to-ground atmospheric propagation paths by using a highly polarized laser source in space. *Opt. Express*, 17(25):22333–22340, Dec 2009.

[89] R.K. Tyson. *Principles of adaptive optics.* Academic Press, 1998.

[90] R.K. Tyson. *Adaptive optics engineering handbook.* Optical Science and Engineering. Marcel Dekker, 2000.

[91] P.B. Ulrich. Hufnagel–valley profiles for specified values of the coherence length and isoplanatic patch angle. *W.J. Schafer Associates*, WJSA/MA/TN-88-013, Arlington, VA, 1988.

[92] R. Ursin, F. Tiefenbacher, T. Schmitt-Manderbach, H. Weier, T. Scheidl, M. Lindenthal, B. Blauensteiner, T. Jennewein, J. Perdigues, P. Trojek, B. Omer, M. Furst, M. Meyenburg, J. Rarity, Z. Sodnik, C. Barbieri, H. Weinfurter, and A. Zeilinger. Entanglement-based quantum communication over 144[thinsp]km. *Nat Phys*, 3(7):481–486, 07 2007.

[93] Alejandra Valencia, Giuliano Scarcelli, and Yanhua Shih. Distant clock synchronization using entangled photon pairs. *Applied Physics Letters*, 85(13):2655–2657, 2004.

[94] P Villoresi, T Jennewein, F Tamburini, M Aspelmeyer, C Bonato, R Ursin, C Pernechele, V Luceri, G Bianco, A Zeilinger, and C Barbieri. Experimental verification of the feasibility of a quantum channel between space and earth. *New Journal of Physics*, 10(3):033038, 2008.

[95] Paolo Villoresi, Fabrizio Tamburini, Markus Aspelmeyer, Thomas Jennewein, Rupert Ursin, Claudio Pernechele, Giuseppe Bianco, Anton Zeilinger, and Cesare Barbieri. Space-to-ground quantum communication using an optical ground station: a feasibility study. volume 5551, pages 113–120. SPIE, 2004.

[96] V. S. Whitehead and K. L. Coulson. Space shuttle as a polarization observation platform. In R. A. Chipman, editor, *Polarization Considerations for Optical Systems II*, volume 1166 of *Society of Photo-Optical Instrumentation Engineers (SPIE) Conference Series*, pages 42–51. SPIE, 1989.

[97] Martin V. Zombeck. *Handbook of Space Astronomy and Astrophysics.* Cambridge University Press, 3rd edition edition, 2006.

Desidero ringraziare i Professori Paolo Villoresi e Giampiero Naletto per questi tre anni di dottorato, per le tante cose fatte insieme e per l'attenzione ed il supporto che mi hanno dato.
Un ringraziamento e un saluto particolare va a tutti i cari Amici e colleghi del laboratorio Luxor e del team Quantum Future e non da ultimo a Cristian Bonato, che se pur lontano, e' sempre stato un punto di confronto e di aiuto.
E' stato un piacere lavorare con voi.